PROCESSING AND PROPERTIES OF Cu-Al AND Cu-ZrB_2 MATERIALS DEVELOPED VIA POWDER METALLURGY

A dissertation work

submitted in partial fulfilment of the requirements

for the award of the degree of

DOCTOR OF PHILOSOPHY

in

METALLURGICAL AND MATERIALS ENGINEERING

by

Shaik Mahammad Ali
(Roll No.715054)

Under the guidance of

Dr. Brahma Raju Golla
Assistant Professor

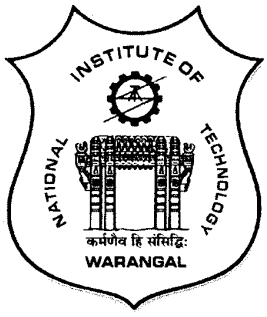

DEPARTMENT OF METALLURGICAL AND MATERIALS ENGINEERING
NATIONAL INSTITUTE OF TECHNOLOGY WARANGAL
WARANGAL-506 004 (T.S.) INDIA

December – 2020

Thesis Approval for Ph.D.

The thesis entitled **"Processing and properties of Cu-Al and Cu-ZrB_2 materials developed via powder metallurgy"** which is submitted by **Mr. Sk. Mahammad Ali (Roll No.715054)** is approved for the degree of **Doctor of Philosophy** in Metallurgical and Materials Engineering.

Examiner

_____

Supervisor

10/07/2020

Chairman

Date: 10/07/2020

DEPARTMENT OF METALLURGICAL AND MATERIALS ENGINEERING
NATIONAL INSTITUTE OF TECHNOLOGY WARANGAL
WARANGAL - 506 004 (T.S.) INDIA

CERTIFICATE

This is to certify that the work presented in the thesis entitled **"Processing and properties of Cu-Al and Cu-ZrB_2 materials developed via powder metallurgy"** which is being submitted by **Mr. Sk. Mahammad Ali (Roll No.715054),** is a bonafide work submitted to National Institute of Technology, Warangal in partial fulfilment of the requirements for the award of the degree of **Doctor of Philosophy** in **Metallurgical and Materials Engineering.** To the best of our knowledge, the work incorporated in this thesis has not been submitted to any other university or institute for the award of any other degree or diploma.

10/07/2020

Dr. Brahma Raju Golla

Assistant Professor and Thesis Supervisor
Department of Metallurgical and Materials Engineering
National Institute of Technology Warangal
Warangal-506 004

DECLARATION

This is to certify that the work presented in the thesis entitled "**Processing and properties of Cu-Al and Cu-ZrB_2 materials developed via powder metallurgy**" is a bonafide work done by me under the supervision of **Dr. Brahma Raju Golla**, and I was not submitted elsewhere for the award of any degree. I declare that this written submission represents my ideas in my own words, and where other ideas or words have been included, I have adequately cited and referenced the original sources. Also, I declare that I have followed all principles of academic honesty and integrity. I was not misrepresented or fabricated or falsified any idea/data/fact/source in my submission. I understand that any violation of the above will be a cause for disciplinary action by the Institute and can also evoke penal action from the sources which have thus not been properly cited or from whom proper permission has not been taken when needed.

Date: 10th July 2020

(Sk. Mahammad Ali)

ACKNOWLEDGEMENTS

I owe my deep sense of gratitude to my research supervisor and mentor **Dr. G. Brahma Raju**, Assistant Professor, Department of Metallurgical and Materials Engineering, National Institute of Technology Warangal for his wholehearted support, encouragement, guidance and patience during the research work. Without his untiring mentorship, constant inspiration, valuable discussions and suggestions, this thesis wouldn't have been possible. I appreciate him for critically going through the draft of my thesis and research papers.

I am grateful to **Prof. N.V. Ramana Rao**, Director, NIT Warangal; **Prof. T. Srinivasa Rao,** former Director, NIT Warangal for giving me an opportunity to carry out research work in the institute.

I am greatly indebted to **Dr. P. Suresh Babu**, Scientist 'D', Centre for Material Characterization and Testing, ARCI, Hyderabad for providing me with the nanoindentation test facilities and his valuable cooperation and guidance for nanoindentation hardness work. I profoundly thank **Dr. A Sambasiva Rao**, Scientist, DMRL, Hyderabad for providing his help in carrying out the EPMA analysis, valuable discussions during the arduous period of research progress.

I thank **Miss. G. Ramya** and **Sri. G. Srinivasulu,** Technical assistants**,** NIT Warangal for their help in carrying out the SEM and XRD studies. Also, I thank Sri. K. Yellaswaamy, Technical officer, Mechanical Engineering Department, NIT Warangal for the help in conducting surface roughness studies.

I take this opportunity to thank **Dr. Asit Kumar Khanra**, Associate Professor and Head of the Department and members of Doctoral Scrutiny Committee – **Prof. G. V. S. Nageswara Rao**, and **Dr. R. Arockia Kumar**, Assistant Professor, Department of Metallurgical and Materials Engineering, and **Dr. T. P. Tezeswi**, Assistant Professor, Department of Civil Engineering, NIT Warangal for their useful suggestions and periodical review of my progress during this course of PhD work. I also would like to thank all the faculty members of MMED for their support and help during my PhD.

I take this opportunity to acknowledge with sincere gratefulness to my fellow colleagues Sri. S. Siva Kumar, Sri. T. Sravan Kumar, Sri S. Vignesh Raja, Sri. K. Siva Kumar, Sri. P. Madhukar, Sri. T. Sarath, Dr. P. Prakash, Sri. C. Ravikanth, Sri. K. Nagabhushanam, Dr.

Bikya Naik, Sri. Venkat Reddy, Sri. Shiva Bejugama, Sri. E. Obulapathi, Sri. K. Ashish, Sri. V. Raju, Sri. K. Bharath and for their valuable help on varied occasions.

I also thank technical staff Sri G. Savvaiah, Mechanic A grade (Retired), Sri. K. Balaswamy, Mechanic A grade (Retired), Sri. Fayaz, Technical Assistant, Sri. Nandu, Technical Assistant and other technical and office staff of Metallurgical and Materials Engineering Department, NIT Warangal for their help during this research work.

I express my profound gratitude to my grandparents, my father **Sri. Sk. Abdul Khadar,** mother **Smt. Sk. Fathima,** father-in-law **Sri. Sk. Khaja**, mother-in-law **Smt. Sk. Rizwana,** my sister **Smt**. **Sk. Baajidbi**, my younger brother **Sk. Jakeer** and other family members for their personal support and encouragement.

My heartfelt gratitude to my elder brother **Sri. Sk. Baaji** for his continuous motivation, support and guidance from my childhood to present day.

Finally, I express my sincere thankfulness to my wife **Sk. Jabeen Taj** and son **Sk. Arsh** for their love, patience and sacrifices to make this achievement a reality. I thank almighty God from the depth of my heart for his constant shower of blessings at all the times of my life.

(Sk. Mahammad Ali)

Abstract

The present work investigates the microstructure and property correlation of hot-pressed copper (Cu)-X wt.% aluminium (Al) (X = 0, 3, 5, 10, 15) alloys and Cu-X wt.% zirconium diboride (ZrB_2) (X= 0, 1, 3, 5 and 10) composites. The starting powder compositions were subjected to mixing and milling processes to understand its effect on the densification, microstructure and properties of both Cu-Al alloys and Cu-ZrB_2 composites. The samples were prepared using hot press under low processing temperature of 500^oC and high pressure of 500 MPa for an optimal holding time of 30 min. The microstructure, mechanical, tribological and electrical properties of the hot-pressed (milled and mixed) compacts were evaluated. The morphology of the ball-milled Cu-Al and Cu-ZrB_2 powders changed from coarse flaky structure to small hard agglomerates with the addition of Al/ ZrB_2. While the mixing of Cu-Al/ZrB_2 powders resulted in uniform distribution of relatively coarse, flaky and soft agglomerate particles; in case of milled powders, relatively fine and hard agglomerates were observed. Considerably high density (min. 95.0% and max. 99.7% of theoretical density (ρ_{th})) was observed in the hot-pressed Cu-Al and Cu-ZrB_2 samples prepared via mixing condition. Whereas the density of Cu-Al and Cu-ZrB_2 samples varied between ~ 92.0-98.0% ρ_{th} for the hot-pressed samples prepared using milled powders. The crystallite size of Cu-Al (milled) and Cu-ZrB_2 (milled) samples decreased for both the milled powders and hot-pressed samples. The XRD, SEM-EDS analysis of the hot-pressed Cu-Al (milled) alloys confirmed the presence of α-Cu solid solution phase for the Cu alloyed with Al up to 5 wt.%. Further addition of Al to Cu lead to the formation of both intermetallic compound (Cu_9Al_4) and α-Cu solid solution phases. In contrast, Cu, α-Cu, γ_1 (Cu_9Al_4), δ (Cu_3Al_2), ζ_1 (Cu_4Al_3), η_2 (CuAl) and θ ($CuAl_2$) phases were observed in the hot-pressed Cu-Al (mixed) samples. Nevertheless, the presence of only Cu and ZrB_2 phases were evident in the hot-pressed Cu-ZrB_2 (milled and mixed) composites. The high hardness of 6.1 GPa was noted in Cu-Al (milled) alloys compared to other Cu-Al (mixed) alloys and Cu-ZrB_2 (milled/mixed) composites. Further, the nanoindentation tests indicated a significant increase in hardness (2.4 to 7.9 GPa) and elastic modulus (121.1 to 177.4 GPa) of hot-pressed Cu-Al (milled) alloys. The Cu-Al (milled) alloys were measured with very high compressive strength (up to 1120.2 MPa) and the low compressive strain varied in the range of 29.8 to 5.8% depending on the Al content. On the other hand, the Cu-Al (mixed) and Cu-ZrB_2 (mixed/milled) samples exhibited moderate compressive strength and high

compressive stain above 50% (except Cu-ZrB_2 (milled) composites). The coefficient of friction (COF) and specific abrasive wear rate of Cu alloys and Cu composites decreased with the addition of Al and ZrB_2, respectively. Low COF (0.49 to 0.16) and specific wear rate (49.3 $\times 10^{-3}$ to 0.8 $\times 10^{-3}$ mm^3/Nm) were observed in Cu-Al (milled) samples compared to Cu-Al (mixed) and Cu-ZrB_2 (milled and mixed) samples after sliding against SiC emery paper. In pure Cu (milled and mixed), the continuous chips (wear debris) were formed during sliding wear by the plowing mechanism. Whereas the major amount of material loss occurred due to the plowing mechanism with discontinuous and short chip formation in Cu-Al alloys and Cu-ZrB_2 composites (both the milled and mixed conditions). The electrical conductivity of Cu-Al and Cu-ZrB_2 samples decreased with the addition of Al and ZrB_2, respectively. The high electrical conductivity about 97.0% IACS was obtained with pure Cu (as received) and the conductivity was reduced to ~75.0% IACS for Cu (milled) due to the lattice strain in the milled Cu. However, Cu-ZrB_2 (mixed) composites showed better electrical properties (68.2-97.0% IACS) than the other Cu alloys and composite systems. On a whole, the Cu-Al/Cu-ZrB_2 materials processed via mixing exhibited moderate or better electrical properties and is advantageous as it lowers processing costs than the milled samples. These results indicate the advantage of Al and ZrB_2 addition and use of milling/mixing conditions in controlling microstructure, mechanical, wear and electrical properties of Cu.

Keywords: Cu, Al, ZrB_2, Ball milling, Hot-pressing, Mechanical properties, Wear and Electrical conductivity.

CONTENTS

NOMENCLATURE

SYMBOLS

β_{anodic}	Anodic Tafel slope
$\beta_{Cathodic}$	Cathodic Tafel slope
δ	Dislocation density
θ	Diffraction angle
λ	Wavelength
ρ	Measured density
ρ_{th}	Theoretical density
υ	Poisons ratio
Ψ	Plasticity index
a	Lattice parameter
A	Area
C	Concentration of species
d	Sliding distance
d_i	Interplanar spacing
D	Diffusion coefficient of species
E	Elastic modulus
E_{corr}	Corrosion potential
E_i	Indentor modulus
E_{oc}	Open circuit potential
E_r	Reduced modulus
E_s	Sample modulus
E_w	Equivalent weight
f	Faraday's constant
H	Hardness
h_c	Contact depth
h_f	Depth of residual impression
hkl	Miller indices
h_{max}	Maximum displacement
I_{corr}	Corrosion current

l	Load
L	Crystallite size
n	No. of electrons transferred
P	Pressure
Q	Constant phase elements
R	Gas constant
R_a	Roughness
R_{ct}	Charge transfer resistance
R_f	Film resistance
rpm	Revolutions per minute
R_s	Electrolyte resistance
R_z	Total depth of roughness
T	Temperature
t	Time
v	Velocity
Hv	Vickers hardness number
W	Weight
W	Warburg impedance
w_e	Elastic recoverable work
w_p	Residual plastic work
w_t	Total work
Z	Impedance

ABBREVIATIONS

ARB	Accumulated roll bonding
ASTM	American Society for Testing and Materials
BHN	Brinnel hardness number
BPR	Ball to powder ratio
BSE	Back scatter electron
C.B	Counter-body
COF	Coefficient of friction
CP	Cold-pressing

CPE	Constant phase elements
CR	Cold rolling
DSC	Differential scanning calorimetry
ECAP	Equal channel angular pressing
EDM	Electric discharge machining
EDS	Energy dispersive spectroscope
EIS	Electrochemical impedance spectroscopic
EPMA	Electron probe microanalyzer
EX	Extrusion
FCC	Face centered cubic
FWHM	Full width half maximum
HIP	Hot isostatic pressing
HP	Hot-pressing
HPT	High-pressure torsion
HR	Hot rolling
HRC	Rockwell hardness C
HRTEM	High-resolution transmission electron microscopy
HT	Heat treatment
IACS	International Annealed Copper Standard
ICSD	Inorganic crystal structure database
JCPDS	Joint Committee on Powder Diffraction Standards
MA	Mechanical alloying
ML	Milling
MX	Mixing
OCP	Open circuit potential
OM	Optical microscope
PM	Powder metallurgy
PS	Pressureless sintering
RD	Relative density
SE	Secondary electron
SEM	Scanning electron microscope
SPD	Severe plastic deformation
SPS	Spark plasma sintering

TEM	Transmission electron microscopy
UTM	Universal testing machine
VHN	Vickers hardness number
VIM	Vacuum induction melting
W-H	Williamson–Hall
XRD	X-ray diffraction

LIST OF FIGURES

S. No. **Name** **Page No.**

LIST OF TABLES

S. No. **Name** **Page No.**

Chapter 1

Introduction

1 Chapter 1

1.1 Background and motivation

Copper (Cu) based materials have been extensively used for various engineering applications such as naval, rail, aerospace, energy and automobile industries etc. [1]. In particular, braking and electro-discharge machining (EDM) electrode applications require the development of Cu based materials with high strength, good electrical conductivity and workability, structural stability at high temperatures (~200 – 450 ^{o}C), good wear, oxidation and corrosion resistance [1,2]. Cu has been alloyed with alloying elements such as Zn, Sn, Al, W, Fe, Cr and Zr, etc. and these alloys were mainly strengthened by solid solution strengthening or precipitation hardening mechanisms [3–7]. In particular, in view of its nonsparking characteristics, good wear and corrosion resistance, the Cu-Al alloys have the potentiality for a range of applications such as welding electrodes, tool material for sheet forming, bearings, rocket nozzle, heat sink, automobile, mining and naval engineering applications etc. [8].

Also, Cu can be strengthened by incorporating with the hard ceramic reinforcements such as Al_2O_3, B_4C, SiC, Si_3N_4, TiB_2, TiC, ZrB_2 and ZrO_2 etc. by dispersion strengthening [9–14]. Among all the ceramic additives, borides and carbides, particularly, TiB_2, SiC, and TiC are widely used as the reinforcements or additive materials to prepare Cu matrix

composites. Especially, in the present study, ZrB_2 was selected as a reinforcement for Cu because it possesses high hardness, high electrical and thermal conductivity, and good chemical stability which enhances the performance of Cu composites for electrical and structural applications as well. Also, As limited studies were available on Cu-ZrB_2 composites in the open literature, the present work widens the understanding of these materials. Because of the potential applications of Cu composites in heavy-duty wear, mining and electric applications, it is essential to improve mechanical and wear properties of Cu with good electrical properties.

Traditionally, Cu based materials were processed by casting route [15]. One of the major disadvantages of the casting route is the coarse grain structure that will lead to poor mechanical properties. Hence, it is required to use other processing technique to control the grain size, particle distribution and improve the mechanical properties of Cu based materials. Mechanical working methods such as severe plastic deformation (SPD) techniques including high-pressure torsion (HPT) [16], equal channel angular pressing (ECAP) [17] twist extrusion [18] accumulated roll bonding [19] repetitive corrugation and straightening [20] cryo-rolling [21] have been applied. Recently, friction stir processing **[**22**]** was also adopted for Cu based materials. Powder metallurgy (PM) processes (including Mechanical alloying (MA), spark plasma sintering (SPS)) and additive manufacturing methods (such as selective laser sintering and selective laser melting) have also been attempted to produce Cu materials with fine structure **[**23–26**]**.

The processing of Cu based materials through powder metallurgy, particularly conventional pressureless sintering technique has been reported by many researchers, in which the powders were consolidated using cold press and further sintered the compact at higher temperatures [27,28]. Shukla et al. [29] prepared the Cu-Cr-Nb alloys via powder metallurgy route at low pressures. They processed at a high temperature of 800-1000 ^{o}C and low pressure of 10-30 MPa. Maximum relative density of upto ~99% was obtained Cu-Cr-Nb alloys and the formation of fine Cr_2Nb precipitates increased the hardness (100 BHN) and tensile strength (400 MPa).

Commercially Cu–Al alloys are popularly known as Cu–Al bronzes or Al bronzes and are of particular interest for marine and automobile applications due to its excellent wear, corrosion resistance and good mechanical properties [30,31]. In particular, Cu–Al alloys are available with various amounts of aluminium addition (up to 10 wt.%) [32]. Krebs

et al. [30] investigated the use of Cu–10Al–5Fe–5Ni as a coating material to reduce cavitation damage of ship rudder. It has to be noted that generally other alloying elements such as Fe, Ni, Si, Mg were added to Cu–Al alloys for improving specific properties [3]. In another work, Meyer et al. **[**31**]** reported that Cu–Al bronze used as non-sparking material since no mechanical sparks occurred when the bronze was in contact with stainless steel. Gyimah [33] developed new Cu–Al alloy based composite material for train brake pad application and it was stated that materials processed at a high sintering temperature of 950 ^{o}C and it exhibited high wear properties in view of its better density. Soliman and Habib [34] observed that ageing (at 450 ^{o}C for 12 h) of Cu–12.5 wt.% Al shape memory alloy doubled the hardness (262 Hv) when compared to unaged alloy.

In recent years, researchers paid more attention towards the mechanical alloying of Cu-based alloys due to its potential and versatility in producing the alloys, and nanocrystalline materials with improved properties [35–38]. Youssef et al. [35] reported the effect of grain size on mechanical and electrical properties of bulk nanocrystalline Cu–1at.% Nb alloy prepared by mechanical alloying. High yield strength of 1035 MPa was reported for Cu–1 at.% Nb alloys and it was attributed to its fine grain structure (~18 nm). In another work, the saturation limit of solubility in Cu–Fe system was significantly enhanced by the mechanical alloying approach [36]. Also, the ball milling procedure was adopted to enhance the solid solubility of Cu–Cr–Mo ternary system [37]. As the milling time increased up to 50 h, the particle size of Cu–20Cr(Mo) alloy considerably reduced to less than 20 nm. Further, these nano-sized powders enhanced the densification of the Cu alloy [37]. Chakravarty et al. [38] explained the grain size stabilization and strengthening of cryomilled nano-Cu–12 at.% Al alloy. It was revealed that the hardness of the nano-sized alloy was significantly high when compared to the raw powders.

Rajkovic et al. [39] prepared the Cu-3.5Al alloys through powder metallurgy (PM) route. They consolidate the ball-milled Cu-Al powders using hot-pressing equipment at a temperature of 800 ^{o}C under a pressure of 35 MPa for 1 h. The hardness of the Cu-3.5Al was observed to be 3.06 GPa due to the formation of solid solution which is 18% high compared to Cu-4Al_2O_3 composites processed at the similar hot-pressing conditions. In another work, Traleski et al. [40] processed the Cu-Al-Ni alloys via. PM route at a pressureless sintering temperature between 900 to 950 ^{o}C. Prior to the consolidation of samples, the powders were ball milled for 8 h with a ball to powder ratio (BPR) of 5:1. The relative density of the Cu-13.2Al-3.8Ni alloys was found to be 78.5% and the corresponding

hardness was 3.72 GPa which was attributed to the developed lattice strains and intermetallic compounds. Saiprasad et al. [41] reported that the dense Cu-5Al alloys could be prepared by the PM route. Initially, the Cu-Al powders were mechanically alloyed for 8 h and then consolidated using spark plasma sintering (SPS) method at 700 ^{o}C under a pressure of 40 MPa for 10 min. The relative density and hardness of the samples was 98.5% and 0.90 GPa, respectively. Gohar et al. [42] investigate the effect of Ag addition on the thermal and mechanical properties of Cu-10Al-XAg (X: 0-6 wt.%) alloys processed through PM technique. They processed the Cu-Al-Ag powders using a planetary ball mill at 200 rpm for 5 h. The powders were consolidated using cold press at 200 MPa and sintered at 850 ^{o}C for 3 h. They achieved relatively low density (~75%) and low compressive strength (155 MPa) for Cu alloys.

As far as the novelty of the present work is concerned in developing Cu-Al alloys, a systematic study on understanding the use of Al on microstructure and properties of Cu is carried out, which is lacking in the open literature. The present work explores whether the high amount of Al addition (upto 15 wt.%) along with the powder preparation (ball milling/mixing) methods have any beneficial effects on properties of Cu.

Shang et al. [28] studied the effect of ZrB_2 (and other factors include the shape and size of ZrB_2 particles) along with hot-press sintering parameters on Cu–ZrB_2 composites. Their work showed that the relative density (~91%–75%) of Cu decreased with the ZrB_2 addition. In recent work, Wang et al. [27] prepared the Cu–ZrB_2 composites through hot-pressing route with the application of high processing temperature and low applied pressure (840°C and 25 MPa). They reported that the use of micron-sized ZrB_2 significantly improved the hardness of Cu up to ~1.0 GPa and electrical conductivity more than 58% IACS. In another study, Fan et al. [9] explored the effect of ZrB_2 on the wear and electrical properties of in-situ Cu–ZrB_2 composites. They found that the addition of ZrB_2 particles to Cu resulted enhancement of the hardness and wear properties of Cu composites by ~2.0 times when compared to pure Cu. In another work, Zhang et al. **[**43**]** reported that the use of low content of ZrB_2 (7 wt.%) improved the hardness up to 1.2 GPa without much change in its electrical conductivity (~70% IACS). From the above discussion, it is clear that the reinforcement amount has a significant effect on the properties of Cu. Restricting the reinforcement content below 12 wt.% reportedly improved the mechanical and wear properties while retaining good electrical conductivity of Cu composites [9,43–45].

However, in the literature, studies on Cu-Al alloys and Cu-ZrB_2 composites have been low and in particular, systematic investigation of Al and ZrB_2 effect on the microstructure and various properties of Cu processed via PM route. In this work, we attempted to process the Cu-Al alloys and Cu-ZrB_2 composites through the hot pressing route. These Cu based materials were consolidated relatively at a low sintering temperature of 500 ^oC with the application of high hot press pressure of 500 MPa in a vacuum environment. It has three implications: (i) achieving good density at low sintering temperature and it can result in improvement of properties due to fine structure, (ii) avoiding the use of multiple combinations of processes, for example, most of the instances heat treatment/mechanical working methods is used as an additional step with the primary process in order to improve properties, and (iii) reducing the processing cost. The high-pressure processes are reportedly advantageous as they facilitate high nucleation rate, reduce atomic diffusion coefficient, restrain grain growth, result in refinement of grain structure and improve the properties [25,26].

1.2 Objectives of the present work

- Processing of Cu-X wt.% Al alloys (X = 0, 1, 3, 5, 10 and 15) and Cu-X wt.% ZrB_2 composites (X = 0, 1, 3, 5 and 10) via two different powder processing conditions (mixing and ball milling/mechanical alloying conditions) and study its effect on the densification and microstructure
- Realizing the usefulness of (high pressure) hot pressing in densifying Cu-Al alloys and Cu-ZrB_2 composites at the low sintering temperature with a good combination of properties
- Evaluating mechanical, wear and electrical properties of Cu-Al alloys
- Assessing the influence of hard ZrB_2 ceramic reinforcement addition on the mechanical, wear and electrical properties of Cu
- Comparing the performance of Cu-Al and Cu-ZrB_2 materials to understand the underlying mechanisms and relating it with other Cu-based materials reported in the literature

1.3 Organization of thesis

The thesis contains 8 chapters. The 1st chapter provides an introduction, highlights the background of present work, objectives and structure of the thesis in brief. The literature review on Cu based materials was presented in the 2nd chapter. The extensive survey of similar work carried out by the other researchers and scientists was covered in this chapter. The relevant reported research works were referred wherever it is necessary to support and explain the present experimental findings. Also, the chapter dedicated to exploring detailed information regarding copper-based materials and processing techniques; the effect of alloying elements on mechanical, tribological and electrical properties. The 3rd chapter deals with the materials and methodology of the current work and details of materials and instruments, sample preparation and characterization procedures were discussed. The 4th, 5th, 6th and 7th chapters present the results and discussion of different copper-based systems, such as Cu-Al alloys and Cu-ZrB_2 composites processed through mixing and milling routes in the form of figures, tables, equations and schematics. Each of these chapters begins with a brief introduction, later detailed discussion of results was made based on the obtained experimental results and summarized with the conclusions and lastly, the relevant references were cited. Finally, the 8th chapter highlights the conclusions based on the experimental findings. The references used in the thesis has been listed at the end of the thesis. The following schematic (see **Fig. 1.1**) illustrates the work plan and methodology of the current research work.

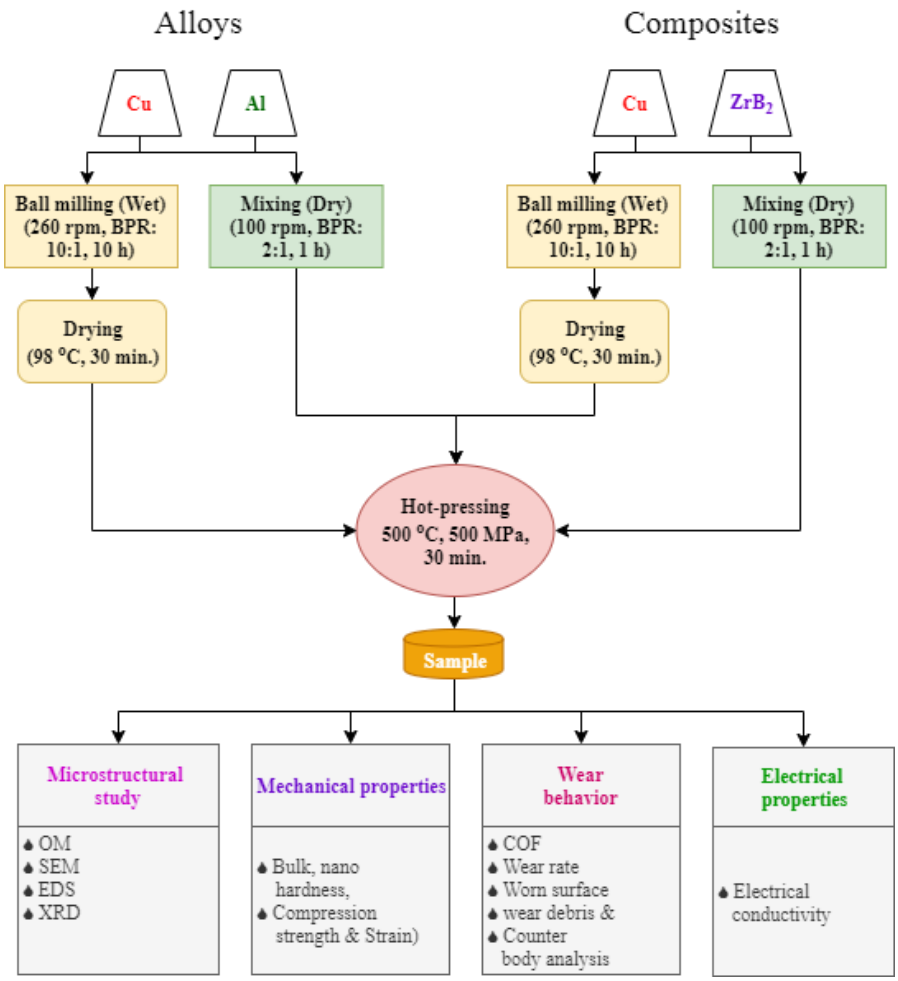

Fig. 1.1 Schematic of the work plan.

1.4 Novelty

Cu based materials are widely used in structural, thermal and electrical applications such as welding electrodes, tool material for sheet forming, bearings, rocket nozzle, heat sink, automobile, mining and naval engineering applications due to the excellent formability, moderate strength, good electrical and thermal conductivity. Numerous studies have been carried out to improve the strength of the Cu; especially, Cu based materials processed through powder metallurgy (PM) route by controlling processing parameters. Based on the literature, we attempted to develop Cu based materials through PM at low processing temperatures with the application of high-pressure hot press (with short holding time: 30 minutes). Such techniques certainly reduce the processing cost, result in materials with fine microstructure and improvement in the densification, mechanical, tribological and electrical properties. In fact, to refine the microstructure and improve mechanical properties

of Cu materials, the additional processing steps (such as heat treatment and mechanical working methods) have been widely followed. In the present work, the effect of mechanical alloying and mixing of powders on the Cu based materials has also been explored. It proved that those processing steps had a significant impact on the microstructure and properties of Cu-Al alloys and Cu-ZrB_2 composites.

Chapter 2

Literature

2 Chapter 2

The present chapter begins with the brief introduction on copper (Cu) and Cu-alloys and its properties followed by a discussion on the use of different processing techniques (such as casting, powder metallurgy, superplastic deformation and other processes) to prepare Cu materials. Particularly, the effect of processing parameters, alloying elements and secondary reinforcements on mechanical, wear and electrical properties of Cu. Finally, the applications of Cu based materials is illustrated.

2.1 Copper

Copper and copper alloys have a big timeline of their usage from the past ~ 10,000 years [46]. One of the major ages of human history was termed as copper age (also, bronze age). The invention of copper played an important role in human civilization from the stone age to modern age. Cu is a non-polymorphous material with face centered cubic (FCC) crystal structure and belongs to the group of non-ferrous metals. It is reddish-brown in colour and having the melting temperature of 1083˚C and density of 8.9 g/cc. Copper is extracted from different ores (Bornite, Chalcopyrite, Chalcocite, Covellite and Cuprite). Copper is

widely extracted from the oxide and sulphide ores. Commercially pure copper is available (> 99.92%) in the market and other impurities kept at the minimum level (during extraction) for its specific applications.

The Cu metal possesses various distinctive properties such as high electrical conductivity (5.96×10^7 S/m), good thermal conductivity (394 W/mK), excellent ductility, corrosion resistance and biofouling resistance [47]. These exceptional qualities of pure Cu make it suitable for electrical, electronic, energy, automobile, petrochemical and marine applications. Some specific applications like electrical wires, switches, connectors, printed circuit boards, electrodes in electro-discharge machines (EDM); pipes in solar heaters, condenser tubes in power plants; filters and valves in corrosive petroleum environments; radiators, braking pads, cylinder liners, gears and fasteners in automobiles; seawater piping, heat exchangers and fuel lines in ships. In particular, bearings, electrical connectors and braking system require good strength, electrical conductivity, thermal conductivity as well as wear resistance. The poor mechanical strength and wear resistance of pure Cu often needs to be improved without much affecting its electrical and thermal conductivity.

2.2 Cu-based alloys

The pure Cu can be strengthened by various strengthening mechanisms such as solid solution strengthening, precipitation hardening, dispersion strengthening, grain boundary strengthening or grain refinement and strain hardening [48,49]. In solid solution strengthening, a minor amount of other alloying elements is added to enhance the desired characteristic properties of copper. **Fig. 2.1** presents the flow diagram of various alloying elements added to Cu in order to prepare Cu alloys. The Cu alloys were designated with Unified Numbering Systems and its specification is provided in **Table 2.1**. The Cu is commonly alloyed with aluminium (Al), chromium (Cr), nickel (Ni), lead (Pb), tin (Sn), zinc (Zn) and zirconium (Zr) to improve its strength, wear resistance and corrosion resistance [47,50–58]. In solid solution strengthening method, the major alloying elements added to copper are Al, B, Be, Cr, Co, Fe, Ga, Ni, Mg, Mn, Pb, Si, Sn, Ti, V, W, Zn and Zr [4–7,34,48,57,59–66].

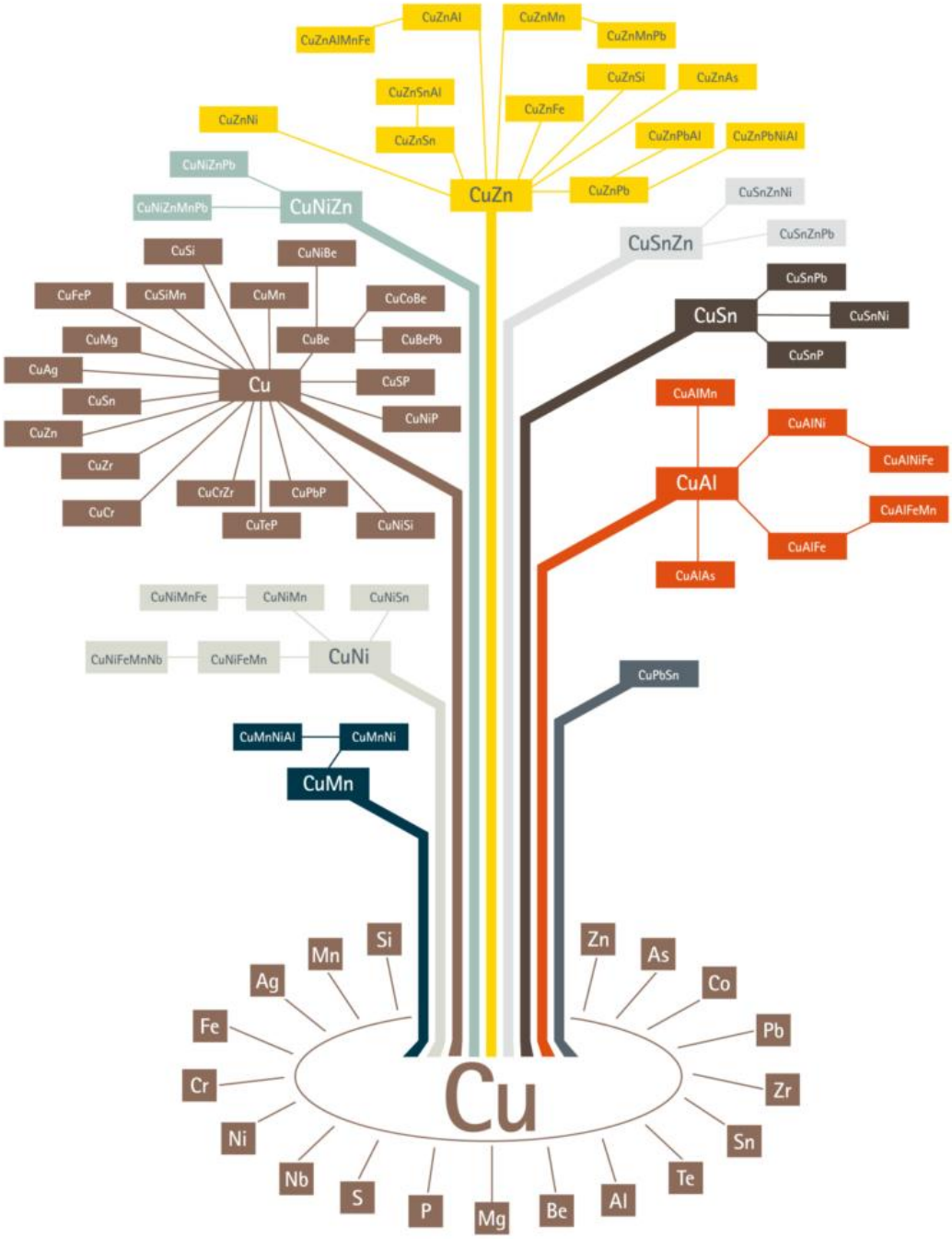

Fig. 2.1 Flow diagram showing different Cu alloys that are formed with the addition of various alloying elements to Cu [46].

The concept of precipitation strengthening was discovered in the first decade of the 20th century. A Cu alloy can be termed as precipitation-hardenable (for example Cu-Al and Cu-Be) when its hardness or strength can be increased with ageing heat treatment [67,68]. In case of precipitation hardening, the strength of Cu alloys enhanced with the fine precipitates while maintaining the good electrical and thermal properties. Further ageing heat treatment is optimized to control the size of precipitates and thus attaining desired

properties of the alloys [69]. In this strengthening method, rapid solidification process produces the ultra-fine precipitates that results in higher mechanical properties [70]. The limitation of precipitation hardening is the lacking of strength at above 500 ^{o}C which detracts the structural stability due to coarsening of the precipitated particles.

Table 2.1 Classification of various Cu alloys and corresponding UNS numbering.

Alloy	**Unified Numbering Systems**	
	Wrought alloys	**Cast alloys**
Copper	C10100 - C15999	C80000 - C81399
High copper alloys (<96% Cu)	C16000 - C19999	C81400 - C83299
Copper-zinc alloys (<40% Zn)	C20000 - C49999	C83300 - C89999
Copper-tin alloys (<10% Sn)	C50000 – C59999	C90000 - C95199
Copper- Aluminium alloys (<10% Al)	C60000 – C69999	C95200 - C95999
Copper-nickel alloys (<30% Ni)	C70000 - C73499	C96000 - C96999
Copper-nickel-silvers	C73500 - C79999	C97000 - C97999
Copper-lead alloys	--	C98000 - C98999
Special alloys	--	C99000 - C99999

2.1.1 Copper – Aluminium (Cu-Al) alloys

Cu-Al alloys are also termed as aluminium bronzes. The commercially available alloys in the market exist as-cast ingots/rods and having Al content ranging between 5 to 11 wt.% [15]. In general, a small quantity of Cr, Fe, Ni, Mn and Si are added to get desired properties of the Cu-Al alloy [71]. These alloys exhibit superior mechanical, non-sparking and corrosion properties compared to the other groups of Cu alloys which make them as the first choice among all Cu alloys. Cu-Al alloys are the promising materials for the application where excellent mechanical properties, high hardness and corrosion resistance are required. Cu-Al alloys have similar strength to that of low alloy steels. Good fatigue, creep and oxidation resistance of Cu-Al alloys gives long service life at elevated temperatures. The Cu-Al alloys are well suitable for the bearing and small gear applications because of the high hardness and wear resistance. Other properties include good weldability, machinability and availability of these alloys make the production more economical. They give outstanding performance in the sea environment similar to the stainless steels due to the excellent corrosion resistance. The Cu-Al alloys have a wide variety of applications in the

various engineering applications such as large bearings and bushings used in mining applications, gear selector forks in automobiles, non-sparking valves used in hydraulic pumps, pipe fittings and tubes of heat exchangers, deep drawing dies, non-magnetic parts in the electric equipment, landing gears in aircraft, underwater fasteners and propellers used in naval ships and structural retrofit building applications.

Cu-Al alloys have been conventionally processed through the casting technique. These alloys expected to have high relative density compared to other processing methods. The cast Cu-Al alloys are available in two distinct forms; one is single-phase alpha alloy and the second one is duplex type alloys. The single-phase alloys consist of Al content below 9% with a minor amount of iron which is suitable for cold working. The duplex alloys consist of Al ranging from 9 - 11% with a small content of Fe and Ni. Addition of a small amount of alloying elements to the Cu may increase the recrystallization temperature and lead to refinement of microstructure which further increases the mechanical properties [72]. The addition of silicon lowers the magnetic permeability of the Cu-Al alloys [73] and the castability of the aluminium bronzes can be enhanced using the magnesium [74].

The mechanical properties of the Cu-Al alloys primarily depend on the Al content. At lower Al content (<8 wt.%), these alloys exhibit good cold working properties which are favourable for the sheet, strip making, tube and wire drawing operations. These alloys are annealed at a temperature in the range between 595 - 650 ^{o}C. Hasan et al. [75] fabricated the Cu-Al alloy through the casting process. They observed the presence of α-phase copper-rich solid solution and exhibited Widmanstatten microstructure with the addition of 10Al. Maki et al. [48] reported that the solid solution strengthening significantly increases the strength of the copper but with a large decrease in electrical conductivity. This can happen due to the solute atoms dissolved in the copper which produces lattice distortion or strain and that lead to more scattering of the electrons. To achieve the high strength along with the good electrical conductivity of copper alloys, precipitation hardening method is preferred [15,76]. However, this method is very expensive due to the use of costly alloying additives such as Ag, Be, Co, Ni or the use of secondary heat treatment processes to produce uniformly distributed fine precipitates [77].

In the recent work, the strength of the copper was improved without affecting its ductility by introducing the gradient structures in the materials using various techniques such as pre-torsional treatment [78,79], surface mechanical grinding treatment [80] and surface

mechanical attrition treatment [81]. In these processes, simultaneous strain hardening and strain softening were produced by the grain refinement and the grain growth, respectively. In another work, Gong et al. [78] fabricated the Cu-6Al alloy through the vacuum induction melting technique. Further, they carried out the hot rolling followed by annealing at 900 ^{o}C for 10 h to obtain the ultra-fine grained structure. Also, pre-torsional treatment was performed to improve the Cu-Al alloys. They found that the size of grains become more than 1 mm after hot rolling, torsion and annealing treatments. The microstructure of the Cu-Al alloy grain structure is shown in **Fig. 2.2**. The hardness of the Cu-6Al alloys reported upto ~2.05 GPa after pre-torsional treatment. The tensile strength of the Cu-6Al alloys increased (~362 MPa) with the torsional pressure without much affecting the strain (~62%). The increase in strength of Cu-Al alloys was attributed to the strain hardening. Chen et al. [82] conducted a oscillating ball-on-disc wear test for Cu-2.2Al alloys (Counter-body: WC-Co) processed through the vacuum induction melting. They reported that the wear resistance of theses alloys was increased with small amount of Al content (0.5 wt.%). With further increase of Al content upto 2.2 wt.%, the wear loss increased due to the increase of fracture in the lamellar recrystallization structure.

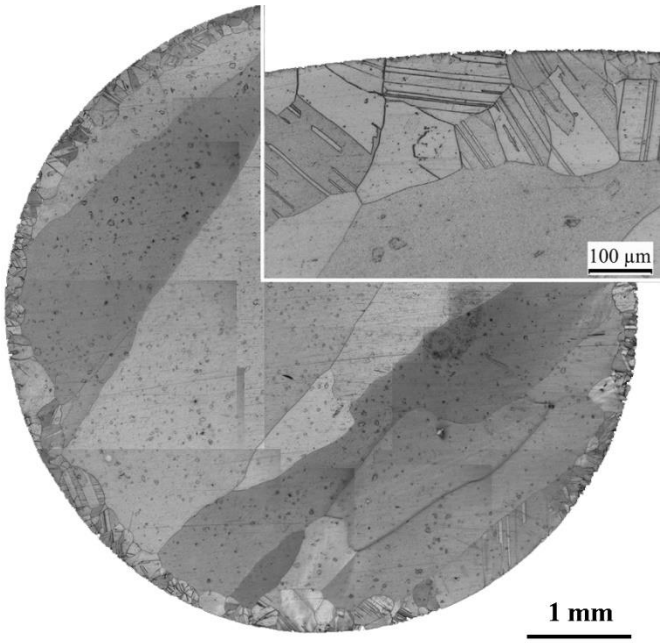

Fig. 2.2 The optical micrographs of the ultra-coarse-grained Cu-6Al alloy with a coarse-grained (CG) surface layer, respectively.

Fig. 2.3 shows the equilibrium phase diagram of Cu-Al alloy. Al completely soluble in the liquid copper. But the solubility of Al is limited upto 9.4 wt.% in the solid solution state [77,83]. According to **Eq. 2.1**, the β phase transforms into the α and γ_2 phases at the

eutectoid reaction. At a temperature of 500 ^{o}C, a maximum amount of aluminium (up to 15.6%) dissolves in copper and forms γ_2 phase. Similar observations were reported for die-casted Cu-11.8 wt.% Al alloy, that formed the γ_2 phase by eutectoid decomposition of β phase at a temperature of 565 ^{o}C [84].

$$\begin{array}{lccccc} & \alpha & + & \gamma_2 & \overset{\text{Heating}}{\underset{\text{Cooling}}{\rightleftharpoons}} & \beta \\ \text{Al wt.\%} & (9.4\ \%) & & (15.6\ \%) & & (11.8\ \%) \end{array} \qquad (2.1)$$

Aluminium bronzes are copper-based alloys with aluminium as the major alloying element usually in the range 5 - 14% compositionally in the alloy, other alloying elements sometimes intentionally introduced are iron, nickel, manganese, silicon and tin depending on the intended application of the aluminium bronze.

As the Al content varied between 8 wt.% to 10 wt.%, the alloys produce secondary harder phase in the soft solid solution phase (Alpha-beta alloys), which strengthen the alloy [68]. These alloys are heat treatable and their heat treatment cycle is shown in **Fig. 2.3.** Slow cooling to room temperature of these alloys produces the alpha and gamma dual phases. Reheating of these alloys above the eutectoid temperature (565 ^{o}C) yields the alpha and beta phases. Further heating of these alloys about 910 ^{o}C, results in beta solid solution phase; which can be converted to the martensitic structure by heating upto 960 ^{o}C followed by quenching [68]. Further increase of Al (>10 wt.%) develops more hard intermetallic compounds; which significantly increases its strength and hardness [50,85]. Ying et al. [86], Feng et al. [87], Abbasi et al. [88], Mai et al. [89], Lee et al. [90] and Chaudari reported that the intermetallic compounds such as Cu_9Al_4, Cu_3Al_2, Cu_4Al_3, CuAl and $CuAl_2$ were formed at the interface junction of Cu and Al due to the variation in diffusion rate from the interface surfaces. Also, Pintore et al. [91] explained the diffusion phenomena of the bilayer Cu-Al prepared using the casting process. They reported formation of Cu_4Al_3, CuAl and $CuAl_2$ at the interface junction of those two layers.

Recently, Alex et al. [92,93] developed the Cu-Al and Cu-Sn based intermetallic alloys for solar energy applications. Their work revealed that the Cu-based intermetallic compounds can be used as a coating material (Hardness: ~2 GPa) in the solar panels to protect the glass surfaces without affecting its reflectance.

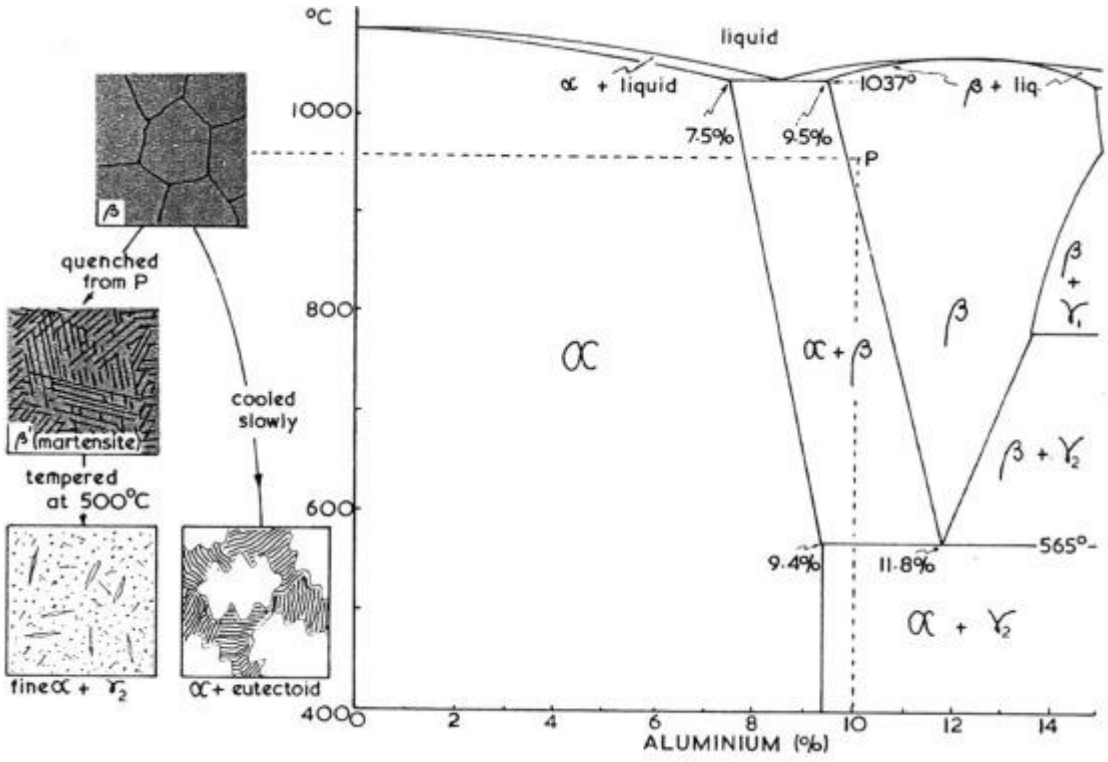

Fig. 2.3 Cu–Al equilibrium phase diagram (copper-rich end). The resultant microstructure with heat treatment indicates the types of phases present in the alloy [68].

The Cu- Al intermetallic alloys prepared through casting route having hardness upto 2.1 GPa; whereas, the alloys fabricate through powder metallurgy technique showed better hardness upto 7.8 GPa compare to cast one due to the combination of fine microstructure and the presence of intermetallic compounds [94]. Chakravarty et al. [38] reported that the grain growth of the nanocrystalline Cu-12 at.% Al alloy was restricted by the pinning effect produced at elevated temperature by the nano-scale intermetallic compounds. The hardness of these alloys slightly decreased with the annealing at 900 ^{o}C.

However, in the literature, studies on Cu-Al alloys have been low and in particular, systematic investigation of Al effect on the microstructure and mechanical properties of Cu. Calvo et al. [95] studied the effect of pressure and temperature on bonding between Cu and Al. Their work revealed that the bonding between Cu and Al was mainly dominated by diffusion (between 400 ^{o}C – 520 ^{o}C and up to 289 h). The diffusion bonding between Cu and Al reportedly starts at around 500 ^{o}C [96]. In particular, Chen et al. [97] proposed the diffusion mechanism in Cu-Al alloy system and the high diffusion rate of Al resulted in the formation of the saturated solid solution at the interface of Cu and Al. In another work, Wu et al. [98] refined the microstructure by reducing the diffusion coefficient with the application of high pressure (5 GPa) heat treatment at 750 ^{o}C for 15 min. Wang et al. [99]

stated that high-pressure heat treatment favours the formation of a fine structure as it reduces the solid phase transformation temperature and activation energy.

2.1.2 Copper – Chromium (Cu-Cr) alloys

Cu-Cr alloys are the high copper alloys consists of Cr content ranging between 0.6 – 1.2 wt.% due to the low diffusivity of Cr in Cu. The higher amount of Cr content results precipitate formation in the Cu at elevated temperatures. Cu-Cr alloys are the most suitable materials for nuclear and aerospace industries due to their excellent mechanical, thermal and electrical properties [100]. Other applications include resistance welding electrodes, spot welding tips, circuit breakers, electric connectors and thermal conductors. The Cu-Cr alloys having better corrosion resistance compared to the pure copper due to the formation of a protective layer under the sea environment. The strength of the Cu-Cr alloys is two times high and electrical conductivity is about 85 % IACS as that of the pure copper. The microstructure of the quenched Cu-Cr alloys is similar to the pure copper where the chromium remains a supersaturated solid solution in the copper. The slow cooling of the alloy allows the pure copper to solidify it in the initial stage, later the eutectic mixture of alpha and chromium. These eutectic materials consist of a lamellar structure in the dendritic regions [101]. TEM image of Cu-43 wt.%Cr alloy showing equiaxed and randomly oriented ultra-fine grains (average grain size ~13.7 nm) after the sample subjected to high-pressure torsion (HPT) sample with 100 rotations (**Fig. 2.4a**) [7]. The HRTEM image shows the presence of Cu and Cr grains with different zone axes (**Fig. 2.4b**).

Recently, Patra et al. [102] processed the Cu-Cr alloys through powder metallurgy technique in which mechanical alloying followed by sintering was carried out. They studied the effect of sintering pressure on the densification and mechanical properties of the Cu-8Cr alloys. Their results reveal that the relative density, mechanical properties and electrical conductivity were increased with the increase in sintering pressure and sintering temperature. Zhang et al. [103] studied the effect of Cr on the mechanical and electrical conductivity of Cu-Cr alloys fabricated through selective laser melting technique. This technique was found to be advantageous where the relative density of the Cu-Cr alloy was reported upto 99.98%. The tensile strength of these alloys after annealing at 480 ^{o}C for 4 h was moderately high (upto 468 MPa). This can be attributed to the Cr precipitates. The electrical conductivity of the Cu-Cr alloys was found to be 98.3% IACS; whereas the

electrical conductivity of these alloys before annealing was 37.7% IACS due to the presence of Cu-Cr solid solution phase which scatters the movement of the electrons.

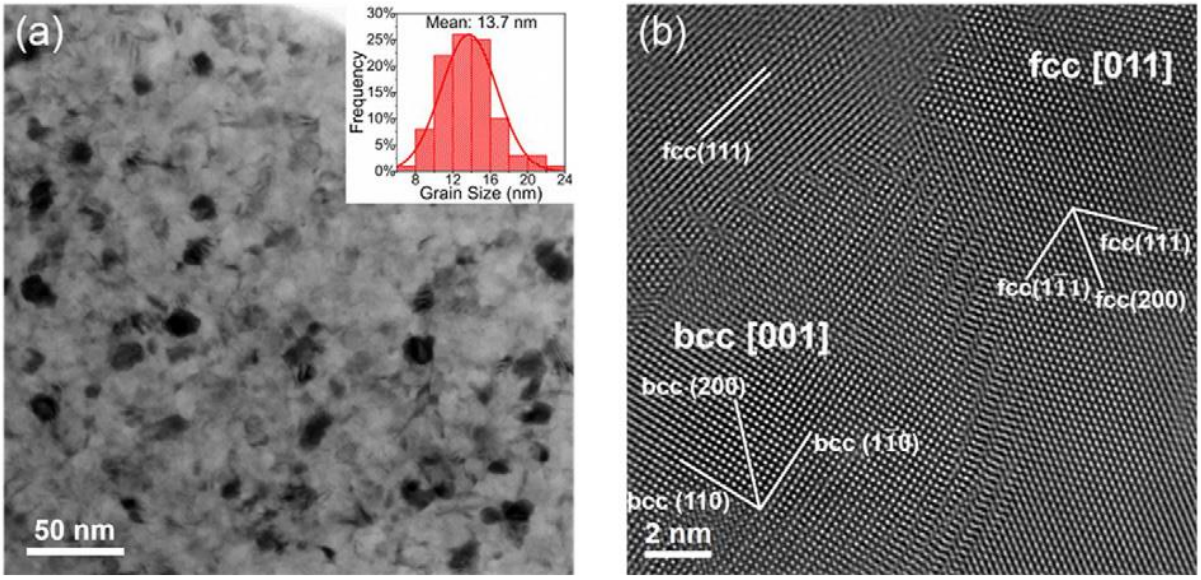

Fig. 2.4 Microstructure of Cu-43 wt.% Cr after subjecting to high-pressure torsion (HPT) sample with 100 rotations. (a) Transmission Electron microscope (TEM) bright-field image and (b) high-resolution TEM (HRTEM) image showing three neighbouring grains of Cu and Cr having different zone axis [7].

2.1.3 Copper – Lead (Cu-Pb) alloys

Cu-Pb alloys are also known as the free machining copper alloys [101]. Generally, lead is added to copper alloys to improve their machinability and lubricating properties. The microstructure of the cast Cu-Pb alloys is similar to the pure copper; since Pb is practically insoluble in the copper. The microstructure of the Cu-Pb alloys primarily consists of alpha-copper dendrites with Pb globules located at the grain boundaries of dendrites. These alloys can be classified into two leaded alloys. One is a low Pb alloy (2 - 4 wt.%) in which Pb is acting as a chip breaker and lubricant in machining operation; whereas, the other one (High leaded copper alloy: more than 4 wt.%) used as bearing material in which it acts as a solid lubricant. High Pb alloys are not suitable for welding and brazing. Cu-Pb alloys are widely used in automotive industries as the electrical connectors and mechanical bearings. Biswas et al. [104] developed the Cu-Pb alloys via. spark plasma sintering method. They used Pb as a sintering additive in the Cu-Pb alloys to densify the Cu samples.

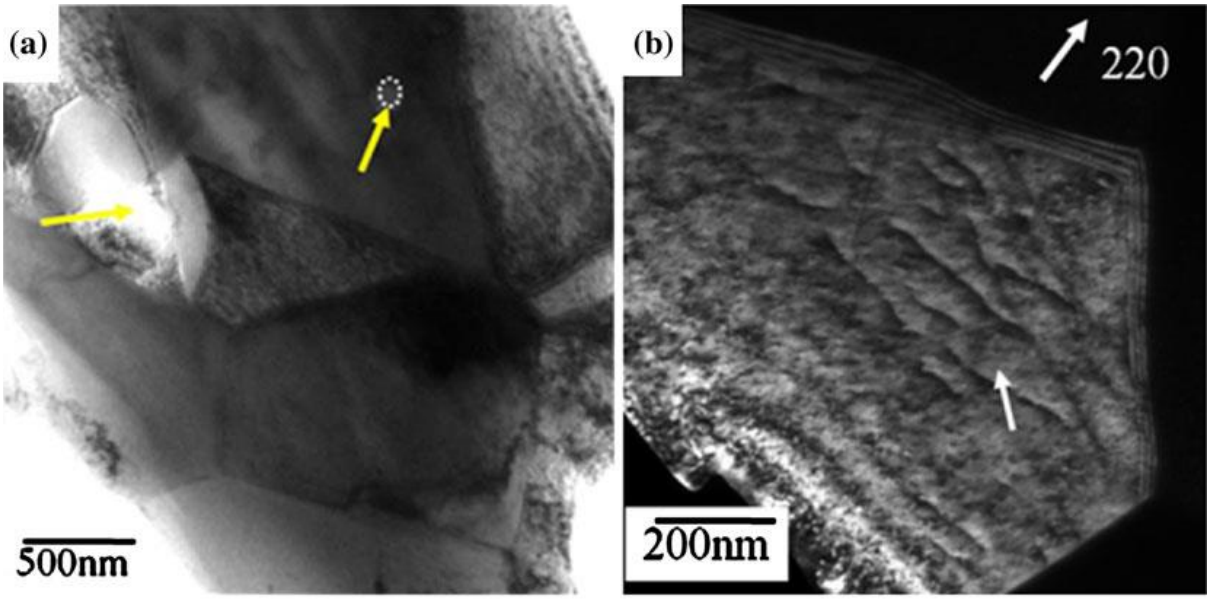

Fig. 2.5 (a) TEM (Bright-field) micrograph of spark plasma sintered Cu-10 wt.%Pb (Temperature: 600 ^{o}C, 100 MPa, 5 min.) and (b) The dislocation activity in Cu grain. In (a), the arrow shows the entrapped Pb-particle inside Cu grains. In (b), the white arrow inside the grain shows dislocations [57].

Sharma et al. [57] reported that the spherical shaped Pb precipitates were located in the grains and at the grain boundaries of the Cu. In **Fig. 2.5**, a representative the TEM micrograph of spark plasma sintered Cu-10wt.% Pb, which shows the dislocations activity in the Cu grains under the processing conditions (Temperature: 600 ^{o}C, 100 MPa, 5 min.) is presented. The relative density of the spark plasma sintered Cu-Pb alloys increased to more than 90% with 10 wt.% Pb and the hardness of upto 2 GPa was reported for Cu-Pb alloys.

2.1.4 Copper – Nickel (Cu-Ni) alloys

In copper-nickel alloys, the nickel content varied from 2 – 30 wt.% [101]. These alloys commonly used in the electrical and electronic applications. In power plants, they are used as tubes for condensers and marine applications include pumps, fittings, valves and ship hulls due to their good corrosion resistance, oxidation resistance, biofouling resistance and thermal stability. The microstructure of these alloys has a single-phase alpha due to the complete diffusion of Ni in Cu. The microstructure of the Cu-Ni alloys has similar microstructure to pure copper which consists of twinned grains. The dendritic structure has large gradient cores due to the wide freezing temperature range (see **Fig. 2.6**).

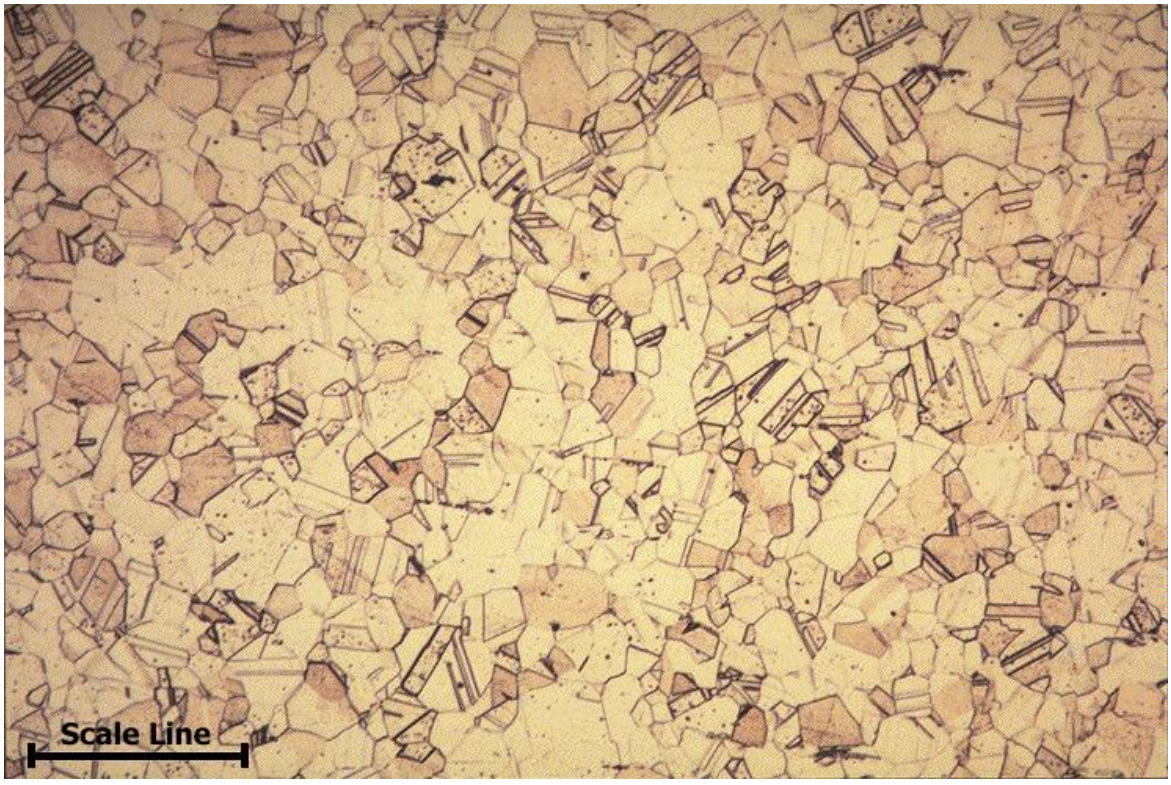

Fig. 2.6 The microstructure of Cu-8.5Ni-1.2Sn alloy [101].

Martinez et al. [65] studied the effect of Ni on the microstructure and mechanical properties of Cu. They synthesized the Cu-Ni alloys by mechanical alloying followed by hot-pressing at 300 ^{o}C with the application of high pressure (900 MPa). The compressive strength and hardness of Cu-50Ni alloy were found to be 330 MPa and 5.1 GPa, respectively. Yang et al. [105] studied mechanical and corrosion behaviour of Cu-Ni-Fe-Mn alloys under the marine environment. The tensile strength of 242 MPa was reported with the Cu-Ni alloys (with the addition of 7 wt.% Ni). These alloys showed better corrosion resistance with the corrosion rate of 0.041 mm/yr in the seawater environment.

2.1.5 Copper – Tin (Cu-Sn) alloys

Cu-Sn alloys are also known for their corrosion resistance [5]. These bronzes are more strong and ductile than the other bronzes. Their high wear resistance and low coefficient of friction make them suitable for bearings, gears, piston rings and valves. Other applications include solders used in printed circuit boards, batteries, corrosion protection layers, decorative items. The single-phase alpha solid solution retains even at low solubility of Sn in copper. The microstructure of the Cu-Sn alloys has cored dendrite structure. The Cu-Sn alloys consist of Sn content more than 15.8%, forms alpha and delta phases. Nassef

et al. [5] studied the effect of Sn on microstructure and mechanical properties of Cu-Sn alloy. They revealed that the compressive strength of the Cu-Sn alloy decreased from 243 MPa to 191 MPa with the addition of Sn (upto 15%). This decrease in strength attributed to the presence of coarse Cu_3Sn and Cu_6Sn_5 intermetallic precipitates. Interestingly, the toughness of the alloys increased with Sn content because of the fineness and soft nature of Sn. Han et al. [106] reported that the mechanical properties of hot-pressed Cu-Sn alloys were affected by the sintering process conditions. In this work, Cu with 25 wt.% of Sn alloys were consolidated using the hot press.

2.1.6 Copper – Zinc (Cu-Zn) alloys

The Cu-Zn alloys are famously known as brass [101]. These alloys are commercially available in the market as the cast rods. The brasses are used in the various industrial applications such as ammunition, the base for gold plates, blanking, coining, drawing, flexible hose, fire extinguishers, jewellery, piercing, lamp fixtures and radiators. They have good mechanical strength and corrosion resistance. But certain Cu-Zn alloys consists of Zn content above 15 wt.% are susceptible to corrosion in the marine environment. The dezincification and stress corrosion cracking of these alloys occur in NaCl environment; as the zinc is removed from the surface of the alloy, they produce a porous structure which leads to poor mechanical properties. The stress corrosion cracking of Cu-Zn alloys occurs in the environment containing amines and ammonia when subjected to the tensile stress loading conditions [101]. Heat treatment processes are required to eliminate the stress corrosion cracking problem of these alloys. The brasses consist of alpha phase solid solution upto 35 wt.% zinc. These alpha phase alloys have good strength along with the ductility which is easily cold worked. The Cu-Zn alloys are also used as jewellery, due to its change in colour from yellow to red, good formability and good castability. As the zinc content varied between 32% to 39%, it produces the dual-phase consists of alpha and beta phases. The beta phase is harder and stronger than alpha and Cu-(more than 39%) Zn alloys are known as the Muntz metal. Fast cooling allows these alloys to induce complete beta structure.

2.3 Cu composites

In the past few decades, Cu-based alloys proven to be potential candidate materials for many engineering applications in the fields of automobile, defence, electrical and mining industries. Alloying elements in Cu can enhance the mechanical and corrosion properties, but the formation of solid solution phases and intermetallic compounds significantly affect the thermal and electrical properties of copper. In such cases, copper composites can perform better than the Cu alloys by enhancing the strength and ductility without much compromising on the thermal and electrical conductivity [69]. The Cu composites have several advantages over alloyed materials including a) improved strength and stiffness of the materials, b) achieving the high strength to weight ratio, c) low coefficient of thermal expansion, d) enhancing the creep strength and e) better electrical conductivity, wear resistance, catalytic and biocompatible properties. The strength of the copper composites can be mainly improved by dispersion strengthening technique [67,107–111].

The dispersion strengthening enhances the strength of the materials by the incorporation of secondary hard particles usually they are inert, highly hard and possess a high melting temperature. The strength of the dispersion strengthened composites can be improved by restricting the movement of dislocations by the fine second phase particles. These materials can withstand at high temperature without losing its strength compared to precipitation strengthened alloys due to the high thermal stability of secondary elements and ensures no diffusion into the matrix at high temperatures. At the same time, the electrical conductivity of dispersion strengthened Cu-based materials can be observed comparatively higher to the precipitate hardened Cu alloys [112,113]. Thus, the high electrical conductivity of about ~ 80-95% IACS can be attained via composites processing route. The Cu composites have been developed using various processing techniques such as conventional casting, in-situ casting, mechanical alloying, powder metallurgy, spray deposition and self-propagating synthesis [114–117]. Generally, Cu-based composites are reinforced with the Oxides, borides, carbides, nitrides ceramic materials (Al_2O_3, B_4C, SiC, TiB_2, TiC and ZrB_2) [11,27,39,118–124].

Among the borides family, titanium diboride (TiB_2) and zirconium diboride (ZrB_2) ceramics are used as reinforcements to Cu. Among these reinforcing elements, TiB_2 have a high melting temperature (~3200°C), high hardness (~34 GPa), low electrical resistivity

(about 14.4 μΩ cm), high thermal conductivity (about 65 W/mK), high Young modulus and better creep resistance [125,126]. Sharma et al. [127] prepared the Cu-10TiB_2 composites using spark plasma sintering technique at a temperature between 400 to 700 ^oC under a pressure of 50 MPa for 5 min. They reported that the relative density varied between ~72% and ~91% and the hardness of samples varied between ~1.5 - 2.0 GPa. In another work, the Cu-30TiB_2 composites processed through in-situ combustion synthesis exhibited a hardness of 48 HRC [128].

It has to be mentioned here that zirconium diboride (ZrB_2) is an interesting ceramic reinforcement for Cu composites due to its superior electrical conductivity (>106 S/m), thermal conductivity (~90 W/m.K), elastic modulus (~450 GPa), hardness (~23 GPa), good chemical stability, good wear and oxidation resistance [129]. Wang et al. [27] studied the effect of ZrB_2 on microstructure and mechanical properties of Cu-ZrB_2 composites fabricated via. casting route. The hardness of these composites is more than 0.1 GPa and the electrical conductivity is more than 85% IACS. In another study, Zhang et al. [43] reported that the hardness of in-situ formed Cu-ZrB_2 composites found to be more than 1.2 GPa and electrical conductivity was more than 70% IACS. However, while reviewing the literature, it was realised that the Cu-based composites require good bonding between reinforcement and matrix material to achieve good properties.

2.4 Processing of Cu-based alloys/composites

Now the different processing techniques which have been used in developing Cu alloys and Cu composites will be discussed in this chapter. The Cu based materials can be processed through several techniques such as melting processing route which include casting [130], vacuum induction melting [131] and plasma arc melting [132]. Also, solid-state processing via powder metallurgy includes pressureless sintering [133], hot-pressing [94], spark plasma sintering [134], microwave sintering [135] and isostatic-pressing and allied processes including electrolysis [136], chemical vapor deposition [137] and additive manufacturing [138] have been used.

2.4.1 Casting

Casting is one of the oldest manufacturing process (around 3400 BC) where the molten metal is poured into the refractive mould cavity and the metal allowed to solidify.

Copper-based alloys and composites fabricated using the casting process possess moderate strength, hardness, good ductility, and excellent electrical conductivity [139]. The castings of Cu and Cu alloys are prepared using different techniques, such as sand casting, investment casting, centrifugal casting, squeeze casting, shell and die casting. **Fig. 2.7** shows the different types of casting processes used for making Cu alloys and Cu composites [140].

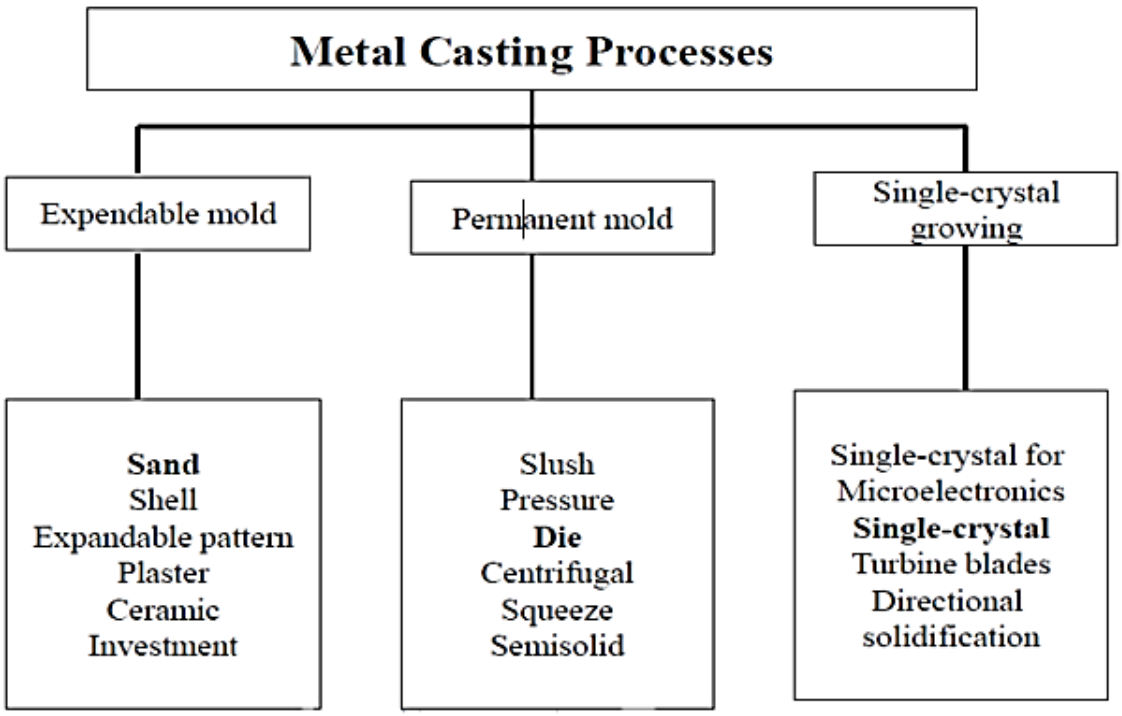

Fig. 2.7 Various metal casting process for producing Cu-based alloys [140].

The cast Cu alloys were categorized into three main groups based on their solidification range. The first group of alloys having the low solidification range upto 50 ^{o}C between solidus and liquidus lines. Example, aluminium bronzes, nickel bronzes and manganese bronzes. The second category belongs to intermediate solidification temperature ranging from 50 ^{o}C to 110 ^{o}C which are silicon brass, silicon bronzes and copper-beryllium alloys. The third category alloys that have high solidification range is about 110 ^{o}C to 170 ^{o}C. These alloys are lead bronzes, tin bronzes and lead-tin bronzes [101]. The casting route is preferred for making copper alloys due to low processing cost and to achieve various properties such as high ductility, moderate tensile strength, moderate compressive strength, good corrosion resistance, excellent machinability (upto 90%) good electrical conductivity (upto 100% IACS) and thermal conductivity (upto 391 W/mK) [15]. In **Fig.2.8**, the effect of arc melting and chill casting on microstructure development of Cu-21.2 at.% Sn ($Cu_{41}Sn_{11}$) alloy is presented.

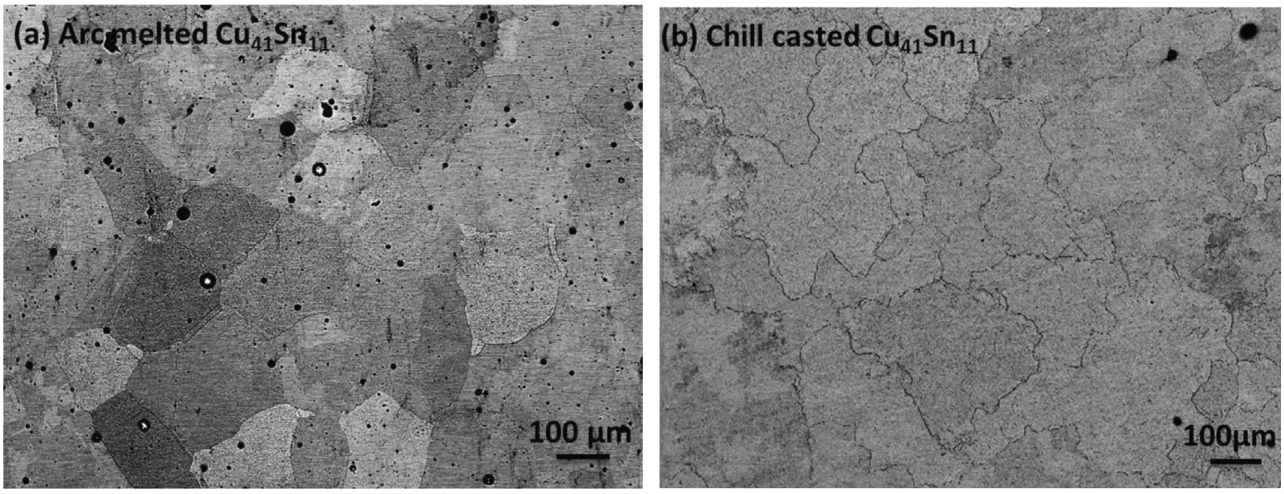

Fig. 2.8 Microstructure of $Cu_{41}Sn_{11}$ (Cu–21.2 at.%Sn) alloy. (a) as arc melted and (b) as chill cast [92].

Since the casting process involves the use of high processing temperature to melt the materials, there could be a possibility of getting coarser grain structure in cast components which could decrease the mechanical properties of Cu alloys. Hence, to develop fine grain structures in Cu alloys, further heat treatment processes are required. These secondary processes increase the production cost of Cu alloys. Generally, the casting process requires various levels of surface finishing operations such as fettling, machining, linishing and shot-blasting to produce final objects which further increases the production cost. Also, the cast components consist of casting defects such as hot tears and cast inclusions which reduce the yield of production. The precise control over various casting parameters is required to minimize these casting defects (maintaining the lowest possible pouring temperature and providing minimum turbulence) [141,142].

The main disadvantage of fabricating Cu composites through casting technique is an agglomeration of secondary particles in the Cu matrix and inhomogeneous mixing which could deteriorate the physical, mechanical as well as wear properties. Hence, an alternative technique is required to produce sound Cu-based composites. Powder metallurgy technique is a proven alternative technique (which uses low processing temperatures) to produce Cu composites with high density (upto 99%) with better properties.

2.4.2 Powder metallurgy

Powder metallurgy (PM) technique involves the powder preparation, mechanical alloying or mixing of powders with additives lubricants, powders compaction and sintering or simultaneous application of both compaction and sintering. Generally, powder metallurgy

method is preferred for the materials which are difficult to process through conventional melting routes such as high melting point metals and ceramics. Also, this technique is used to produce near-net-shape products which minimize the machining cost. The main applications for copper and copper-based powder metallurgy materials include structural parts, electrical components, friction materials, contact brushes, bearings and oil filters [143]. The conventional processing of powder metallurgy route is presented in **Fig. 2.9**. Usually, the processed powders were consolidated in closed die and subsequent desired compact pressure is applied to achieve a good green strength of the components. Low compaction pressures can be susceptible to more porosity in the components whereas, the high-pressure leads to layer and crack formation of green compacts which lowers the strength and electrical conductivity. After compaction, the components are heated up to the sintering temperature of the materials. The sintering temperature of the materials can be considered as 2/3 of the melting temperature of the base material/metal.

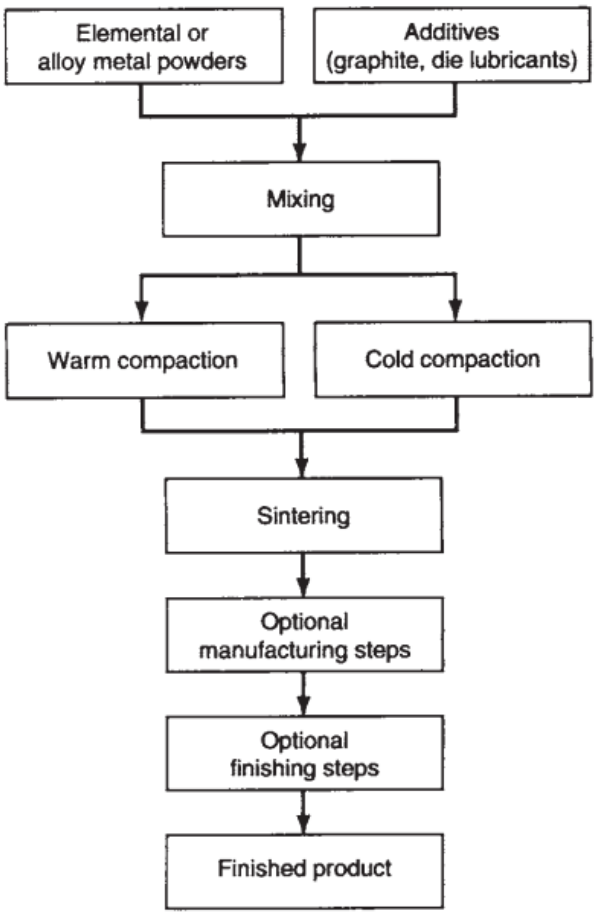

Fig. 2.9 Steps involved in conventional processing of Cu-based powder metallurgy components [47].

The powder metallurgy process mainly classified into two types namely the pressureless sintering process and pressure-assisted sintering (hot-pressing) process. In the pressureless sintering process, the powders are consolidated in cold press at room temperature and sintered in a furnace. One of the advantages of the pressureless process is that the density variation can be avoided in the final product. While the pressure-assisted sintering process involves the simultaneous application of pressure and heat. The pressure-assisted sintering process can be adopted to produce full dense objects. Thereby enhancement in the mechanical, wear, thermal and electrical properties of the materials can be achieved.

Copper alloys and copper composites are widely used in many industrial applications such as marine, energy and transportation etc. Especially, Cu-Al alloys or Al bronzes are widely used as electrodes for spot welding, machining of metals such as electric discharge machines (EDM), heat-exchangers in thermal power plants, brazing alloy for diamond grits and over-head power collectors in electric trains [46,48,49]. For such applications, high strength, good electrical and thermal conductivity, high thermal stability, good corrosion and wear resistance are very essential. Conventionally, most of the Cu-Al alloys have been primarily produced by casting process [47]. However, this process cannot improve the mechanical or wear properties significantly, due to its limitation in controlling grain growth and in turn the properties. Also, the wear rate of Cu-Al alloys can be decreased by achieving a fine-grain structure [50]. In the light of this, use of alternative processing techniques such as powder metallurgy and sinter forging processes were attempted to improve the required properties of Cu-Al alloys [48,50].

Table 2.2 Various copper-based composites prepared via. powder metallurgy route.

Composites	**Processing technique**	**Relative density (%)**	**Hardness (GPa)**	**Strength (MPa)**	**Elonga-tion (%)**	**Ref**
(Cu-14Zn-4Si)	HP	97.0	2.98	475.6 (C)	25.2	[144]
(Cu-14Zn-4Si)-3B_4C	HP	95.1	3.31	647.0 (C)	22.9	[144]
(Cu-14Zn-4Si)-6B_4C	HP	94.5	3.69	823.8 (C)	22.2	[144]
(Cu-14Zn-4Si)-9B_4C	HP	93.6	4.25	968.9 (C)	23.0	[144]
(Cu-14Zn-4Si)-12B_4C	HP	91.9	4.75	1077.8 (C)	21.5	[144]
Cu	CP + Sintering	95.1	0.53	410.2 (C)	50	[118]
Cu-2.5Al_2O_3	CP + Sintering	92.5	0.71	490.5 (C)	30	[118]

Cu-7.5Al_2O_3	CP + Sintering	78.9	0.78	530.6 (C)	20	[118]
Cu-12.5Al_2O_3	CP + Sintering	87.8	0.86	620.1 (C)	15	[118]
Cu-1Fe	VIM + HT	-	0.61	160 (T)	-	[62]
Cu-1Cr	VIM + HT	-	0.63	180 (T)	-	[62]
Cu-1.5Ti	VIM + HR	-	0.86	300 (T)	-	[145]
Cu-2.7Ti	VIM + HR	-	1.20	430 (T)	-	[145]
Cu-4.5Ti	VIM + HR	-	2.12	630 (T)	-	[145]
Cu-5.4Ti	VIM + HR	-	3.06	780 (T)	-	[145]
Cu	HP	99.7	0.97	129.6 (C)	-	[146]
Cu-2 vol.% SiC-2 vol.% CNT	HP	98.8	0.92	257.6 (C)	-	[146]
Cu-2 vol.% SiC-4 vol.% CNT	HP	98.4	1.05	285.2 (C)	-	[146]
Cu-2 vol.% SiC-6 vol.% CNT	HP	97.4	1.08	279.5 (C)	-	[146]
Cu-0.2SWCNT	HP	91.3	0.69	220.2 (C)	-	[147]
Cu-5SWCNT	HP	98.2	0.52	345.5 (C)	-	[147]
Cu-10SWCNT	HP	94.8	0.33	350.6 (C)	-	[147]
Cu-5MWCNT	HP	94.0	0.53	175.8 (C)	-	[147]
Cu-10MWCNT	HP	98.5	1.06	249.5 (C)	-	[147]
Cu	CR + sinter + EX	99.2	0.83	209.0 (T)	-	[148]
Cu-0.2La_2O_3	CR + sinter + EX	98.7	0.87	258.0 (T)	-	[148]
Cu-0.6La_2O_3	CR + sinter + EX	98.3	0.93	286.0 (T)	-	[148]
Cu-1La_2O_3	CR + sinter + EX	97.9	1.05	312.0 (T)	-	[148]
Cu-1.3La_2O_3	CR + sinter + EX	97.6	1.18	329.0 (T)	-	[148]

CP: Cold-pressing; HP: Hot-pressing; HT: Heat treatment; CR: Cold rolling; EX: extrusion; VIM: Vacuum induction melting; (T): Tensile strength and (C): Compressive strength.

From the literature (see **Table 2.2**), it is evident that the copper and copper-based composites processed via. powder metallurgy route showed better mechanical properties over the conventional casting technique [62,118,144–148]. Effect of the addition of nano B_4C on the density and hardness of **[**82Cu-4Si-14Zn**]**$_{100-x}$ - x wt.% B_4C (x=0, 3, 6, 9, and 12)

nanocomposite (after vacuum hot pressing) is presented in **Fig. 2.10**. With increasing B_4C content the relative density decreased from 97 to 91.5% and hardness increased from 3 to 4.8 GPa for Cu-Si-Zn-B_4C composite [144]. Zhu et al. [149] processed nano Cu-10Ag-10W ternary alloy via mechanical alloying and hot pressing and studied its wear phenomena against stainless steel. Their study revealed the formation of precipitates, solid solution and heat treatment of alloys also improved the mechanical and wear properties. Particularly, these alloys exhibited a maximum microhardness of 3.61 GPa and nanohardness of 4.61 GPa. In a different work, Purcek et al. [150] reported the tribological properties of coarse-grained and ultrafine Cu-0.7Cr-0.07Zr alloy. The ultrafine grains considerably increased the hardness, strength and wear resistance of Cu-alloys.

It was reported that adhesion wear mechanism was predominant in Cu-Cr-Zr alloys with coarse grain structure and the wear mechanism transformed to abrasion with ultrafine grains. Zheng et al. [148] studied the effect of La_2O_3 on mechanical and wear properties of nano-copper composites, which were developed for contact material applications in satellites and spacecraft. In view of the potential application of Cu for brake pad applications in high-speed trains, Zhang et al. [151] reported the effectiveness of the use of Fe (22 to 35 wt.%) as an additive for copper composite. Chen et al. [152] investigated the effect of solid lubricants (graphite and h-BN) on wear properties of Cu and suggested that the wear of Cu lowered due to the tribo-film formation. In another work, Pellizzari et al. [153] explored the effect of mechanical milling and mechanical alloying on wear behaviour of spark plasma sintered Cu materials. The reinforcement of Cu with hard TiB_2 ceramic reportedly exhibited significant improvement of tensile strength and hardness; however, the electrical conductivity of Cu was compromised [154]. Li and co-workers [66] suggested that the refinement of grain size in Cu can significantly improve the mechanical and wear properties of Cu-0.1 wt.% Zr alloy.

It is also observed that high pressure in powder metallurgy affects the structure of Cu-based materials. Rohatgi et al. [155] studied the behaviour of cold working on Cu-Al alloys by varying the pressure. They estimated the dislocation density of Cu-Al alloys from the DSC curve *i.e.,* by calculating the energy released during recrystallization. It was reported that the dislocation density of Cu-4Al increased from 1.22×10^{14} m^{-2} to 17.64×10^{14} m^{-2} by increasing pressure from 10 to 35 GPa.

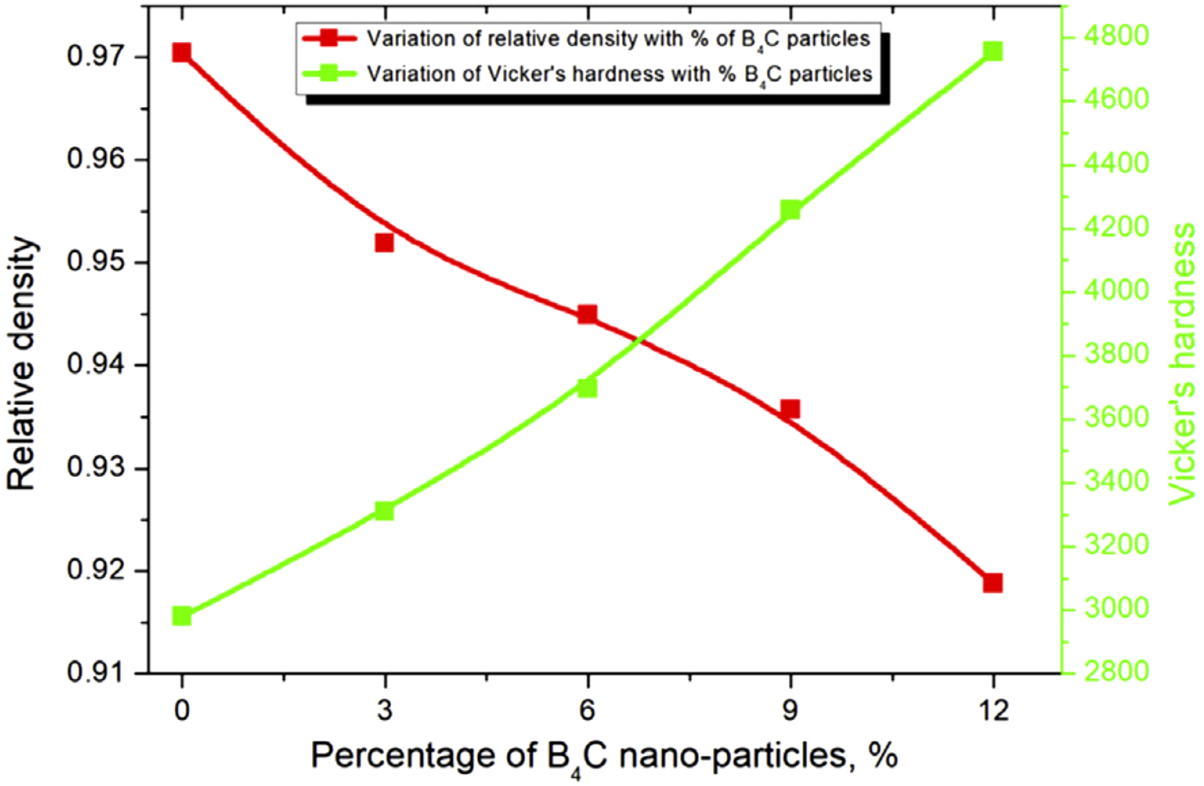

Fig. 2.10 Density and hardness variation of **[**82Cu-4Si-14Zn**]**$_{100-x}$ - x wt.% B_4C (x=0, 3, 6, 9, and 12) nanocomposite [144].

Zhao et al. [156] reported the dislocation density of 2.3×10^{14} m^{-2} for ultra-fine copper and 5.9×10^{14} m^{-2} for ultra-fine bronze that was processed by high-pressure torsion (HPT) at 6 GPa pressure and cold rolling. In another study, the dislocation density of 4.3×10^{14} m^{-2} was reported for equal channel angular pressing (ECAP) processed copper [157]. From these studies, it can be observed that the dislocation density of Cu based alloys is varying with the function of temperature and pressure *i.e.*, the dislocation density of Cu alloys was observed to be low at the higher processing temperature and lower pressures. Also, the calculated dislocation density values of Cu-Al alloys in the present study are comparable with the reported Cu alloys. In summary, the use of high-pressure in PM proven to be advantageous the dislocation density and lattice strain enhances the densification and densification rate of Cu-Al samples.

2.4.3 Severe plastic deformation

The Severe plastic deformation (SPD) is the metal forming process in which the materials undergo severe plastic deformations and large plastic strains induced to obtain ultra-fine grain structure in the bulk materials. The SPD process can be used where obtaining the ultra-fine grain structure is difficult. Various types of SPD techniques have been

extensively reported for Cu-based materials such as high-pressure torsion (HPT) [7,16,158] equal channel angular pressing (ECAP) [17] twist extrusion [18] accumulated roll bonding (ARB) [19] repetitive corrugation and straightening [20] cryo-rolling [21], friction stir processing [22]. The components produced by the SPD process have high strength, ductility and fatigue resistance. Thus, this process is widely used in automobile, aerospace and defense industries especially in structural applications. **Fig. 2.11** presents the various SPD processes include ECAP, HPT and ARB.

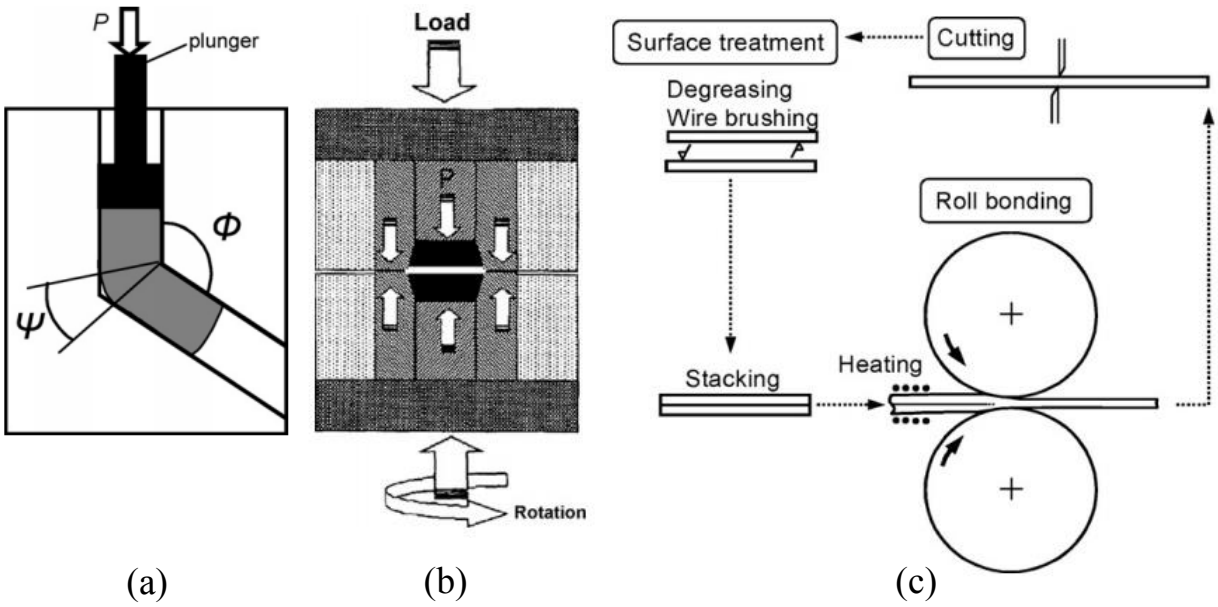

Fig. 2.11 Schematic representation of various SPD processes. (a) ECAP [159], (b) HPT [160] and (c) ARB [161].

(A) EQUAL CHANNEL ANGULAR PRESSING (ECAP)

The ECAP process consists of pressing the material using a punch through the die in which the channel is bent at an angle equals to 90 ^{o}C. **Fig. 2.11a** shows the schematic representation of the ECAP process. The material is extruded at an angle (Φ) where the shear deformation is imposed continuously on the material. Also, the material undergoes large plastic deformations without changing the cross-sectional area of the sample. This process can be used to process solid materials and consolidate the metal powders [162]. The total strain experienced by the material when it extruded through the channel is given by the **equation 2.2** [159].

$$\varepsilon = \frac{1}{\sqrt{3}}\left\{2\cot\left(\frac{\emptyset}{2}+\frac{\psi}{2}\right)+\psi\csc\left(\frac{\emptyset}{2}+\frac{\psi}{2}\right)\right. \quad (2.2)$$

where Φ: the angle between inlet and outlet channels and ψ: the angle subtended by the arc of curvature at the point of intersection. The total strain of the material in the pass is 1.15; in a cyclic process, it is equal to no. of passes multiplied by strain per pass. Qu et al. [163] prepared the ultra-fine grained Cu-Al alloys processed through ECAP method. **Fig. 2.12** presents the micrographs of Cu-Al alloys before and after the ECAP process. The Cu-Al alloys were annealed at 800 ^{o}C for 2 h to obtain the grain size of 100-500 nm. The ultra-fine grains (~152 nm) were produced after 4 passes of pressing.

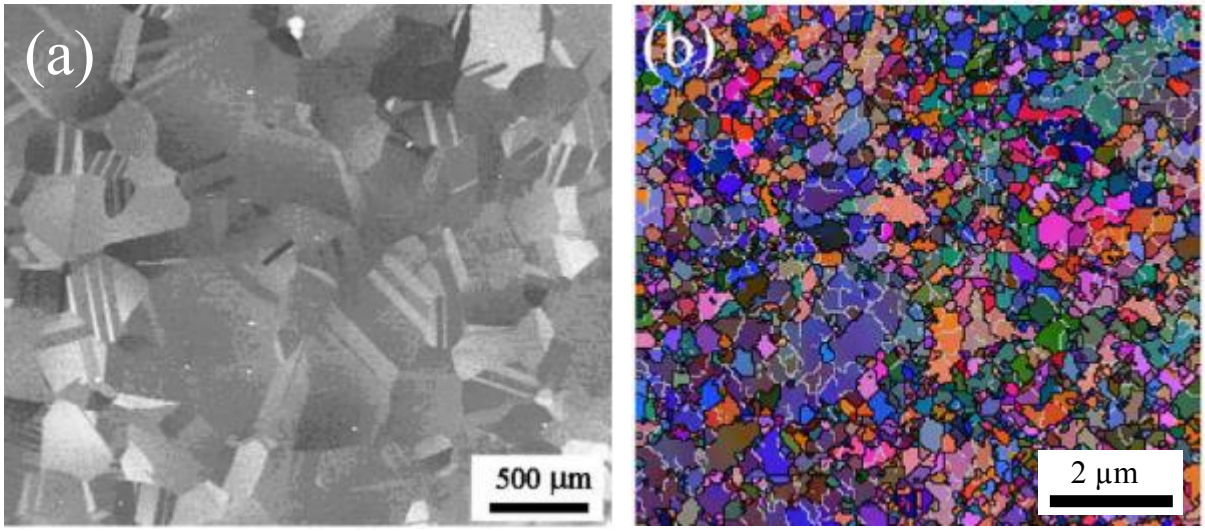

Fig. 2.12 The microstructure of Cu-8 at.% Al alloys before and after ECAP process. (a) SEM image and (b) EBSD maps after 4-passes [163].

In another work, Li et al. [66] reported that the ultrafine grain microstructure (~350 nm) of Cu-0.1Zr alloy can be produced after 8 passes through the ECAP process. As the no. of passes increased to produce ultra-fine grains, the processing cost increases. Hence, the use of the ECAP process is limited due to low productivity and high production cost.

(B) HIGH-PRESSURE TORSION (HPT) PROCESS

In the HPT process, a very thin disc specimen is compressed in a closed die by very high pressure and the torque is applied by the punch. The schematic diagram of the HPT process is shown in **Fig. 2.11b.** The total strain in HPT process is given by the **Eq. 2.3** [159].

$$\varepsilon\,(r) = \frac{2\pi n r}{\sqrt{3}\times l} \qquad (2.3)$$

Jiang et al. [164] reported that the ultra-fine grain microstructure (~150 nm) of Cu after HPT for 5 turns. The hardness of the Cu was observed to be increased from the center

to the outer surface of the sample (see **Fig. 2.13**) and the maximum hardness of ~1.9 GPa was observed at the edge.

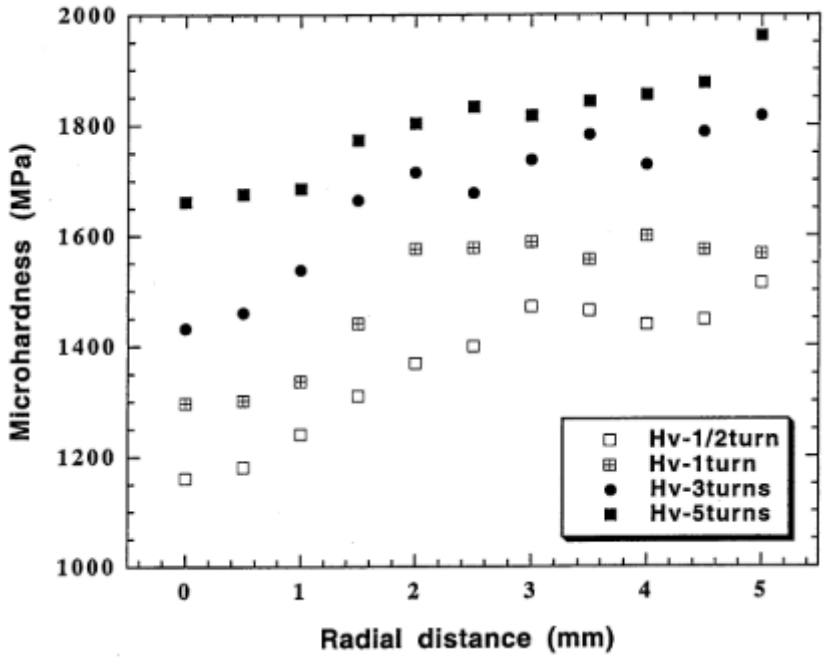

Fig. 2.13 The distribution of hardness across the radial distance of the Cu disc after HPT process [164].

Purcek et al. [150] have studied the influence of high-pressure torsion on microstructure and tribological properties of Cu-Cr-Zr alloy. The size of the sample used in this process was about 20 mm dia. and 2.5 mm in thickness. The ultra-fine grains about ~155 nm were produced after application of torsional pressure. The strength of the alloy after HPT process was increased by 3.5 times compared to other alloys without HPT. At the same time, the electrical conductivity of these alloys decreased by 2 times after HPT process. The HPT process is limited to its use because the specimens used for this process are small in size and difficult to produce the bulk samples.

(C) ACCUMULATIVE ROLL-BONDING (ARB) PROCESS

In the ARB process, the sheets are stacked and pressed by conventional rolls. Initially, the interface of the two strips is surface treated to avoid contamination. After rolling of the strips, they are cut into two halves and again surface treated, repeated roll bonded (see **Fig. 2.11c**). This process continues until the desired properties of the materials are obtained. The total strain after the ARB process is given by **Eq. 2.4** where t_o is the initial thickness of sheet and t is the final thickness after the ABR process.

$$\varepsilon = \frac{\sqrt{3}}{2}\ln\left(1 - \frac{t}{t_o}\right) \quad (2.4)$$

In this process, the elongated ultra-fine grains are developed after *n* number of passes. Takata et al. [165] prepared the ultra-fine grain structured bulk Cu by the accumulative roll-bonding process. The grain size of the Cu decreased extensively from 100 µm to 200 nm (lamellar grains) after 8 passes of the ARB process. The tensile strength of the ultra-fine grained Cu increased by 3 times compared to untreated Cu which is having micro-sized grains. In another work, Lee et al. [166] studied the effect of temperature on the microstructure of the Cu-Fe-P alloy processed through ARB method. Their work revealed that the ultra-fine grains (~400 nm) were produced in Cu-Fe-P alloys after 8 passes of ARB process. These ultra-fine grains are replaced with equated and coarse grains with the increase of temperature from 250 ^{o}C to 300 ^{o}C due to the recrystallization of the material.

2.5 Mechanical properties

The Cu materials can be strengthened by the solid solution, dispersion strengthening, precipitation hardening, work hardening and grain refinement or grain boundary strengthening [124] **[**159**]**. Among these strengthening methods, solid solution strengthening and dispersion strengthening techniques are widely used to improve the mechanical properties of Cu. Especially, solid solution strengthening of Cu significantly enhances the strength of Cu by changing the atomic structure of the materials. The addition of alloying elements to Cu results in the development of solid solution phases and intermetallic compounds in the material. These microstructural phases interfere with dislocation motion and thereby enhances the mechanical properties of the Cu.

2.5.1 Effect of alloying elements

The addition of a minor amount of alloying elements significantly affects the strength of Cu. In case of Cu-Al system, solid solution phases such as α-Cu and intermetallic compounds such as γ_1 (Cu_9Al_4), δ (Cu_3Al_2), ζ_1 (Cu_4Al_3), η_2 (CuAl) and θ ($CuAl_2$) phases improves the hardness and strength of the Cu. Liu et al. [167] processed the Cu-xAl (x:1, 2, 4 and 6) alloys by arc melting technique at a temperature range between 710-800 ^{o}C. The effect of Al content and multi-axial compression on the hardness of Cu-Al alloy is presented in **Fig. 2.14**. The hardness of the Cu-Al alloys increased with the increase of Al content.

Also, it can be observed that the multi-axial compression significantly increased the hardness of Cu-Al alloys due to the increase of dislocation density; after 2 passes, the hardness of the alloys decreased because of the dislocation annihilation. Further application of large strains on the compacts results in no change of hardness values due to recovery phenomena.

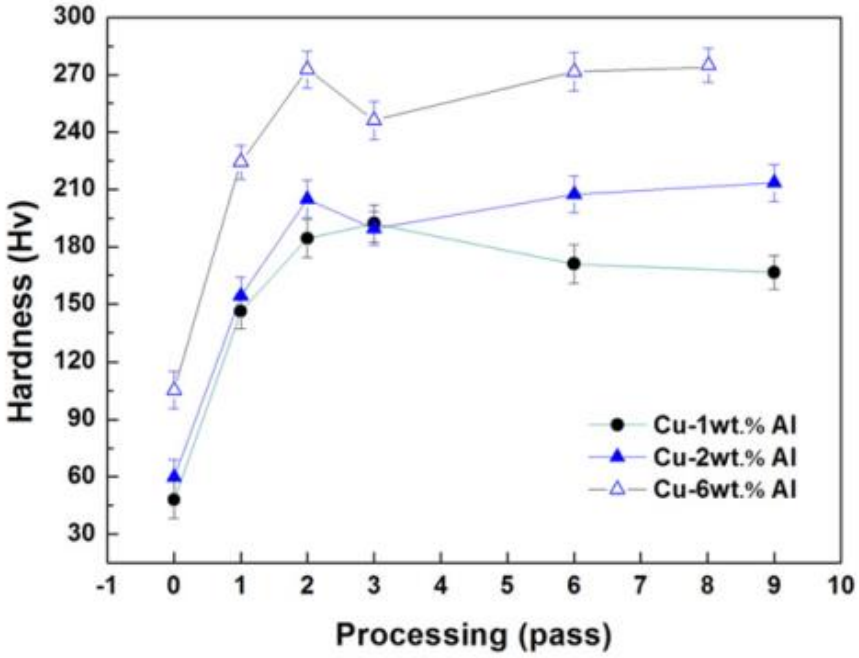

Fig. 2.14 The evolution Vickers hardness (Hv) of Cu–Al alloys during different passes of multi-axial compression [167].

In another work, Glas [168] reported hardness of 2.95 to 3.7 GPa for Cu-Al alloys processed by casting technique (at 1150 ^{o}C). Nassef et al. [58] produced the Cu-Sn and Cu-Pb alloys through hot pressing route; depending on the composition the hardness of Cu-10Pb alloys varied between 1.01 to 2.10 GPa; whereas, for Cu-10Sn-10Pb it varied between 1.08 to 2.22 GPa. Biswas et al. prepared the Cu-Pb alloys and Cu-TiB_2 composites using spark plasma sintering at a sintering temperature between 350-400 ^{o}C and uniaxial pressure of 50 MPa for 5 min. The Cu-Pb alloy exhibited the hardness upto 1.9 GPa even after obtaining the high densification of the alloy due to the soft nature of Pb addition to Cu. Relatively high hardness (2 GPa) and low densification were observed in case of Cu-TiB_2 composites due to the hard TiB_2 particles resist the dislocation movement. Also, So far in the literature, for Cu based materials a maximum hardness of 4.1 GPa was reported [5,58,104,169]. The mechanical properties of various Cu-based alloys [34,62,74,145,170–172] is given in **Table 2.3**.

Table 2.3 Mechanical properties of copper alloys processed through various techniques.

Alloys	**Processing technique**	**Processing conditions**	**Density (g/cc)**	**Hardness (GPa)**	**Phases**	**Strength (MPa)**	**Strain (%)**	**Ref**
Cu-11Al	Casting	-	7.74	38.4 (HRC)	α and β	230.4 (T)	11.2	[74]
Cu-11Al	Casting + HT + 20% CR	HT: 900 ^{o}C for 15 h	,,	51.3 (HRC)	α and γ_2	321.8 (T)	58.7	[74]
Cu-12Al	Casting +HT + 10% CR	HT: 800 ^{o}C for 24 h	-	1.32	β	-	-	[34]
Cu-12Al	Casting + HT + aging	HT: 800 ^{o}C for 0.5 h; aging: 450^{o}C for 12 h	-	2.62	α and γ_2	-	-	[34]
Cu-12.5Al-4Fe	Spray formed + extruded	1080 ^{o}C	7.2	300 (HB)	α, β and γ_2	1200 (C)	5.0	[170]
Cu-14.5Al-4Fe	,,	,,	7.0	380 (HB)	,,	1600 (C)	5.0	[170]
Cu-10Al-2.5Ti	Casting	1200 ^{o}C	-	2.36	γ and κ	385 (T)	-	[171]
Cu-10Al-2.5Zr	,,	,,	-	2.28	γ and κ	348 (T)	-	[171]
Cu-0.8Cr-0.08Zr	HT	HT: 1020 ^{o}C for 20 min.; aging: 470 ^{o}C for 5 h		0.93	Cu_2Cr	189 (T)	59.0	[172]
Cu-0.8Cr-0.08Zr	HT + aging	,,		1.60	Cu_2Cr	369 (T)	15.0	[172]
Cu-0.8Cr-0.08Zr	HT + ECAP	,,		1.73	Cu_2Cr	618 (T)	14.9	[172]
Cu-0.8Cr-0.08Zr	HT + ECAP + aging	,,		2.10	Cu_2Cr	742 (T)	9.0	[172]

HT: Heat treatment; CR: Cold rolling, ECAP: Equal channel angular pressing; (T): Tensile strength and (C): Compressive strength.

Donatus et al. [74] studied the mechanical behaviour of cast Cu-11Al alloys under cold rolling. The strength of the Cu-Al alloys found to be increased by 39% with the grain refinement which was caused by the 20% cold rolling. Kudashov et al. [170] reported that the compressive strength of Cu-XAl-4Fe-Co-Mn (X: 12.5-14.5 wt.%) alloys processed through the spray coating technique found to be in the range between 1200-1600 MPa due to the fine grain structure and Cu_9Al_4 intermetallic compounds. Nwambu et al. [171] studied the effect of Zirconium and titanium addition on microstructure and mechanical properties of Cu-Al alloys. The addition of zirconium and titanium (upto 2.5 wt.%) enhanced the tensile strength of Cu-10Al alloy by ~95% and ~105% due to the formation of γ and κ intermetallic compounds during the casting process. Rohatgi et al. [173] reported that the small amount of (2 wt.%) Al addition improves the tensile strength of Cu by ~22% compared to pure Cu due to the formation of solid solution. In another work, Nagarjuna et al. [145] fabricated the Cu-Ti alloys by vacuum induction melting technique. The 2.7 wt.% of Ti addition increased the tensile strength of the Cu by ~34%. From the above literature, it can be noted that the maximum compressive strength of Cu-based alloys was 1600 MPa, which is obtained with the addition of several alloying elements and application of additional heat treatment process to Cu alloys.

2.5.2 Effect of reinforcing elements

The dispersion strengthening of Cu-based materials improves the strength, wear properties with good electrical and thermal properties. In this technique, the strength of the materials depends on the several factors such as the quantity of reinforcement, size and shape of reinforced particles, wettability between the reinforcement and matrix materials, hardness of the reinforcing elements [174]. The list of various mechanical properties of Cu-based composites is tabulated in **Table 2.4**. Clinktan et al. [144] prepared the brass-B_4C composites via. mechanical alloying and hot press (at a temperature of 900 ^{o}C, the pressure of 25 MPa for 45 min.) followed by heat treatment at 900 ^{o}C for 1 h. **Fig. 2.15** presents the effect of B_4C on densification and mechanical properties of Cu-Si-Zn alloy. They achieved relative density upto 97% and it observed to reduce with the B_4C addition due to the strain hardening of ball-milled powders. The hardness (3.0 to 4.7 GPa) and compressive strength (445 – 1077 MPa) of the composites increased with the fine B_4C reinforcement. Also, they reported that the increased compressive strength of composites attributed to the presence of solid solution phases which formed with the addition of Zn and Si to copper, fine B_4C particles obstruct the dislocation motion, lattice strains in the material and good wettability between B_4C brass matrix.

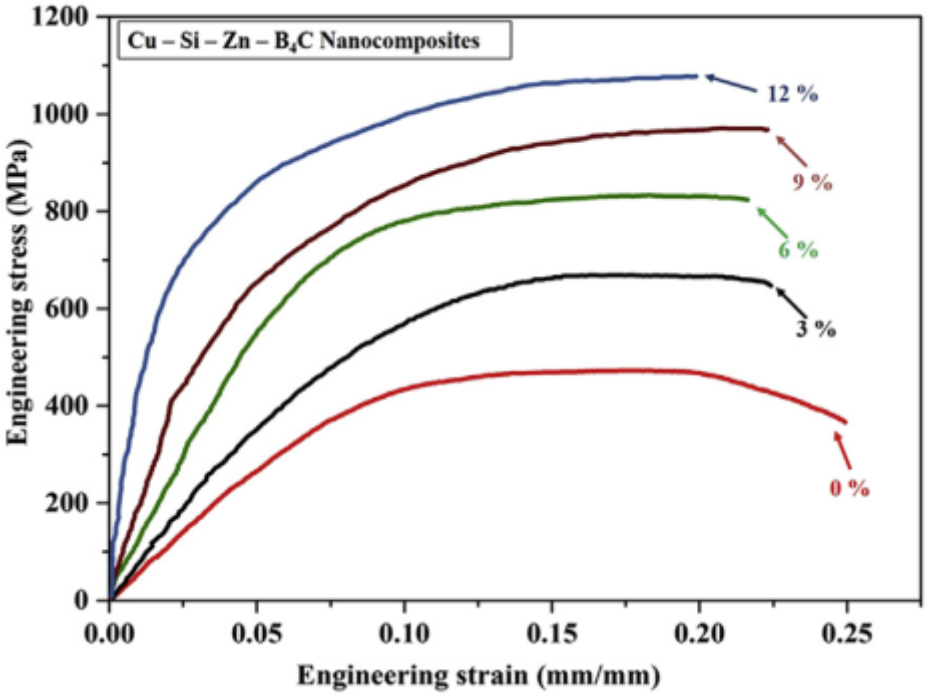

Fig. 2.15 The influence of B_4C on stress-strain behaviour of (Cu-Si-Zn)-B_4C nanocomposite [144].

Shehata et al. [133] investigated the effect of Al_2O_3 on the mechanical properties of Cu. The Cu-Al_2O_3 composites were processed through the powder metallurgy route (pressureless sintering at 850 ^oC). The hardness and compressive strength of the Cu- Al_2O_3 composites found to be increased with the Al_2O_3. The hardness of composites varied between 59.8 BHN to 79.4 BHN and the compressive strength varied in the range between 490 – 620 MPa. It was observed that the addition of Al_2O_3 to Cu has more effect on the hardness and compressive strength rather than the densification of composites. In another investigation, Akbarpour et al. [146] studied the combined effect of SiC and CNT content on mechanical properties of Cu. The consolidation of mechanically alloyed Cu-(SiC-CNT) powders was processed by using a hot press (conditions: 700 ^oC, 150 MPa, 30 min.) to prepare Cu-based hybrid composites. Their work revealed that the relative density of composites was slightly decreased (98 to 97%) with the addition of CNT (2 to 6 wt.%). The compressive strength of composites varied between 257 to 285 MPa, but significant improvement in compressive strength has been observed in composites when compared to pure Cu.

Table 2.4 The relative density and various mechanical properties of Cu-based composites processed through PM route.

Composites	Processing technique	Density (%)	Hardness (GPa)	Strength (MPa)	Strain (%)	References
Cu-14Zn-4Si	HP (900 ^{o}C, 25 MPa for 45 min.) + HT (900 ^{o}C for 1h)	97.0	2.98	475.6 (C)	25.2	[144]
(Cu-14Zn-4Si)-3B_4C	,,	95.1	3.31	647.0 (C)	22.9	[144]
(Cu-14Zn-4Si)-6B_4C	,,	94.5	3.69	823.8 (C)	22.2	[144]
(Cu-14Zn-4Si)-9B_4C	,,	93.6	4.25	968.9 (C)	23.0	[144]
(Cu-14Zn-4Si)-12B_4C	,,	91.9	4.75	1077.8 (C)	21.5	[144]
Cu-2.5Al_2O_3	CP (600 MPa) + Sintering (850 ^{o}C)	92.5	59.83 (HB)	490.5 (C)	30	[133]
Cu-7.5Al_2O_3	,,	89.9	67.9 (HB)	530.6 (C)	20	[133]
Cu-12.5Al_2O_3	,,	87.8	79.4 (HB)	620.1 (C)	15	[133]
Cu-2 vol.% SiC-2 vol.% CNT	HP (700 ^{o}C, 150 MPa, 30 min.)	98.8	0.92	257.6 (C)	-	[146]
Cu-2 vol.% SiC-4 vol.% CNT	,,	98.4	1.05	285.2 (C)	-	[146]
Cu-2 vol.% SiC-6 vol.% CNT	,,	97.4	1.08	279.5 (C)	-	[146]
Cu	HP (840 ^{o}C, 25 MPa, 2 h)	96.7	0.57	-	-	[27]
Cu-1ZrB_2	,,	96.1	0.69	-	-	[27]
Cu-5ZrB_2	,,	92.6	0.91	-	-	[27]
Cu-9ZrB_2	,,	91.2	0.81	-	-	[27]
Cu-7vol% ZrB2	HP (950 ^{o}C, 35 MPa for 2.5 h)	95.0	0.16	614.2	-	[175]

CP: Cold-pressing; HP: Hot-pressing; HT: Heat treatment; CR: Cold rolling, EX: Extrusion; (T): Tensile strength and (C): Compressive strength.

Wang et al. [27] studied the effect of ZrB_2 on mechanical properties of Cu. They prepared the Cu-ZrB_2 composites by varying the ZrB_2 content from 0 to 9 wt.% through hot-pressing method at a temperature of 840 ^oC and pressure of 25 MPa for 2 h. The relative density of the Cu-ZrB_2 composites decreased from 96.7% to 91.2% with the addition of ZrB_2. The hardness of these composites increased upto 1.0 GPa with the increase of ZrB_2 content to 7 wt.%; the increase in hardness is due to the fine ZrB_2 particles acting as obstacles to dislocation movement in Cu matrix.

In another work, Ruzic et al. [175] demonstrated the effect particle size and ZrB_2 content on mechanical properties of Cu-ZrB_2 composites processed using hot-pressing equipment at 950 ^oC and 35 MPa for 2.5 h. **Fig. 2.16** shows the influence of milling time on the particle size and various mechanical properties of the mechanically alloyed Cu-7 vol% ZrB_2 composites. The Cu, Zr and B powders were ball milled at 330 rpm with a time duration between 5 to 30 h.

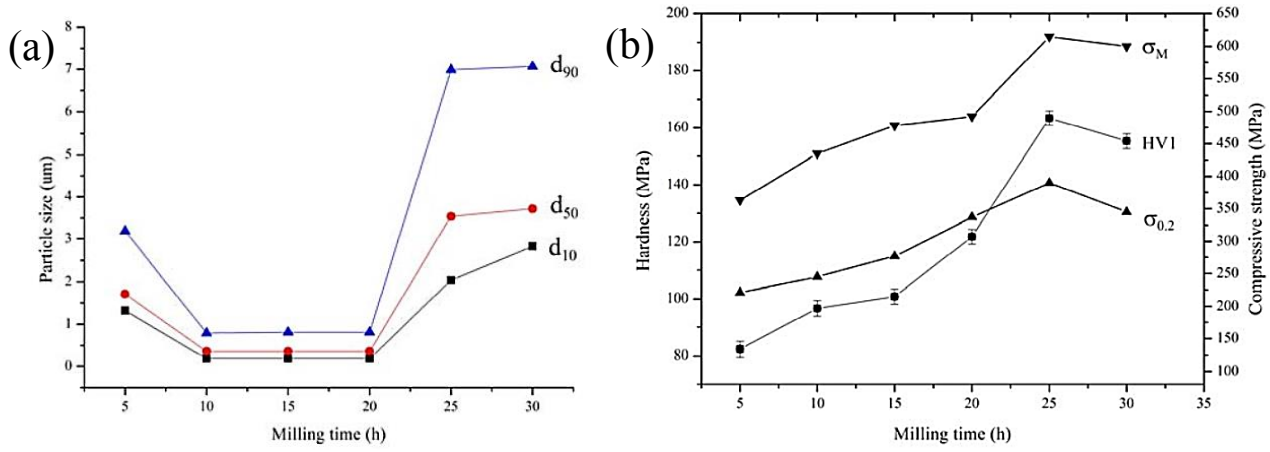

Fig. 2.16 The effect of milling time on (a) particle size and (b) mechanical properties of hot-pressed Cu-ZrB_2 composites [175].

The maximum particle size reduction was observed after 10 h and ball milling upto 20 h does not affect particle size. In the initial stage of the ball milling process, the hard Zr particles embed into soft Cu particles due to the high energy collision between balls and particles. Further collision leads to the cracking and fracture in the brittle Zr rather than the soft Cu particles. The Zr embed Cu particles get flatten due to the repeated cold welding of soft particles. In the later stages after 10 h milling, the size of the particles reduced due to the work hardening of fractured particles. Further ball milling upto 30 h lead to agglomeration of powder particles and the particle size increased (see **Fig. 2.16a**). The density of Cu-ZrB_2 composites was reported upto 95%. The hardness and compressive strength of Cu-ZrB_2 composites were found to increase

with the ball milling duration and they exhibited maximum hardness and compressive strength values of 0.16 GPa and 614.2 MPa, respectively (see **Fig. 2.16b**).

2.6 Tribological properties

In general, wear is a system property. The wear of Cu-based materials is highly affected by the load, sliding velocity, counter body material and wear environment. Other factors include material hardness, thermal properties of the material, temperature, roughness, geometry and cleanliness. Many attempts have been made by the researchers to reduce the COF and shear stresses thereby wear rate of Cu alloys. The COF is also depending on the roughness, type of material and bulk density. The wear properties of various Cu-based alloys and composites processed by various techniques [144,148,149,176–181] are given in **Table 2.5**. Especially, the bearing materials used in mining machines and dump trucks should possess high strength, good corrosion and abrasive wear resistance [182]. The abrasive wear properties of Cu-based materials mainly affected by the counter body/hard particles, test parameters and environmental conditions along with the material composition and morphology of reinforcement [183].

Abundant reports are available on the sliding wear of Cu-based materials. Nassef et al. [58] investigated the dry sliding wear behaviour of Cu10Sn alloys at various contact pressures of 0.4 – 1.2 MPa at a sliding velocity of 1.8 m/s. It is observed that the wear rate of the Cu-Sn alloys increased significantly from 7.66×10^{-3} mg/m to 64.31×10^{-3} mg/m with the increase of contact pressures due to the severe damage of the worn surface caused by abrasion and delamination. The electrical sliding wear of the Cu-Cr-Zr alloys tested at a low sliding velocity of 0.2 m/s revealed that the wear rate of Cu alloy is independent of sliding distance [179]. Adhesive, abrasive and erosion wear mechanisms were reportedly observed for the Cu-0.4Cr-0.2Zr alloys.

Ma et al. [176] studied the wear behaviour of hot-pressed Cu-5Gr composites which slide against the Ti6Al4V alloy at low speeds ranging between 0.01 to 0.5 m/s with a low contact pressure of 0.25 MPa for a sliding distance about 120 m. They reported that the specific wear of the Cu-5Gr varied between 15 to 22 $\times 10^{-5}$ mm^3/Nm with a low coefficient of friction ranging from 0.14 to 0.17. The self-lubricating property of graphite lowers the COF of the composite, but the higher wear rates observed due to the abrasive wear. The intensity of this abrasion the wear was severe with the increase in speed. In another work, Spate et al. [177]

reported that the Cu-40SiC composites showed a high COF of 0.55 at the sliding velocity of 0.5 m/s with low contact pressure (0.25 MPa). The high value of COF in composites was developed due to the abrasion mechanism as well as the removal of SiC reinforcing particles by shearing mechanism during sliding which further caused damage to the surface of composite material.

Soleimanpour and co-workers [184] studied the effectiveness of Al_2O_3 reinforcement on the wear of Cu. The wear resistance of Cu was reportedly enhanced with Al_2O_3 reinforcement compared to Cu alloys. Xu et al. [185] observed a reduction in wear (4.2×10^{-3} mg-m) for Cu-graphite composites with the addition of graphite content of 5 wt.%. (due to its lubrication property). In another work, Zheng et al. [148] explored the wear of Cu-La_2O_3 composites and observed reduction in wear of Cu with nano-sized La_2O_3 (<50 nm). Also, the wear mechanism changed from abrasion to severe plastic deformation with the applied load. **Fig. 2.17** shows the influence of La_2O_3 on the coefficient of friction and wear rate of Cu-La_2O_3 composites. The coefficient of friction of Cu-La_2O_3 composites observed to increase while the wear rate reduced with the La_2O_3 addition.

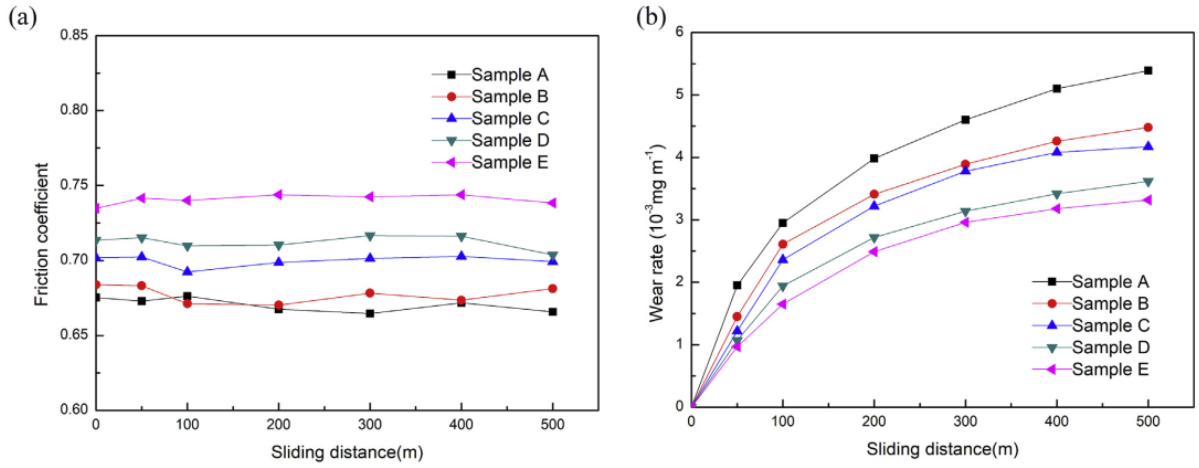

Fig. 2.17 The effect of La_2O_3 ceramics on (a) coefficient of friction and (b) wear rate of Cu-La_2O_3 composites. Sample reference A to E: Cu-X La_2O_3 (0, 0.2, 0.6, 1 and 1.3 wt.%) [148].

Fathy et al. [44] studied the tribological properties of Cu-nano ZrO_2 composites. In recent work, Fan et al. [9] investigated the effect of ZrB_2 on the tribological properties of in-situ Cu-ZrB_2 composites. The COF of the Cu composites reduced with the addition of ZrB_2. However, the COF of composites increased with the increase in the load.

Particularly, the abrasive wear behaviour of Cu composites was also attempted for understanding the severe wear behaviour of Cu [45,111,186–189]. The abrasive wear of Cu-B_4C nanocomposites was carried out against the 400 grit SiC abrasive paper [186]. It was

reported that the nano-sized B_4C particulates (50 nm) enhanced the wear resistance of Cu due to the increase in hardness of Cu. Fathy et al. [118] reported the abrasive wear of thermo-chemically treated Cu-Al_2O_3 nanocomposites processed through the powder metallurgy route. **Fig. 2.18** presents the effect of Al_2O_3 on the wear rate of Cu-Al_2O_3 nanocomposites.

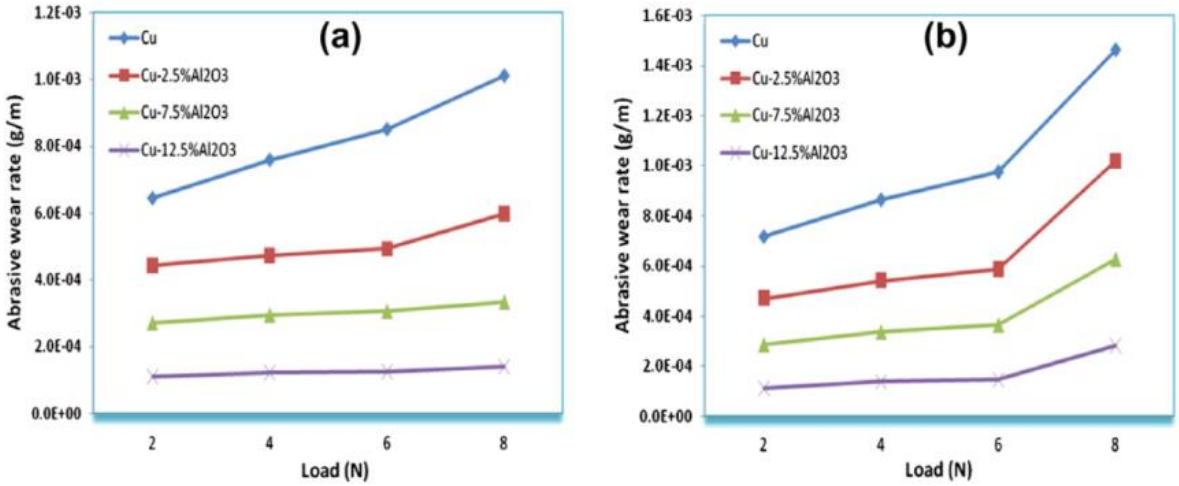

Fig. 2.18 Abrasive wear rate of Cu-Al_2O_3 nanocomposites with varying load [118].

The wear resistance of Cu was considerably reduced with the addition of hard Al_2O_3. This was attributed to the strong bonding between Cu and Al_2O_3 particles; which was evidenced by the formation of $CuAlO_2$ new phase at the Cu-Al_2O_3 interface during sintering. Also, the wear rate of Cu-Al_2O_3 composites observed to increase with the applied load. Reddy et al. [187] investigated the abrasive wear of Cu-SiC and Cu-SiO_2 composites under similar abrasive wear conditions. The addition of SiC to Cu exhibited better wear resistance than SiO_2 reinforced Cu because of the high hardness of former one. In both the composites, the material loss was dominated by plowing and micro-cutting wear mechanisms. In another work, the abrasive wear of Cu was supposedly enhanced with TiB_2 [45]. In a different work, Fathey et al. [188] studied the wear characterization of thermo-chemically treated Cu-ZrO_2 materials.

Table 2.5 Wear properties of different copper-based alloys/composites.

Alloy	Processing conditions	Wear test conditions	Hardness, Hv (GPa)	COF (C.B: SS)	Sp. wear rate (mm^3/Nm)	Ref.
Cu-5Gr	*HP*: 820 ^oC, 20 MPa for 30 min.	*p*: 0.25, *v*: 0.01-0.5, *d*: 120, *t*: 4-200	~0.71	0.14-0.17	15-22 × 10^{-5}	[176]
Cu-40SiC	*CP*: 450 MPa, 900 ^oC for 2 h	*p*: 0.25, *v*: 0.5-2, *d*: 1500, *t*: 12.5-50	1.17	~0.55	--	[177]
Cu-1.3La_2O_3	*CP*: 300 MPa, 850 ^oC for 3 h; Extrusion: 750 ^oC	*p*: 0.35 - 1.41, *v*: 0.2 – 1, *d*: 500, *t*: 8-41	1.18	~0.74	3.30 ×10^{-3} mg/m	[148]
Cu-10Sn	*HP*: 550 ^oC, 314 MPa for 30 min.	*p*: 0.4, *v*: 1.8, *d*: 500-2000, *t*: 4-18	1.79	--	7.66 × 10^{-3} mg/m	[178]
Cu-10Sn	*HP*: 550 ^oC, 314 MPa for 30 min.	*p*: 0.8, *v*: 1.8, *d*: 500-2000, *t*: 4-18	1.79	--	21.76 × 10^{-3} mg/m	[178]
Cu-10Sn	*HP*: 550 ^oC, 314 MPa for 30 min.	*p*: 1.2, *v*: 1.8, *d*: 500-2000, *t*: 4-18	1.79	--	64.31 × 10^{-3} mg/m	[178]
Cu-0.4Cr-0.2Zr	Extrusion; *HT*: 920 ^oC for 30 min.; Aged: 420 ^oC for 2 h	*p*: 0.2, *v*: 14, *d*: 1500, *t*: ~1.8	0.54	--	40.00 × 10^{-3} mg/m	[179]
Cu-0.4Cr-0.2Zr	Extrusion; *HT*: 920 ^oC for 30 min.; Aged: 420 ^oC for 2 h	*p*: 0.2, *v*: 14, *d*: 5000, *t*: ~6	0.77	--	34.00 × 10^{-3} mg/m	[179]
Cu-0.4Cr-0.2Zr	Extrusion; *HT*: 920 ^oC for 30 min.; Aged: 420 ^oC for 2 h	*p*: 0.2, *v*: 14, *d*: 8500, *t*: ~10	0.7	--	41.1 × 10^{-3} mg/m	[179]
Cu-0.5TiB_2	Casting: 1500 ^oC	*p*: 1.02-7.13, *v*: 0.44, *d*: 667, *t*: ~25-139	0.77	--	1 - 25 × 10^{-3} mg/m	[180]
Cu-1.5TiB_2	Casting: 1500 ^oC	*p*: 1.02-7.13, *v*: 0.44, *d*: 667, *t*: ~25-139	0.98	--	1 - 19 × 10^{-3} mg/m	[180]

Cu-2.5TiB_2	Casting: 1500 ºC	*p*: 1.02-7.13, *v*: 0.44, *d*: 667, *t*: ~25-139	1.25	--	1 - 17.5 × 10^{-3} mg/m	[180]
Cu-10 at.% Ag	*HP*: 300 ºC, 1 GPa	*p*: 1.38, *v*: 0.25, *d*: 450, *t*: 30	5.2	0.64	1.70 × 10^{-5}	[181]
Cu-10 at.% Ag	*HP*: 300 ºC, 1 GPa; *HT*: 450 ºC for 1 h	,,	4.2	0.63	1.49 × 10^{-5}	[181]
Cu-10 at.% Ag	*HP*: 300 ºC, 1 GPa; *HT*: 600 ºC for 1 h	,,	3.1	0.67	1.28 × 10^{-5}	[181]
Cu-10 at.% Ag	*HP*: 300 ºC, 1 GPa; *HT*: 750 ºC for 1 h	,,	2.5	0.64	0.91 × 10^{-5}	[181]
Cu-10Ag-10W	*HP*: 300 ºC, 1 GPa for 1 h	*p*: 1.38, *v*: 0.25, *d*: 2700, *t*: 180	3.71	0.43	11.00 × 10^{-5}	[149]
(Cu-14Zn-4Si)	*HP*: 900 ºC, 25 MPa, 45 min	*p*: 30, *v*: 1.5, *d*: 450, *t*: 300	2.98	0.61	2.71 × 10^{-3}	[144]
(Cu-14Zn-4Si)-3B_4C	,,	,,	3.31	0.60	2.13 × 10^{-3}	[144]
(Cu-14Zn-4Si)-6B_4C	,,	,,	3.69	0.53	1.13 × 10^{-3}	[144]
(Cu-14Zn-4Si)-9B_4C	,,	,,	4.25	0.46	1.03 × 10^{-3}	[144]
(Cu-14Zn-4Si)-12B_4C	,,	,,	4.75	0.39	0.83 × 10^{-3}	[144]

* C.B: Counter-body, *HP*: Hot pressing, *CP*: Cold pressing, *HT*: Heat treatment, *l*: Load (N), *p*: Contact pressure (MPa), *v*: Sliding velocity (ms^{-1}), *d*: Sliding distance, *t*: Time (min) and *K*: Wear coefficient.

Tu et al. [180] investigated the wear behaviour of Cu-TiB_2 nanocomposites sliding against the medium carbon steel under a high contact pressure of 7.13 MPa. The wear rate of composites showed a decreasing trend with the increasing TiB_2 content due to the local plastic deformation of the Cu. Also, no transition of wear (mild wear to severe wear) was observed with the increase of load. Also, some other investigators studied the wear behaviour of Cu alloys and composites at high loading conditions [149]. It can be observed that the COF of the Cu-based alloys and composites increased with the contact pressure.

In recent work, the effect of hot-press pressure on mechanical and wear properties of Cu-15 Al was reported [94]. Zhu et al. [149] processed nano Cu-10Ag-10W ternary alloy via mechanical alloying and hot pressing and studied its wear phenomena against stainless steel. Their study revealed the formation of precipitates, solid solution phases and the heat treatment improved mechanical and wear properties of alloys. Particularly, these nanoalloys exhibited a maximum microhardness of 3.61 GPa and nanohardness of 4.61 GPa. In a different work, Purcek et al. [150] reported the tribological properties of coarse and ultrafine Cu-0.7Cr-0.07Zr alloy. The ultrafine grains considerably increased the hardness, strength and wear resistance of Cu-alloys. It was reported that adhesion wear was the dominant mechanism in Cu-Cr-Zr alloys with coarse grain structure and the wear mechanism changed to abrasion with ultrafine grain structure.

2.7 Physical properties

2.7.1 Electrical conductivity

Cu and Cu-based materials are known for their excellent electrical conductivity. The pure copper possesses low electrical resistivity of 16.730 nΩ m at 20 °C. Cu is widely used in electrical and electronics industries as electrical contacts, induction wiring, electronic circuits (Printed circuit boards), integrated circuits and transmission and distribution lines [101]. Especially, some applications such as rail overhead current collector shoes, commutator in alternators and electrical discharge machines (EDM) requires good electrical conductivity as well as wear resistance. The alloying and dispersion strengthening are adopted to improve the strength of the pure Cu without affecting much on the ductility and workability. But they can affect the electrical conductivity of Cu and the level of effectiveness depends on the amount of alloying elements, concentration and location of particles in the microstructure.

It is also observed that the densification, dislocations, lattice strain and grain size affect the electrical properties of the materials. The electrical conductivity of Cu based materials depends upon the following factors: (a) low densification in samples causes the increase of porosity, these pores (insulating sites) make the charge transfer break off and increase the scattering of electrons [190]; (b) the lattice strain developed in the materials, which leads to more scattering for electrons movement; (c) the use of nano-sized secondary elements develops large fraction of grain boundary in the Cu matrix; this results in the scattering of the movement of the electrons, and (d) addition of low electrical conductive reinforcements or additives in Cu reduces the electrical conductivity. **Fig. 2.19** shows the effect of densification on the mechanical and electrical properties of Cu. From **Fig. 2.19**, it can be observed that as the density increased, the tensile strength and electrical conductivity of the Cu increased.

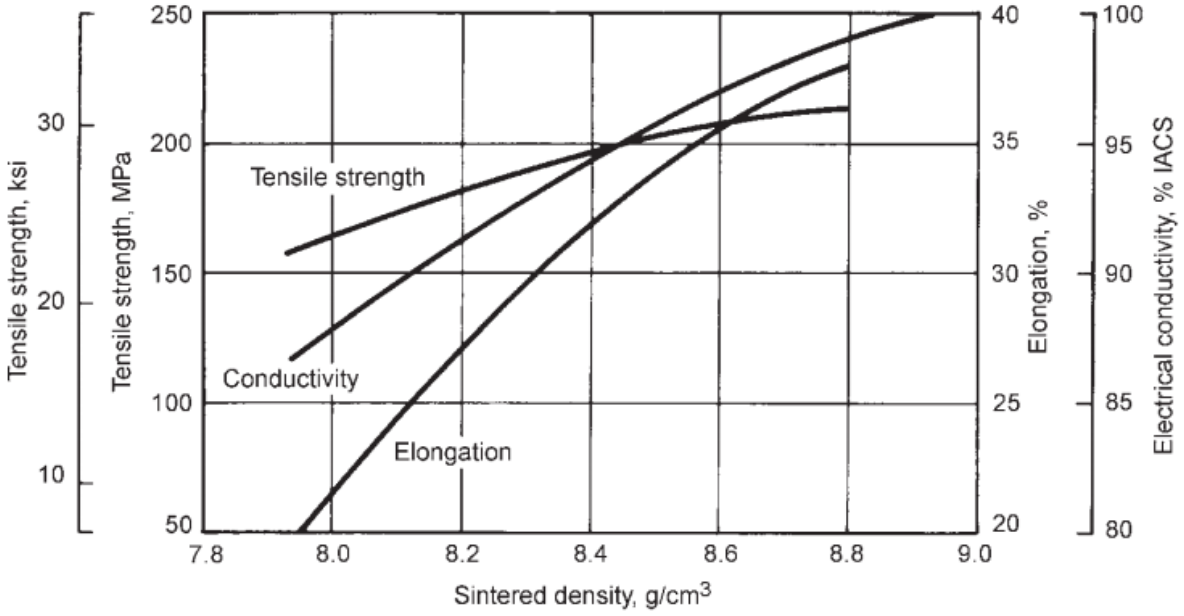

Fig. 2.19 Effect of density on electrical conductivity and tensile strength of pure copper [8].

Most of the times, a tie exists between strength and electrical conductivity while selecting a strengthening technique which depends on the type of alloying element and quantity of alloying element added to the Cu. From **Fig. 2.20**, it can be observed that the strength and electrical conductivity of Cu based materials are interrelated each other. As strength increased, the electrical conductivity of Cu based materials decreased and vice-versa. Pure Cu showed a low tensile strength of 66.6 MPa and high electrical conductivity of 99.5% IACS; whereas Cu-2Be alloy exhibited a high tensile strength of 196.4 MPa and low electrical conductivity of 16.4% IACS. Formation of intermetallic compounds in Cu-2Be alloy drastically decreased the

electrical conductivity. Precipitation-hardening method exhibits an optimal trade-off between strength and electrical conductivity compared to other strengthening methods. In precipitation-hardening of Cu alloys, it strengthens the Cu based materials without much affecting its electrical conductivity due to the formation of intermetallic compounds which were precipitated from the supersaturated solid solutions. But increased production cost due to the use of costly alloying elements or extra heat treatment processes limits the use of this method.

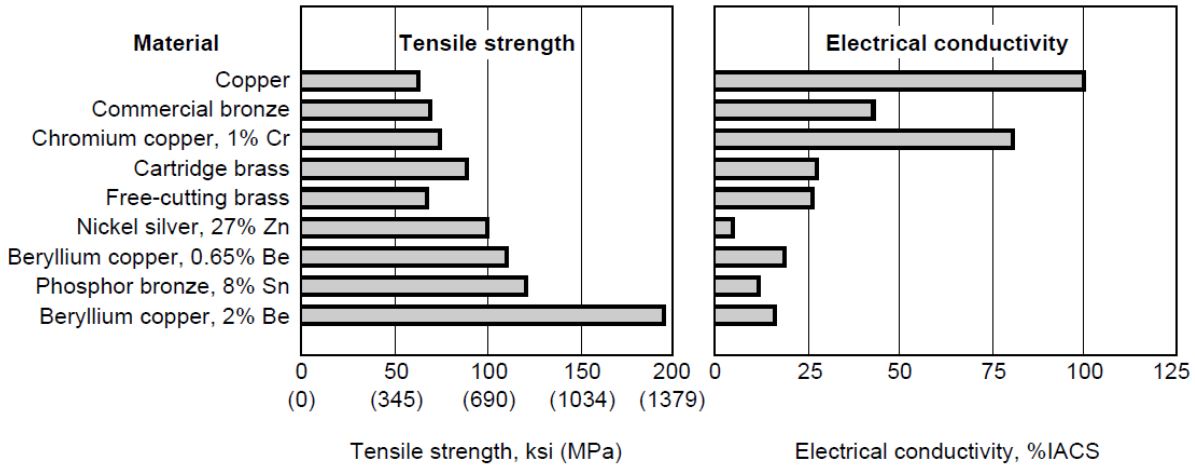

Fig. 2.20 Relationship between strength and electrical conductivity for copper and copper alloys [8].

The electrical properties of different copper alloys [39,118,172,175,191–194] and composites processed through the various processing techniques are given in **Table 2.6**. Lee et al. [90] studied the effect of an intermetallic compound on mechanical and electrical properties on friction welded Cu/Al joints. They found that the electrical resistivity (45 to 85 μΩcm) of the Cu/Al interface increased with the increase of thickness of intermetallic compound due to the formation of various phases such as CuAl and $CuAl_2$. Gomidzelovic et al. [191] studied the alloying effect on the electrical conductivity of Cu-Al-Zn alloys. It was observed that the electrical conductivity severely reduced by 6.0 times compared to pure Cu due to the presence of α and β phases.

Table 2.6 Electrical properties of different copper alloys and composites processed through the various processing methods.

Alloy	Processing technique	Electrical conductivity (%IACS)	Ref.
Cu	CP	92.7	[118]
Cu-5Cr	VM	84.2	[192]

Cu-Cr-Al_2O_3	HP	66.4	[192]
Cu-3.5Al	MA + HP	39.0	[39]
Cu-4Al_2O_3	MA +HP	46.0	[39]
Cu-4Al-23Zn (mol%)	Casting	19.4	[191]
Cu-4.6Al-24.4Zn (mol%)	Casting	17.4	[191]
Cu-8.3Al-16.6Zn (mol%)	Casting	17.9	[191]
Cu-0.5Al-1Ni	CP + sintering	35.0	[193]
Cu-1Al-1Ni	CP + sintering	30.0	[193]
Cu-5Al-5Ni	CP + sintering	28.0	[193]
Cu-8Cr-4Nb (at.%)	HP	66.1	[194]
Cu-8Cr-4Nb (at.%)	HP + HR (50%)	68.0	[194]
Cu-8Cr-4Nb (at.%)	HP + HR (75%)	70.1	[194]
Cu-8Cr-4Nb (at.%)	HP + HR (90%)	70.5	[194]
Cu-0.8Cr-0.08Zr	HT	67.0	[172]
Cu-0.8Cr-0.08Zr	HT + aging	76.0	[172]
Cu-0.8Cr-0.08Zr	HT + ECAP	35.0	[172]
Cu-0.8Cr-0.08Zr	HT + ECAP + aging	70.0	[172]
Cu-7ZrB_2 (vol%)	MA + HP	36.0	[175]

CP: cold press; HP: hot press; MA: mechanical alloying; HT: heat treatment; VM: vacuum melting; HR: hot-rolling and ECAP: equal channel angular pressing.

In another work, Monteiro et al. [193] fabricated the Cu-Al-Ni alloy through powder metallurgy technique at 780 ^oC. The electrical conductivity of these alloys was found to be decreased with the increase of alloying amount. Shukla et al. [194] prepared the Cu-Cr-Nb alloys via hot-pressing equipment (at a temperature of 1000 ^oC, 30 MPa for 30 min). In their work, it was revealed that the increase of hot rolling deformation per cent can reduce the electrical conductivity of Cu alloys due to the increase of dislocation density (with hot rolling) and increases the scattering of electrons. Fan et al. [9] studied that effect of ZrB_2 on mechanical and electrical properties of as-cast Cu-ZrB_2 composites. **Fig. 2.21** present the hardness and electrical conductivity of Cu-ZrB_2 composites. They reported that the hardness of Cu increased and the electrical conductivity decreased with the addition of ZrB_2. This could be attributed to the increased dislocation density with the hard ZrB_2 particles in the Cu matrix.

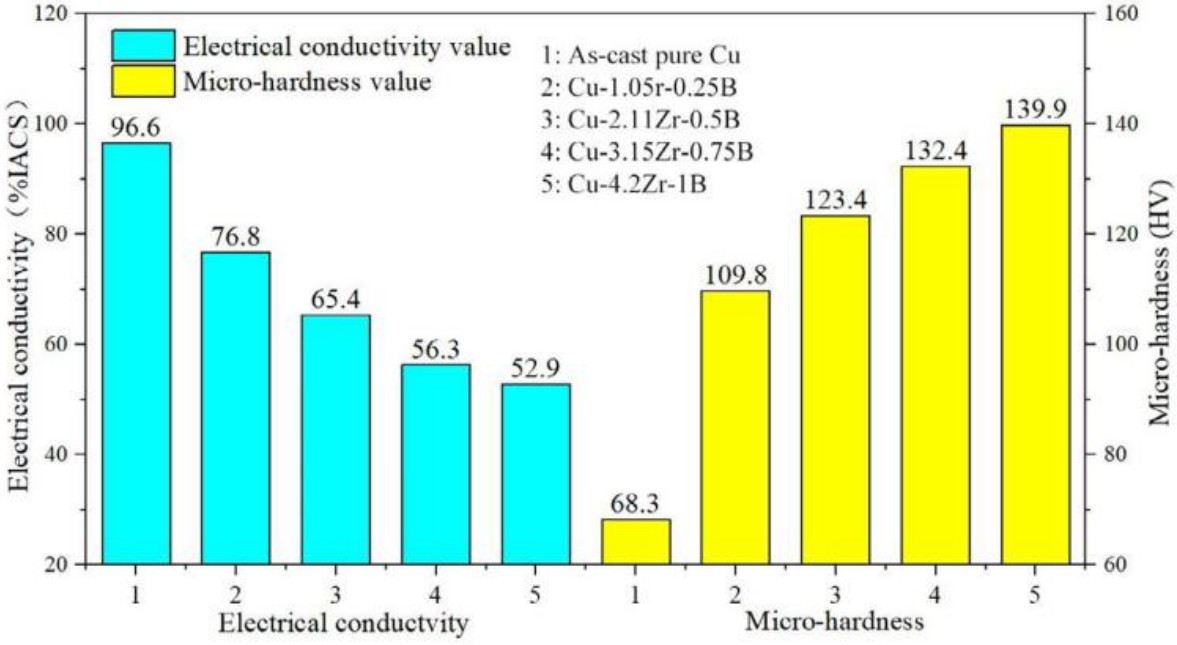

Fig. 2.21 The effect of ZrB_2 on hardness and electrical conductivity of Cu-ZrB_2 composites [9].

Ruzic et al. [175] developed Cu-ZrB_2 composites using hot-pressing (at a temperature of 950 ^oC and 35 MPa) technique. The residual porosity and lattice strains caused the reduction of electrical conductivity of the Cu composites. By observing the above results, it can be understood that the processing conditions and secondary elements affects the electrical conductivity of the Cu.

2.8 Chemical properties

2.8.1 Corrosion

Most of the metals and alloys behave abnormally under saline seawater environment. Corrosion is one of the main problems in marine applications which affects the inherent properties of this class of materials. Hence, corrosion of metals is an ongoing topic of interest among researchers and continuous efforts are being made to reduce their corrosion in such an environment. In particular, Cu and Cu-based materials can be considered as very promising materials for the marine applications due to its high corrosion resistance, moderate strength and good physical properties [195,196]. Use of Cu alloys in naval industries may have positive effects in terms of the low maintenance cost, good service life, high recyclability and reliability [196]. Generally, use of corrosion inhibitors or alloying copper with other elements (Zn, Sn,

Ni, Al, Mn, Ag and Ti etc.) or ceramic reinforcements, and the combination of both have been practised to prevent corrosion of Cu [60,195–200]**.** Aluminium (Al) is one of the attractive alloying elements used to inhibit corrosion of copper-based alloys, which forms a protective layer on the surface of copper [201].

Cu-Al alloys possess excellent thermal, electrical, mechanical, non-sparking and tribological properties. They are widely used in thermal power plants for condenser and heat exchanger applications due to their high strength, high-temperature oxidation resistance and good biofouling properties [202]. Also, these alloys are preferred in suction pumps, centrifugal impellers, valves and turbine blades due to their high resistance to erosion [203]. The corrosion resistance of Cu-Al alloys is mainly because of the formation of a protective passive layer of Cu_2O and Al_2O_3 on the surface when exposed to corrosion environment [204,205]. **Fig. 2.22** shows the formation of an oxide layer after immersed in a salt solution. The formation of these stable passive layers on Cu-Al alloys is mainly due to the higher affinity of aluminium towards oxygen than copper in salt solutions [136,206].

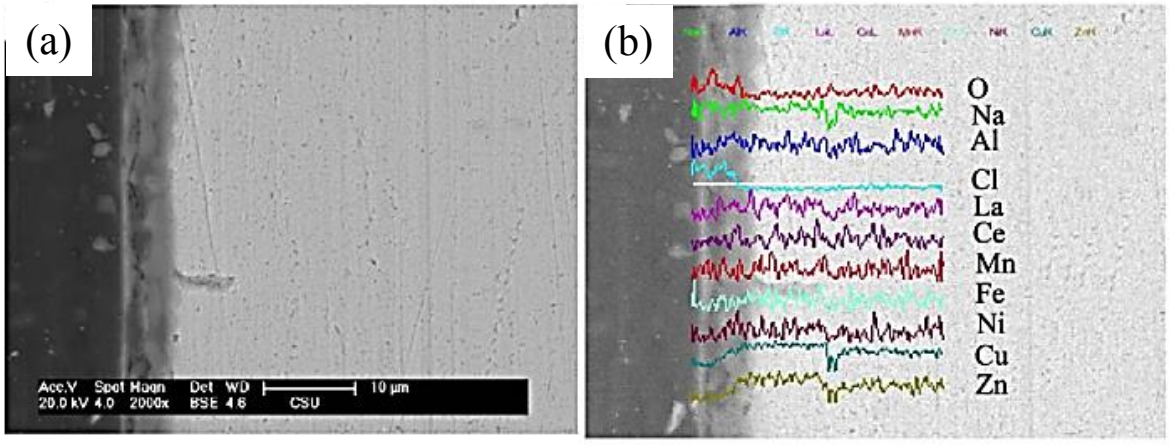

Fig. 2.22 Cross-sectional morphology of Cu-Al alloys after immersion in NaCl solution. (a) Presence of protective layer and (b) elemental mapping of protective layer [205].

In the past 40 years, extensive research has been carried out on Cu based alloys to understand its corrosion mechanisms [207,208]. The corrosion rate of various Cu alloys tested under seawater environment is listed in **Table 2.7**. Mansfeld et al. [209] discussed the corrosion of Cu alloys such as Cu-Ni, Cu-Al and Cu-Zn alloys under natural seawater environment. The de-alloying effect was observed in all these three Cu based alloys when they were exposed to the corrosive medium, while intergranular corrosion was noticed as the exposure time extended up to 30 days. Yamashita et al. [210,211] observed intergranular corrosion and stress corrosion

cracking for Cu-9 at.% Al alloy. Recently, the corrosion behaviour of different Cu alloys (Cu-8Al-2Fe, Cu-30Zn and Cu-30Ni) under NaCl media (pH: 6.5 and 10) was studied by Alfantazi et al. [197]. The de-alloying effect was minimal in Cu-Al alloys in comparison to Cu-Ni alloys due to high reversible potentials and solid-state diffusion between the Cu and Al. Also, the passivity of these binary alloys was high in buffered chloride (pH: 10) solution than low buffered solutions.

Table 2.7 Corrosion properties of different copper alloys.

Sample reference	**Processing technique**	**Corrosion environment**	I_{corr} **(μA-Cm^{-2})**	E_{corr} **(mV)**	**Corrosion rate (mpy)**	**Ref.**
Cu	Casting	3.5 % NaCl	11.3	293	18.6	[212]
Cu	Casting	3.5 % NaCl+0.001 MAP*	1.25	-304	2.05	[212]
Cu	Wire drawing	0.9 % NaCl	1.95	-188	1.83	[213]
Cu	Wire drawing	0.9 % NaCl + 0.005 M cephradine*	0.14	-170	0.13	[213]
Cu	Casting	0.5 M HCl	23.4	-245	21.52	[214]
Cu	Casting	0.5 M HCl +10mM ATA*	5.9	-241	5.43	[214]
Cu	Casting	Tequila (Agave Azul Tequilana Weber, pH: 3.6)	2.2	-60	5.33	[215]
Cu-7Al-2Fe	Casting	1M NaCl pH6	9.5	-412	--	[197]
Cu-9Al-1.7Mn	Casting	Artificial ocean water pH 7.68	12.06	-276	--	[216]
Cu-9Al-4Ni-4Fe	Casting	3.5 % NaCl	13.4	-284	--	[217]
Cu-9Al-30Ni	Casting	3.5 % NaCl pH 7.0	3.3	-418	1.49	[218]
Cu-9Al-45Ni	Casting	,,	1.6	-455	0.71	[218]
Cu-10Al-10Zn	Casting	3.5 % NaCl	23.3	-509	10,787.40	[219]
Cu-10Al-10Ni	Casting	,,	7.4	-463	3,448.81	[219]
Cu-10Ni-10Zn	Casting	,,	0.8	-442	350.39	[219]
Cu-11Al-5Ni	Casting	3.5 % NaCl pH 7.0	12	-318	5.47	[218]
Cu-11Al-10Ni	Casting	,,	10.2	-322	4.64	[218]
Cu-11.5Al-4.5Ni	Casting	3.5 % NaCl	6.93	-307	5.04	[204]
Cu-11.9Al-4Ni	Casting	3.5 % NaCl	6.9	-307	6.22	[206]

Cu-11.9Al-4Ni-0.7Mn	Casting	,,	1.4	-267	1.28	[206]
Cu-11.9Al-4Ni-0.7Ti	Casting	,,	2.8	-249	2.52	[206]
Cu-11.5Al-0.44Be-0.2Mn	Casting	Artificial ocean water	0.14	-220	103.39	[59]
Cu-12Al-0.49Be-0.3Mn	Casting	,,	0.20	-158	146.13	[59]
Cu-12.5Al-0.54Be-0.25Mn	Casting	,,	0.19	-191	130.56	[59]
Cu-12.5Al-0.56Be-0.25Mn	Casting	,,	0.23	-190	168.27	[59]
Cu-12Al-4Ni	Vacuum induction melting	0.5 M NaCl	2.75	-329	--	[136]

Note: NaCl: Sodium chloride, HCl: Hydrochloric acid; Corrosion inhibitors* are ATA: 4-amino 1,2,4-triazole and MAP: 2-mercapto-4-amino-5-nitroso-6-hydroxy pyrimidine

Khaled et al. explained the corrosion behaviour of cast (pure) copper under 3.5 % NaCl environment. The corrosion rate of copper was 18.6 mpy which was decreased by adding a corrosion inhibitor to NaCl such as 2-mercapto-4-amino-5-nitroso-6-hydroxy pyrimidine (MAP) [212]. At low concentration of NaCl (0.9 %), a low corrosion rate of 1.83 mpy was recorded pure copper [213]. The corrosion rate of copper was reduced by approximately 4 times by adding a 4-amino 1,2,4-triazole corrosion inhibitor [214]. In another work, Carreon et al. [215] reported the corrosion rate of 5.33 mpy for copper under tequila alcoholic environment.

Badawy et al. [219] explained the alloying effect on the corrosion of Cu. They reported a very high corrosion rate for three different Cu alloys (namely Cu-10Al-10Zn, Cu-10Al-10Ni and Cu-10Ni-10Zn alloys) in a saline environment. Among all, Cu-Ni-Zn alloy was found to be more resistant to corrosion. Safaa et al. [204] studied the corrosion of Cu-11.5Al-4.5Ni ternary alloy (5.04 mpy) in ocean water conditions. Whereas in a different study, Cu-Al-Ni-X (X: Mn, Ti) high entropy alloys reportedly exhibited the low corrosion rate under NaCl solution [206]. When the 0.7 wt.% Ti added to the ternary alloy, the corrosion rate was minimized to 2.52 mpy; while the 0.7 wt.% Mn added, the corrosion rate was reduced to 1.28 mpy. Nady et al. [218] studied the effect of Ni on corrosion behaviour of Cu-Al alloy under chloride environment. It was reported that the corrosion rate of alloys decreased with the addition of Ni content upto 45 wt.%. **Fig. 2.23** shows the open-circuit potential (OCP) and oxide layer resistance of Cu-Al-Ni alloys.

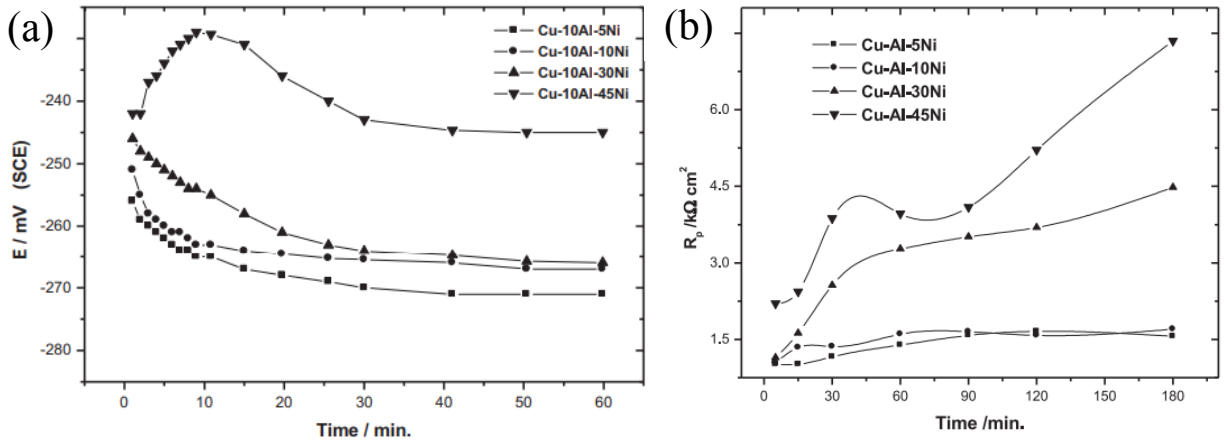

Fig. 2.23 Variation of the (a) open-circuit potential and (b) corrosion resistance of the barrier layer of the different Cu-Al-Ni alloys immersed in stagnant 0.6 mol dm-3 chloride solution [218].

The lowest corrosion rate of 0.71 mpy was observed for Cu-9.5Al-45Ni under 3.5% NaCl solution. The addition of a high amount of Ni (45 wt.%) and Al (9.5 wt.%) resulted in a high passivation effect for Cu. The corrosion resistance of these alloys increased mainly due to the formation of CuO_2, Al_2O_3 and the replacement of cation vacancies of Cu oxide by the Ni. From the above discussion, it can be observed that the Al was considered to be an effective alloying element for improving the corrosion-resistance of Cu.

2.9 Applications

Copper-based materials are widely used in applications that require superior corrosion resistance, good bearing-surface qualities, high thermal or electrical conductivity, and other special properties. These applications may be divided into five principal groups which are presented in **Fig. 2.24**.

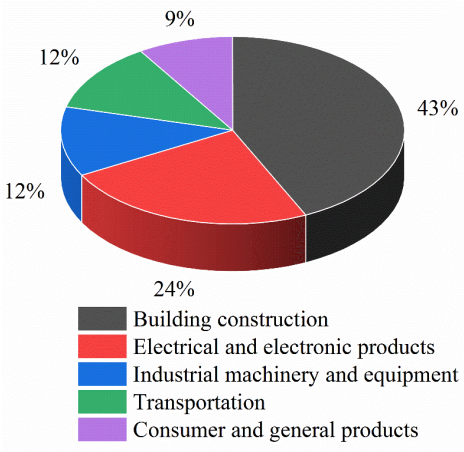

Fig. 2.24 The usage of copper and copper-based materials in various fields of Engineering [8].

2.9.1 Building construction

The usage of copper in building construction sector is classified into two main categories such as plumbing and electric wiring applications. The plumbing goods include tubes, taps, valves, connectors and fittings. Other applications include heating and cooling systems; safety appliances such as fire sprinklers, lightning arresters, door hinges, doorknobs, door fittings, locks; roofing and flashings [220].

2.9.2 Electrical and electronic products

The high usage of Cu-based materials is the electric wires and cables in industrial as well as domestic sectors. The cables are mainly used for the power generation, transmission and distribution. Also, the copper cables used for the electronic circuits, instrumentation and telecommunication. In the electronic industry, pure copper is mainly used in printed circuit boards (PCBs) as copper foil and connectors.

2.9.3 Industrial machinery and equipment

In power generation industries, copper and its alloys are widely used in heat exchangers and condensers. The Cu-Al, Cu-Ni, aluminium brasses and tin brasses are commonly used materials in condensers. The condenser tubes are the critical parts of the power plant cooling system due to the use of saltwater in condensers causes hydrogen embrittlement of boiler tubes. In such cases, the use of Cu-based alloys plays a vital role in minimizing the effect of stress corrosion cracking in condenser tubes. Another use of Cu-based alloys in electric motors is bearings. The commonly used materials for bearing applications are bronzes, Cu-Pb alloys and tin bronzes.

2.9.4 Transportation

The main usage of Cu-based maters in the transportation sector is automobiles and trucks. The application includes ships, aircraft and trains where Cu-based materials mostly used for heat transfer devices (radiators and oil coolers), electrical elements and sleeve bearings.

The Cu-Al alloys are one of the versatile materials that exhibit excellent strength under high corrosive stress environment. For example, the bearings used in mining industry such as

earth moving equipment and rock crushers require high proof strength, fatigue strength, abrasive wear resistance, corrosion resistance since they need to work under heavy loads, a dusty environment which contains hard SiC debris and the corrosive environment consists of high moisture levels [221]. The bearings of Cu-Al alloys can perform better at heavy loads and low speeds compared to cast bronzes [222]. Also, the Cu-Al alloys are widely used in marine applications such as shafts, propellers, pumps, valves, fire-fittings and mechanical components for seawater cooling systems due to their excellent antifouling properties. The non-sparking properties of Cu-Al alloys make them use in oil and gas industries as hand tools. Because of the non-magnetic properties of Cu-Al, they are used in chains and slings in mining. In recent work, Alex et al. [93] reported that the thin films of Cu-Al alloys can be used as flexible reflective coatings in solar power applications. Blanchet et al. [223] suggested that the Cu-Al alloy can be most suitable for high wear-resistant applications such as jackscrew in aircraft's horizontal stabilizer assembly.

The other significant materials of Cu-based materials are Cu composites which are having high strength, high toughness, excellent electrical and thermal conductivity. The Cu composites have been used in various industrial applications such as electrodes in electric discharge machines (EDM), braking and bearing materials [224–230]. Hussain et al. [224] reported that the Cu-Al_2O_3 composites processed through powder metallurgy route are used as electrodes in electric discharge machines. Similarly, Khanra et al. [225] and Jin et al. [226] suggested the use of Cu-ZrB_2 composites for the EDM applications. In another work, Xiao et al. [227] proposed Cu-Fe-Gr hybrid composites can be best suitable for brake pad materials in high-speed trains. In a similar work, Prabhu et al. [228] reported that the Cu-SiC-Gr hybrid composites can be used for frictional materials for brakes and clutches. Also, Cu-Sn-Ni/Al_2O_3 composites can be suitable for bearing applications such as bearings in motors of electric vehicles [229]. Norasetthekul et al. [230] reported the use of Cu-ZrB_2 composites as an electrode in plasma applications.

Chapter 3

Materials and methodology

3 Chapter 3

This chapter describes the raw powders analysis, powders processing, consolidation of powders and detailed procedure of various characterization techniques such as microstructural characterization using an optical microscope (OM) and scanning electron microscope (SEM) equipped with energy dispersive spectroscope (EDS), electron probe microanalyzer (EPMA) and phase analysis using X-ray diffraction (XRD); the hardness evaluation using nano, micro-hardness indentation techniques and compressive strength properties measurement using a universal testing machine (UTM); the wear tests (dry sliding and two-body abrasion test) using the pin-on-disc machine and electrical conductivity measurement.

3.1 Materials

Commercial copper (Padmasree enterprises, Hyderabad, India) and aluminium powders (SRL™, India) with a mean particle size less than 45µm and purity greater than 99% (as per the supplier's data) and ZrB_2 powders (H.C. Starck, Grade B) with a mean particle size of 3-5 µm and purity greater than 97% were used as starting materials in the present study. From SEM analysis (see **Fig. 3.1**), it was observed that the Cu powders are spherical in shape with a mean

particle size of ~9.98 µm, Al powders are characterized with irregular particle shape and with the size of ~6.47 µm and ZrB_2 powders having an irregular shape with a mean particle size of ~2.96 µm. After high energy ball milling (conditions: Speed: 500 rpm, BPR:20:1 for 10 h), the size of ZrB_2 particles was considerably reduced to about 0.29 µm (**Fig. 3.1**). However, the ball-milled ZrB_2 powders were in the agglomerated form. In the literature, the milling of Cu-based materials has been reportedly carried out at a milling speed in the range between 120 and 600 rpm, milling time between 1 and 50 h, and ball-to-powder weight ratio (BPR) ranging from 1.5:1 to 10:1 [231–234]. Based on the literature and our preliminary experiments, in the present work, the milling parameters were selected to reduce the particle size and to ensure uniform mixing and dispersion of Al or ZrB_2 in Cu. The elemental powders were milled in stainless steel vials for 10 h duration at 260 rpm (BPR ~ 10:1), using toluene as dispersing medium.

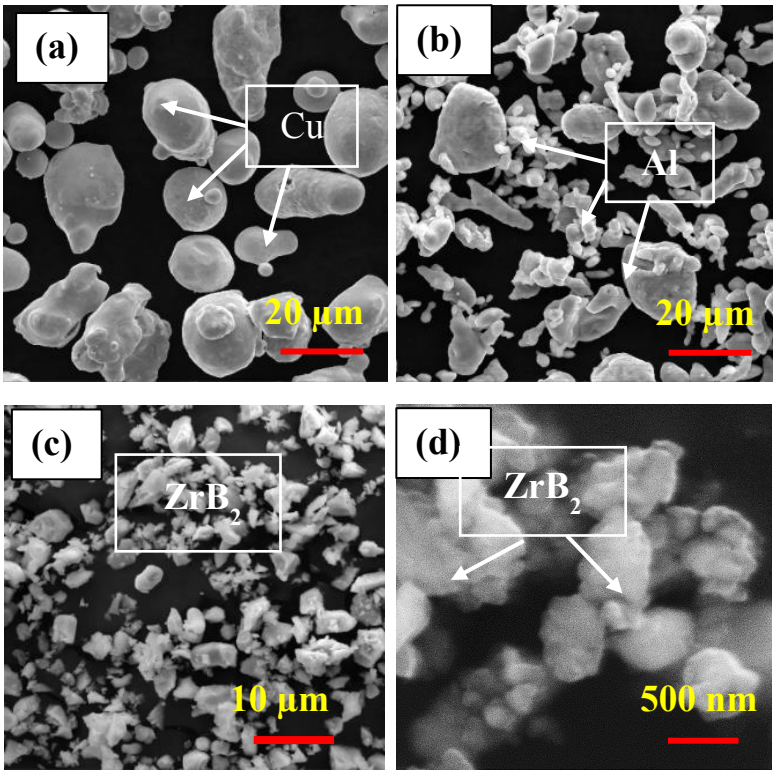

Fig. 3.1 SEM images of as received (a) copper, (b) aluminium (c) ZrB_2 and (d) ultra-fine (milled) ZrB_2 powders

The ball-milled powders were dried using rotary vacuum evaporator at 98 ^oC for 30 min. Appropriate amounts of Al powders were added to Cu and the compositions were mechanically alloyed at severe milling (wet) conditions with a planetary ball mill to prepare Cu-X wt.% Al (X = 0, 3, 5, 10 & 15) nominal compositions; they were referred as Cu (ML), C3Al (ML), C5Al (ML), C10Al (ML) and C15Al (ML). Also, ZrB_2 powders were reinforced with Cu and mechanically alloyed at severe milling conditions to prepare Cu compositions in the range

between 0 to 10 wt.% (0, 1, 3, 5 and 10 wt.%) ZrB_2. They were referred as Cu (ML), C1Z (ML), C3Z (ML), C5Z (ML) and C10Z (ML).

A similar set of Cu-Al and Cu-ZrB_2 powder compositions were also prepared via mixing (dry condition). In case of mixing route, the starting elemental powders were mixed uniformly using a planetary ball mill at a low speed of 100 rpm (BPR ~ 2:1) for 1 h. The Cu-Al (mixed) compositions were designated as Cu (MX), C3Al (MX), C5Al (MX), C10Al (MX) and C15Al (MX). Similarly, Cu-ZrB_2 (mixed) compositions were referred as Cu (MX), C1Z (MX), C3Z (MX), C5Z (MX) and C10Z (MX). In fact, Cu (MX) represents the use of as-received Cu powders and hence for convenience it was referred as Cu (MX).

The hot press processing parameters were optimized by varying the hot press pressure and time (see **Fig. 3.2**). From **Fig. 3.2a,** it can be observed that the relative density of C15Al (ML) was increased from 88.4% to 97.0% and hardness significantly improved from 2.2 to 6.16 GPa with the change in hot press pressure from 100 to 500 MPa. This reveals that the high hot press pressure promotes good densification and properties of alloys.

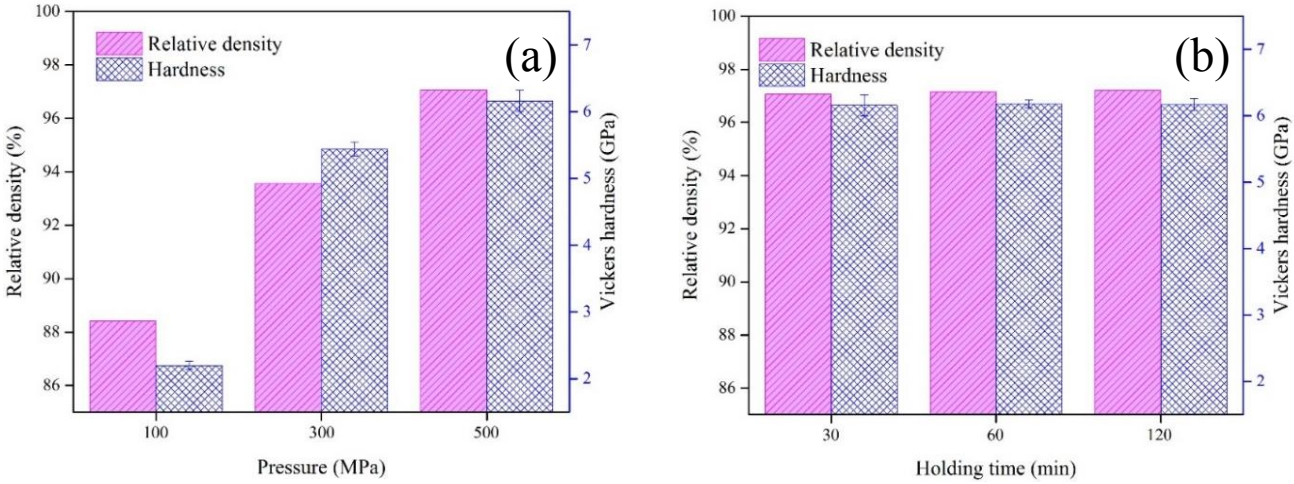

Fig. 3.2 Optimization of hot press processing conditions for C15Al (ML). (a) Effect of pressure at constant T = 500 ^oC, t = 30 min. and (b) effect of holding time at T = 500 ^oC, P = 500 MPa.

No considerable effect on relative density (97.0 – 97.2%) and hardness (6.16 – 6.19 GPa) of the C15Al alloys was evidenced with changing holding time in the range of 30 - 120 min (see **Fig. 3.2b**). Hence, holding time of 30 min was realized as the optimal and cost-effective process parameter. Thus, the hot-pressing temperature of 500 ^oC, pressure of 500 MPa and the holding time of 30 min was selected as optimal processing parameters for the hot-pressing process.

3.2 Processing of the bulk Cu-Al alloys and Cu-ZrB_2 composites

After conducting several trial hot press experiments (at different sintering conditions in order to optimize the processing parameters), it was observed that both pure Cu (milled) and Cu (mixed) could be densified to 98.6 and 99.7% theoretical density (ρ_{th}), respectively at the optimal hot pressing condition of 500^{o}C (temperature), 500 MPa (pressure) and 30 min. (time). Hence, this hot press condition was used as a reference to process the Cu-Al and Cu-ZrB_2 systems in the current work.

The hot pressing of Cu-Al and Cu-ZrB_2 (milled and mixed) powders were consolidated using a hot press (Model: CMM, VB Ceramic Consultants, India) at a sintering temperature of 500 ^{o}C under hydraulic ram pressure of 500 MPa for 30 min in a vacuum (1.3×10^{-2} mbar) environment (see **Fig. 3.3**). The heating rate during the heating cycle of hot pressing was programmed at 10 ^{o}C/min. and after furnace cooling, the sintered samples were ejected from the H13 steel die at room temperature.

Fig. 3.3 Hot press equipment with vacuum pump arrangement

The samples were prepared with the dimensions of 15 mm in diameter and height of 5 mm. The density measurements of hot-pressed samples were carried out using a precision weighing balance attached to the density measurement setup (Model: BSA224S-CW, Sartorius). The bulk density of compacts was measured by the Archimedes technique according to ASTM B962-08.

To compare the densification response of various compositions, the bulk densities were normalized with respect to theoretical density.

3.3 Characterization

3.3.1 Microstructural characterization

The microstructure of powders and hot-pressed samples were carried out using an optical microscope and the scanning electron microscope (SEM: Tescan Vega 3 LMU). The compositional analysis of Cu-Al alloys was carried out by energy dispersive spectroscopy (EDS: Oxford Instruments). Metallographic sample preparation was done to reveal the microstructure of hot-pressed samples. The polishing of samples was carried out using grinding, disc polishing with silicon carbide papers up to 2000 grade and they were further polished to mirror finish by using alumina liquid suspension. The surface of these samples was etched with ammonia (50%) and distilled water (50%) solution for a few seconds.

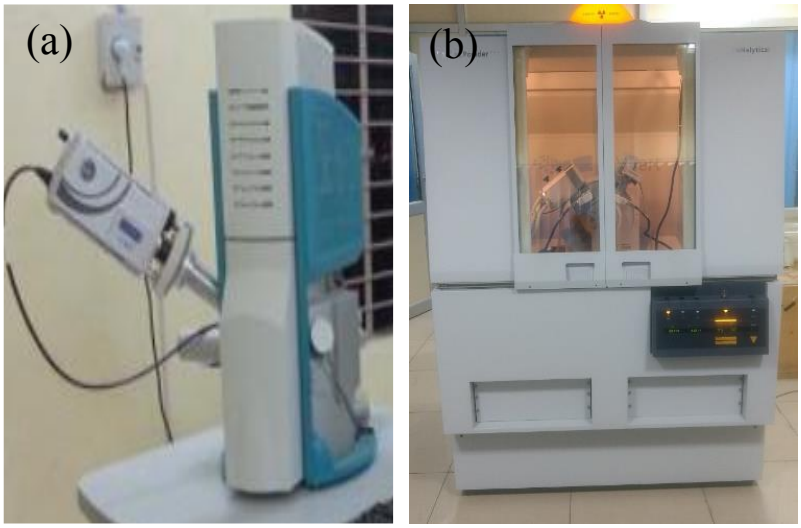

Fig. 3.4 (a) Scanning electron microscope with EDS arrangement and (b) X-ray diffraction equipment.

The microstructural characterization of etched and fracture surface of Cu-Al and Cu-ZrB_2 samples were inspected with SEM-EDS (**Fig. 3.4a**). The elemental quantification of the Cu-Al alloys was measured using the electron probe micro-analysis (EPMA: Camebax Micro, Cameca). The phase analysis of starting, milled powders and the sintered compacts were carried out by X-ray diffraction (XPERT-Pro, Pan Analytical), using CuK_α radiation (λ=1.5405Å), which was operated at 45 kV and 30 mA (**Fig. 3.4b**). The volume fraction of

individual phases in the hot-pressed samples was estimated by the Rietveld analysis of XRD patterns. The XRD data were collected at a scanning rate of 0.0166 ^{o}/sec and the patterns analyzed by X'Pert High Score software with Inorganic Crystal Structure Database (ICSD). For dislocation density measurements, the curve was fitted after stripping the Kα2 component from the raw data using X'Pert High score software. The full width half maximum (FWHM) values and diffraction angles of major peaks from the X-ray diffraction patterns were considered for Williamson–Hall analysis.

3.3.2 Mechanical properties measurement

The hardness of polished samples was measured using Vickers Micro-hardness tester (Shimadzu, HMV, Japan) at 100 g load for 30 seconds (s) according to ASTM E384-11e1. **Fig. 3.5a** shows the photograph of Vickers microhardness tester. A minimum of five indentations was made to evaluate the hardness. The nanoindentation test was used to understand load-displacement behaviour, elastic and plastic properties of Cu alloys.

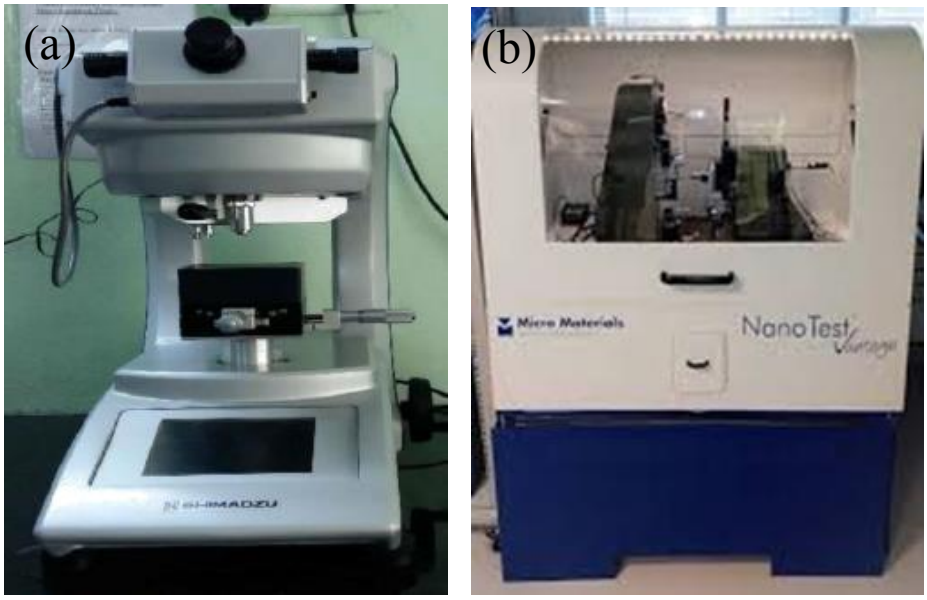

Fig. 3.5 Photographs of (a) Vickers microhardness tester and (b) Nanoindentation testing machine.

Before the nano-indentation test, the samples were finely polished using colloidal silica suspension for 2 h to get the good surface finish and the nanoindentation test (Model: Nano Test Ventage, Micro Materials, UK) was carried out using Berkovich indenter (see **Fig. 3.5b**). The test was performed at a constant load of 20 mN with a loading and unloading rate of 2.0 mN/s. The area (an array of 10×10 matrix with 40 μm spacing) was selected on the sample

surface such that 100 indentations could be made to get good representative data. **Fig. 3.6** shows the photograph of a Universal testing machine. The compression test of Cu-Al alloys and Cu-ZrB_2 composites was conducted on the Universal Testing Machine (UTM) (Instron, Model No: 5982, USA) at a strain rate of 0.02 mm/min. In order to minimize the friction during the compression test, grease was applied on the top and bottom specimen-platen interfaces. The cylindrical samples having the dimensions of 10 mm diameter (*d*) and 15 mm length (*l*) with *l*/d ratio of 1.5 were prepared for the compression test. A minimum of two measurements was taken for reporting the compression test results.

Fig. 3.6 Photograph of Universal testing machine.

3.3.3 Wear test

The wear test of Cu-Al alloys (milled and mixed) and Cu-ZrB_2 composites (milled and mixed) was carried out using a pin-on-disc wear testing machine (Ducom Bangalore, Model: TR-20). The pin-on-disc wear testing setup is shown in **Fig. 3.7** In case of the abrasive wear test for Cu-Al and Cu-ZrB_2 (both milled and mixed) samples was conducted using the pin-on-disc testing machine with SiC emery sheet (220 grit size) attachment on the disc. In this test, the specimens were ground up to 1500 grit SiC abrasive paper to ensure complete contact with the counter body. Before the test, polished specimens were cleaned thoroughly with ethanol. The cylindrical samples (10 mm × 15 mm) were prepared for the wear tests. The samples having a contact area of 78.5 mm^2 were maintained for each sample. The abrasive wear test parameters were listed in **Table 3.1**. The average of three test values was considered to calculate weight

loss and wear coefficient. An accurate analytical weighing balance of 0.0001 g resolution was used to measure the initial and final weights of samples.

Table 3.1 Summary of abrasive wear test conditions.

Parameters	**Remarks**
Applies force (N)	5
Counter-body	SiC emery paper
SiC abrasive particle size (μm)	~68 (220 mesh)
Pin diameter (mm)	10
Sliding velocity (m/s)	1
Sliding distance (m)	60
Temperature (^{o}C)	Room temperature
Test environment	Air

The sliding wear test was additionally used only for Cu-Al (milled condition) samples to understand both the abrasive and sliding wear performance of the Cu-Al alloys as they exhibited superior hardness when compared to all the other Cu-Al/Cu-ZrB_2 samples. The sliding wear test of the Cu-Al (milled) alloys was tested against stainless steel disc at a contact pressure of 0.5 MPa and the tests were run for a sliding distance of 2000 m.

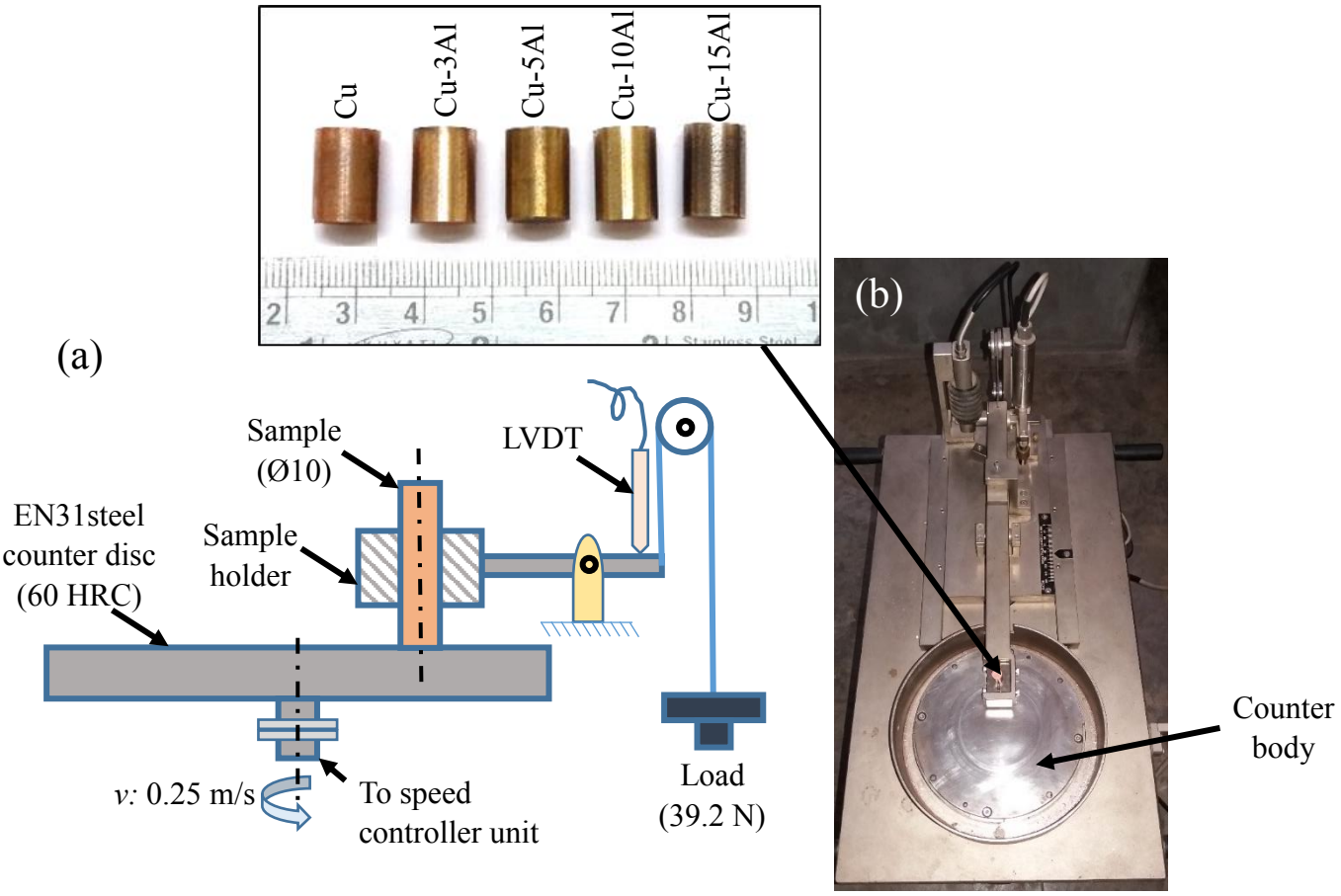

Fig. 3.7 Pin-on-disc wear test setup for Cu-Al alloys. (a) Schematic representation and (b) Photograph of sliding wear tester.

The pin-on-disk wear test was conducted according to ASTM G99 standard in dry sliding conditions under a maximum load of 39.2 N and sliding velocity of 0.25 m/s. In general, low sliding velocity was used to be selected for the wear test of Cu alloys in order to suppress flash temperature at the contact surface [181]. Hence, in the current study, wear tests of Cu-Al specimens were conducted at a sliding velocity of 0.25 m/s. The wear test samples were prepared with the dimensions of Ø10 × 15 mm. For the sliding wear test, Cu-Al alloy (milled) specimens were polished with 1500 grit size silicon carbide papers; further, the samples were ultrasonically cleaned using ethanol before and after the wear test. The surface roughness (Ra) of all the samples was maintained upto 0.12 µm before the wear test. The EN 31 Grade steel disc (C: 0.90-1.20%, Si: 0.10-0.35%, Mn: 0.30-0.75%, Cr: 1.00-1.60%, S: 0.05%, and P: 0.05%) with the hardness of 60 HRC (~ VHN: 7.2 GPa) was used as a counterbody for the wear test.

The wear volume loss was calculated by measuring the weight loss and density of samples. The specific wear rate (w) is calculated using the **Eq. (3.1)**; whereas, Archard wear equation, **(Eq. 3.2)** was used to determine the wear coefficient (t).

$$Sp.wear\,rate, w = \frac{(W_{initial} - W_{final})}{\rho \times \ell \times d} \quad (3.1)$$

$$Wear\,coefficient = w \times H \quad (3.2)$$

Where, $W_{initial}$: weight of the sample before the wear test, $W_{final:}$ weight of the sample after the wear test, ρ: experimental/measured density of the sample, ℓ : Applied load, d: sliding distance and H: hardness. At least two tests were done under similar wear test conditions and the average values were reported.

After the wear test, worn surfaces of the Cu-Al and Cu-ZrB_2, wear debris and the counter body surfaces were characterized with SEM-EDS to perceive the underlying material removal or wear mechanisms.

3.3.4 Electrical conductivity test

The electrical conductivity of Cu-Al alloys and Cu-ZrB_2 composites was measured using the digital electrical conductivity meter (Model: DCM-580-2000, Technofour). The electrical conductivity testing setup is shown in **Fig. 3.8.** The test was performed according to the ASTM E1004 standard. The cylindrical samples with a size of Ø15 × 5 mm were tested at an accuracy of ± 0.1%. At least two measurements were considered for measuring electrical conductivity.

Fig. 3.8 The photograph of an electrical conductivity test setup

3.3.5 Corrosion measurement

Polishing of working electrodes ((Cu (ML), C15Al (ML)) was done using emery papers upto 2000 grit size and the samples were thoroughly washed with distilled water. After polishing, a three-electrode cell glass assembly with Cu alloys as a working electrode with an exposed area of 0.7854 cm^2, Ag/AgCl /1M KCl electrode as a reference electrode and platinum spiral electrode as a counter electrode was used for corrosion tests. All electrochemical experiments were conducted in a stagnant, naturally aerated neutral 3.5 mass per volume (m/v) % NaCl solution (pH: ~ 8.2) at room temperature. The electrochemical impedance spectroscopic (EIS) studies and polarization experiments were performed using PARSTAT 4000 Potentiostat/Galvanostat (see **Fig. 3.9**).

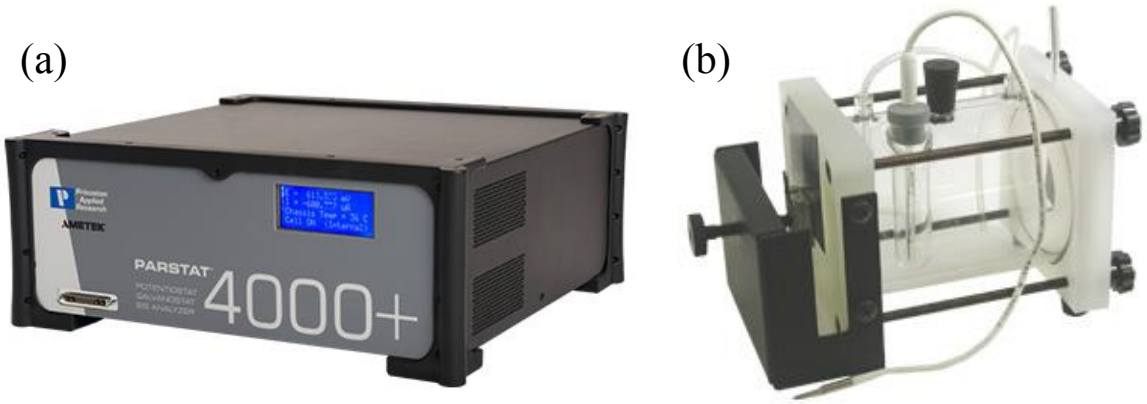

Fig. 3.9 The photograph of the corrosion test setup. (a) Corrosion work station and (b) corrosion test cell.

The electro-potentials were measured against the standard potential of the saturated calomel electrode and standard hydrogen electrode at 0.245 V. The polarization studies were carried out at a scan rate of 1 mVs^{-1} and the impedance (Z) measurements were taken in the frequency range from 0.1 Hz to 60 kHz. The superimposed AC signal amplitude was set to 20 mV with a peak to the peak measuring system. All electrochemical experiments were conducted at least two times for repeatability. After electrochemical studies, the surface morphology of the Cu-Al alloys was investigated using SEM-EDS to understand the corrosion behaviour.

Chapter 4

Effect of Al addition on densification, mechanical, wear and electrical properties of Cu processed via milling condition

4 Chapter 4

The present chapter discusses the morphology and phase analysis of starting powders and milled powders. The densification mechanisms of Cu-Al (milled) alloys processed through hot-pressing technique was discussed. Further, the microstructural studies were performed by the optical microscope and SEM. The phase identification and elemental quantification were carried out by XRD, EPMA and EDS. Later, the mechanical properties such as nanohardness, hardness and compression strength were investigated and the properties were correlated with the densification and microstructure of samples. The abrasive wear test of Cu-Al alloys was conducted against SiC (abrasive) emery paper and the related wear mechanisms were explained. Additionally, few selected tests such as sliding wear and corrosion of high strength (C15Al (ML)) alloys was conducted to assess its potentiality. Finally, the electrical conductivity of the Cu-Al (milled) alloys was measured and is related to Al content or microstructure.

4.1 Microstructure of Cu-Al (milled) powders

As discussed in the previous chapter, the copper powders are spherical shape and the morphology of aluminium powder particles are observed to be semi-spherical and in the elongated form (see **Fig. 3.1a-b**). However, during the ball milling, the elemental Cu powders deformed into flaky shape due to its cold welding (see **Fig. 4.1a**). The mean particle size of Cu-Al powders after 10 h ball milling was estimated based on the SEM images. The particle size of milled Cu reduced from 84.3 to 9.2 µm with the addition of Al (pure copper: 84.3 ± 8 µm, C3Al (ML): 75.1 ± 9 µm, C5Al (ML): 47.4 ± 5 µm, C10Al (ML): 17.6 ± 1 µm and C15Al (ML): 9.2 ± 0.9 µm). The particle-particle cold welding in pure Cu might be leading to the formation of large flakes. Conversely, the flaky size of Cu reduced considerably and hard agglomerates formed with the addition of Al as it can be seen in **Fig. 4.1 (a-d).** With the increasing addition of Al to Cu, the size of agglomerated particles reduced due to continuous fracture and cold welding.

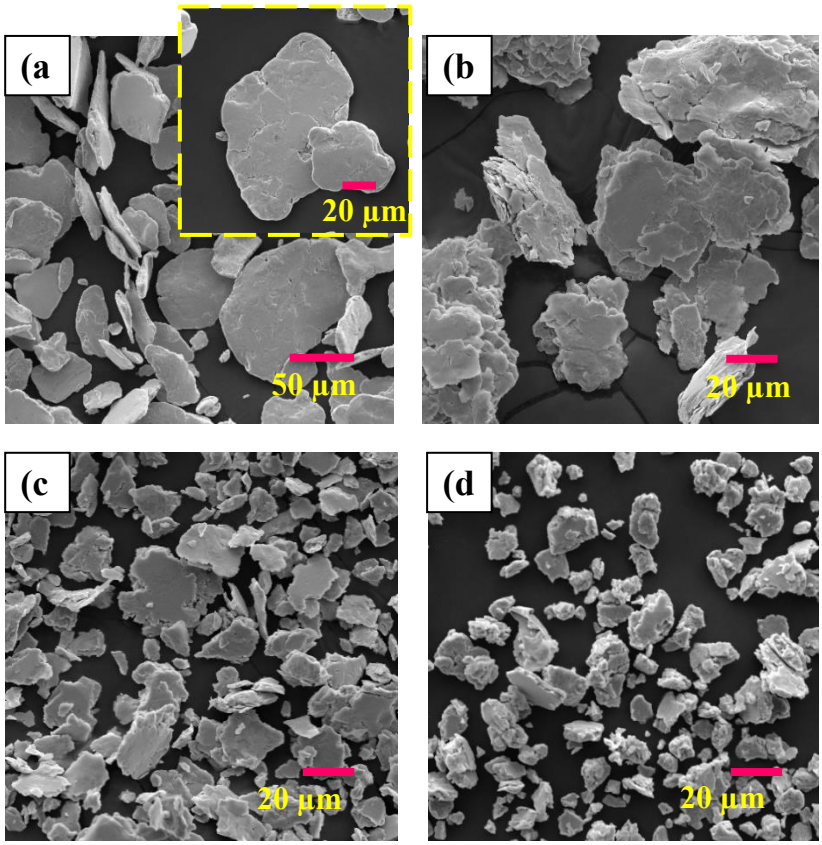

Fig. 4.1 SEM images milled powders after 10 h ball milling at 260 rpm (a) Cu (ML), (b) C5Al (ML), (c) C10Al (ML) and (d) C15Al (ML). The transition of flake-like shape to small aggregates has been seen as Al content increased.

The presence of fine agglomerates in Cu-Al powders indicates relatively easy fragmentation of aggregates than in pure Cu. As the Al content increased, the size of flakes and agglomerates got reduced due to its continuous impact, cold welding, fracture, re-welding and solid solution formation during ball milling**.** The particle welding in Cu-Al powders during milling might be hindered due to the formation of Cu-Al solid solution (see **Fig. 4.2**) and fragmentation of agglomerates.

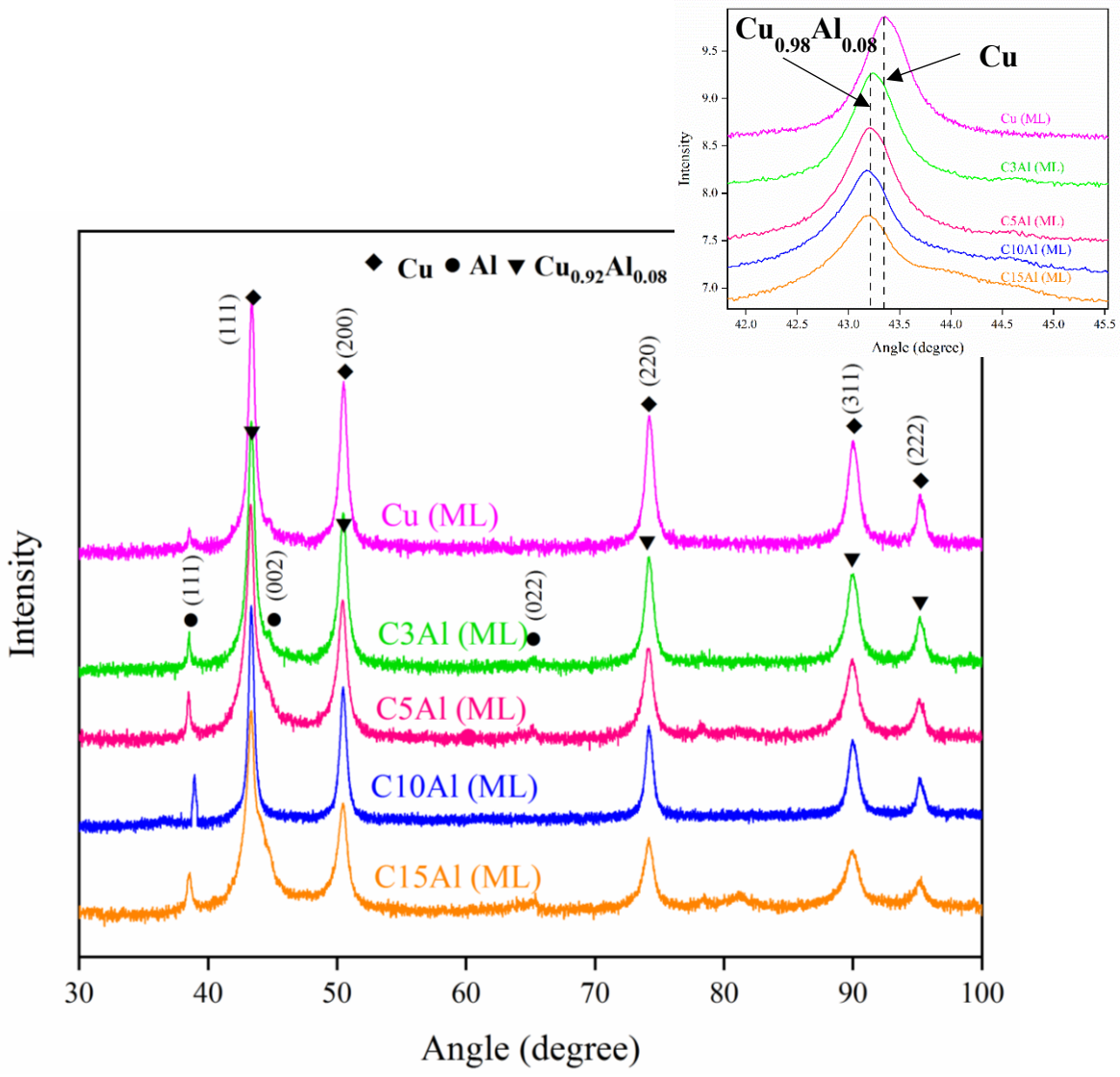

Fig. 4.2 Comparison of X-ray diffraction patterns of Cu-X wt.% Al milled powders (260 rpm, 10 h.). Where the nominal composition (X) of Al alloying element is ranging from 0-15 wt.%. The inset diagram shows a peak shift of Cu with the addition of Al and indicates the solid solution formation.

The corresponding X-ray diffraction patterns of ball-milled Cu-Al powders were presented in **Fig. 4.2**. During the ball milling process, the copper-rich solid solution α-Cu

($Cu_{0.92}Al_{0.08}$) with a small amount of aluminium was noticed in all alloy powders. The peak intensity of Cu for the alloys was observed to decrease as the Al content increased and peak shift (which can be attributed to the formation of the solid solution), internal stress and grain refinement by cold deformation.

4.2 Phase analysis and microstructure of hot-pressed Cu-Al (milled) alloys

The X-ray diffraction patterns of hot-pressed samples are presented in **Fig. 4.3**. The XRD patterns of Cu-X wt.% Al (X = 0, 3, 5, 10 & 15) sintered samples revealed the presence of α-Cu ($Cu_{0.92}Al_{0.08}$), α ($Cu_{0.78}Al_{0.22}$), and γ_2 (Cu_9Al_4) phases.

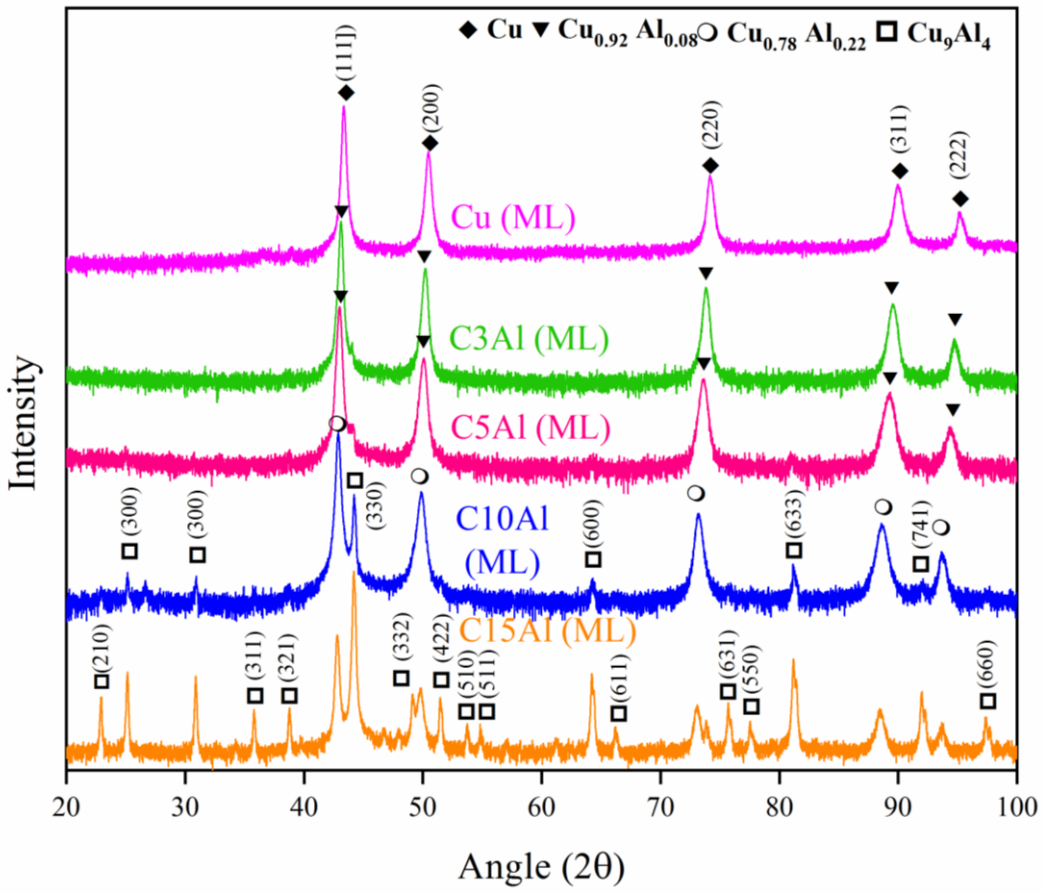

Fig. 4.3 Comparison of X-ray diffraction patterns of hot-pressed Cu-X wt.% Al alloys (hot press conditions: 500 °C, 500 MPa, 30 min.). Where the nominal composition (X) of Al alloying element is ranging from 0-15 wt.%.

According to the Cu-Al equilibrium phase diagram, α-Cu solid solution formation is expected up to 9.4 wt.% Al addition and α solid solution, and γ_2 intermetallic phases (from 9.4

to 15.6 wt.%) with the Al addition to Cu [96,235]. The phases that were formed in the hot-pressed Cu-Al (milled) alloys are similar to the phases of the Cu-Al phase diagram. The quantification of XRD phases was carried out through Rietveld analysis using X'Pert High Score software.

The results obtained from the XRD patterns of hot-pressed are given in **Table 4.1**. In case of C3Al (ML) and C5Al (ML) alloys, the α-Cu solid solution was the only phase identified from the XRD.

Table 4.1 Densification, microstructural phases of hot-pressed Cu-Al (milled) alloys.

Sample reference	**Theoretical density (g/cc)**	**Bulk density (g/cc)**	**Relative density (%)**	**XRD phases**	**Wt.% of phase based on Rietveld analysis of XRD patterns**
Cu (ML)	8.96	8.84	98.66	Cu	100.00
C3Al (ML)	8.38	8.07	96.30	$Cu_{0.92}Al_{0.08}$	100.00
C5Al (ML)	8.38	7.97	95.16	$Cu_{0.92}Al_{0.08}$	100.00
C10Al (ML)	7.37	7.01	95.10	$Cu_{0.78}Al_{0.22}$	86.60
				Cu_9Al_4	13.30
C15Al (ML)	6.98	6.61	94.60	$Cu_{0.78}Al_{0.22}$	24.70
				Cu_9Al_4	75.30

On the other hand, the formation of major α phase (86.6 wt.%) and minor γ_2 phase (13.4 wt.%) for C10Al (ML) and presence of γ_2 major phase (75.3 wt.%) along with α (24.7 wt.%) were identified for C15Al (ML). To further confirm the presence of these phases in the Cu-Al (milled) alloys, Bragg's law was used to estimate the lattice parameter (a) of each phase from the XRD analysis (using **Eq. 4.1-4.2**); which was compared with the standard lattice parameter (JCPDS). Where, wavelength (λ), diffraction angle (2θ), interplanar spacing (d_i) and Miller indices (hkl) were related to Cu-Al alloy diffraction peaks. The lattice parameters measured from the XRD patterns of Cu-Al (milled) alloys and their corresponding JCPDS values were specified in **Table 4.2**.

$$d_i = \frac{n\lambda}{2\sin\theta} \tag{4.1}$$

$$a = \frac{d_i}{\sqrt{\left(h^2 + k^2 + l^2\right)}} \tag{4.2}$$

Table 4.2 Crystallographic information of hot-pressed Cu-Al (milled) alloys obtained from the XRD patterns

Sample reference	XRD phases	Crystal structure	Interplanar space, d (nm)	Miller indices (hkl)	Calculated lattice parameter, a (nm)	Lattice parameter from JCPDS, a (nm)
Cu (ML)	Cu	FCC	0.2097	111	0.3632	0.3616
C3Al (ML)	$Cu_{0.92}Al_{0.08}$	FCC	0.2098	111	0.3632	0.3634
C5Al (ML)	$Cu_{0.92}Al_{0.08}$	FCC	0.2098	111	0.3642	0.3634
C10Al (ML)	$Cu_{0.78}Al_{0.22}$	FCC	0.2119	111	0.3648	0.3670
	Cu_9Al_4	Complex Cubic	0.2051	330	0.8680	0.8702
C15Al (ML)	$Cu_{0.78}Al_{0.22}$	FCC	0.2119	111	0.3605	0.3670
	Cu_9Al_4	Complex Cubic	0.2051	330	0.8685	0.8702

The strong XRD patterns were selected to calculate the lattice parameter (*a*). The lattice parameter of *α-Cu* phase at its major peak was calculated to be 0.3632 – 0.3642 nm, for *α* phase: 0.3605 – 0.3648 nm and γ_2 phase: 0.868 – 0.8715 nm. These lattice parameter values are in good agreement with the JCPDS values and thus matches the presence of *α-Cu*, *α* and γ_2 phases in the hot-pressed Cu-Al (milled) alloys.

Fig. 4.4 shows the SEM images of the hot-pressed Cu-Al (milled) alloys which were analyzed using the electron probe micro-analyzer (EPMA). Fig. 4.4a shows the SEM of Cu (ML) sample and the EPMA of Cu surface indicated presence of 99.9 wt.% Cu (Table 4.3). The EPMA results of Cu-Al (milled) alloys were tabulated in **Table 4.3**. In C3Al (ML) and C5Al (ML) alloys, three distinct phases were identified as Cu, α-Cu and α_2; where a very low amount of Cu and α_2 phases are present in the sample. Similarly, the C10Al (ML) alloy has three distinct phases which were identified as α-Cu, α_2 and γ where a negligible amount of α-Cu phase is present in the sample. In case of C15Al (ML), two distinct phases namely grey phase as α_2 and dark phase as γ were identified. The EPMA results have good agreement with the phases identified by the XRD.

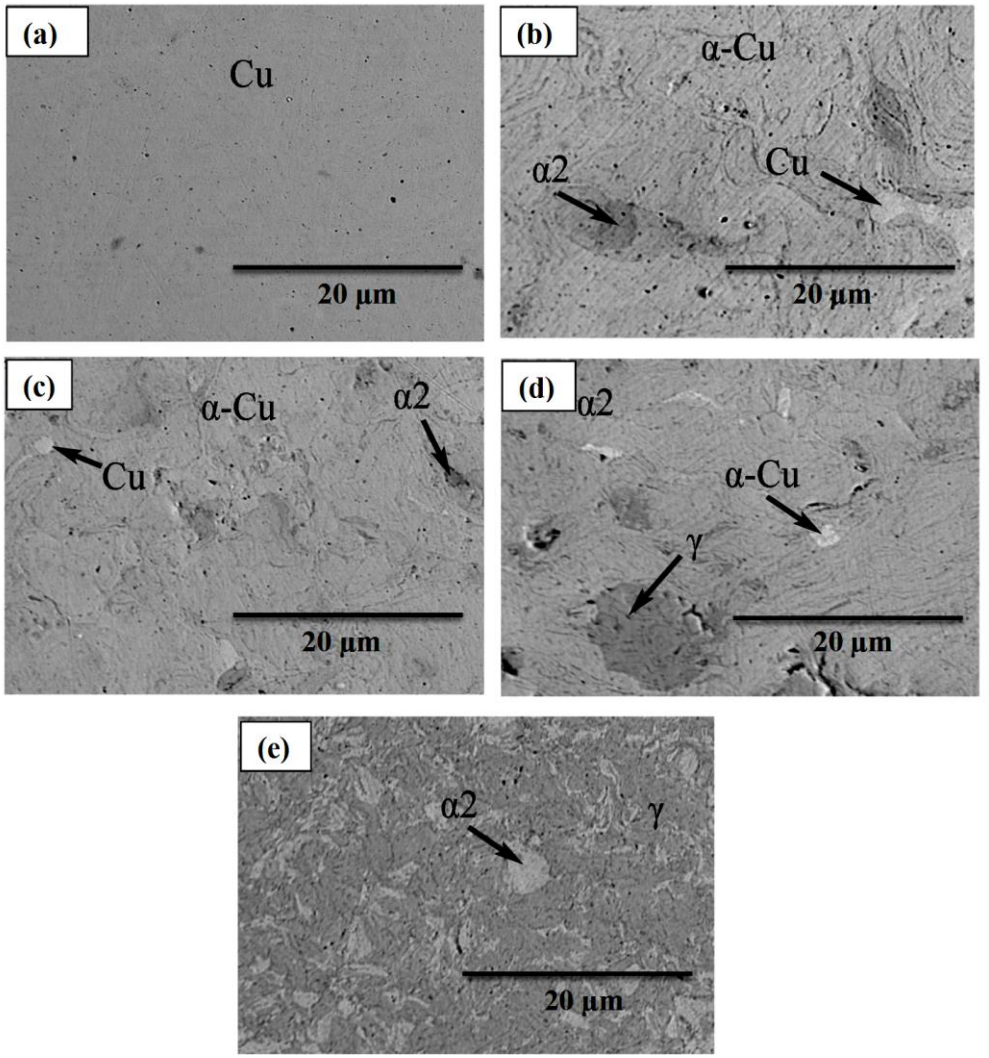

Fig. 4.4 SEM (BSE) images of Cu-Al (milled) alloys. (a) Cu (ML), (b) C3Al (ML) (c) C5Al (ML) (d) C10Al (ML) and (e) C15Al (ML).

Table 4.3 Summary of EPMA result consists of elemental composition of Cu-Al (milled) alloys.

Sample reference	Microstructural Phases	Copper (wt.%)	Aluminium (wt.%)
Cu (ML)	Cu	99.90	--
C3Al (ML)	Cu	99.65	0.35
	α-Cu	96.75	3.25
	α_2	91.41	8.59
C5Al (ML)	Cu	99.64	0.36
	α-Cu	95.15	4.85
	α_2	90.26	9.74
C10Al (ML)	α-Cu	95.71	4.29
	α_2	89.31	10.69

	γ	79.62	20.38
C15Al (ML)	α_2	88.45	11.55
	γ	80.01	19.99

Fig. 4.5 presents the representative microstructure of etched C3Al (ML) and C5Al (ML) alloys. The SE and BSE images of both the alloys reveal the presence of a single constituent phase (α-Cu solid solution) in its microstructure. It can be observed that the grain size of C3Al (ML) is relatively coarser than C5Al (ML). The corresponding SEM-EDS confirms the presence of Cu and Al elements, which validates the presence of α-Cu ($Cu_{0.92}Al_{0.08}$) solid solution phase.

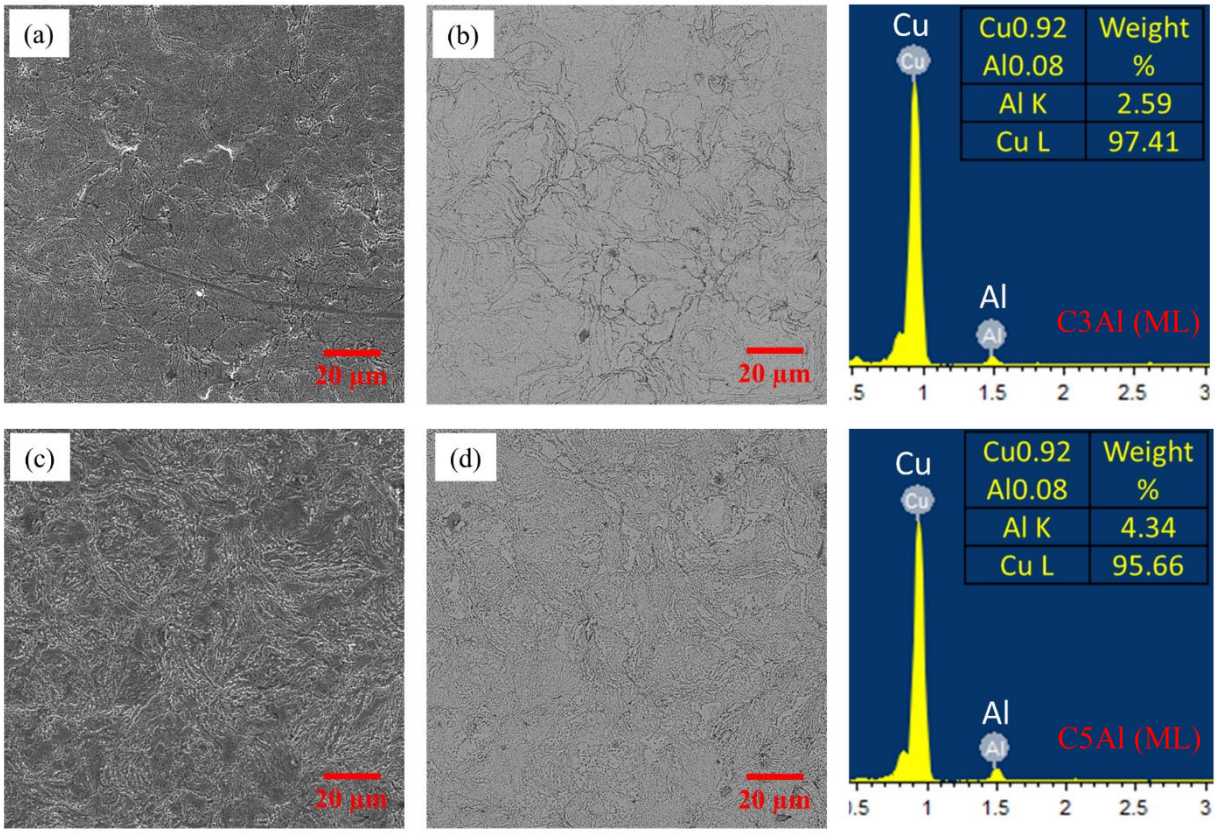

Fig. 4.5 SEM images of Cu-Al (milled) hot-pressed samples (at 500 ºC, 500 MPa, 30 min. under vacuum). (a-b) The microstructure (SE and BSE images) of C3Al (ML) alloy and (c-d) the SE and BSE images of C5Al (ML) alloy. The corresponding EDS of alloys is shown along with elemental compositions.

Fig. 4.6 shows the BSE-SEM images having bright grey (unetched regions: 1) and dark grey contrasting phases (etched regions: 2) in a C15Al (ML) alloy. The EDS compositional analysis of the two contrasting phases reveals that these phases are measured with different amounts of Al content. The quantification of elements from different phases in Cu-Al (milled)

alloys is listed in **Fig. 4.6**. From SEM-EDS results, C15Al (ML) alloy consists of bright and dark grey regions, which are identified as α ($Cu_{0.78}Al_{0.22}$), and γ_2 (Cu_9Al_4) phases, respectively.

From the Cu-Al equilibrium phase diagram, the solid solution α phase completely dissolves up to 9.4 wt.% of Al [236,237]. According to **Eq. 4.3**, the β phase transforms into the α and γ_2 phases at the eutectoid reaction. At a temperature of 500 ºC, a maximum amount of aluminium (up to 15.6%) dissolves in copper and forms γ_2 phase [238]. Therefore, the excess amount of Al leads to formation γ_2 phase in C10Al (ML) and C15Al (ML) alloys.

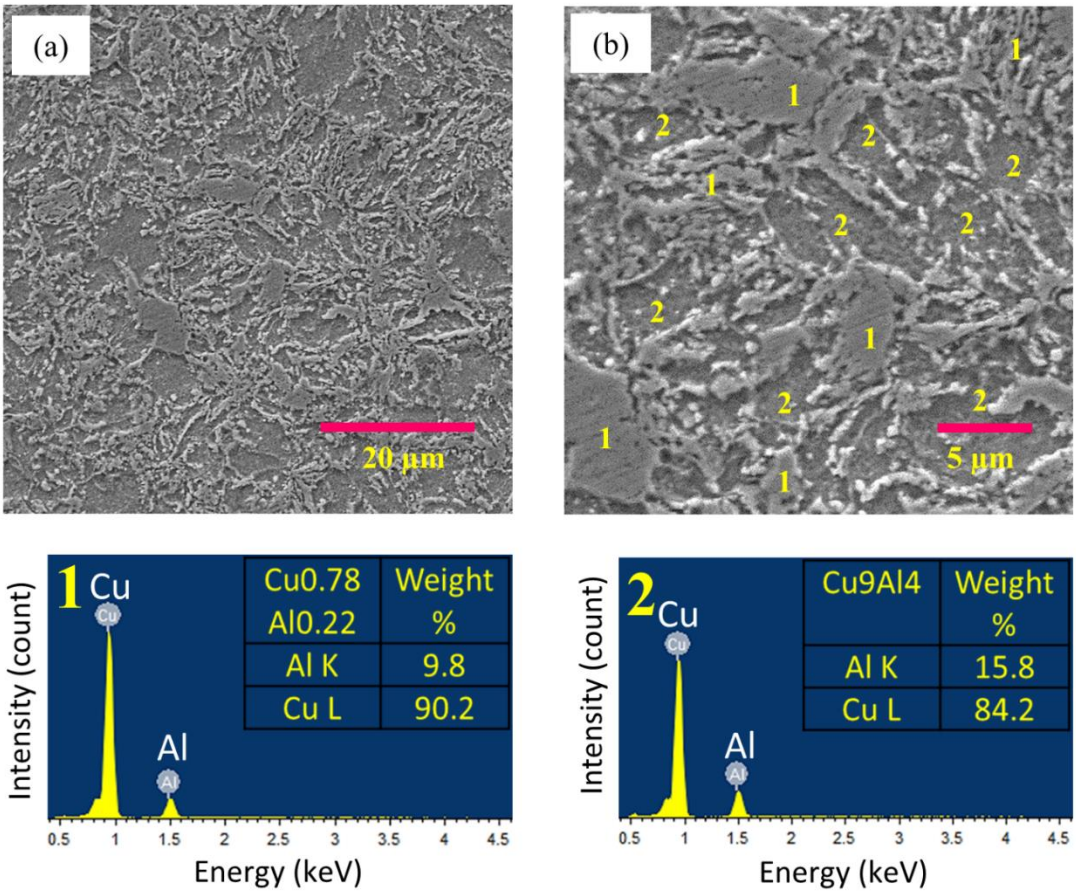

Fig. 4.6 SEM (BSE) images of C15Al (ML) hot-pressed samples (at 500 ºC, 500 MPa, 30 min. under vacuum) having different phases. (a) low magnification and (b) high magnification image. The corresponding EDS analysis of phases is also shown. (1, Unetched regions: $Cu_{0.78}Al_{0.22}$, 2, Etched regions: Cu_9Al_4).

In the present work, γ_2 intermetallic phase formation is evident for both C10Al (ML) and C15Al (ML) alloys. Similar observations were reported for die-casted Cu-11.8 wt.% Al alloy, that forms the γ_2 phase by eutectoid decomposition of β phase at a temperature of 565 ºC [84].

$$\underset{\text{Al Wt.\%}}{\alpha\ (9.4\ \%)} + \underset{}{\gamma_2\ (15.6\ \%)} \underset{\text{Cooling}}{\overset{\text{Heating}}{\rightleftharpoons}} \underset{}{\beta\ (11.8\ \%)} \qquad (4.3)$$

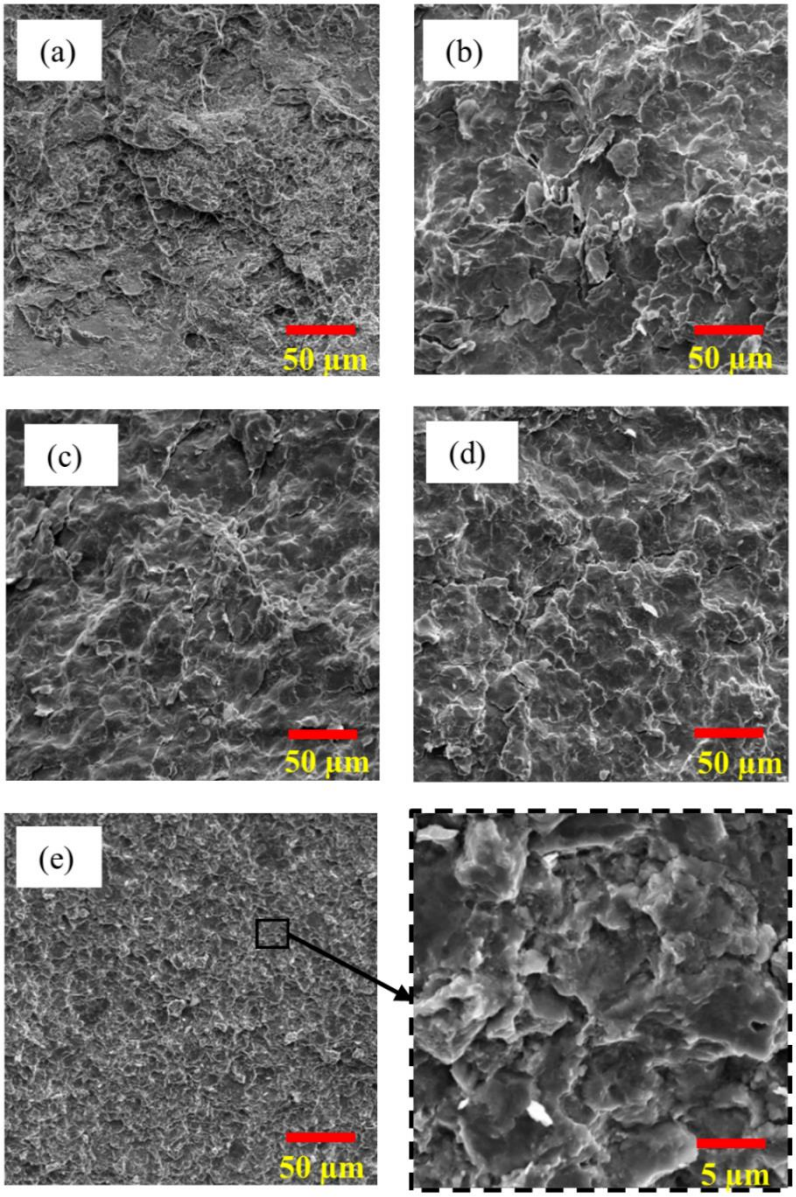

Fig. 4.7 Fracture surfaces of Cu-Al (milled) hot pressed (at 500 ºC, 500 MPa, 30 min. under vacuum) samples. (a) Cu (ML), (b) C3Al (ML), (c) C5Al (ML), (d) C10Al (ML), (e) C15Al (ML) and the magnified image of C15Al (ML) is shown for acumen. All the samples are characterized by the mixed (intergranular and transgranular) mode of fracture.

Fig. 4.7 shows the SEM images of fracture surfaces of hot-pressed Cu-Al (milled) samples. Both pure copper and alloys consist of the mixed mode of fracture (the samples were fractured manually with a hammer to observe the microstructure). A careful look at **Fig. 4.7** indicates

that the % of intergranular fracture increased with the addition of Al to Cu. It also should be clear that the fineness of grains increased with the addition of Al to Cu.

4.3 Densification of Cu-Al (milled) alloys

Since aluminium is a light metal with considerably low density (2.73 g/cc) when compared to copper (8.96 g/cc), it is expected that the addition of aluminium significantly lowers the density of Cu. The density and corresponding hardness of the hot-pressed Cu-Al (milled) alloys as a function of Al content is shown in **Fig. 4.8**.

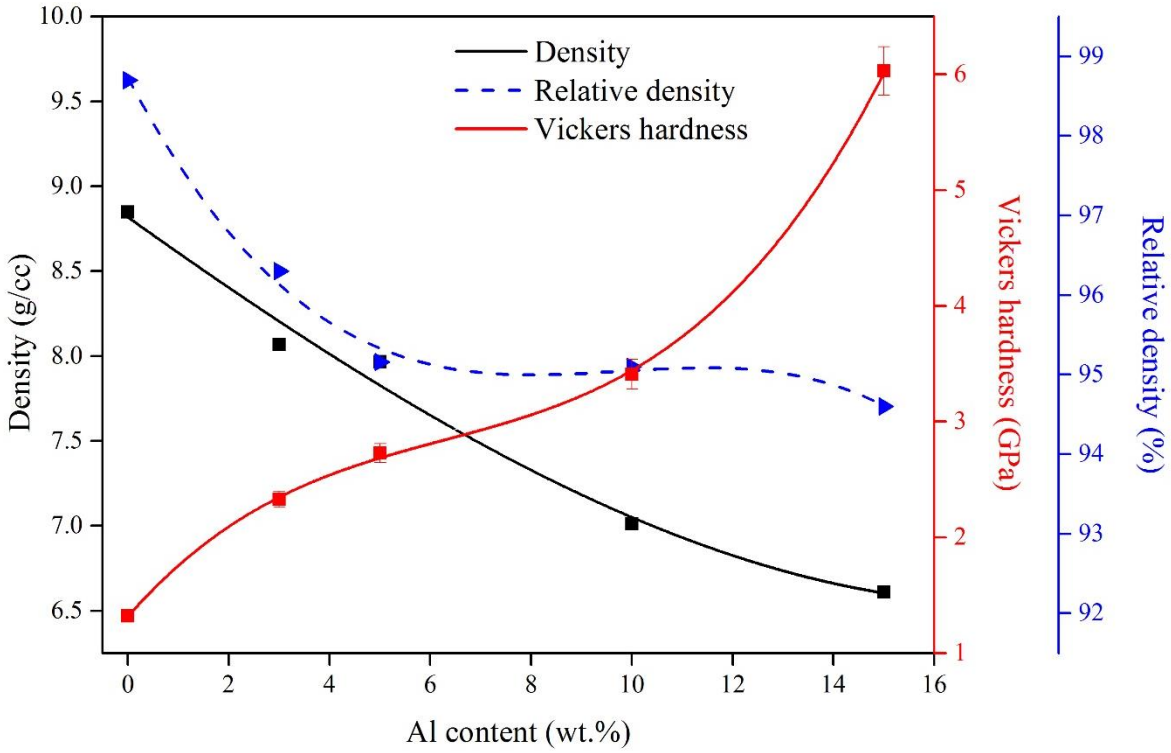

Fig. 4.8 Effect of Al content on the density and hardness of Cu-Al (milled) alloys after hot pressing at 500 ^{o}C, 500 MPa pressure for 30 minutes under vacuum.

To calculate theoretical densities of Cu-Al (milled) alloys, the densities of $Cu_{0.92}Al_{0.08}$ [239], $Cu_{0.78}Al_{0.22}$ [240] and Cu_9Al_4 [32] phases were taken as 8.39 g/cc, 7.46 g/cc and 6.84 g/cc, respectively. The theoretical density was calculated using the rule of the mixtures and the relative amount of phases in the alloy (that were estimated by the Rietveld analysis of XRD patterns) (**Table 4.1)**. The theoretical density (ρ_{th}) of Cu-Al (milled) alloys was observed to decrease from 8.96 to 6.98 g/cc with the addition of Al (up to 15 wt.%) and the measured experimental/bulk density of samples varied between 8.84 to 6.61 g/cc. From **Table 4.1**, it is

evident that pure Cu could be densified to 98.66% ρ_{th} and the relative density of Cu-Al (milled) alloys observed to vary between ~ 95 to 96% ρ_{th} depending on the Al content. The decrease in density of Cu with Al addition can be attributed to hard agglomerates (ball-milled powders) and intermetallic phase formation during sintering, which might have hindered the densification. Among all Cu alloys, C15Al (ML) composed of finer grain structure with a relatively low density of 94.6% ρ_{th}. The densification of Cu (ML) samples can be attributed to mechanical milling, solid-state sintering and large plastic deformations due to the milling and application of high pressure during hot pressing.

It has to be noted here that Rajkovic et al. [39] could achieve a maximum density of 85.1% ρ_{th} for hot-pressed Cu-3.5Al even after using high sintering temperature of 800 ^{o}C, the pressure of 35 MPa for 1 h. He et al. [241] reported almost full density (99% ρ_{th}) for mechanically alloyed Cu-5Cr after using a combination of hot pressing (900 ^{o}C, 1 h) and extrusion process (600 ^{o}C). In another work, Sharma et al. [57] processed Cu-10Pb via spark plasma sintering technique at 350 ^{o}C under 100 MPa pressure for 5 min. They could achieve a maximum relative density of ~90% ρ_{th}. Nassef et al. [58] studied the use of Pb, C in densifying Cu-Sn alloys, which were hot-pressed at 550 ^{o}C, 314 MPa for 30 min. A very low density of 78%, 74% and 72% ρ_{th} were reported for Cu-50Ni, Cu-50Zr and Cu-10Ni-40Zr alloys, respectively which were processed considerably at a low hot press temperature of 300 ^{o}C and high pressure of 900 MPa. [65] From the above discussion, it can be understood that higher densification of Cu based alloys is possible by careful selection of sintering conditions. The present work indicates the advantage of using the high hot press pressure to achieve higher densities (~ 95 to 96% ρ_{th}) of Cu-Al (milled) alloys at a relatively low sintering temperature of 500 ^{o}C and application of high pressure of 500 MPa for 30 min. It is a promising result as the overall processing costs in developing Cu based materials can be reduced. In most commonly used conventional processes, use of high temperature and low-pressure sintering conditions result in coarser grain structure and poor mechanical properties. Hence additional heat treatment processes or mechanical working methods need to be adopted to improve materials properties of Cu further. High-temperature processes or additional processing steps add up the cost as well.

To understand the effect of milling and hot press on densification of Cu-Al (milled) alloys, the dislocation density is evaluated from the Williamson-Hall (W-H) model [242] that is based on the crystallite size (*d*) determination. The W-H model plots obtained from the X-

ray diffraction patterns of milled powders as well as sintered compacts are presented in **Fig. 4.9** to estimate the dislocation density and lattice strains.

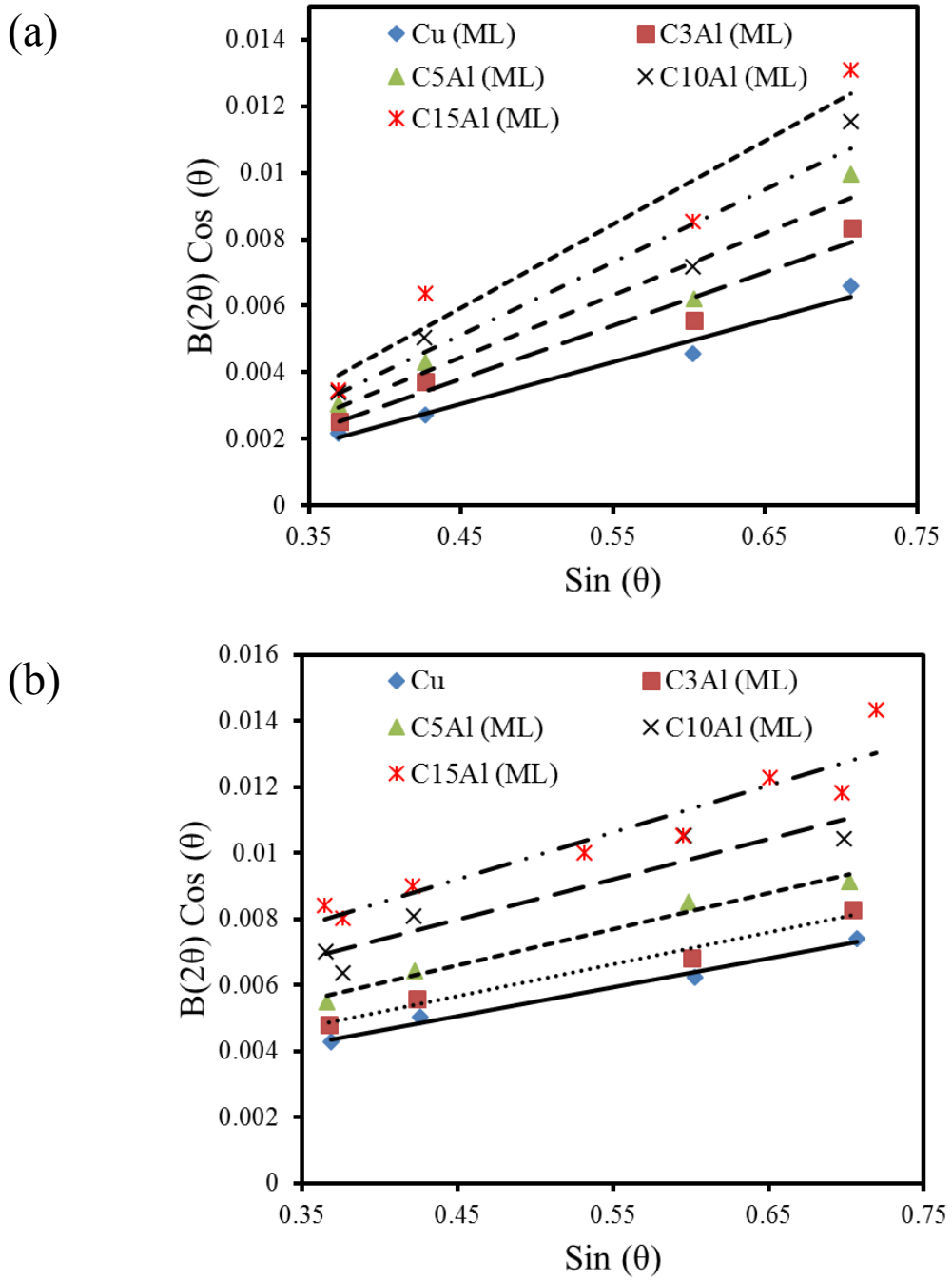

Fig. 4.9 Williamson–Hall plot obtained from the X-ray diffraction patterns of (a) planetary ball milled powders, (b) hot pressed Cu-Al (milled) alloys. (Hot pressing conditions: Temperature: 500 ^{o}C, Pressure: 500 MPa, Time: 30 min under vacuum environment).

According to Williamson-Hall model, the lattice strain of Cu-Al (milled) powders after planetary ball milling process was calculated to be in the range between 0.31×10^{-2} - 0.62×10^{-2}, whereas, the lattice strain for hot-pressed samples estimated in the range of $0.22\text{x}10^{-2}$ -

$0.36x10^{-2}$. It was observed that the lattice strain of milled powders and the hot-pressed Cu samples increased with the addition of Al content and is mainly due to mechanical alloying, formation of solid solutions (*α-Cu)* and γ_2 intermetallic compound. According to **Eq. (4.4-4.5)** [243], (Where, Bragg angle (θ), radiation wavelength (λ = 1.54056 Å for Cu-Kα radiation), geometric constant (κ = 0.94) [242] and full-width at half maximum (B(2θ)) are related to dislocation density (δ) and crystallite size (L)). the dislocation density(δ) of milled powders were calculated using the Williamson-Hall model and it varied from 3.52×10^{14} m^{-2} to 14.61×10^{14} m^{-2}. Also, the dislocation density of hot-pressed compacts was calculated to be in the range of 0.63×10^{14} m^{-2} - 4.08×10^{14} m^{-2}. The lattice strain and dislocation density of milled powders are significantly higher than the hot-pressed samples.

$$\delta = \frac{1}{L^2} \tag{4.4}$$

$$B(2\theta)\cos\theta = \frac{0.9\lambda}{L} + 2^2 e \sin\theta \tag{4.5}$$

The intercept and slope data of milled powders and hot-pressed Cu-Al (milled) samples which were obtained from W-H methodology are provided in **Table 4.4**. The slope of the curves has an inverse relation with the crystallite size of milled powders and hot-pressed samples. The crystallite size for Cu decreased for both the milled powders (from 53.33 to 26.16 nm) and hot-pressed materials (from 126.04 to 49.52 nm) with the addition of Al.

Table 4.4 W-H plot linear fit results of Cu-Al (milled) milled powders and hot-pressed compacts.

Sample reference	**Milled powders**		**Hot-pressed compacts**	
	Slope ($x10^{-2}$)	Intercept ($x10^{-3}$)	Slope ($x10^{-2}$)	Intercept ($x10^{-3}$)
Cu (ML)	1.26	2.60	0.88	1.10
C3Al (ML)	1.59	3.40	0.97	1.30
C5Al (ML)	1.87	4.00	1.09	1.70
C10Al (ML)	2.19	4.70	1.23	2.40
C15Al (ML)	2.51	5.30	1.42	2.80

The crystallite size of both milled powders and hot-pressed compacts decreased with the Al content due to the formation of solid solution phases. It lowers the ductility in powder

particles during the milling process, where the particles get fractured and re-welded with hard agglomerates formation. During hot pressing at 500 ^{o}C, the samples exposed to high activation energy which increases the crystallite size of Cu. Thus, the crystallite size of hot-pressed samples is high when compared to milled powders. It was observed that the micro-strain of Cu-Al (milled) powders and hot-pressed compacts directly relates to the dislocation density. With the addition of 15 wt.% Al to Cu, a maximum micro-strain of 0.63% was calculated for milled powders, whereas the hot-pressed samples were having the maximum strain of 0.36%.

Table 4.5 Calculated dislocation density using Williamsons-Hall model in milled Cu-Al powders (after planetary ball milling at 260 rpm for 10 h) and hot-pressed Cu-Al (milled) alloys (after hot pressing at 500 ^{o}C, 500 MPa for 30 min).

Sample reference	**Milled powders**			**Hot-pressed compacts**		
	Crystallite size, L (nm)	Micro-strain, e (%)	Dislocation density (x10^{14} m^{-2})	Crystallite size, L (nm)	Micro-strain, e (%)	Dislocation density (×10^{14} m^{-2})
Cu (ML)	53.33	0.32	3.52	126.04	0.22	0.63
C3Al (ML)	40.78	0.40	6.01	106.65	0.24	0.88
C5Al (ML)	34.66	0.47	8.32	81.56	0.27	1.50
C10Al (ML)	29.50	0.55	11.49	57.77	0.31	3.00
C15Al (ML)	26.16	0.63	14.61	49.52	0.36	4.08

The dislocation density of Cu-Al (milled) samples after hot pressing decreased when compared to milled powders. The dislocation density might have decreased due to recovery and recrystallization processes of Cu at the hot press temperature. Since very high hot press pressure was used, that is why probably the decrease in dislocation density is slightly low after hot press than the milled samples. In case of Cu-Al (milled) alloys, the alloying element affects the dislocation density by forming the solid solution phases (α-Cu) and intermetallic compounds (γ_2); as the amount of Al content increased up to 15 wt.%, the dislocation density increased by 6.47 times. The calculated dislocation density using the Williamson-Hall model in milled Cu-Al powders and hot-pressed Cu-Al (milled) compacts is listed in **Table 4.5.**

Rohatgi et al. [155] studied the behaviour of cold working on Cu-Al alloys by varying the pressure. They estimated the dislocation density of Cu-Al alloys from the differential scanning calorimetry (DSC) curve *i.e.,* by calculating the energy released during recrystallization. It was reported that the dislocation density of Cu-4Al increased from

$1.22x10^{14}$ m^{-2} to 17.64 $x10^{14}$ m^{-2} by increasing pressure from 10 to 35 GPa. Zhao et al. [156] reported the dislocation density of $2.3x10^{14}$ m^{-2} for ultra-fine copper and $5.9x10^{14}$ m^{-2} for ultra-fine bronze that was processed by high-pressure torsion (HPT) at 6 GPa pressure and cold rolling. In another study, the dislocation density of $4.3x10^{14}$ m^{-2} was reported for Equal Channel Angular Pressing (ECAP) processed copper [157]. From these studies, it can be observed that the dislocation density of Cu based alloys is varying with the function of temperature and pressure *i.e.,* the dislocation density of Cu alloys was observed to be low at the higher processing temperature and lower pressures. Also, the calculated dislocation density values of Cu-Al (milled) alloys in the present study are comparable with the reported Cu alloys.

As far as the densification of Cu-Al (milled) samples is concerned, both ball milling and hot pressing and Al alloying element content resulted in a significant increment in the lattice strain and dislocation density of Cu (Table 4.5). It is well known that the lattice strain and dislocations present in the powders (due to ball milling/pressure-assisted sintering processes) activate the diffusion of atoms/material transport during sintering and enhances sinterability or densification [244, 245]. For example, the ball milling resulted in increasing of the internal energy of tungsten powders [244]. It was attributed to the significant strain of the powder particles because of high impact forces (during ball milling) that serve as a driving force for sintering [244]. Keiback and Hermel [245] reported that a minimum dislocation density of 10^{11} m^{-2} or higher is required for the noticeable effect of material transport for improving sinter density. In the present work, the dislocation density of Cu-Al (milled) alloys was observed to be in the range between 0.63×10^{14} m^{-2} to 4.08×10^{14} m^{-2} and is much higher than the required dislocation density of 10^{11} m^{-2}. Hence, it is obvious that lattice strains and dislocations in the material aid in the densification.

In summary, the dislocation density and lattice strain enhances the densification and densification rate of Cu-Al (milled) samples. For example, as it was reported, Rajkovic et al. [39] could only achieve a maximum density of 85.1% ρ_{th} for hot-pressed Cu-3.5Al even after using high sintering temperature of 800 ^{o}C, the pressure of 35 MPa for 1 h. Whereas in the present work, it was observed a maximum density of 96.3% ρ_{th} for C3Al (ML) after hot press at a low temperature of 500 ^{o}C, the pressure of 500 MPa for 30 min. In case of pure Cu (ML), a very high density of 98.66% ρ_{th} could be achieved under similar processing conditions.

4.4 Mechanical properties of Cu-Al (milled) alloys

4.4.1 Hardness

The hardness of Cu increased with the amount of Al, in particular, C15Al (ML) alloy exhibited a significantly high hardness of 6.16 GPa when compared to pure Cu (1.32 GPa) (see **Fig. 4.8**). It is also to be noted here that the hardness measured for pure copper in the current study is relatively high than reported values of Cu (in the literature) and it can be attributed to its high density and fine structure. The Cu-Al (milled) alloys with low Al content (preferably C3Al (ML) and C5Al (ML)) that consist of *α-Cu* solid solution phase exhibited high hardness in the range of 2.33 GPa to 2.73 GPa (almost two times of Cu). Such high hardness of these alloys is due to solid solution strengthening. Whereas the presence of γ_2 intermetallic phase along with α solid solution in C10Al (ML) and C15Al (ML), the hardness of these alloys measured to be much high and varied between 3.41 GPa to 6.03 GPa. This improvement in hardness of Cu-Al (milled) alloys can be attributed to the reduction of grain size, solid solution strengthening and intermetallic phase formation. Liu et al. [167] reported low Vickers hardness (2.00-2.75 GPa) for Cu-xAl (x:1, 2, 4 and 6) alloys which were processed by arc melting technique (at a temperature range between 710-800 ^{o}C). In another work, Glas [168] reported hardness of 2.95 to 3.7 GPa for Cu-Al alloys processed by casting technique (at 1150 ^{o}C). Also, Nassef et al. [58] produced the Cu-Sn and Cu-Pb alloys through hot pressing route; depending on the composition, the hardness of Cu-10Pb alloys varied between 1.01 to 2.10 GPa. In case of Cu-10Sn-10Pb, it varied between 1.08 to 2.22 GPa. So far in the literature, for Cu based materials a maximum hardness of 4.1 GPa was reported [5,58,104,169]; however, in the present work, very high hardness of 6.16 GPa was achieved for hot-pressed Cu-Al (milled) alloys.

4.4.2 Nano-indentation behaviour

The nanohardness and elastic modulus of hot-pressed Cu-Al (milled) alloys were determined from the loading and unloading curves using the method proposed by Oliver–Pharr [246,247].

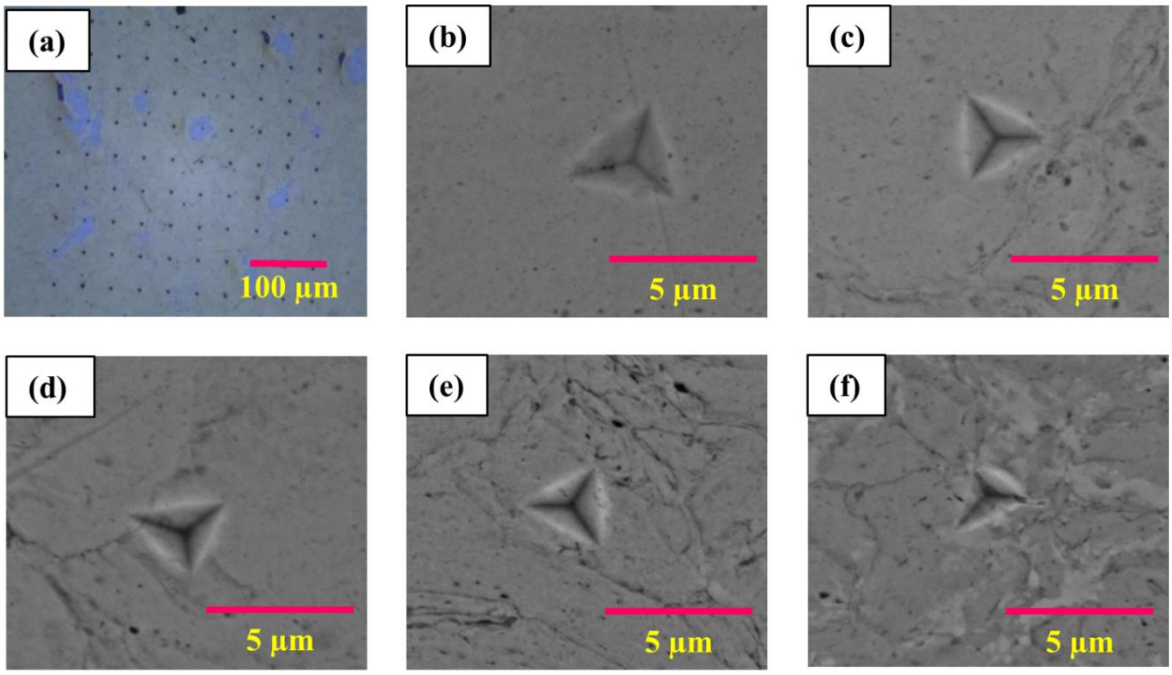

Fig. 4.10 SEM image showing typical nano-indents obtained on hot-pressed Cu-Al (milled) alloys. (a) Optical microscopic image C10Al (ML) alloy having the array of 100 indentations and corresponding indents of (b) Cu (ML), (c) C3Al (ML), (d) C5Al (ML), (e) C10Al (ML) and (f) C15Al (ML).

Fig. 4.10a shows an optical microscopic representative image of nano-indentations taken on the C15Al (ML) alloy with an array of 10 × 10 sizes with 40 µm indent spacing. From **Fig. 4.10 (b-f)**, the indentation size of the pure copper sample was measured to be 3.75 ± 0.1 µm; the indentation size of Cu was reduced to 1.98 ± 0.08 µm as the Al content added up to 15 wt.%. The schematic of the typical load-displacement curve of nanoindentation for viscoelastic-plastic materials is shown in **Fig. 4.11a.** Where h_{max} represents the maximum displacement of indenter at peak load, h_f is the depth of residual impression after unloading, h_c is the contact depth under the indenter. The elastic modulus (E_s) of hot-pressed samples was calculated using the **Eq. (4.6)**; where, the reduced modulus (E_r) obtained directly from the nanoindentation system and the poisons ratio (υ) of the Cu-Al alloys, which was taken to be 0.3, indentor elastic modulus (E_i) ~ 1141 GPa and it's poisons ratio (υ) ~ 0.07 [248].

$$\frac{1}{E_r} = \frac{\left(1-\upsilon_s^2\right)}{E_s} + \frac{\left(1-\upsilon_i^2\right)}{E_i} \qquad (4.6)$$

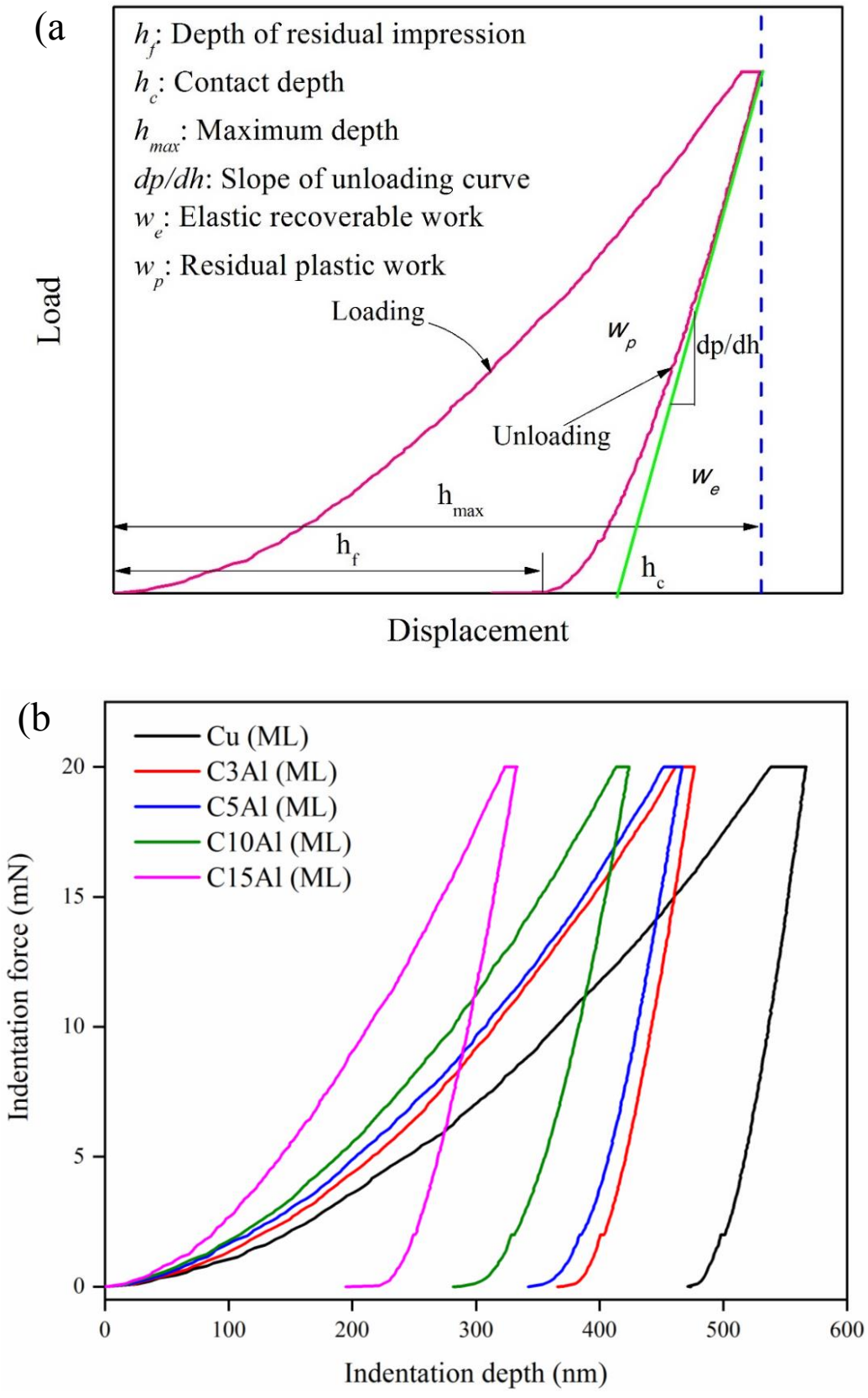

Fig. 4.11 (a) Schematic of typical load (P) - displacement (h) curve of nanoindentation for viscoelastic-plastic materials, (b) indentation load Vs. penetration depth curves of Cu-Al (milled) alloys at an indent peak load of 20 mN (loading and unloading rate: 2.0 mN/s).

The loading-unloading curves of hot-pressed Cu samples obtained at a constant peak load of 20 mN and the loading-unloading rate of 2 mN/s are presented in **Fig. 4.11b**. It is clear from the loading-unloading curves that the Al content has a significant effect on the indentation behaviour of hot-pressed Cu-Al (milled) samples. The presence of plateau, which indicates the creep of Cu-Al (milled) alloys as can be seen in **Fig. 4.11b**. It was evident that the length of the plateau is small for C10Al (ML) and C15Al (ML) when compared to other Cu materials. In particular, pure Cu (ML) witnessed with the maximum plateau. It indicates that the creep deformation of C10Al (ML) and C15Al (ML) alloys is considerably low than the other alloys. The indentation depth decreased with the increase of Al in Cu-Al (milled) alloys. The indentation depth of the pure copper was measured as ~576 nm, whereas for the C15Al (ML) it reduced to ~324 nm. The average nano-indentation hardness (*H*) of Cu-Al (milled) alloys increased considerably from 2.38 ± 0.18 GPa to 7.88 ± 0.98 GPa.

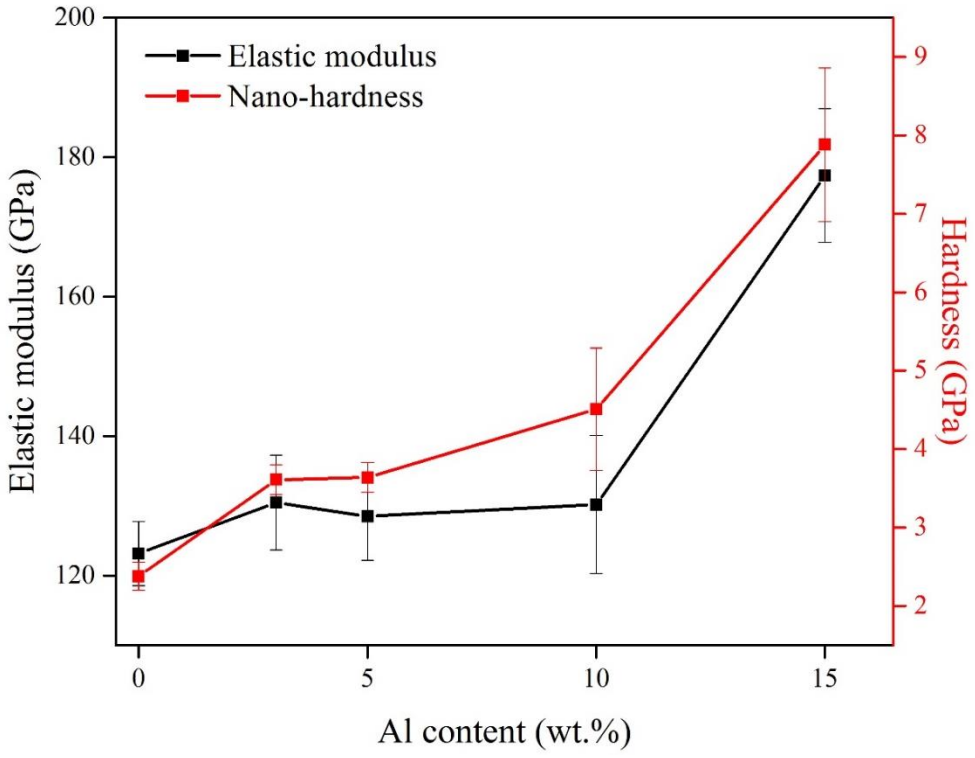

Fig. 4.12 The effect of Al content on elastic modulus and hardness of Cu-Al (milled) alloys measured from the P-h plots of nanoindentation.

The nanohardness represents materials resistance to deformation. The improved nanohardness of Cu-Al (milled) alloys reflects the deformation resistance of these alloys with Al content. From the unloading portion of the load-depth curves, the elastic modulus (*E*) of hot-pressed samples were calculated and found to be increased from and 123.18 ± 4.6 GPa to 177.35 ± 9.6 GPa (see **Fig. 4.12**). The mechanical properties of Cu-Al (milled) alloys evaluated from

the nanoindentation test are listed in **Table 4.6.** In the literature, it was reported that the ratio of hardness (H) to elastic modulus (E) has a relation with wear resistance [98]. Higher the H/E ratio higher will be the wear resistance. As it is shown in **Table 4.6**, the H/E ratio of Cu increased with Al and the H/E ratio increased from 0.019 for pure Cu to 0.044 for C15Al (ML).

Table 4.6 Mechanical properties of Cu-Al (milled) alloys based on the nano-indentation test.

Sample Reference	**Hardness (*H*) (GPa)**	**Reduced Modulus (E_r) (GPa)**	**Elastic Modulus (*E*) (GPa)**	**H/E**	**Maximum displacement (h_{max}) (nm)**
Cu (ML)	2.38 ± 0.2	121.07 ± 4.0	123.18 ± 4.6	0.019	565 ± 5.28
C3Al (ML)	3.61 ± 0.2	127.44 ± 3.6	130.47 ± 6.3	0.027	476 ± 7.12
C5Al (ML)	3.64 ± 0.2	125.72 ± 3.4	128.49 ± 6.3	0.028	465 ± 5.42
C10Al (ML)	4.51 ± 0.8	129.19 ± 7.5	135.18 ± 9.9	0.033	423 ± 6.35
C15Al (ML)	7.88 ± 0.9	166.58 ± 6.2	177.35 ± 9.6	0.044	324 ± 5.68

Based on the literature, the mechanical properties of various Cu alloys obtained by the nanoindentation test are summarized in **Table 4.7.** Most of the nano-indentation studies were made for Cu alloy coatings. The nanohardness of Cu alloys reportedly varied between 3.38 to 6.50 GPa and the elastic modulus varied from 100 to 170 GPa [85,98,249–254].

Table 4.7 Nanoindentation properties of various Cu-based alloys reported in the literature.

Alloy	**Manufacturing process**	**Nano indentation test conditions**	**Hardness (*H*) (GPa)**	**Elastic Modulus (*E*) (GPa)**	**Maximum displacement (h_{max}) (nm)**	**Ref.**
Cu-22Al	As casting	*I*:Berkovich, *l*: 1 mN *v*: 100 μNs^{-1}	3.52	112.27	102.56	[98]
Cu-11.76Al	As casting + annealed at 500 ^oC, 15 min.	*I*:Berkovich, *l*: 10 nN *v*: 100 μNs^{-1}	3.38	111.87	105.65	[249]
Cu-11.76Al	Cryogenic treated at -196 ^oC, 30 min.	*I*:Berkovich, *l*: 10 nN *v*: 100 μNs^{-1}	3.67	115.35	94.62	[249]
Cu-Al*	Hot pressing, 350-650 ^oC, 10 min.	*I*:Berkovich, *d*: 150 nm	6.06	--	--	[85]
Cu-11Ni-1P	Annealed at 500 ^oC, 2h	*I*:Berkovich, *d*: 1000 nm	3.63	--	1010.00	[251]

Cu-11Ni-1P	Electrodeposition	*I*:Berkovich, *d*: 1000 nm	5.22	--	1025.00	[251]
Cu-Sn*	Solid state aging + annealing at 200 ^{o}C, 341h	*I*:Berkovich, *l*: 0.7 – 9.5 mN *v*: 1 mNs^{-1}	6.58	128.00	98.00	[252]
Cu-6.5 at.% Ti	Magnetron sputtering deposition	*I*:Berkovich, *l*: 2.6 mN *v*: 0.01 nNs^{-1}	~4.97	--	130.00	[253]
Cu-8 at.% Mo	Magnetron sputtering deposition	*I*:Berkovich, *l*: 2.6 mN *v*: 0.01 nNs^{-1}	~5.00	--	155.00	[253]
Cu-30Ag	Thermal deposition	*I*:Berkovich, *d*: 80 nm	4.00	100-170	~800.00	[254]
Cu-11.2Al-6.9Fe	Plasma transferred arc welding deposition	*I*:Berkovich, *d*: 500 nm	4.95	121.00	500.00	[250]

* Diffusion bonding, *I:* Type of Indenter, *l*: Load, *v*: loading/unloading speed, *d*: Depth

The plastic deformation and its behaviour of hot-pressed samples under nano-indentation can be understood by using the plasticity index (ψ) parameter [255,256]. From the load vs. indenter penetration depth curves, recovered elastic work (*We*) and residual plastic work (*Wp)* can be measured by integrating the area under unloading curve and the area between loading-unloading curves, respectively [257]. The plasticity index of the hot-pressed samples can be calculated by using the **Eq. (4.7).** The elastic recoverable work, residual plastic work and plasticity index of hot-pressed samples calculated from the load-displacement curves are given in **Table 4.8**.

$$\psi = \frac{W_p}{W_t} \tag{4.7}$$

Table 4.8 Elastic recoverable work, residual plastic work and plasticity index of Cu-Al (milled) alloys.

Sample reference	**Elastic recoverable work (W_e) ($\times 10^{-6}$ J)**	**Residual plastic work (W_p) ($\times 10^{-6}$ J)**	**Plasticity index (ψ)**
Cu (ML)	0.66	3.79	0.85
C3Al (ML)	0.75	2.83	0.79
C5Al (ML)	0.81	2.75	0.77
C10Al (ML)	0.91	2.28	0.71

C15Al (ML)	0.85	1.73	0.66

The plasticity index of the Cu-Al (milled) alloys found to be reduced as the Al content increases; for the pure copper, it was estimated to be 0.85, whereas for C15Al (ML) alloy ~0.66. The reduction in plasticity index of the C15Al (ML) alloy is 22.5% when compared to pure copper. This is indicating that the Cu-Al (milled) alloys still retains a significant amount of plasticity under indentation conditions. The distribution of hardness of Cu-Al (milled) alloys is presented in **Fig. 4.13.**

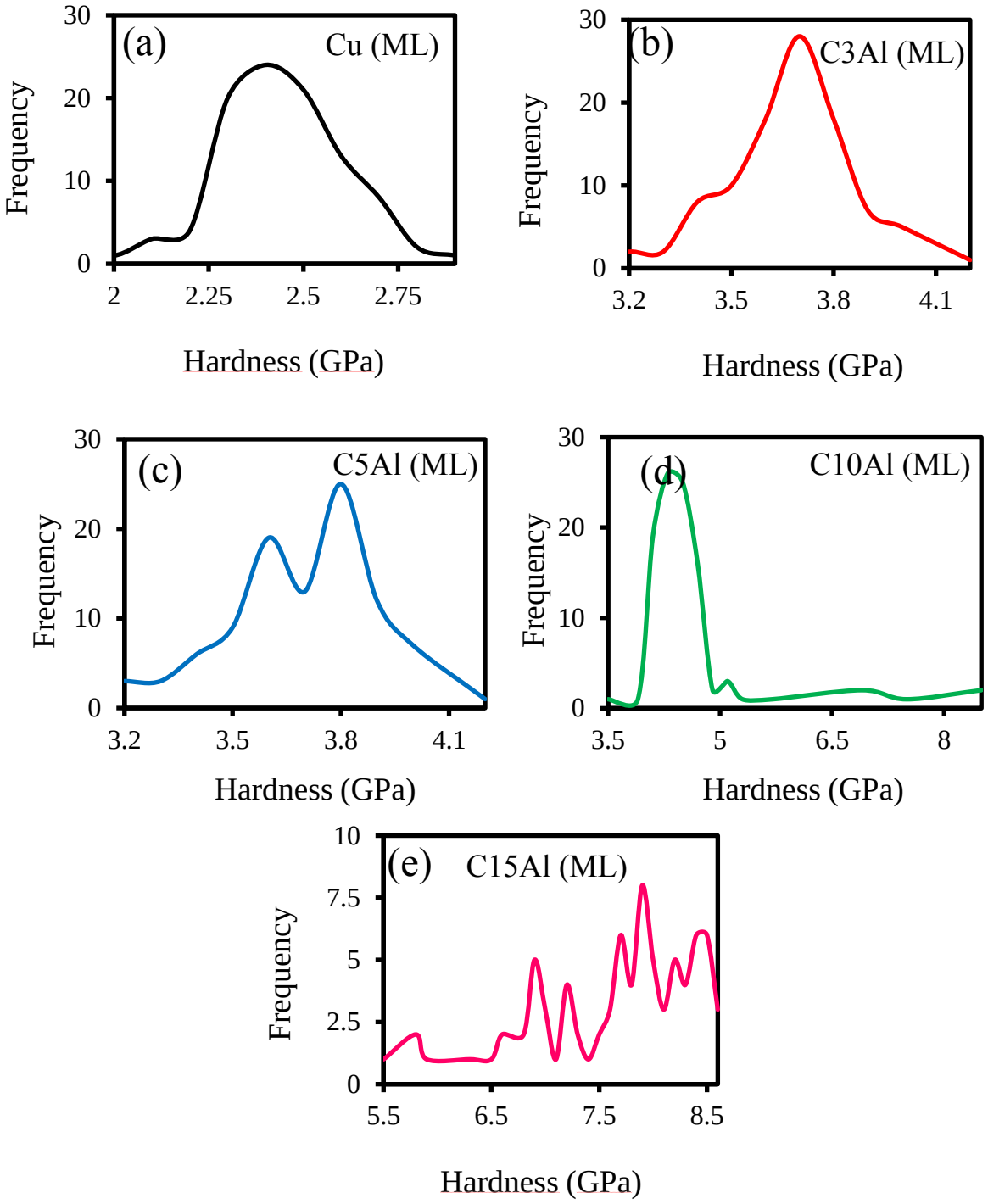

Fig. 4.13 Distribution of nanohardness at various phases of Cu-Al (milled) alloys plotted form load vs. penetration depth curves at an indent peak load of 20 mN (loading and unloading rate: 2.0 mN/s) (a-e).

The nanohardness of Cu-Al (milled) alloys varied between 2.38 GPa to 7.88 GPa, nevertheless C15Al (ML) exhibited maximum hardness. Scattering in the hardness of Cu-Al (milled) alloys can be attributed to its microstructure. In the case of Cu (ML) and Cu alloys up to 5 wt.% Al, the hardness is almost uniformly/narrowly distributed due to its single phase.

There is a wide deviation or scatter in the hardness of C10Al (ML) and C15Al (ML) as they consisted of two different phases. The cumulative values of the hardness of Cu-Al (milled) alloys are shown in **Fig. 4.14.**

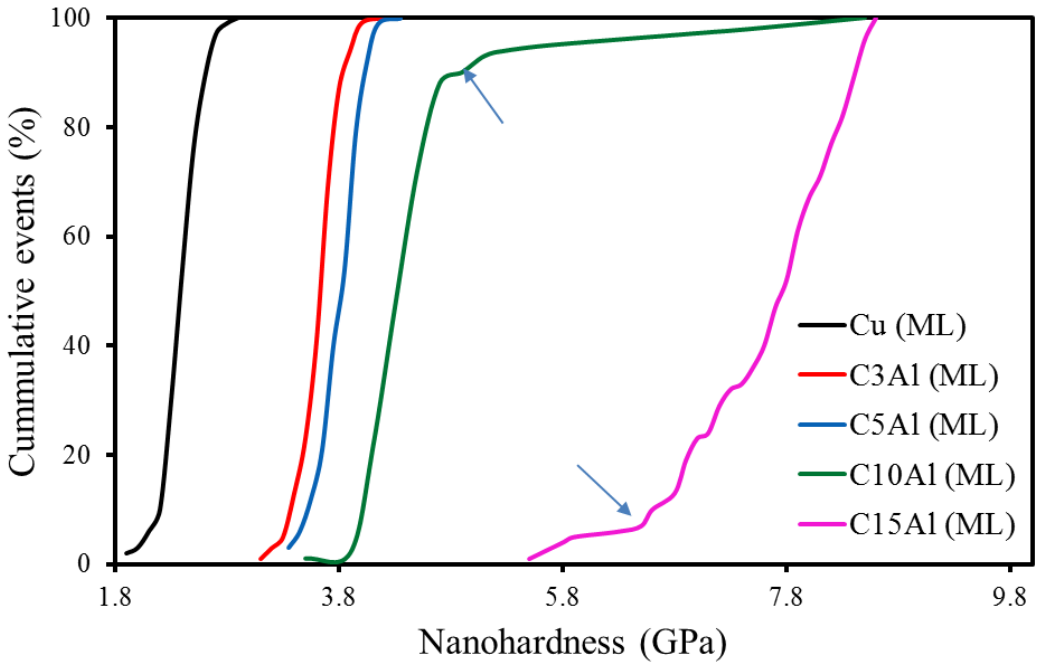

Fig. 4.14 Cumulative events (%) of nanohardness of Cu-Al (milled) alloys. The pop-in effect shows the presence of different phases.

The cumulative hardness of Cu-Al (milled) alloys shows the pop-in effect which is associated with phase variations or microstructure and correspondingly represents hardness. In pure copper, no pop-in effect has been observed as it does not have any phase change. The pop-in effect was not observed for pure Cu (ML), C3Al (ML) and C5Al (ML) alloys as their microstructure consists of a single phase. On the other hand, the pop-in was found at 4.7 GPa corresponding to the hardness of the α phase in the C10Al (ML) alloy. The C15Al (ML) alloy shows the different pop in effects [258], which indicates the broad range of hardness regarding α and γ_2 phases.

4.4.3 Compression behaviour

Fig. 4.15 shows the compression stress-strain curves of Cu-Al (milled) alloys. From **Fig. 4.15a**, it can be observed that the compressive strength of Cu-Al (milled) alloys increased significantly and the compressive strain decreased with Al addition. The compression properties of Cu-Al (milled) alloys are presented in **Table 4.9**.

Table 4.9 Compression test results of Cu-Al (milled) alloys.

Sample reference	Compressive strength (MPa)	Strain (%)
Cu (ML)	813.75 ± 11	29.81 ± 0.9
C3Al (ML)	954.71 ± 21	8.61 ± 0.6
C5Al (ML)	1120.18 ± 28	8.00 ± 0.7
C10Al (ML)	1077.05 ± 30	5.93 ± 0.4
C15Al (ML)	1013.82 ± 25	5.81 ± 0.3

The compressive strength of Cu (ML) increased from 813.75 ± 11 MPa to 1120.18 ± 28 MPa with the addition of Al. Whereas, the compressive strain reduced from 29.81 ± 0.9% to 5.81 ± 0.3% (see **Fig. 4.15c).** From **Fig. 4.15b**, a common observation is that a significant high compressive strength of 1120.18 ± 28 MPa is achieved for C5Al (ML) with a reasonable amount of strain (8.0 ± 0.7%).

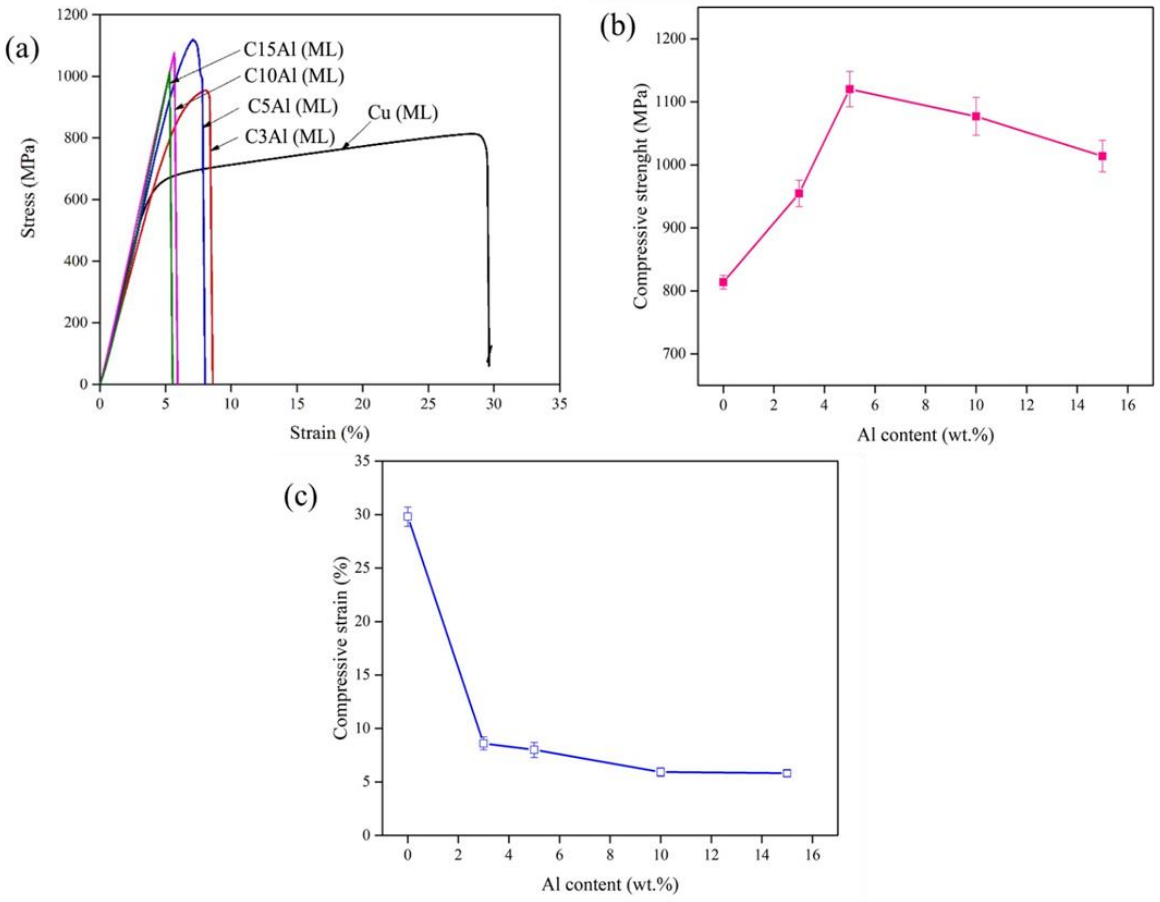

Fig. 4.15 (a) Compression stress-strain curves of Cu-Al (milled) alloys, effect of Al on (b) compressive strength (c) compressive strain of Cu.

Since the C5Al (ML) alloy has the major constituent of *α-Cu* and the combined features of a microstructure such as finer and elongated grains might have contributed to its good combination of properties. Due to the formation intermetallic phase (γ_2) and rich solid solution phase in C10Al (ML) alloys, its strength (1077 ± 30 MPa) lowered when compared to C5Al (ML) alloy. The similar kind of behaviour was observed in the case of C15Al (ML), which is having the compressive strength of 1077.05 ± 30 MPa with a moderate compressive strain of 5.81 ± 0.3.

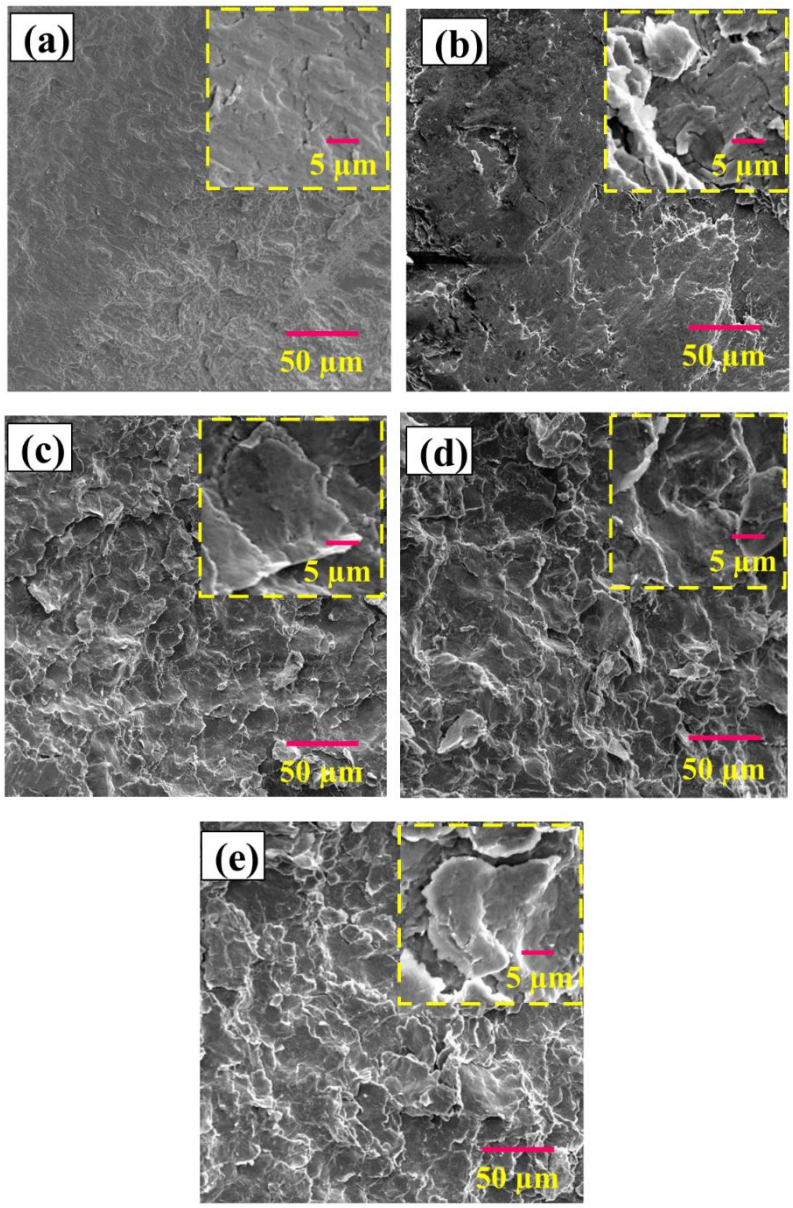

Fig. 4.16 Fractured surfaces of compression tested Cu-Al (milled) alloys (Hot press conditions: 500 ^{o}C, 500 MPa for 30 min.). (a) Cu (ML), (b) C3Al (ML), (c) C5Al (ML), (d) C10Al (ML) and (e) C15Al (ML). The insets represent high magnification images.

The fractured surfaces of pure copper and Cu-Al (milled) alloys after the compression test is presented in **Fig. 4.16**. During the compression test, the Cu-Al (milled) alloys showed an inclined fracture surface, about 45^{o} with the applied load axis, which is a similar failure criterion of hard materials [259]. The change in strength behaviour of Cu-Al (milled) alloys is mainly because of the change in the mode of fracture. From Fig. 4.5, it can be realized that the microstructure of C5Al (ML) alloy consisted of finer and elongated grains. Also, the fracture surface of C5Al (ML) revealed the presence of relatively finer grain structure and the mode of fracture was predominantly transgranular (Fig. 4.16). However, the mode of fracture changed from the transgranular to mixed mode (transgranular and intergranular) of fracture for Cu-Al alloys with the further addition of Al (> 5 wt.%) to Cu (Fig. 4.16). Moreover, the microstructure of these Cu alloys consisted low amount (*α-Cu*) and high amount of brittle Cu_9Al_4 phase. The good combination of properties of C5Al (ML) can be attributed to its microstructural phase (*α-Cu*), finer microstructure and transgranular mode of fracture. Therefore, the compressive strength and strain of C10Al (ML) and C15Al (ML) samples were observed to be lower than C5Al (ML) samples. In fact, as discussed above the Cu with up to 5 wt.% Al, the fracture mode is predominantly of transgranular and it changed to more of intergranular with the further addition of Al to Cu (Fig. 4.16).

Aluminium bronzes (Cu-Al alloys) have been used as a tool material in sheet metal forming of stainless steel, which is used for the production of washing, refrigeration and cooking equipment [260]. It was reported that the tool wear of these alloys is sensitive to its limited hardness. In this context, achieving the high hardness and good compression strength of Cu-Al (milled) alloys is very promising.

4.5 Abrasive wear behaviour of Cu-Al (milled) alloys

4.5.1 Coefficient of friction (COF)

The COF of Cu-Al (milled) alloys sliding against SiC (220 grit size) emery paper is shown in **Fig. 4.17**. The COF of Cu-Al (milled) alloys was significantly decreased with the addition of Al upto 15 wt.%. The run-in period of the COF curves showed an initial rise of COF due to the interlocking of asperities at the junction of mating surfaces [261]. The COF of Cu-Al (milled) alloys attained steady-state about a sliding distance of 20 m after the contact pressure reduced.

The steady-state of COF was attained due to the worn-out of SiC abrasives. The minor fluctuations were observed in Cu (ML) samples due to sudden detachment of SiC abrasives form the emery paper due to the higher frictional forces developed between two contacting surfaces. In case of C3Al (ML) and C5Al (ML) alloys which were having rich solid solution phase (α-Cu), the gradual detachment of wear debris and worn out of SiC abrasives may result in fluctuations of the COF. In C10Al (ML) and C15Al (ML), almost no fluctuations were observed due to the presence of hard intermetallic phase surface. Thus, the lower frictional forces thereby lower COF in alloys attributed to the high hardness of the samples.

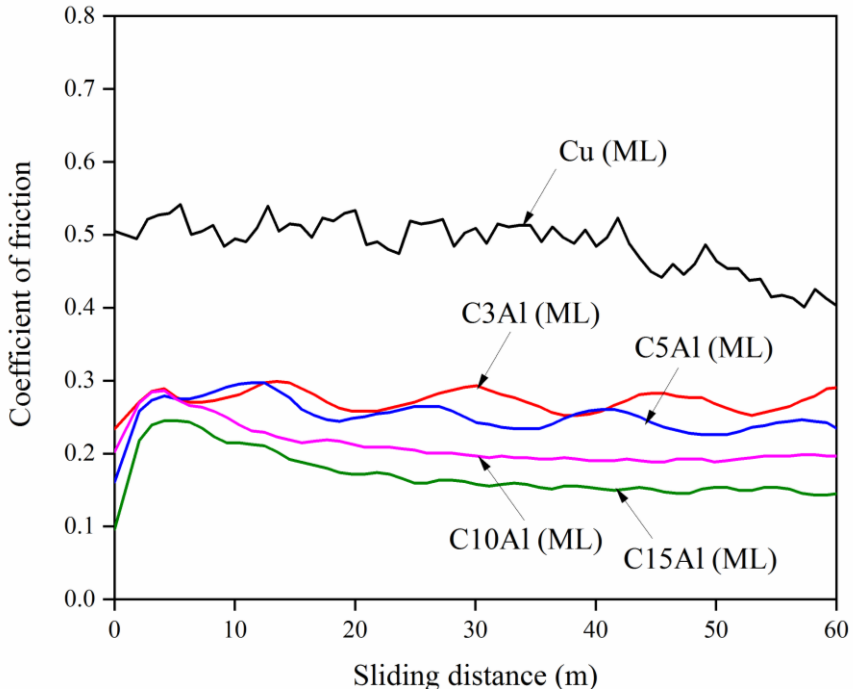

Fig. 4.17 Coefficient of friction of Cu-Al (milled) alloys sliding against SiC abrasive of 220 grit size at a sliding velocity of 1 m/s.

The wear results of the Cu-Al (milled) alloys after the abrasive wear test are listed in **Table 4.10**. The COF of the Cu (ML) was found to 0.49 ± 0.05 because of the high frictional forces produced between two mating surfaces. The COF of Cu-Al (milled) alloys decreased from 0.27 ± 0.08 to 0.16 ± 0.03 as the Al content varied from 3 to 15 wt.%. The COF of C15Al (ML) found to be low due to the presence of the high amount of intermetallic phases (75.03%). The entrapped of hard wear debris between contacting surfaces which also a factor responsible for producing the rolling effect, thus the low COF of alloys.

Table 4.10 The wear results of the Cu-Al (milled) alloys after the abrasive wear test

Sample reference	Coefficient of friction	Sp. wear rate ($\times 10^{-3}$ mm^3/Nm)
Cu (ML)	0.49 ± 0.05	49.30 ± 05
C3Al (ML)	0.27 ± 0.08	11.50 ± 02
C5Al (ML)	0.24 ± 0.08	8.50 ± 03
C10Al (ML)	0.19 ± 0.02	4.90 ± 01
C15Al (ML)	0.16 ± 0.03	0.80 ± 0.4

4.5.2 Effect of Al on wear rate of Cu-Al (milled) alloys

The effect of Al addition on the specific wear rate of Cu-Al (milled) alloys is presented in **Fig. 4.18**. The wear rate of the Cu-Al (milled) alloys drastically reduced from the 49.3 $\times 10^{-3}$ to 0.8 $\times 10^{-3}$ mm^3/Nm. The Cu (ML) sample exhibited the specific (sp.) wear rate of 49.3 $\times 10^{-3}$ mm^3/Nm. While the low sp. wear rate of 0.8 $\times 10^{-3}$ mm^3/Nm was found in C15Al (ML) alloys which is ~62 times lower compared to pure copper. The drastic reduction of specific wear rate of C15Al (ML) alloys is because of the formation of intermetallic compounds (hardness: 6.16 GPa). The sp. wear rate of C3Al (ML), C5Al (ML) and C10Al (ML) alloys was found to 11.5 $\times 10^{-3}$, 8.5 $\times 10^{-3}$ and 4.9 $\times 10^{-3}$ mm^3/Nm, respectively.

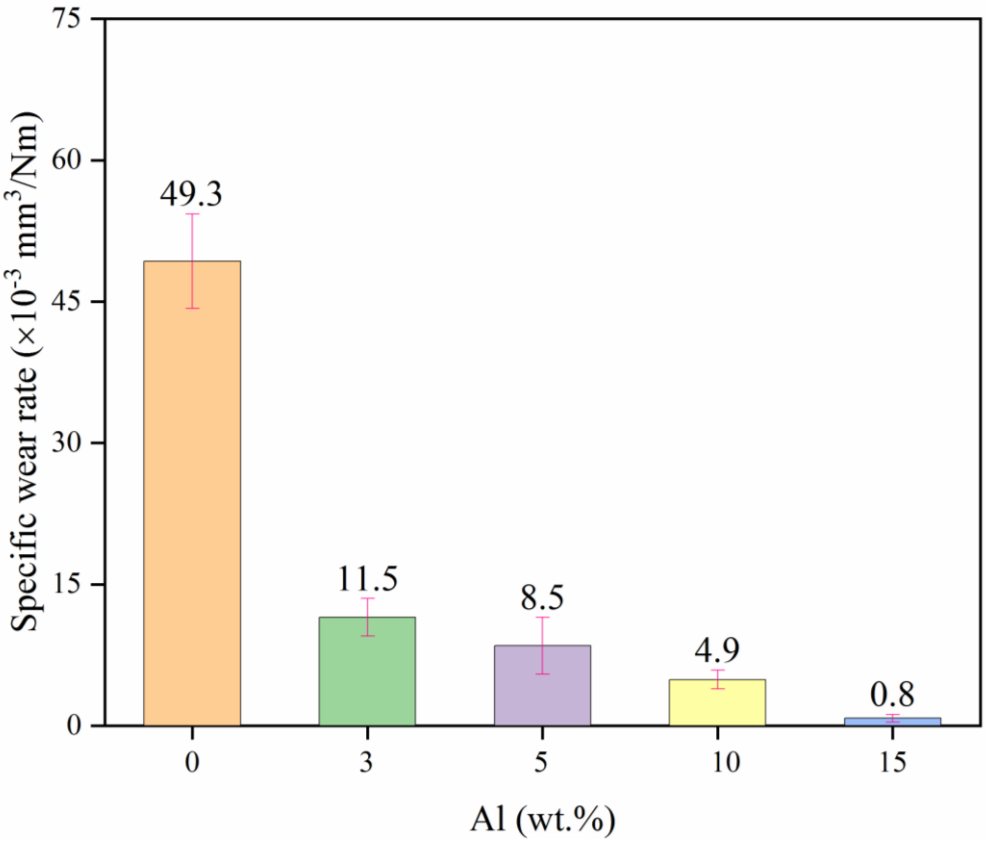

Fig. 4.18 Effect of Al content on sp. wear rate of Cu-Al (milled) alloys

4.5.3 Worn surface analysis and wear mechanisms

The worn surface of the Cu-Al (milled) alloys sliding against SiC, which slid at a velocity of 1 m/s and the load of 5 N is presented in **Fig. 4.19**. The Cu (ML) samples have the narrow grooves and the ridges along with the wear debris formed after wear test which can be observed from Fig. 4.19 (a,d). Also, there could be a possibility of hard SiC particles may penetrate the soft Cu and causes the deep grooves by plowing mechanism which resulted in high volume loss of the material.

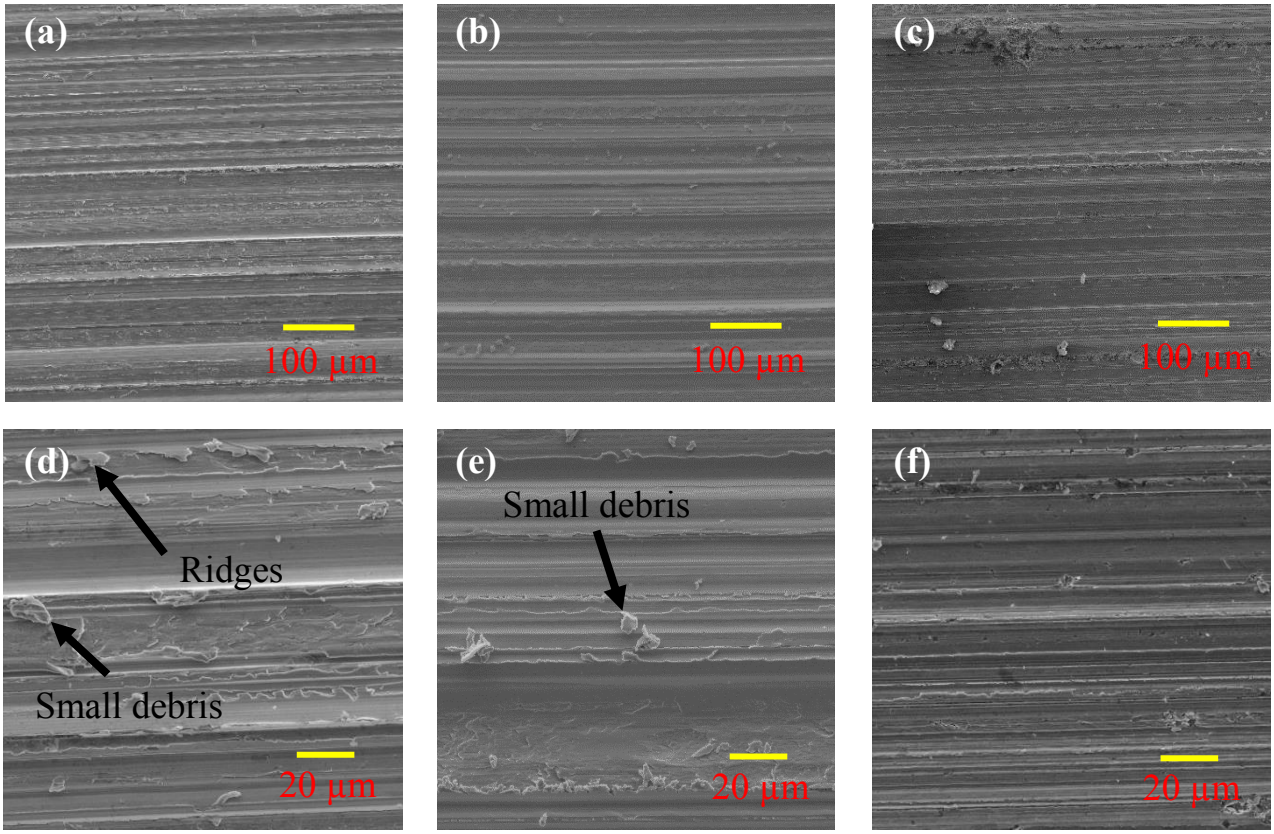

Fig. 4.19 SEM images of worn tracks of Cu-Al (milled) alloys. (a,d) Pure copper (b,e) C5Al (c,f) C15Al and (d-f) corresponding higher magnification images.

In C5Al (ML) samples, broad grooves and the presence of fine debris were observed on the worn surface (**Fig. 4.19b**). It indicates that the material is removed by the abrasive cutting mechanism. These observations were well correlated with the hardness of the C5Al (ML) alloy (2.73 GPa). The presence of solid solution (α) phase improved the wear resistance of the sample. In case of C15Al (ML), broad grooves and no wear debris were observed on the worn surface (see **Fig. 4.19c**). Based on these observations, the material loss in C15Al (ML) alloy is mainly due to the abrasion cutting mechanism. The presence of high intermetallic compound amount in C15Al (ML), significantly improved the wear resistance of the alloy. The above results indicate the transformation of wear mechanisms from the plowing mechanism of pure Cu (ML) to the cutting mechanism of C15Al (ML).

4.5.4 Wear debris analysis

Fig. 4.20 presents the SEM images of wear debris formed during abrasive wear of samples. In Cu (ML) samples, continuous and thick chips (wear debris) were formed during wear test by the plowing mechanism. This indicates the more material loss from the Cu (ML) samples. The thickness and length of wear debris decreased with the addition of the Al due to the presence of solid solution and intermetallic compound phases in the Cu-Al (milled) alloys which significantly increased the hardness of the Cu (ML). In case of C5Al (ML) and C15Al (ML) alloys, thin and broken (short) chips were found after abrasive wear test.

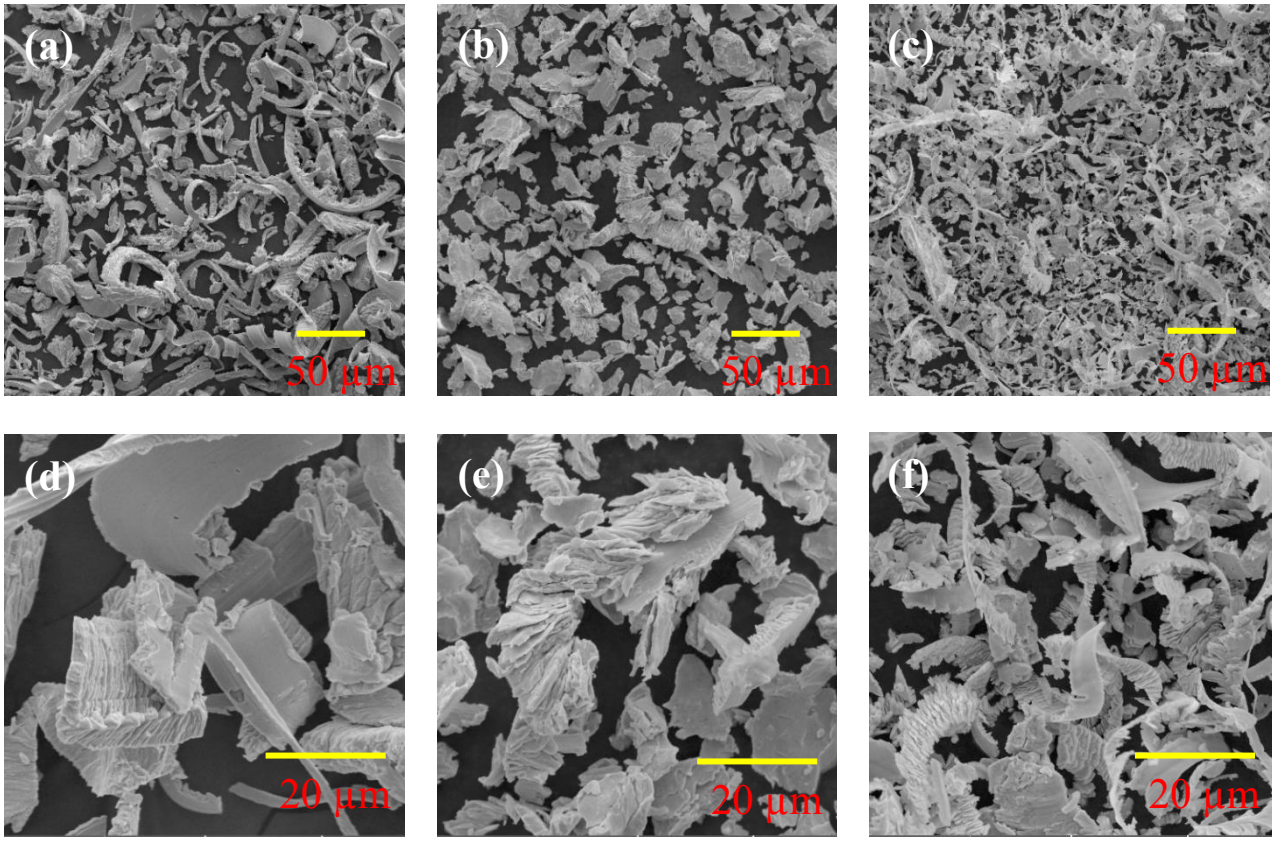

Fig. 4.20 Wear debris of Cu-Al (milled) alloys. (a,d) Pure copper (b,e) C5Al (ML) (c,f) C15Al (ML); (d-f) corresponding higher magnifications of wear debris.

In view of the interesting results of Cu-Al (milled) alloys, additional experiments were performed to understand its sliding wear and corrosion behaviour. In fact, the wear studies were carried out for all the Cu-Al alloys and corrosion tests were done for a few selected samples. It also has to be noted here that such studies were not carried out either for other Cu-Al (milled) alloys and Cu-ZrB_2 (Milled & Mixed) composites.

4.6 Sliding wear behaviour of Cu-Al (milled) alloys

4.6.1 Coefficient of friction

Fig. 4.21 shows the COF plots of Cu-Al (milled) samples after sliding against EN31 steel disc at a load of 39.2 N. After sliding for a distance of 200 m, the steady-state COF was reached for Cu with Al (upto 10 wt.%). Interestingly, the steady-state COF is noticeable for C15Al (ML) from the very beginning of wear test. It can be said that the duration to achieve steady-state COF reduced with the addition of Al to Cu. Another observation is that the oscillations of COF is evident for Cu (ML), C3Al (ML) and C5Al (ML) samples and is mainly due to the occurrence of stick-slip phenomena by adhesive wear and oxidative wear. Negligible fluctuations in COF was observed for C10Al (ML) and very stable COF was obvious for C15Al (ML) samples.

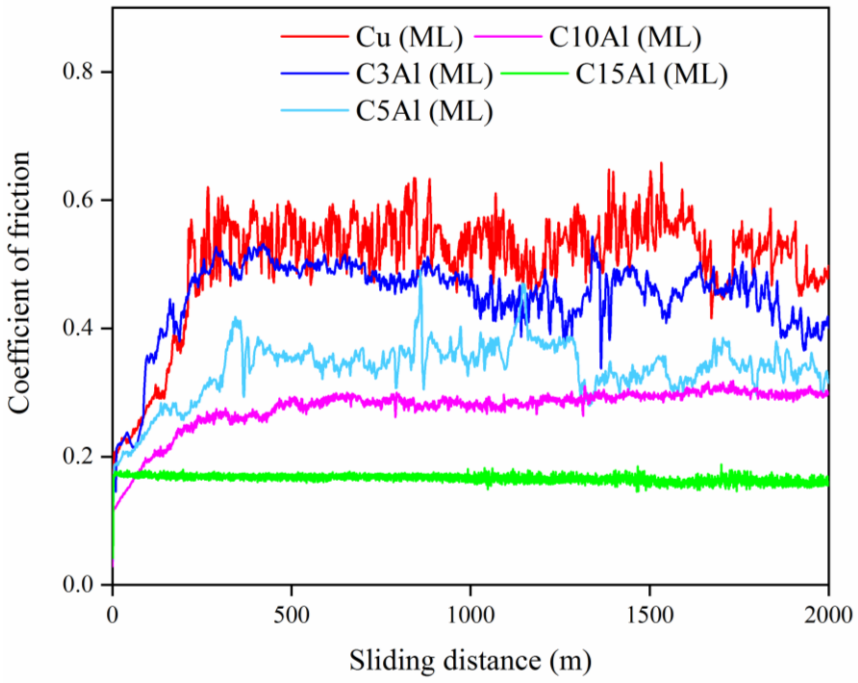

Fig. 4.21 Coefficient of friction of Cu–Al alloys after sliding against EN 31 steel disc at a sliding velocity of 0.25 m/s and the normal load of 39.2 N.

The average COF of Cu samples after the wear test is shown in **Fig. 4.22a**. The COF of Cu (ML) was reduced from 0.54 ± 0.05 to 0.16 ± 0.02 with the addition of Al. Pure Cu (ML) was recorded with a maximum COF of 0.54 and the minimum COF of 0.16 for C15Al (ML). Such a significant reduction in COF indicates that different wear mechanisms are operative

during sliding of Cu-Al (milled) alloys against steel. The higher COF in pure Cu (ML) can be attributed to the generation of high heat due to adhesive wear of contacting bodies. Pellizzari and Cipolloni [153] reported high COF (~ 1) at an early stage of wear and low steady-state COF of 0.7 due to change of wear mechanism from adhesive to tribo-oxidative wear. Their work also revealed that COF decreased with an increase of load due to the change in wear mechanism.

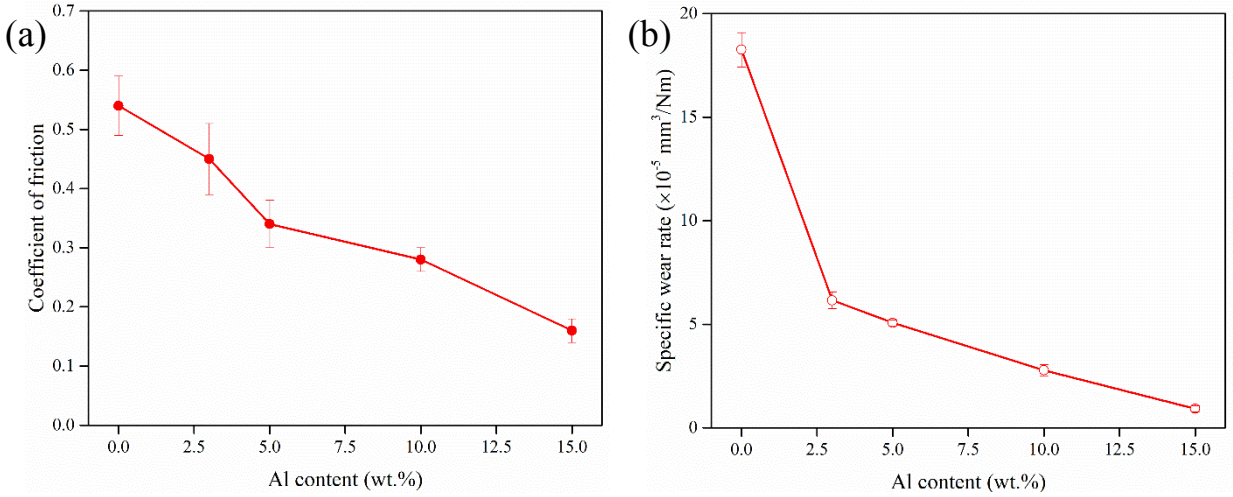

Fig. 4.22 Wear test results of Cu-Al (milled) alloys at different weight fractions of Al. The average (a) coefficient of friction and (b) specific wear rate of the Cu–Al alloys after sliding against EN 31 steel disc at a normal load of 39.2 N, sliding velocity of 0.25 m/s and sliding distance of 2000 m.

4.6.2 Wear of Cu and Cu-Al (milled) alloys

The weight of samples before and after wear test was precisely measured to calculate the weight loss of the materials. The weight loss of Cu decreased from 129.17 mg to 4.91 mg with increasing the amount of Al. The specific wear rate of Cu-Al (milled) alloys were found to be reduced considerably from 18.2 ± 0.6 $\times 10^{-5}$ mm^3/N-m to 0.92 ± 0.17$\times 10^{-5}$ mm^3/N-m with the Al amount (see **Fig. 4.22b**). The pure Cu measured with a high wear rate of 18.26 ± 0.64 $\times 10^{-5}$ mm^3/N-m. In case of C3Al (ML) alloys, the specific wear rate was drastically reduced to 6.16 ± 0.17 $\times 10^{-5}$ mm^3/N-m. It is mainly due to its high hardness than pure Cu (ML). Almost similar wear was observed for C5Al (ML) alloys as its hardness is almost similar to C3Al (ML) and even the microstructure ($Cu_{0.92}Al_{0.08}$). Further, the specific wear rate of C10Al (ML) and C15Al (ML) was reduced considerably as its hardness is higher than the other Cu alloys. Such a difference in wear behaviour also can be related to its microstructure as it consists of a solid solution phase ($Cu_{0.78}Al_{0.22}$) and γ_2 intermetallic phase (Cu_9Al_4). In particular, the presence of

the high amount of γ_2 intermetallic phase (Cu_9Al_4) contributed to its high hardness and wear resistance of C15Al (ML).

Depending on the application, the wear tests of Cu are carried out at a sliding velocity in the range of 0.01 to 14 m/s with the contact pressures varying between 0.2 to 7.13 MPa; the COF of Cu-based alloys varied in the range of about 0.14 to 0.74 and wear rate between 0.91×10^{-5} mm^3/Nm to 22×10^{-5} mm^3/Nm depending on wear test conditions [176,177,179–181,262–264]. In the present work, the Cu-Al (milled) alloys were tested at a contact pressure of 0.5 MPa and sliding velocity of 0.25 m/s in dry sliding condition. The specific wear rate of presently developed C10Al (ML) and C15Al (ML) alloys were found to be comparable as that of the other Cu alloys, which were tested under similar sliding conditions.

4.6.3 Characterization of worn surfaces and wear mechanisms

Fig. 4.23 presents the worn surface of the pure Cu (ML) after sliding against EN31 steel disc. Adhesion wear is expected during the sliding due to the metal-metal (steel-Cu) contact. In fact, the high COF and more oscillations in COF also corroborates the adhesion wear of pure copper (see **Fig. 4.21**). The material transfer takes place on the mating parts when its asperities come in contact. In the present case, Cu might transfer to the steel counterbody as it is a very soft metal.

The SEM of worn surfaces reveals the sticking of material along with the presence of very fine wear debris (**Fig. 4.23 b-c**). The size of the wear debris might have become very fine due to repeated sliding between the contacting surfaces. Also, the debris immediately gets oxidised and thus observed to be very stable. The EDS analysis of worn surface showed the presence of oxygen and Cu. There are no traces of Fe, indicating no Fe transfer to Cu pin material. Considerably low amount of oxygen (2.04 wt.%) was detected from the EDS of worn surface of Cu when compared to wear debris (12.54 wt.%).

Although the transfer of material from both the mating bodies is expected for adhesive wear, the presence of Fe could not be detected on the worn surface of either pure Cu or the wear debris present on the Cu pin, and it is mainly due to the softness of Cu (Fig. 4.23). Indeed, the hardness of pure Cu (ML) samples (Hv: 1.3 GPa) is very low when compared to the steel (EN31) counter-body (Hv: 7 GPa). Thus more Cu might have transferred to the steel counter-body due to the wear. On the other hand, interestingly the EDS analysis of wear debris

(collected on the steel counter-body) revealed the presence of Fe, O and Cu (Fig. 4.27). This affirms that adhesive wear is the main wear mechanism for pure Cu. Similar observations were also reported in the literature with the wear of soft metals (like Cu and Al) [265, 266]. It was reported that only the soft metal transferred to the hard counter-body during wear, but there was no evidence of transfer of counter-body material to the soft metal surface.

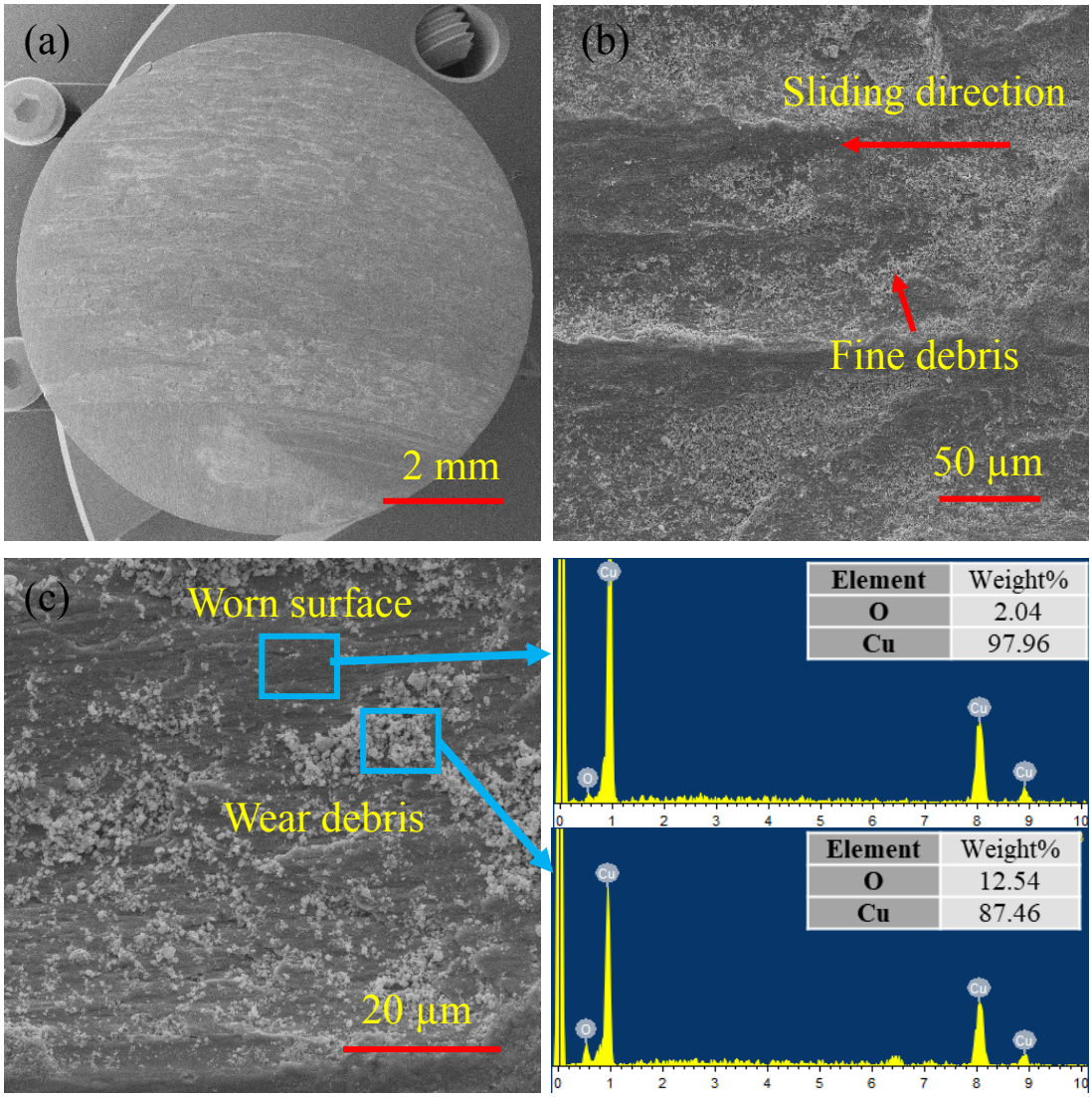

Fig. 4.23 SEM micrographs of worn surfaces of the pure copper (ML) after sliding against EN 31 steel disc at an applied load of 39.2 N, a sliding distance of 2000 m and sliding velocity of 0.25 m/s. (a) Overview of the Cu (ML) sample surface, (b) low magnification of worn surface and (c) High magnification worn surface. The corresponding EDS of worn surface and wear debris.

From the EDS analysis of wear debris, it is evident that they are of Cu_2O oxide particles. Since adhesion is the dominant mechanism for pure Cu (ML), maximum wear rate was observed for pure Cu (ML) when compared to all the other Cu-Al (milled) samples (see **Fig. 4.22b**).

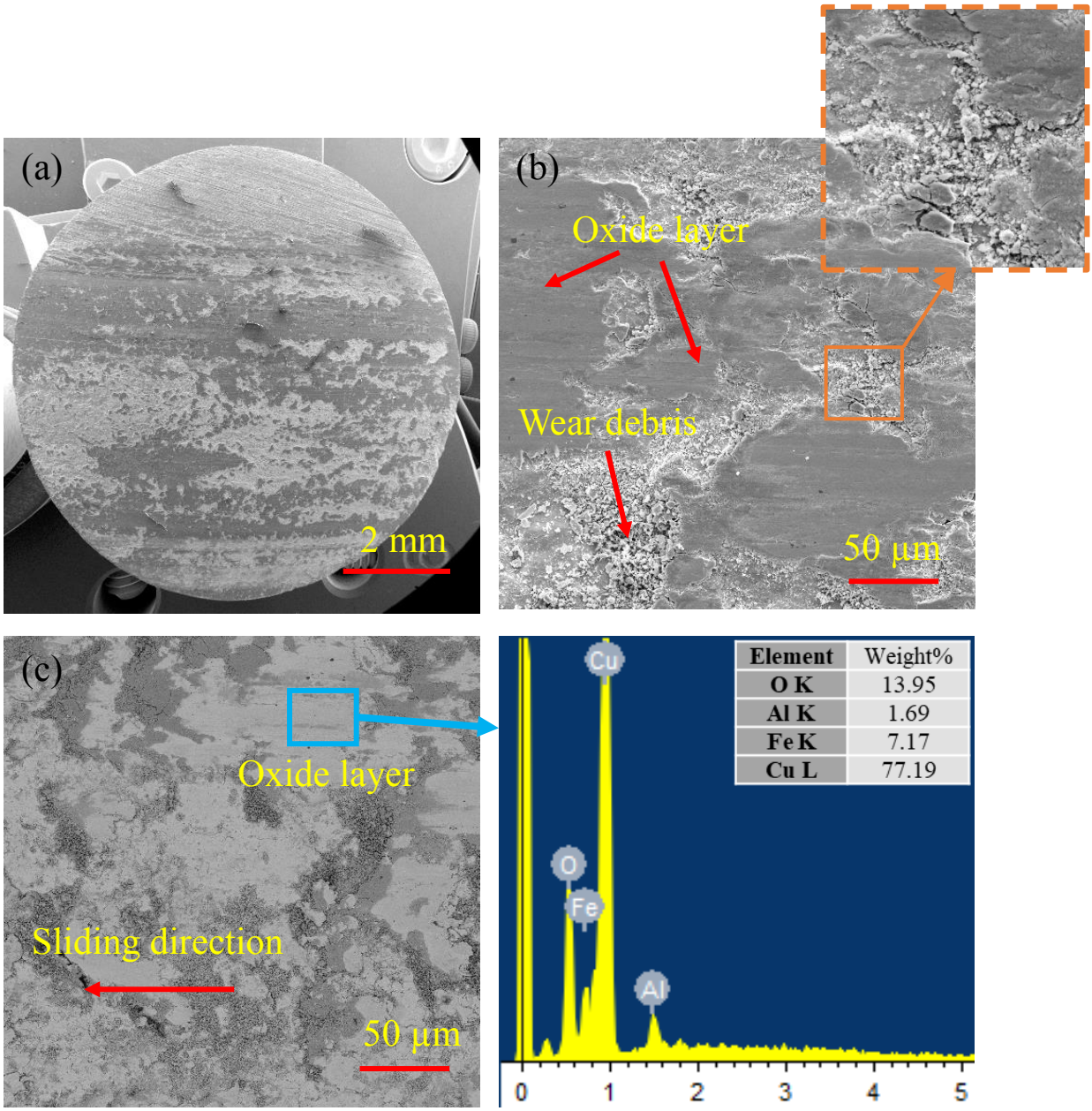

Fig. 4.24 SEM micrographs of worn surfaces of the C5Al (ML) alloy after sliding against EN 31 steel disc at an applied load of 39.2 N, the sliding distance of 2000 m and sliding velocity of 0.25 m/s. (a) Overview of C5Al (ML) sample surface, (b) SE micrograph of worn surface and high magnification of worn surface is shown as an inset and (c) BSE micrograph of worn surface. The corresponding EDS of the oxide layer.

Oxide layer formation and the presence of wear debris were observed for Cu with Al (upto 5 wt.%) (**Fig. 4.24**). The C5Al (ML) alloy worn surface is composed of two distinct regions, which can be identified from secondary electron (SE) and backscatter electron (BSE) images (**Fig. 4.24b and c**). The bright region indicates the formation of an oxidative thick layer with the presence of high oxygen content (13.95 %), which was confirmed by the EDS analysis (**Fig. 4.24c**). The wear debris can be seen as a dark contrast phase in **Fig. 4.24c**. Presence of

stable oxide layer and wear debris at regions of layer detachment can be seen on the worn surface. The oxide layer is getting fragmented at some locations and leading to the formation of wear debris. The COF of C3Al (ML) and C5Al (ML) samples show similar behaviour. The fluctuations in COF can also be attributed to the fragmentation of the oxide layer and wear debris formation. The SEM-EDS of oxide layer indicated the presence of oxygen, Fe along with Cu and Al. It represents adhesion and tribo-oxidation mechanisms controlling the wear of C5Al (ML). Sanderson et al. [267] reported that the addition of aluminium to copper leads to the formation of the Al_2O_3 and Cu_2O layers in Cu-7.5Al-2Si alloy.

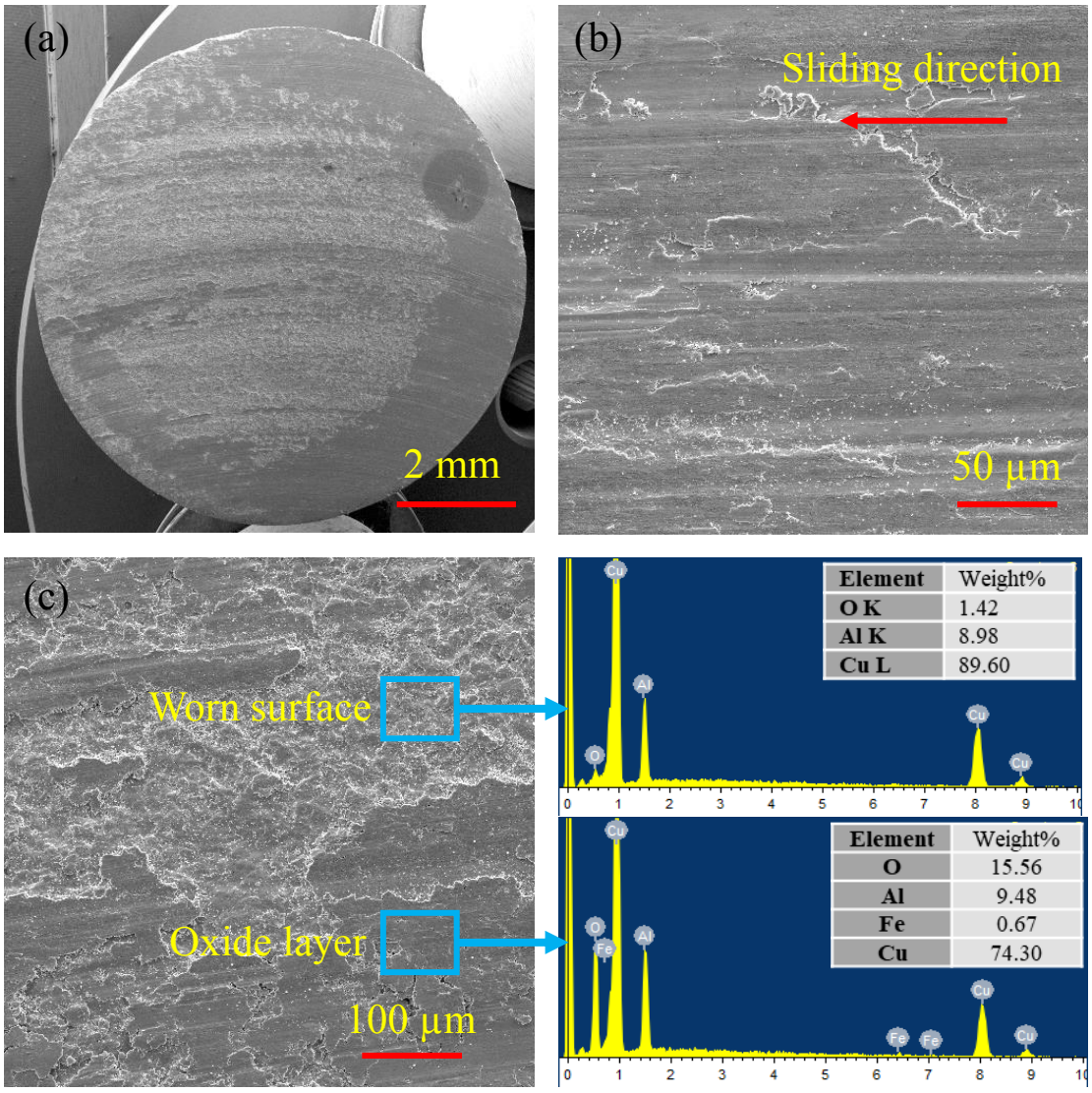

Fig. 4.25 SEM micrographs of worn surface of the C10Al (ML) alloy after sliding against EN 31 steel disc at an applied load of 39.2 N, the sliding distance of 2000 m and sliding velocity of 0.25 m/s. (a) Overview of C10Al (ML) sample surface, (b) high magnification of worn surface and (c) Low magnification of worn surface. The corresponding EDS of worn surface and oxide layer is also presented.

In C10Al (ML), the worn surfaces are characterised with an oxide layer and a relatively very small amount of wear debris can be seen (**Fig. 4.25**). Less amount of wear debris was noticed on the worn surface of C10Al (ML), hence probably the fluctuations in COF is low (see **Fig. 4.21**). A careful look at the worn surface also reveals the presence of abrasion grooves on the oxide layer and its delamination (**Fig. 4.25 b-c**). The oxide layer consists of a large amount of oxygen and a minute fraction of Fe along with the base Cu and Al elements. The presence of less amount of Fe represents that adhesion may be negligible in the wear of C10Al (ML). The low COF of C10Al (ML) than Cu, C3Al (ML) and C5Al (ML) can be related to its microstructure and high hardness. As Al content increased, the stability of the oxide layer decreased. It may be due to the formation of the Al_2O_3 layer, which is nonprotective in nature during sliding. Poggie et al. [268] reported that the Al_2O_3 oxide layer decreases the adhesion between Cu_2O layer and alloy surface. The mechanical instability of the oxide layer thereby leads to the delamination.

In case of Cu alloys with Al (up to 10 wt.%), as mentioned earlier the SEM-EDS of oxide layer indicated the presence of oxygen, Fe along with Cu and Al. The presence of a high amount of O on the worn surface is a clear indication of the involvement of oxidative wear mechanism. Also, the transfer of Fe from the steel counter-body to the Cu alloys reveals the contribution of adhesive wear (Figs. 4.24 and 4.25). In case of Cu-Al alloys, the presence of hard microstructural phases leads to the enhancement of its hardness (upto 3.4 GPa). The combined effect of high hardness and adhesion wear mechanism resulted in a transfer of material from counter-body to sample worn surface and vice-versa. These observations clearly indicate the adhesive and tribo-oxidative wear mechanisms mainly responsible for the wear of Cu-Al alloys.

The worn surface of C15Al (ML) indicates abrasive grooves (**Fig. 4.26**). The SEM of the worn surface of C15Al (ML) alloys hardly shows the presence of wear debris. The SEM-EDS analysis indicates the presence of a very small amount of oxygen along with base Cu and Al (**Fig. 4.26d**). Hence there is no indication of transfer Fe from the counterbody. The COF curve is also very stable and the COF is the lowest among all the Cu-Al (milled) samples. These observations clearly indicate a transition in wear mechanism. In case of sliding wear of C15Al (ML) alloys, a very small quantity of wear debris could be observed in comparison to the other Cu and Cu-Al samples (Figs. 4.23, 4.24, 4.25 and 4.26). The relatively stable COF with very minute fluctuations of the C15Al alloy can be attributed to the small quantity of wear debris.

The wear of C15Al (ML) is mainly dominated by abrasion. Since its microstructure is mainly composed of Cu_9Al_4 (75.30 %) and $Cu_{0.78}Al_{0.22}$ (24.7 %) phases, the contact between mating parts may be a dissimilar type. During sliding, it may be possible that the abrasive wear of C15Al (ML) takes place either by hard steel counterbody or any hard Cu_9Al_4 intermetallic pull out particles. In fact, the hardness of EN31 steel (*H*: 7.2 GPa) body is higher than the hardness of C15Al (ML) (*H*: 6.16 GPa). Among the microstructural phases that are present in C15Al (ML), Cu_9Al_4 expected to have much high hardness than $Cu_{0.78}Al_{0.22}$. Indeed, the hardness of C15Al (ML) measured exceptionally high than the other Cu-Al (milled) samples due to the presence of a large amount of Cu_9Al_4.

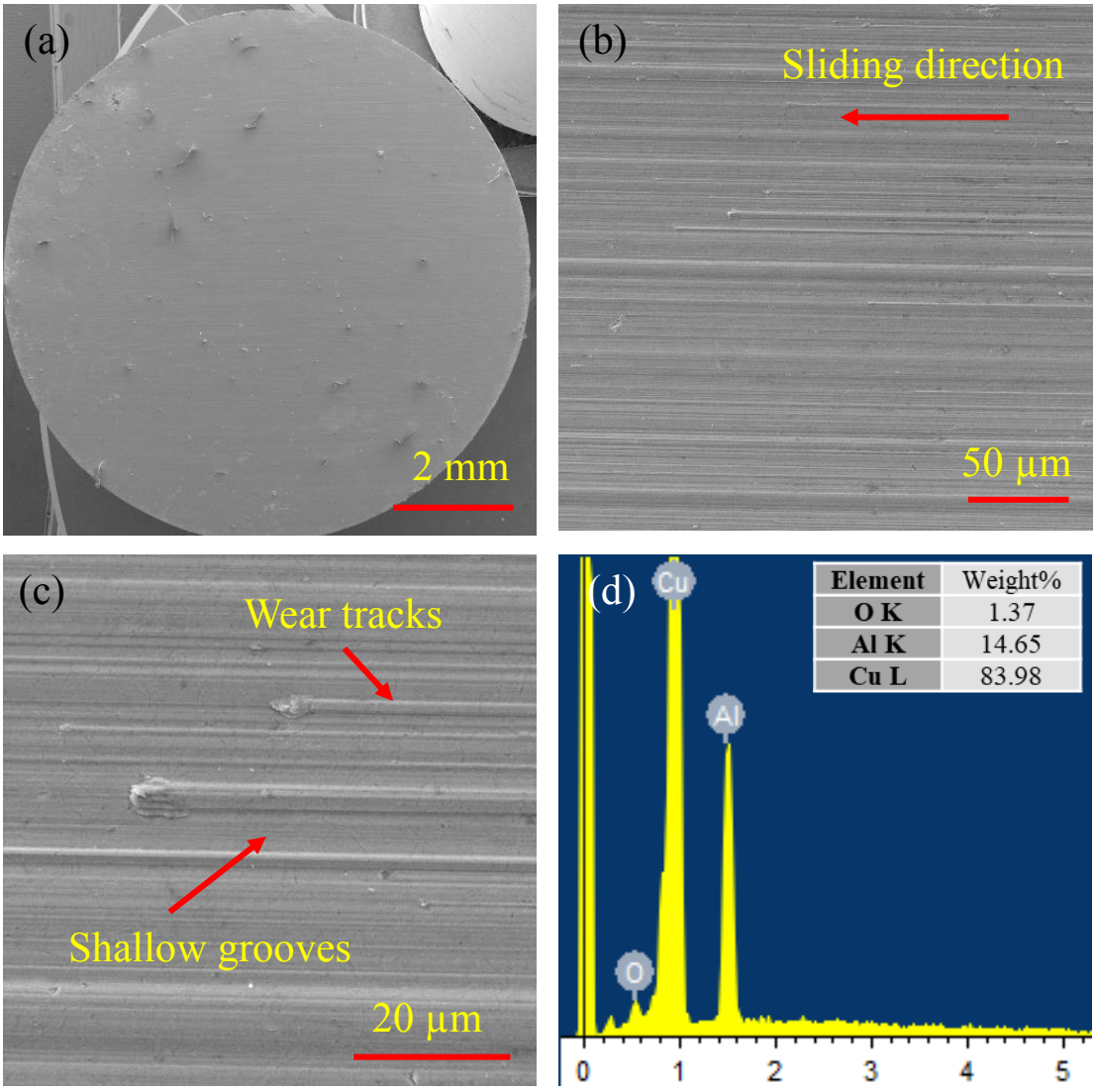

Fig. 4.26 SEM micrographs of worn surface of the C15Al (ML) alloy after sliding against EN 31 steel disc at an applied load of 39.2 N, the sliding distance of 2000 m and sliding velocity of 0.25 m/s. (a) Overview of C15Al (ML) sample surface, (b) low magnification worn surface, (c) High magnification worn surface and (d) the corresponding EDS of worn surface.

4.6.4 Wear debris analysis

To understand the wear mechanisms, the detailed microstructural analysis of wear debris was carried out. **Fig. 4.27** shows SEM micrographs of collected wear debris that were retained on the steel disk after wear test for the pure Cu (ML) and C15Al (ML) alloy after sliding against EN 31 steel disc. From **Fig. 4.27a and b**, it can be observed that the presence of fine agglomerated wear debris for pure copper. On the contrary, the size of the wear debris is significantly coarse and flaky for C15Al (ML) alloy (**Fig. 4.27 d and e**). During wear of C15Al (ML), the flaky wear debris was developed by the micro-cutting action of harder particles. These big flaky debris slides between the hard contacting pairs during sliding. Also, the characteristic features of abrasion grooves and micro-cracks were observed on the coarse wear debris (**Fig. 4.27e**). The EDS analysis of pure Cu (ML) represents the presence of a high amount of oxygen (14.87 %) and iron content (18.27 %); whereas, C15Al (ML) wear debris composed of oxygen (18.17 %) and very low amount of Fe content (1.32%). The high amount of Fe content in pure copper wear debris can be attributed to the adhesive nature of wear after sliding against steel disc. Zhu et al. [149] reported the formation of coarse and flaky wear debris in nano Cu-Ag-W ternary alloy after sliding against stainless steel. At the same time, very fine wear debris was noticed for the same alloy in the thermal annealed condition. Adhesion and fatigue wear were attributed for coarse debris formation, adhesion and abrasion for the fine debris formation.

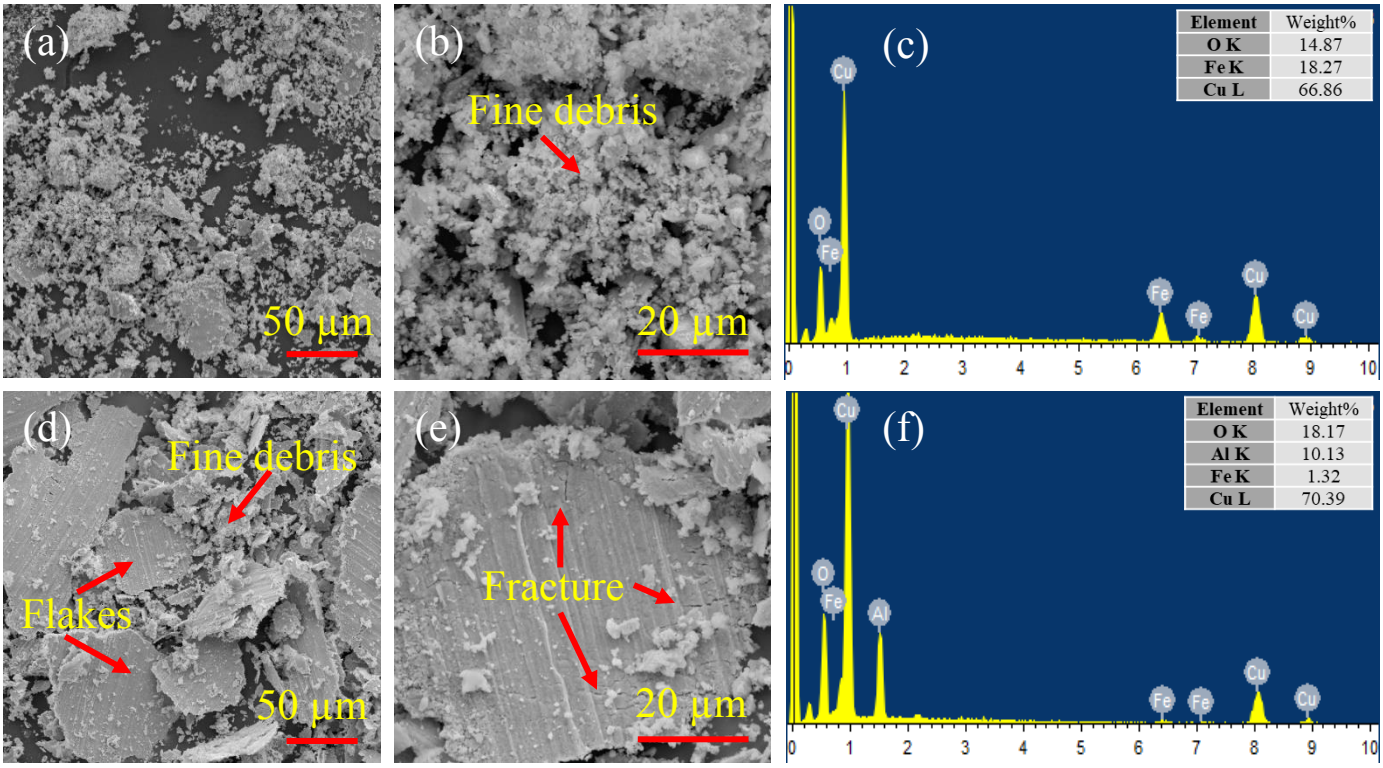

Fig. 4.27 SEM micrographs of collected wear debris after wear test for the pure copper and C15Al (ML) alloy after sliding against EN 31 steel disc at a load of 39.2 N, sliding velocity of 0.25 m/s and sliding distance of 2000 m. SEM of pure copper wear debris (a) low magnification, (b) high magnification and (c) EDS of pure copper wear debris. SEM of C15Al (ML) wear debris (d) low magnification, (e) high magnification of C15Al (ML) wear debris and (f) EDS of C15Al (ML) sample wear debris.

In summary, from the COF, wear measurements, microstructure and surface roughness measurements it is obvious that Al addition is very beneficial in improving the wear resistance of Cu. Particularly, the C15Al (ML) sample is exhibiting outstanding wear resistance because of its high hardness. These results clearly indicate the efficacy of the addition of a high amount of Al in improving the wear resistance of Cu (ML).

4.7 Corrosion behaviour

4.7.1 Open Circuit Potential (OCP)

The Open Circuit Potential (OCP) of Cu (ML) and C15Al (ML) alloy immersed in 3.5 % (w/v) NaCl solution was traced over 60 min. The potential (E_{oc}) was measured using VersaStudio software. The results of the OCP experiments are presented in **Fig. 4.28**. The OCP curve of Cu shows a negative shift at a steady-state potential about -120 mV, while C15Al (ML)

alloy has a negative shift with a steady-state potential of -355 mV. The E_{oc} of Cu and C15Al (ML) alloy was decreased immediately after immersing in NaCl solution. This indicates the breakdown of the oxide film and exposing the underlying surface.

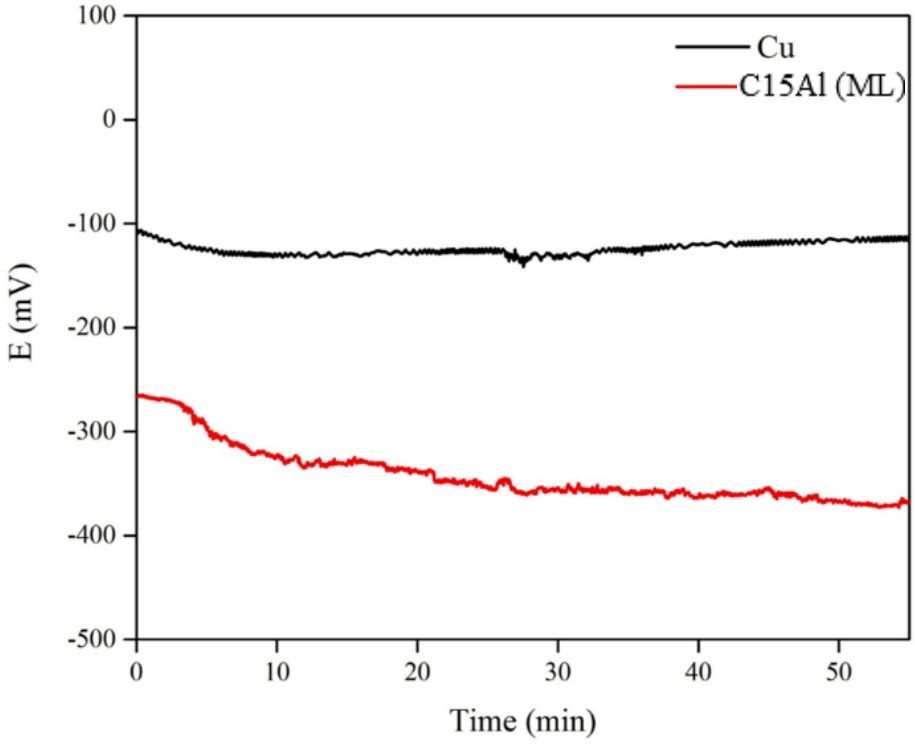

Fig. 4.28 Variation of open circuit potential (OCP) of hot-pressed Cu (ML) and C15Al (ML) alloy after immersion in stagnant 3.5 (m/v) % NaCl solution at 30 ^{o}C for 60 min.

The steady-state potential of both materials was reached within 10 min. and results in the gradual formation of passive oxide layers on the surface. Similarly, the OCP of Cu-8Al-2Fe alloy initially decreased sharply and then increased to the similar potential of pure copper after testing in 1 M NaCl (pH 6) for 60 min [197]. Formation of Al_2O_3 and $Cu_2O{\cdot}Al_2O_3{\cdot}xH_2O$ oxide layers on the surface of Cu-Al was attributed to the enhancement of corrosion resistance of Cu-Al alloy [59,212,219,269].

4.7.2 Polarization behaviour

Fig. 4.29 shows the polarization behaviour of Cu (ML) and C15Al (ML) alloy. It can be observed that the difference in negative potential is recorded with C15Al (ML) alloy as that of the Cu (ML) sample. The negative potential of the C15Al (ML) alloy (440.23 mV) is significantly higher than the negative potential of pure copper (237.78 mV). The similar

negative change was observed from the OCP measurements. This change in negative potential can be attributed to passive layer formation on the C15Al (ML) alloy.

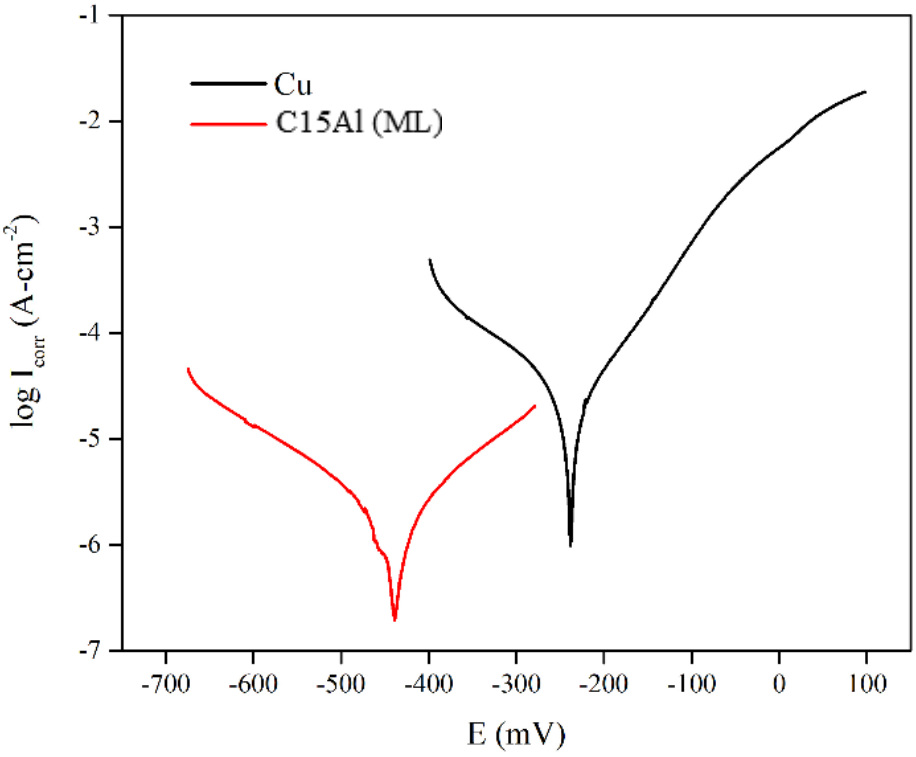

Fig. 4.29 Potentiodynamic polarization curves for hot-pressed Cu (ML) and C15Al (ML) alloy after immersion in stagnant 3.5 (m/v) % NaCl solution at 30 ^{o}C for 60 min.

Further, as the immersion time increases, the thickness of the passive layer increases. The measured values from potentiodynamic polarization experiments were tabulated in **Table 4.11.** The corrosion rates of Cu (ML) and C15Al (ML) alloy are calculated under the same conditions. From the Tafel plot with a best-fitting curve which is extrapolated through corrosion potential (E_{corr}) and corrosion current density (I_{corr}).

Table 4.11 Polarisation parameters and corrosion rate of Cu (ML) and C15Al (ML) alloy in 3.5 (m/v) % NaCl after 60 min. of electrode immersion at room temperature.

Sample reference	I_{corr} (µA-Cm^{-2})	E_{corr} (mV)	$\beta_{Cathodic}$ (mV. dec^{-1})	β_{Anodic} (mV. dec^{-1})	**Corrosion rate (mpy)**
Cu (ML)	33.59	-237.75	176.53	118.46	20.70
C15Al (ML)	2.90	-440.22	234.52	200.15	1.65

* I_{corr}: Corrosion current density E_{corr}: Corrosion potential $\beta_{(Cathodic)}$: Cathodic Tafel slope $\beta_{(Anodic)}$: Anodic Tafel slope

The corrosion rate was calculated using the **Eq. (4.8)**. Where, *Ew*: equivalent weight in grams, ρ: density in g/cc and *A*: exposed area.

$$Corrosionrate = \frac{0.13 \times I_{corr} \times Ew}{A \times d} \quad (4.8)$$

From **Table 4.11**, it can be observed that the corrosion rate of C15Al (ML) alloy significantly lowered upto 12.5 times compared to Cu (ML). The corrosion rate of Cu (ML) and C15Al (ML) alloy was measured to be 20.7 mpy and 1.6 mpy, respectively. This remarkable decrease in corrosion rate is due to the formation of Al_2O_3 passive layer on the surface of the Cu alloy.

4.7.3 Electrochemical Impedance Spectroscopy (EIS) and corrosion mechanisms

To confirm the presence of oxide passive layer on the sample surface after the electrochemical test, the EIS data analysis was carried out. The EIS data were generated using VersaStudio software (2.42.3 version). Further, the data was imported to ZSimpWin software (3.21 version) and the analysis was executed with several different circuit models and the best fit was considered for the equivalent circuit model that provided minimum chi-square value.

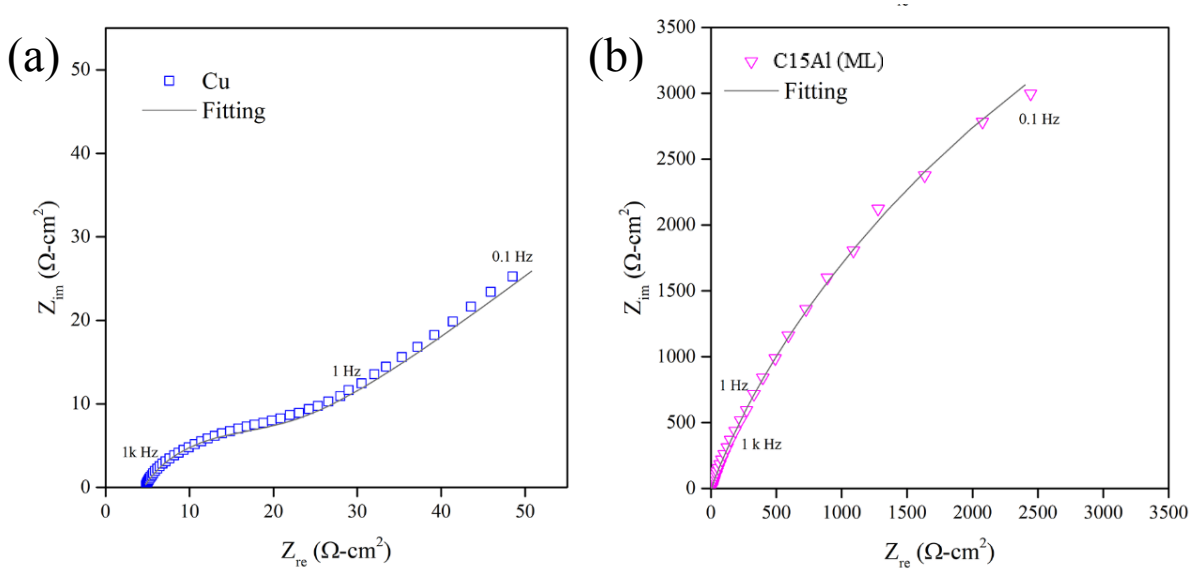

Fig. 4.30 Nyquist impedance plots of (a) hot-pressed Cu (ML) and (b) C15Al (ML) alloy after 60 min. immersion in stagnant 3.5 (m/v) % NaCl solution at 30 ^{o}C.

The impedance (*Z*) spectra of the samples were fitted to propose an equivalent circuit. The Nyquist impedance plot along with the equivalent circuit model used for impedance data

fitting of Cu (ML) and C15Al (ML) alloy is shown in **Figs. 4.30 and 4.31**, respectively. From **Fig. 4.30a**, it can be derived that the Nyquist impedance curve of Cu (ML) is fitted with R(Q((R(Q(RW)))). The same type of equivalent circuit model has been proposed by various researchers [212,213,270]. It represents two time-constant having Warburg impedance circuit model with a chi-square value of 5.5×10^{-4}, which consists of electrolyte resistance (R_s), film resistance (R_f), charge transfer resistance (R_{ct}), constant phase elements (Q_1, Q_2) that replace the capacitance of electrochemical double layer and W: Warburg impedance.

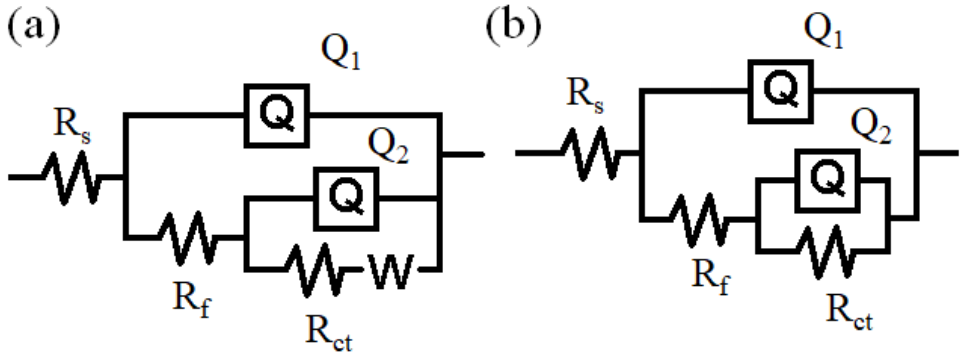

Fig. 4.31 Equivalent circuit models used for impedance data fitting of (a) Cu (ML) and (b) C15Al (ML). where, R_s: Electrolyte resistance, R_f: Film resistance R_{ct}: Charge transfer resistance *and* Q_1, Q_2: Constant phase elements (CPEs), W: Warburg impedance.

The Nyquist plot of Cu (ML) shows the one capacitive semicircle, which indicates the dissolution of samples through a single path. Also, a Warburg impedance characteristic curve is observed in the low-frequency region of the curve. The impedance characteristics of pure copper are similar to the work reported by Chen et al. [270] The capacitive semicircle at high-frequency region indicates the fast charge process due to the dissolution of Cu in NaCl solution. Warburg region indicates the diffusion of Cl^- ion spices into Cu. The semi-infinite medium or electrolyte is NaCl. In pure copper, the electroactive species are Cu, Cl. In the case of C15Al (ML), the electroactive species are Cu, Al and Cl. The diffusion coefficient can be calculated from the following **Eq. 4.9** [271]**.**

$$W = \frac{RT}{\sqrt{2} \times n^2 F^2 A}\left(\frac{1}{C\sqrt{D}}\right) \qquad (4.9)$$

Where,

W: Warburg coefficient, $\Omega m^2/\sqrt{s}$

R: Gas constant, J/K. mol

T: Temperature, K

n: No. of electrons transferred,

F: Faraday's constant, C/mol

A: Area of the electrode, m^2

C: concentration of species, mol/m^3

D: Diffusion coefficient of species, m^2/s

Using the above equation, the diffusion coefficient of Cl (8.08×10^{-12} m^2/s) could be calculated. However, the diffusion coefficient of Cu and Al could not be determined due to the constraint to estimate its concentration with the experimental setup.

The Nyquist impedance curve of C15Al (ML) alloy is fitted with R(Q(R(QR))), two time-constant circuit model with the chi-square value of 4.9×10^{-3} (see **Fig. 4.31b**); which consists of electrolyte resistance (R_s), film resistance (R_f), charge transfer resistance (R_{ct}), and constant phase elements (Q_1, Q_2). The Nyquist curve for C15Al (ML) alloy represents the one capacitive loop and the diameter of the loop is high when compared with Cu (ML). The bigger capacitive loop diameter indicates the low current density i.e high resistance to corrosion. The observation of higher impedance values (R_f: 1209 Ω-cm^2 and R_{ct}: 1886 Ω-cm^2) of the Nyquist plot indicates the formation of a thick protective oxide layer on sample surface which drastically decreases the corrosion rate of C15Al (ML) alloy than pure copper (**Table 4.11**). The EIS results for Cu (ML) and C15Al (ML) alloy after 60 min. of immersion in 3.5 % NaCl solution is presented in **Table 4.13**. From the EIS results, it can be observed that the film resistance (R_f) of the Cu (ML) increased from 16.1 to 1209 Ω-cm^2, while charge transfer resistance (R_{ct}) increased from 775 to 1886 Ω-cm^2 with the addition of Al.

Table 4.12 Equivalent circuit parameters for Cu (ML) and C15Al (ML) alloy after 60 min. of immersion in stagnant naturally aerated in 3.5 (m/v) % NaCl solution.

				Q₁		***Q₁***		***W***
Sample reference	***Rs* (Ω-cm^2)**	***Rf* (Ω-cm^2)**	***Rct* (Ω-cm^2)**	***CPE* (×10^{-3} S-sec^n cm^{-2})**	***n***	***CPE* (×10^{-3} S-sec^n cm^{-2})**	***n***	**(×10^{-3} S-sec^0.5 cm^{-2})**
Cu (ML)	4.59	16.1	775	1.58	0.67	28.29	0.41	0.70
C15Al (ML)	6.66	1209	1886	0.40	0.87	0.21	1.00	--

R_s: Electrolyte resistance, R_f: Electrolyte resistance R_{ct}: Charge transfer resistance and Q_1, Q_1: Constant phase elements (CPEs), *W*: Warburg impedance.

At the same time, the constant phase element (Q_1) of the Cu (ML) sample is decreased from 1.58 to 0.4 $\times 10^{-3}$ S-sec^n cm^{-2} and Q_2 are decreased from 28.29 to 0.21 $\times 10^{-3}$ S-sec^n cm^{-2}. The increase of R_f value denotes the formation of a thick protective layer on the C15Al (ML) alloy. This protective layer reduces the further reaction of chloride ions with the sample surface. The corrosion resistance of C15Al (ML) is enhanced by forming the Al_2O_3 protective layer and incorporation of Al ions into Cu_2O layer.

4.7.4 Corrosion surface analysis

Fig. 4.32 (a-c) presents SEM-EDS of the surface morphology of the Cu (ML) sample after immersion in 3.5 (m/v) % NaCl solution for 60 min. The occurrence of localized corrosion on Cu (ML) sample can be observed in **Fig. 4.32a**. From the high magnification SEM images, it is clear that corrosion of pure copper takes place mainly due to pitting and intergranular type of corrosion (**Fig. 4.32b**). From EDS analysis, it is evident that the presence of oxygen (O) and chlorine (Cl) on the Cu surface after immersion in NaCl solution. The quantification of these elements is shown in **Fig. 4.32c**.

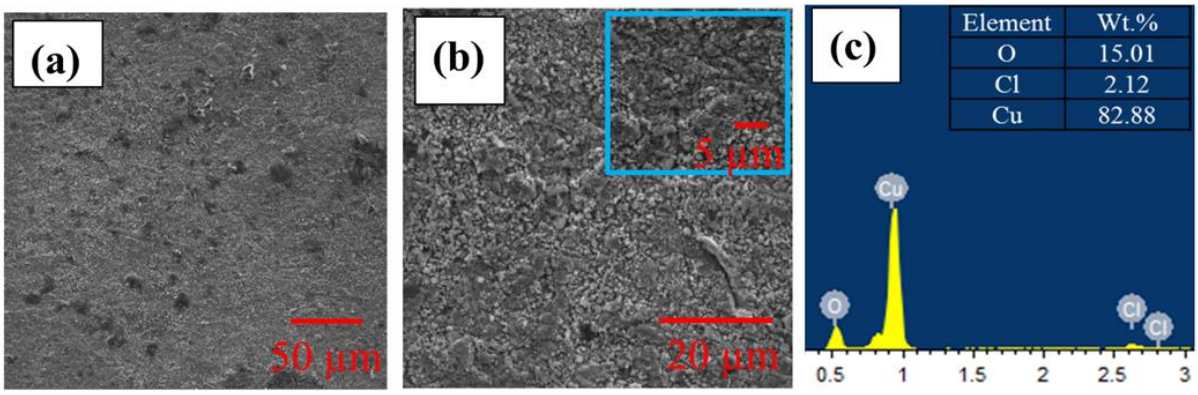

Fig. 4.32 The microstructure (SEM) of (a) pure copper (ML) sample after 60 min. immersion in 3.5 (m/v) % NaCl solution, (b) the corresponding magnified image and (c) elemental distribution spectrum taken from EDS.

The presence of a higher amount of Cl (2.12 wt.%) indicates the higher corrosion rate of Cu (ML) sample. The pure copper sample is highly corroded in NaCl and the Cu_2O is expected to form on the surface. The Cu_2O film breaks and dissolves into the NaCl solution with the time and a fresh surface is exposed to the corrosive environment. Also, the diffusion parameter (n) value of Cu from the equivalent circuit is less than 0.5 indicating that the reaction is highly inhomogeneous (see **Table 4.13**). The possible reactions (**Eq. 4.10-4.11**) for the formation of corrosion products ($CuCl_2$ and Cu_2O) on pure copper are as the following:

$$Cu + 2Cl^{-} \rightarrow CuCl_2^{-} + 1e^{-} \quad (4.10)$$

$$2CuCl_2 + H_2O \rightarrow Cu_2O + 4C^{-} + 2H^{+} \quad (4.11)$$

$CuCl_2^-$ complex formation developed either due to the dissolution of copper or CuCl [269]. In fact, it was proposed that cuprous chloride (CuCl) as the initial corrosion product when Cu reacts with NaCl. The stability of Cu_2O depends on the chloride ions concentration and it has an inverse relation.

From **Fig. 4.33**, the microstructure of corrosion tested C15Al (ML) alloy can be observed. The corrosion site at point 1 in **Fig. 4.33b** shows the mild corrosion area which is of 'α' solid solution phase, while at point 2 ('γ' intermetallic phase) selective regions are prone more corrosion. It happened due to the formation of the local cell between two phases. No preferential dissolution was observed in α solid solution phase as it acted as an electron source region/cathode, while the anodic oxidation of γ intermetallic phase results in the higher dissolution of material in chloride media. Also, the high magnification SEM images clearly reveal pitting and intergranular type of corrosion at different regions of the γ phase. Nevertheless, it has to be noted that as mentioned above the corrosion rate of C15Al (ML) is significantly lower than Cu (ML). The SEM-EDS of the alloy at different regions reveals the presence of a high amount of oxygen (21.06 to 30.33 wt.%) and low amount of chlorine (0.27 – 0.41 wt.%) along with base Cu and Al elements. The oxygen content is relatively high and chlorine significantly low for Cu-Al (milled) alloy when compared to pure copper (compare **Fig. 4.32 and 4.33**).

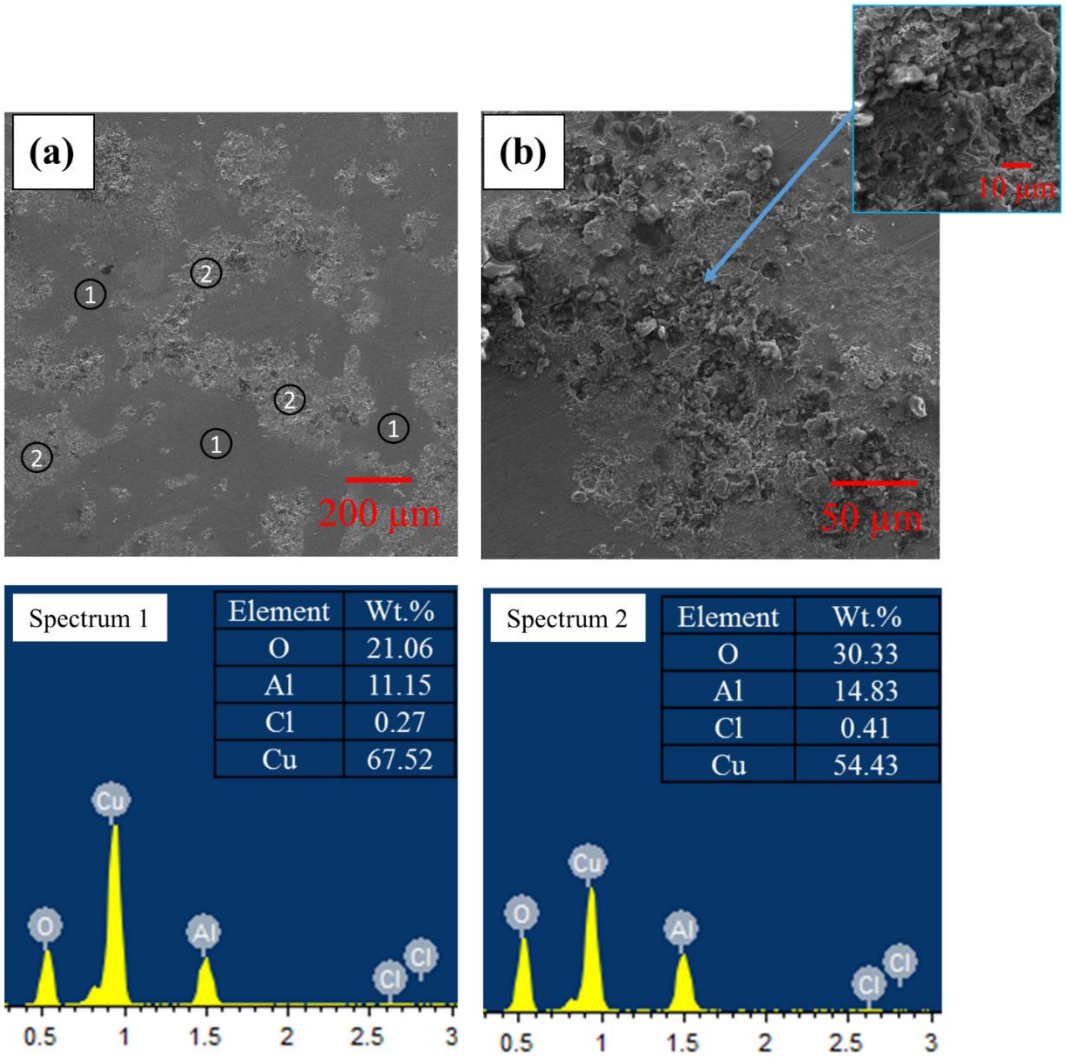

Fig. 4.33 The microstructure (SEM) of (a) C15Al (ML) after 60 min. immersion in 3.5 (m/v) % NaCl solution, (b) the corresponding magnified image and elemental distribution measured from two regions by EDS.

By comparing EDS of α and γ phases of C15Al (ML) before and after corrosion, it can be realized that the Al content increased and Cu reduced significantly along with a large amount of oxygen for α and γ phases of corrosion tested samples (**Fig. 4.33**). From this, it can be understood that the stable oxide layer is forming at α phases and the stability of the layer is poor, which forms at the γ phase. Dealuminization should have taken place near γ phase regions. The corrosion surface of C15Al (ML) alloy might be composed of different products (Cu_2O, $CuCl_2$, Al_2O_3, $AlCl_4$ etc.). The formation of Cu_2O and $CuCl_2$ and its characteristics are explained for corrosion of pure Cu (ML). Al reacts with Cl^- ions and forms $AlCl_4$ as per **Eq. 4.12**. Since the chlorides are thermodynamically unstable in the presence of oxygen and these chlorides react with water and forms Al_2O_3 oxide layer according to **Eq. 4.13**, which protects the sample surface.

$$Al + 4Cl^- \rightarrow AlCl_4^- + 3e^- \quad (4.12)$$

$$AlCl_4^- + 3H_2O \rightarrow Al_2O_3 + 6H^+ + 8Cl^- \quad (4.13)$$

Saud et al. proposed that hydrolysis of Al_2O_3 causes local acidity and acceleration of dealuminification, which ultimately leads to thinning of barrier film or its breakdown at some locations [206]. This work clearly shows the efficacy of the use of a high amount of Al in improving the corrosion resistance of Cu.

4.8 Electrical conductivity

Fig. 4.34 presents the effect of Al content on the electrical conductivity of Cu-Al (milled) alloys processed at 500 ºC, 500 MPa for 30 min. The electrical conductivity of Cu-Al (milled) alloys varied in the range between 12.3 - 75.7% IACS. The total resistivity (1/conductivity) of a material influenced by the several factors such as dislocations, grain boundary interface, phonon and impurities [194]. The total resistivity of the material is given by the **Eq. (4.14)**. Where $\rho_{dislocations}$ is caused due to the presence of dislocations, $\rho_{interface}$ is a contribution from the grain boundaries and reinforcement and matrix interface, ρ_{phonon} is caused due to the phonon scattering and $\rho_{impurities}$ is contributed from the foreign contamination.

$$\rho_{Total} = \rho_{dislocations} + \rho_{interface} + \rho_{phonon} + \rho_{impurities} \quad (4.14)$$

The high electrical conductivity of 75.7% IACS was noted for Cu (ML) and it is relatively less than the theoretically expected values. On the other hand, the electrical conductivity of Cu-Al (milled) alloys found to decrease with the addition of Al due to the finer grain microstructure, increase of solid solutions and intermetallic phases. Also, it is evident that the electrical conductivity of hot-pressed alloys directly varies with the function of relative density. Since the relative density of Cu-Al (milled) alloys decreased with the addition of Al, the electrical conductivity also might be reduced. As the porosity acts as the electrical insulating sites in the conducting path of electrons, the conductivity decreases with the porosity.

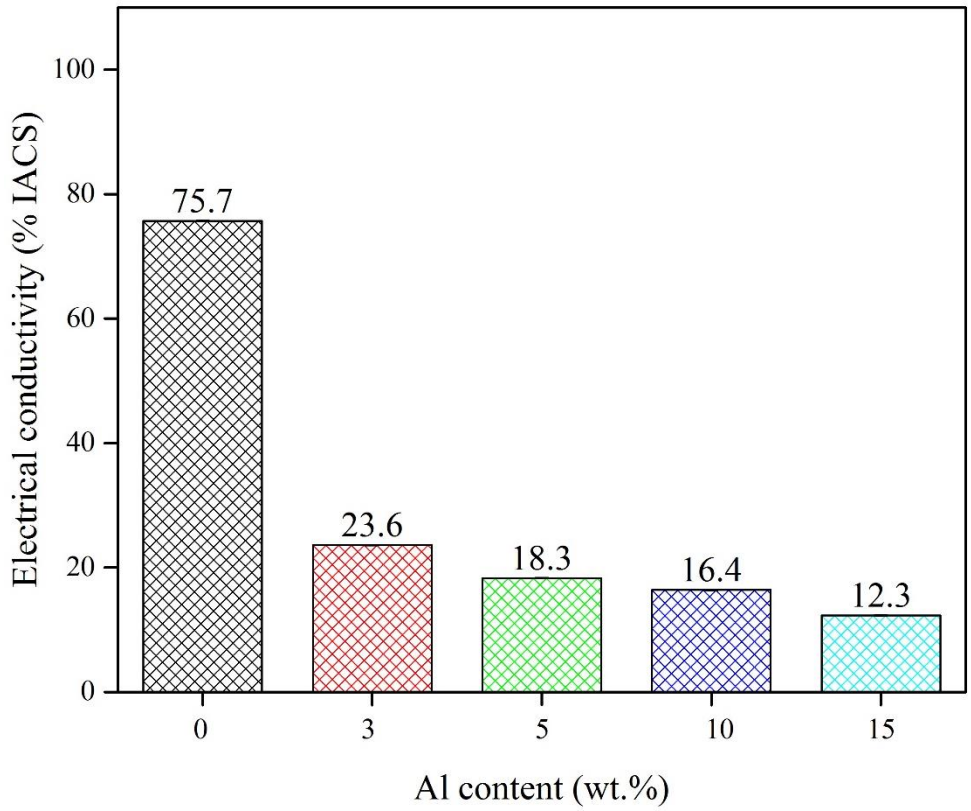

Fig. 4.34 Effect of Al content on electrical properties on Cu-Al (milled) alloys.

A drastic reduction in the electrical conductivity with the addition of Al to Cu was evident for Cu-Al (milled) alloys. The electrical conductivity of C3Al (ML) and C5Al (ML) was found to be 23.6% IACS and 18.3% IACS, respectively due to the presence of solid solution phases. In solid solution, the similar lattice structure of two different metals forms a new distorted structure; where the electrons scatter between the atoms. Further addition of Al (upto 15 wt.%) reduced the electrical conductivity to 16.4% IACS and 12.3% IACS for C10Al (ML) and C15Al (ML) alloys, respectively and is because of the presence of intermetallic compound phase presence besides the solid solution phase. The intermetallic compounds exhibit more scattering of electrons between different atomic lattice structures. These results indicate that Al addition and milling operations adversely affecting the electrical conductivity of Cu.

Chapter 5

Densification, mechanical, wear and electrical properties of Cu-Al alloys processed via mixing route

5 Chapter 5

This chapter explains about the Cu-Al alloys processed via hot-pressing (mixing route). The Cu-Al alloy powder compositions were mixed to achieve uniform mixing of powders without much concerned about the reduction of its particle size. The microstructural phase evolution in Cu-Al (mixed) alloys after hot-pressing have been characterized by optical microscopy, SEM-EDS and XRD analysis. Also, the hardness and compressive strength of the Cu-Al (mixed) alloys were measured. The abrasive wear behaviour of Cu-Al (mixed) alloys was studied against SiC (abrasive) emery paper. Further, SEM analysis of worn surfaces, wear debris and counter body materials was carried out to determine the underlying wear mechanisms. Also, the electrical conductivity of Cu-Al (mixed) alloys was determined to predict the suitable applications for the same materials.

5.1 Morphology and phase analysis of Cu-Al (mixed) powders

In case of mixing Cu-Al powder compositions, the starting elemental powders were mixed uniformly using a planetary ball mill at a low speed of 100 rpm (BPR ~ 2:1) for 1 h. The morphology of raw Cu, Al powder particles and the mixture of Cu-Al (mixed) powders are shown in **Fig. 5.1**. From **Fig. 5.1(a-b)**, it can be observed that the Cu and Al powders are spherical and semi-spherical/rod-like form, respectively. After ball milling at low speed (mixing), the morphology of the Cu-Al (mixed) powders did not change much and the Al powder particles were uniformly mixed in the Cu powders (see **Fig. 5.1c and Fig. 5.1d**).

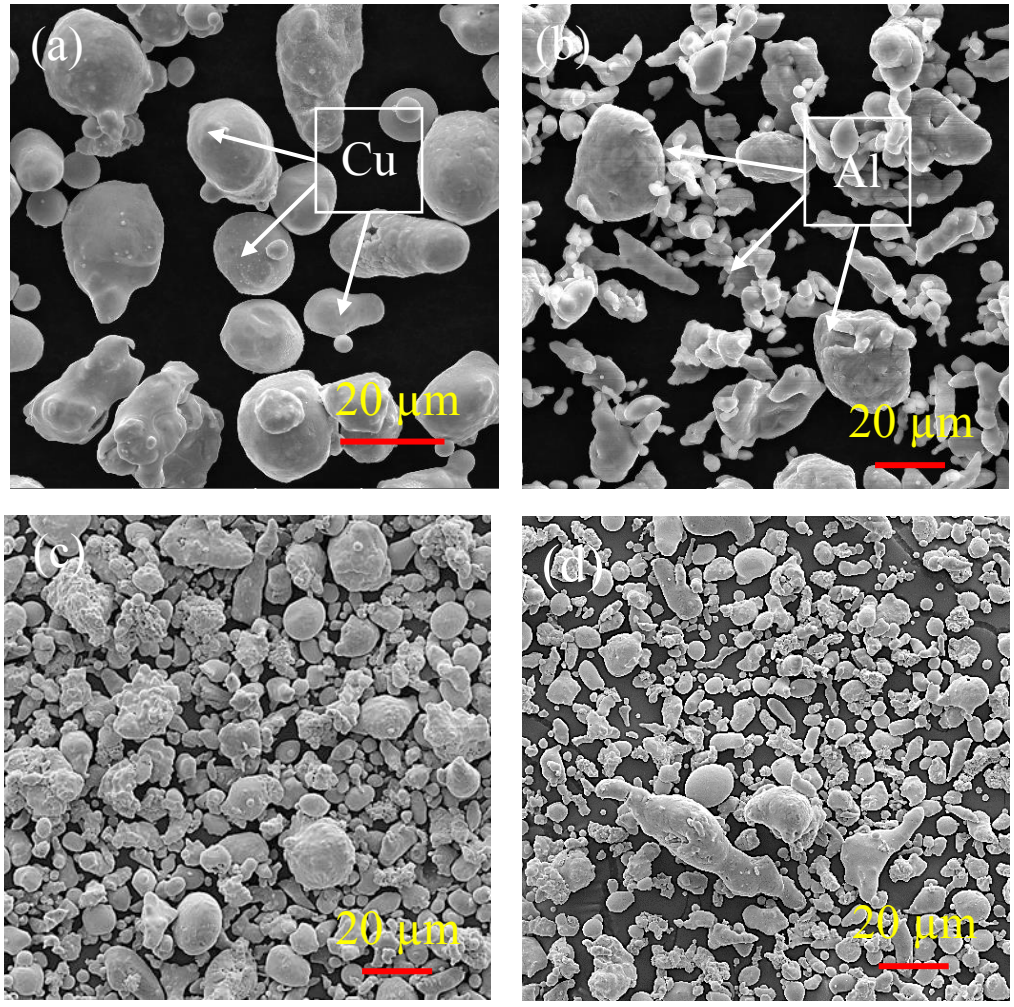

Fig. 5.1 SEM images mixed powders after 1 h ball milling at 2:1 BPR (a) Cu, (b) Al, (c) C5Al (MX) and (d) C15Al (MX).

The morphology of the powder particles affects the densification of compacts in powder metallurgy process [272,273]. Miyake et al. [272] reported that the relative density of Al_2O_3 sintered compacts was effected by the shape of powder particles. The sphere and rod-shaped

particles were achieved the relative density upto ~98% and ~94%, respectively at 1600 ^{o}C. Whereas the disc-shaped particles could be densified to ~64% only due to low surface contact area. Also, Ekpy et al. [273] explained the effect of powder particle hardness on densification behaviour of cold isostatically pressed powders. They reported that the 99% densification was achieved with the soft aluminium powders and the relative density reduced (92%) with the use of moderate hard iron powders. Further reduction in relative density (70%) was observed with the use of highly hard alumina powders.

The XRD of Cu-Al (mixed) powders was presented in **Fig. 5.2**. The XRD patterns reveal that the Cu and Al peaks remain unchanged and no new phases were observed after mixing operation. No much change in the peak intensity of Cu was observed and the intensity of Al peaks increased as the Al content increased. From these observations, it can be realized that there is no chemical interaction or diffusion between Al and Cu atoms occurred in mixing operation (100 rpm and BPR: 2:1). Unlike the severe ball milling of Cu-Al (milled) powders (compare **Fig. 4.2**); where the solid solution phases were developed due to the cold welding and micro-fracture of powder particles.

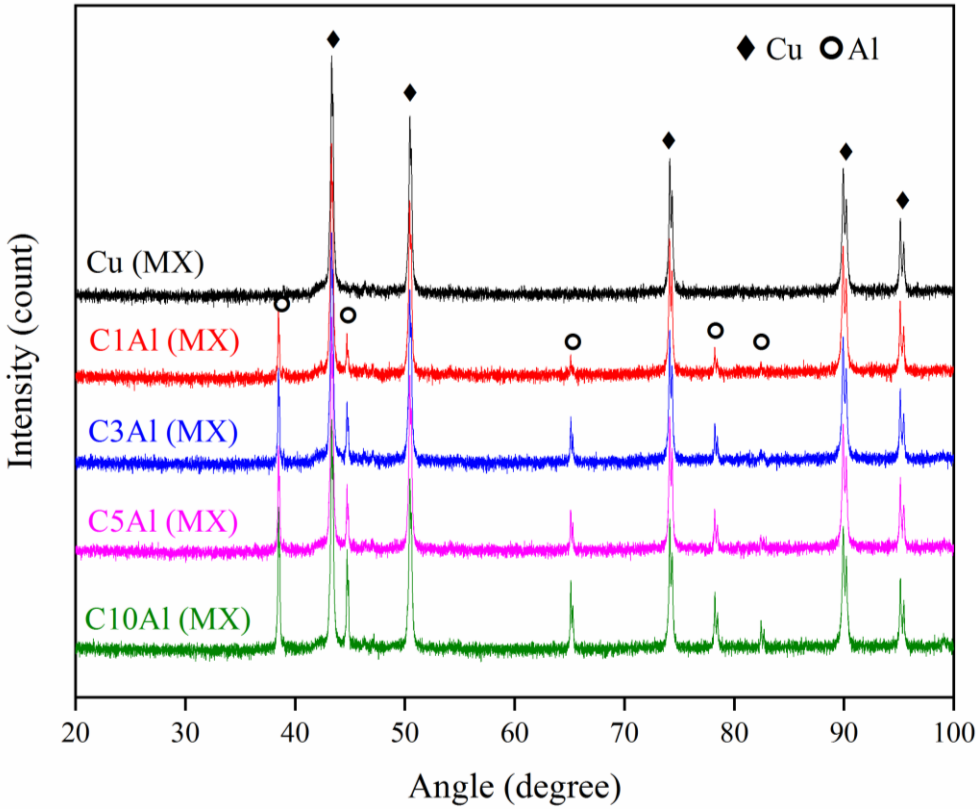

Fig. 5.2 XRD of mixed powders after ball milling at 100 rpm for 1 h with BPR (2:1).

5.2 Phase analysis of hot-pressed Cu-Al (mixed) alloys

The mixing of Cu and Al powders at low speed has no significant influence on the phase evolution of powder compositions. Nevertheless, various new phases such as Cu, α-Cu, γ_1 (Cu_9Al_4), δ (Cu_3Al_2), ζ_1 (Cu_4Al_3), η_2 (CuAl) and θ ($CuAl_2$) were formed in the Cu-Al (mixed) alloys after hot pressing at 500 °C, 500 MPa for 30 min. These phases are similar (as indicated by point 1-4) to the phases in equilibrium phase diagram as shown in **Fig. 5.3**. X-ray diffraction patterns of hot-pressed Cu-(X wt.%) Al (mixed) alloys are shown in **Fig. 5.4**. It can be realized that the XRD phases of Cu-Al (mixed) alloys are different from Cu-Al (milled) samples (compare **Fig. 4.3 and Fig. 5.4**).

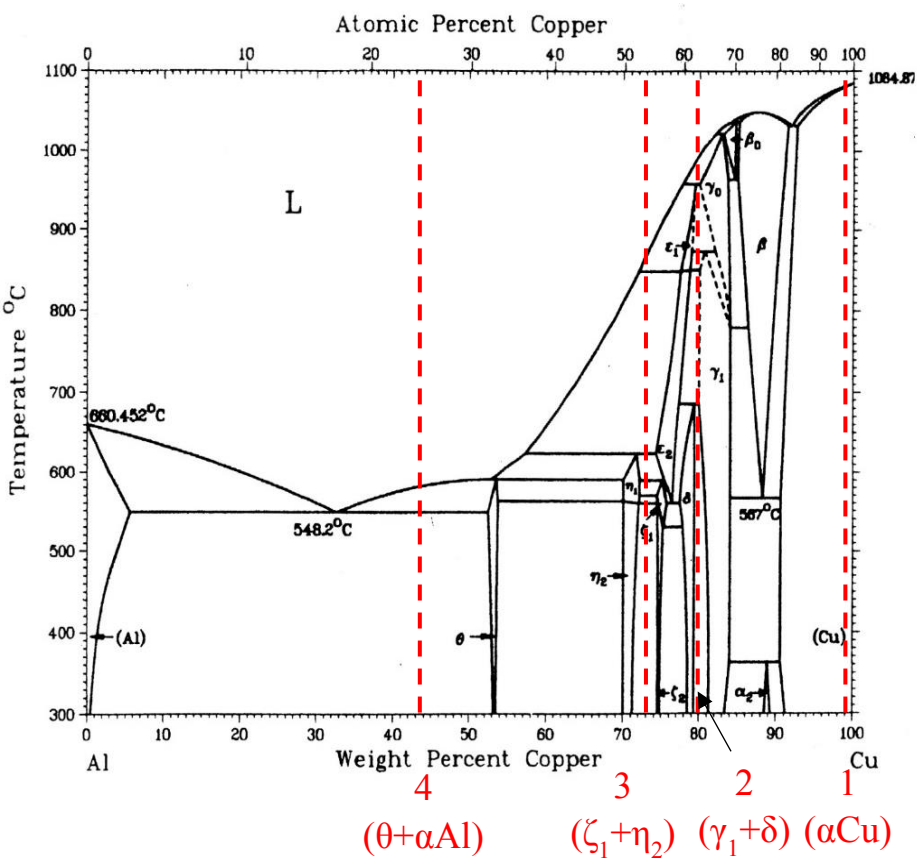

Fig. 5.3 Equilibrium phase diagram of Cu-Al alloy

A similar work by Guo et al. [96] reported the solid-state reaction sequence between Cu and Al as Cu + Al → $CuAl_2$ + Cu → Cu_9Al_4 + Cu + Cu(Al). In another work, Lee et al. [85] investigated the Cu-Al samples prepared using a vacuum hot pressing method and their work revealed the formation of various compounds at the interface between Cu and Al such as $CuAl_2$,

$CuAl$, Cu_4Al_3 and Cu_9Al_4. Similarly, Divandari et al. [274] reported that different compounds such as $CuAl_2$, CuAl and Cu_3Al_2 were formed at the interface of Cu and Al in the cast samples.

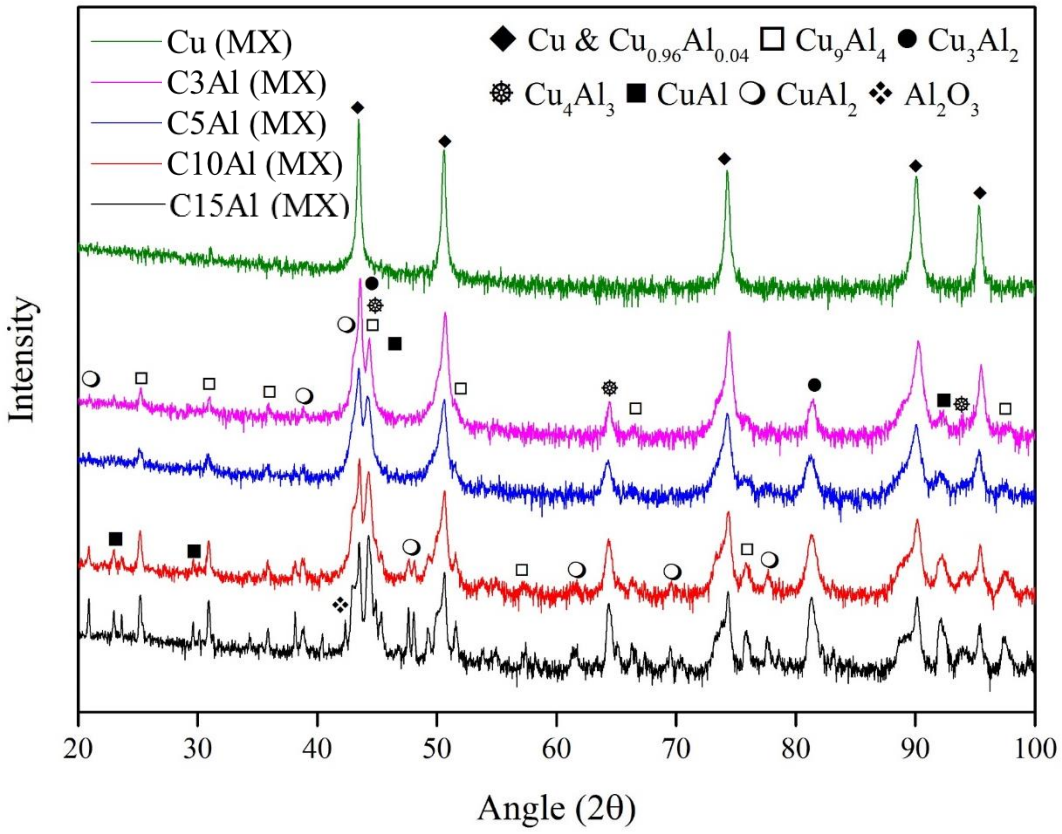

Fig. 5.4 Comparison of X-Ray diffraction patterns of hot-pressed Cu-Al (mixed) alloys (at 500 ^oC, 500 MPa, 30 min.).

5.3 Densification of Cu-Al (mixed) alloys

The relative density (RD) is calculated using the rule of a mixture of different phases identified in the XRD analysis. The densities of γ_1 (Cu_9Al_4), δ (Cu_3Al_2), ζ_1 (Cu_4Al_3), η_2 (CuAl) and θ ($CuAl_2$) phases are considered for calculating the theoretical density. The effect of Al content on density and relative density of Cu-Al (mixed) alloys is presented in **Fig. 5.5.** The density of Cu-Al (mixed) alloys decreased by adding Al content. The density of Cu (MX) is measured to be 8.71 g/cc with a relative density of 99.76 %. In case of C3Al (MX) to C15Al (MX) alloys, the density decreased from 8.26 to 6.75 g/cc and the relative density decreased slightly from 95.26 to 95.01%. A little variation in relative density was observed in Cu-Al (mixed) samples with the addition of Al (from 3 to 15 wt.%). The density and relative density of C15Al (MX) was reduced by 24.4% and 4.75%, respectively in comparison to pure Cu sample. The relative density of pure Cu (milled) was observed to be 98.6%, while the Cu (MX)

samples were prepared with full densification (RD: 99.76%). This slight decrease of RD in milled Cu (ML) samples was due to hard agglomeration and oxide impurities presence during the milling process. Whereas, the Cu-Al alloys processed via milling and mixing routes had almost similar relative densities (~95%) because of the presence of the intermetallic compound in both the samples.

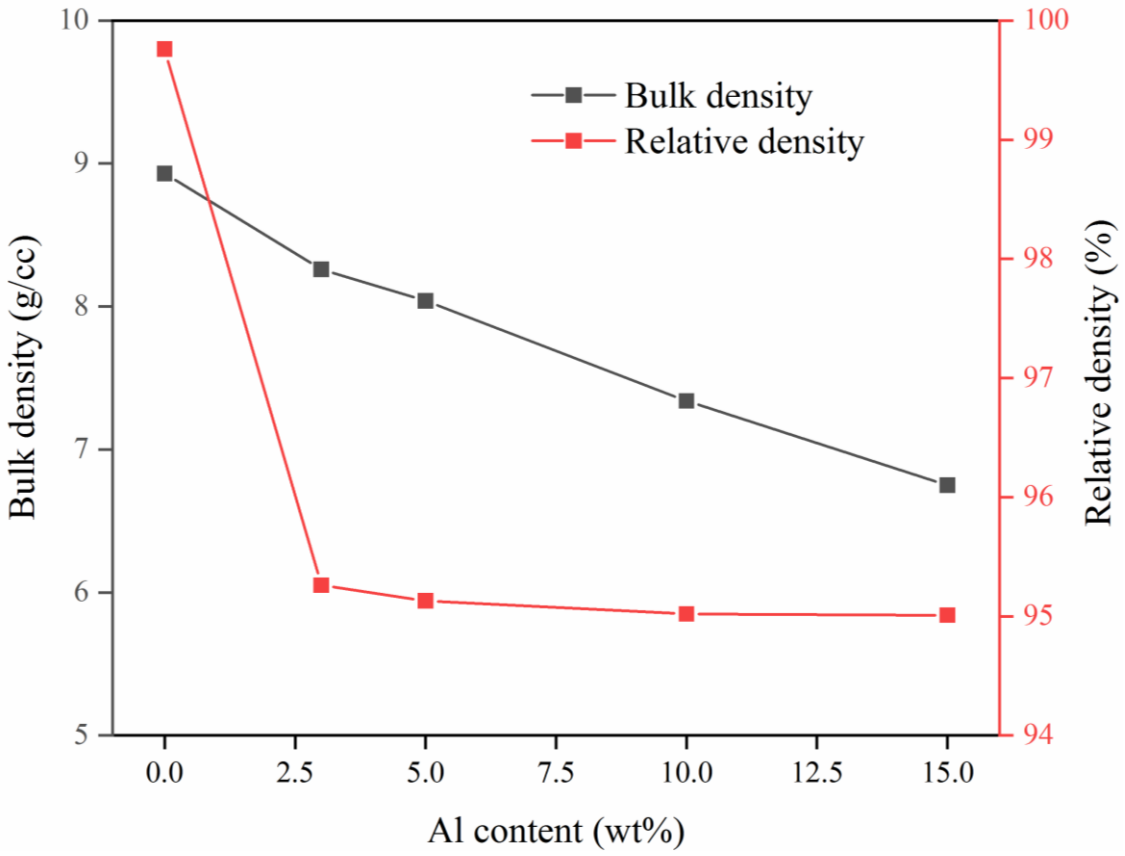

Fig. 5.5 Effect of Al content on the density of Cu-Al (mixed) alloys.

The experimental density and relative density values of Cu-Al (mixed) alloys are given in **Table 5.1**. Various studies on Cu-based alloys revealed that the relative density of Cu- (40-50) Ni hot-pressed samples processed at 300 ^{o}C, 900 MPa for 5 h is 78% [275]. The hot pressed Cu-25Sn compacts reported with the relative density ranging from 88.4 – 90.7 % which were prepared at 421 – 600 ^{o}C, 104 – 201 MPa for 4 min [58]. Cu-50Ni, Cu-50Zr and Cu-10Ni-40Zr alloys processed by hot pressing having the relative density of 78%, 74% and 72%, respectively [65]. From this, it can be realised that the use of optimal hot-pressing parameters (500 ^{o}C, 500 MPa and 30 min.) in the present study resulted in better densification of Cu-Al (mixed) compacts.

Table 5.1 The bulk density, theoretical density and relative density of the Cu-Al (mixed) alloys.

Sample reference	Al content (wt.%)	Bulk density (g/cc)	Theoretical density (g/cc)	Relative density (%)
Cu (MX)	0	8.93	8.96	99.76
C3Al (MX)	3	8.26	8.67	95.26
C5Al (MX)	5	8.04	8.45	95.13
C10Al (MX)	10	7.34	7.73	95.02
C15Al (MX)	15	6.75	7.10	95.01

5.4 Microstructure of hot-pressed Cu-Al (mixed) alloys

Fig. 5.6 shows the optical microscopy images of Cu-Al (mixed) alloys. From the colour contrast, it can be observed that the presence of core-shell structures in all Cu-Al (mixed) alloys (Al: 3-15 wt.%). The dark colour phase is surrounded by the bright colour phase; similarly, these two phases were surrounded by the brown colour phase.

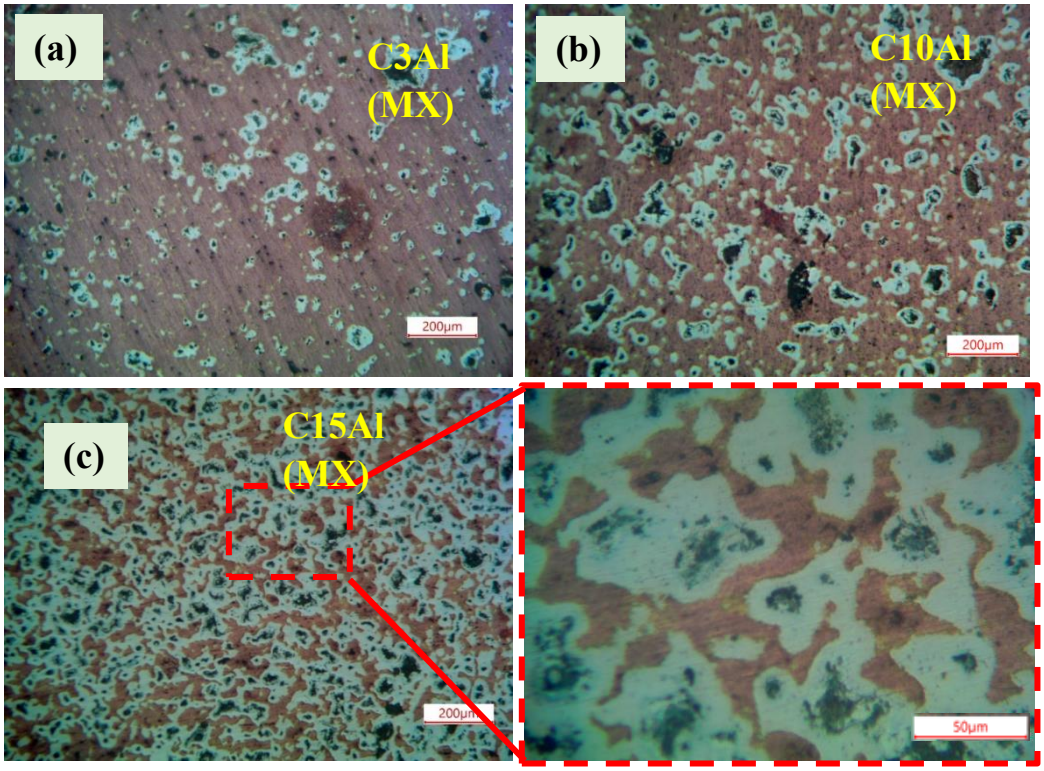

Fig. 5.6 Optical microscopy images of Cu-Al (mixed) alloys. (a) C3Al (MX), (b) C10Al (MX) and (c) C15Al (MX) alloys

The interconnecting brown phase is observed in the C3Al (MX), C5Al (MX) and C10Al (MX) alloys. Whereas the brown interconnecting phase reduced as the Al content increase to 15 wt %. In the case of C15Al (MX) alloy, the interconnectivity of the brown phase is discontinuous and the bright phase is the interconnecting phase. The similar kind of phase distribution was also observed from SEM microstructures (see **Fig. 5.7**).

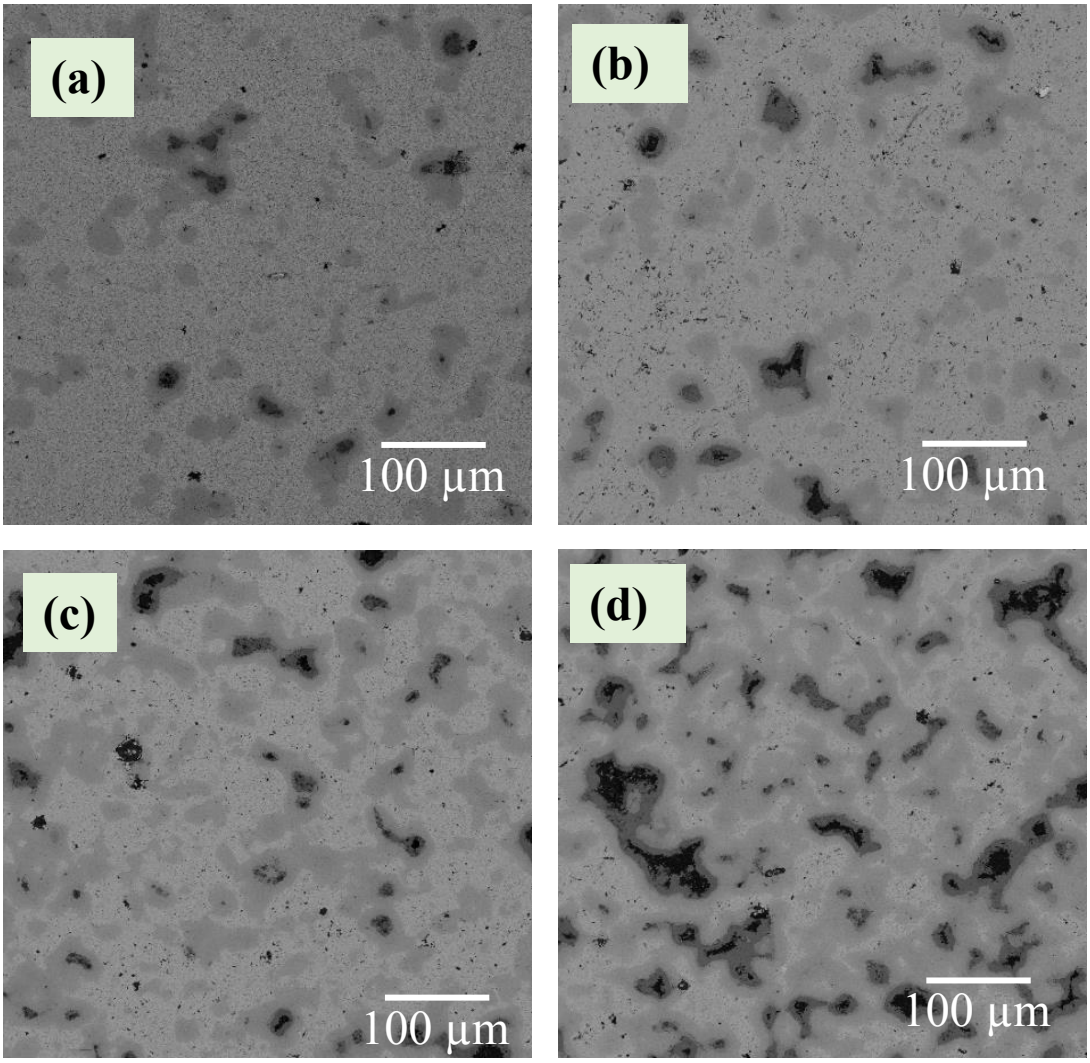

Fig. 5.7 SEM images of hot-pressed Cu-Al (mixed) alloys. (a) C3Al (MX) (b) C5Al (MX) (c) C10Al (MX) (d) C15Al (MX).

The increase in grey and dark phases can be observed as the Al amount increased in Cu. From **Fig. 5.7,** it is evident that the grey and dark phases are increasing with thinning of bright phase from C3Al (MX) to C15Al (MX) alloys. **Fig. 5.8** represents the high magnification SEM images of core-shell structure of Cu-Al alloys along with corresponding EDS spectrums. The EDS analysis reveals the core-shell structure is having different intermetallic phases as was indicated by XRD.

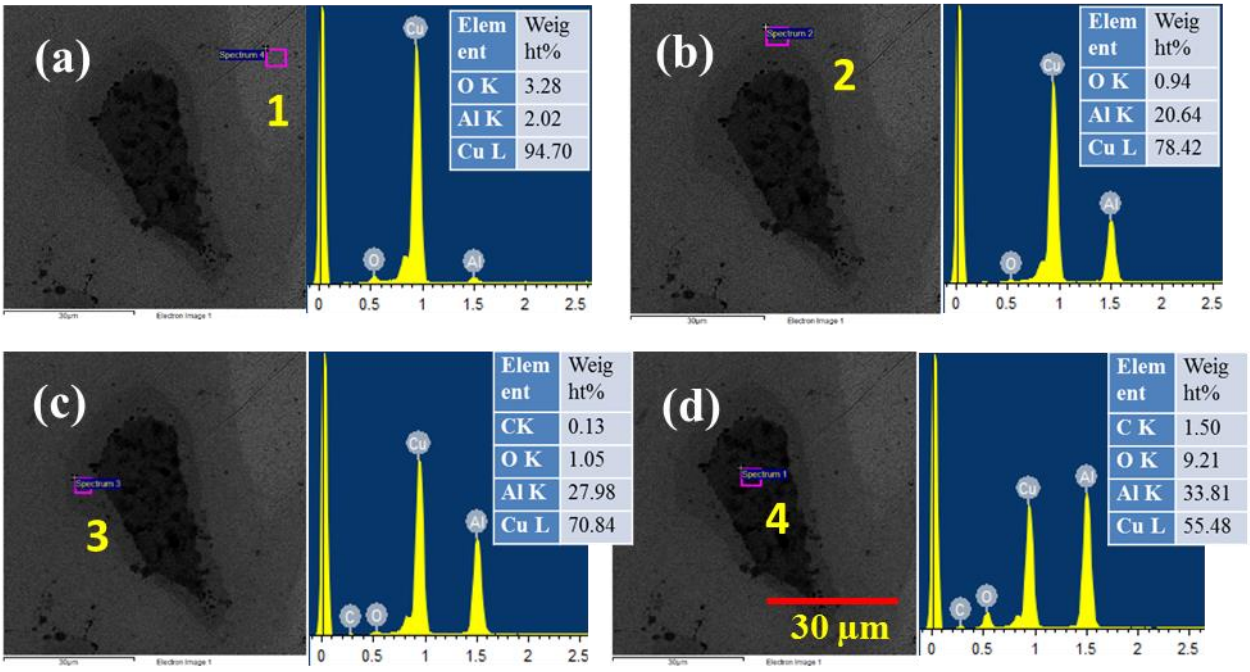

Fig. 5.8 (a-d) Core-shell microstructure in Cu-Al (mixed) alloys; Corresponding EDS spectrums.

From the EDS analysis, the region at point 1 (bright contrast) is identified as α-Cu solid solution phase, point 2 (light grey) is having γ_1 (Cu_9Al_4) + δ (Cu_3Al_2) phases, point 3 (dark grey) is having ζ_1 (Cu_4Al_3) + η_2 (CuAl) phases and point 4 (dark contrast) is having θ ($CuAl_2$) + α-Cu solid solution phases. The identified phases are similar to the phases found from the XRD analysis and show good agreement with that XRD results. Ying and co-workers [86] proposed the solid-state reactions between Cu and Al as Cu + Al → $CuAl_2$ + Cu → Cu_9Al_4 + Cu + Cu(Al). In another work, Lee and Kwon [85] investigated Cu-Al composites prepared using a vacuum hot pressing method and results showed the presence of various compounds of $CuAl_2$, CuAl, Cu_4Al_3 and Cu_9Al_4 at the interface. Divandari and Golpayegani [274] also reported the formation of $CuAl_2$, CuAl and Cu_3Al_2 compounds at the interface of cast Cu-Al composites.

5.5 Mechanical properties of Cu-Al (mixed) alloys

5.5.1 Hardness

From **Fig. 5.9,** it is evident that the hardness of Cu increased with the amount of Al, in particular, C15Al (MX) alloy exhibited a significantly high hardness of 4.56 GPa. Cu alloys with low Al content (preferably C3Al (MX) to C5Al (MX)) exhibited hardness in the range of

1.72 GPa to 2.33 GPa due to solid solution strengthening and intermetallic compounds formation. Whereas, the high amount of intermetallic phase along with α solid solution in C10Al and C15Al (MX), the hardness of these alloys measured to be high and varied between 3.28 GPa to 4.56 GPa. However, these hardness values are low when compared to Cu-Al (milled) alloys (as discussed in Chapter, 4.4.1).

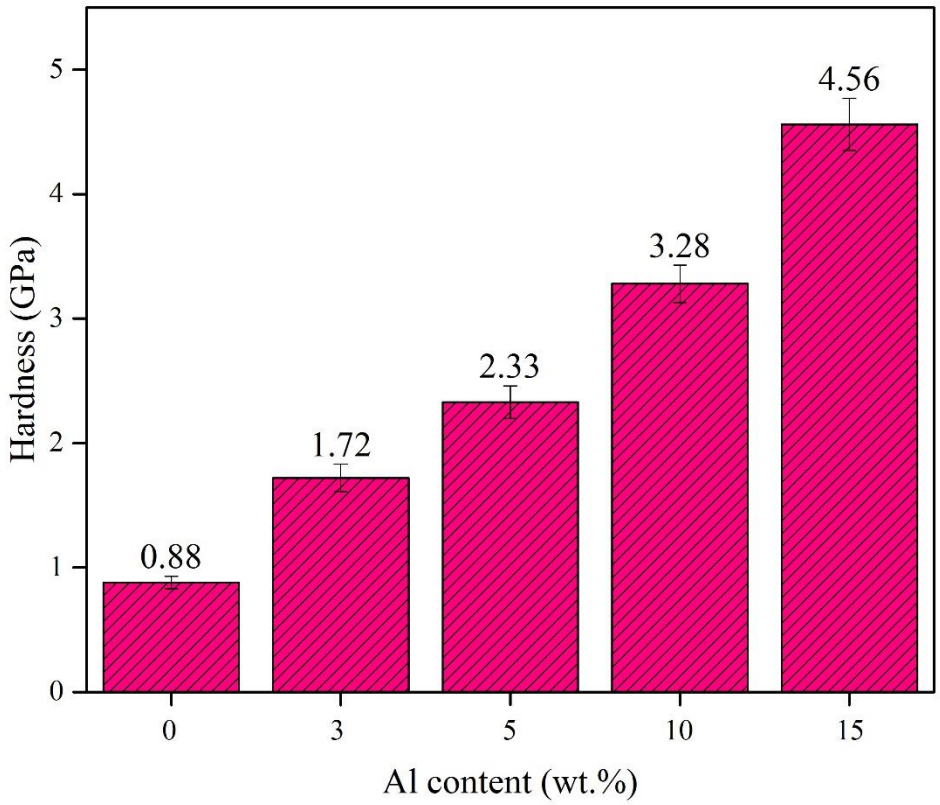

Fig. 5.9 Vickers hardness of hot-pressed Cu-Al (mixed) alloys

Liu et al. reported the Vickers hardness of Cu-xAl (x:1, 2, 4 and 6) alloys varied from ~2.00-2.75 GPa and the alloys were processed by arc melting technique at a temperature range between 710-800 ^{o}C [167]. Also, Nassef et al. produced the Cu-Sn and Cu-Pb alloys through hot pressing route; depending on the composition, the hardness of Cu-10Pb alloys varied between 1.01 to 2.10 GPa; whereas Cu-10Sn-10Pb reportedly varied between 1.08 to 2.22 GPa [5]. Glas stated that the hardness of Cu-Al alloys varied from 2.95 to 3.7 GPa processed by casting technique at 1150 ^{o}C [168]. By comparing the above literature results with the present work, it can be noted that the hot-pressed Cu-Al alloys prepared through mixing as well as milled route at low sintering temperature of 500 ^{o}C and the pressure of 500 MPa showed better hardness property.

5.5.2 Compressive strength

A representative stress-strain curves of Cu-Al (mixed) alloys after compression test are shown in **Fig. 5.10**. From the test results, the maximum yield strength of Cu-Al (mixed) alloy is measured to be 653 MPa at 15 wt.% Al content with a reasonable amount of strain (6.5%). In the case of C3Al (MX) to C10Al (MX) alloys, the strain is observed to be more than 50% due to the inter-connectivity of the solid solution phase. The yield strength of Cu-Al (mixed) is increased from 215 MPa to 276 ± 21 MPa with the addition of Al content from 3-10 wt.%. It was observed that as the Al content is increased in Cu-Al (mixed) alloys, the yield is increased. The yield and compressive strength values are listed in **Table 5.2**.

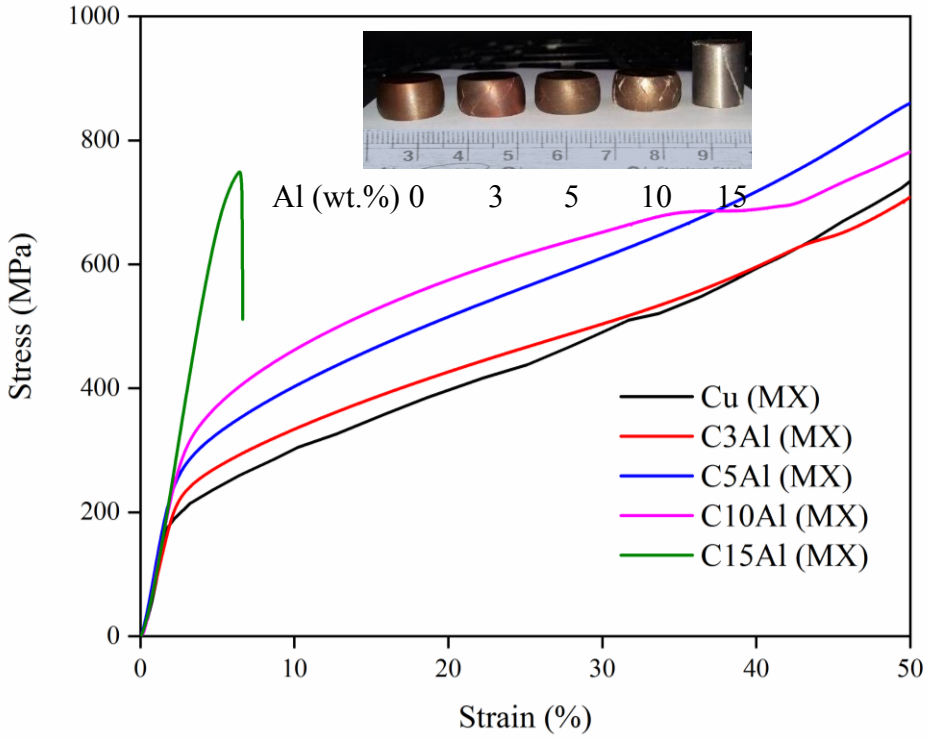

Fig. 5.10 Stress-strain curves of Cu-(X wt.%) Al alloys (at 500 ^{o}C, 500 MPa, 30 min.) where X: 0-15 wt.%.

The average compressive strength values of hot-pressed Cu-Al (mixed) alloys are similar to other copper alloys processed with melting route with various secondary heat treatment operations, but yield strength and strain of hot-pressed Cu-Al (mixed) alloys showed better properties. Compared to cast copper alloys having Al content ranging from 13 to 15 wt.% processed at an elevated temperature of 1150 ^{o}C [168], the hot-pressed C15Al (MX) which was processed at 500^{o}C exhibited better yield strength and strain.

Table 5.2 Compression test results of Cu-Al (mixed) alloys.

S. No.	Sample reference	Processing parameters	Yield strength (MPa)	Compressive strength (MPa)	Strain (%)
1	Cu (MX)	500 ^{o}C, 500 MPa, 30 min.	174.0 ± 2	540.3 ± 8	50 ± 0*
2	C3Al (MX)	,,	215.8 ± 6	547.5 ± 4	50 ± 0*
3	C5Al (MX)	,,	236.6 ± 5	658.8 ± 9	50 ± 0*
4	C10Al (MX)	,,	276.5 ± 8	682.8 ± 11	50 ± 0*
5	C15Al (MX)	,,	653 ± 12	747.9 ± 14	6.5 ± 1

* Fracture was not observed in the specimens even up to 50% elongation.

Li et al. reported a high compressive strength of 1015 MPa for Cu-14Al processed by sand casting (1180 – 1240 ^{o}C) with a low strain of 3.5% [276]. Jayakumar et al. studied the bonding behaviour of ultrafine copper and Cu alloys through the ECAP process. The maximum yield strength and compressive strength of Cu-Cr-Zr alloys prepared via ECAP process followed by annealing at 940 ^{o}C were 450 MPa and 600 MPa, respectively with the strain of 50% [277].

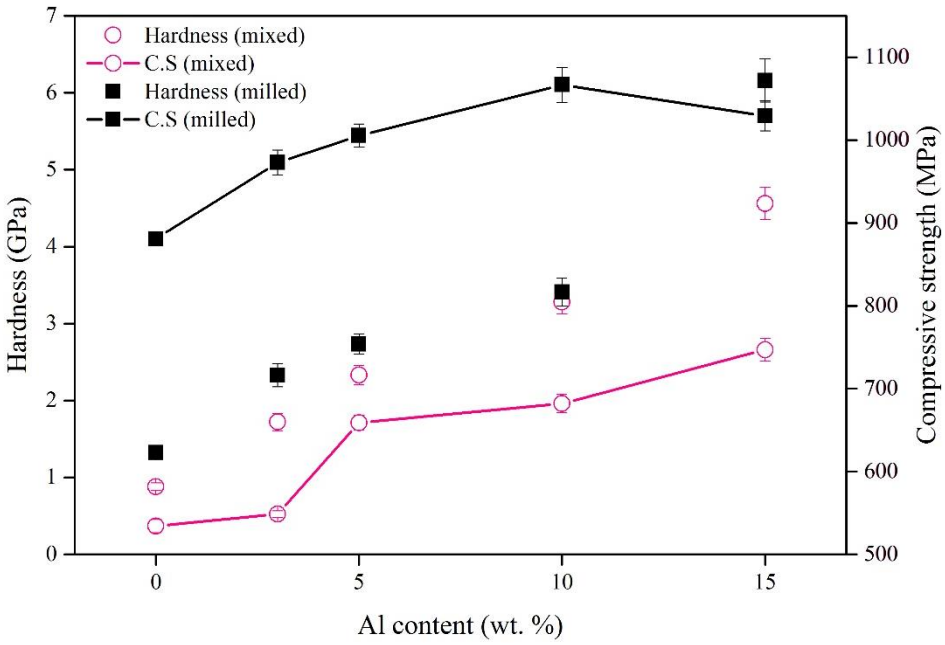

Fig. 5.11 Comparison of mechanical properties of Cu-Al alloys processed by milling and mixed routes.

The comparison of hardness and compressive strength of Cu-Al alloys processed via milling and mixing routes in the current work has been presented in **Fig. 5.11**. The Cu-Al (milled) alloys showed higher hardness (6.16 GPa) and compressive strength (1077 MPa) values compared to Cu-Al (mixed) alloys due to the formation intermetallic phase (γ_2) and solid solution phase. Also, the combined features of a microstructure such as finer grains might have contributed to its good combination of properties. Whereas the Cu-Al (mixed) alloys exhibited moderate strength and higher compressive strains upto 50% compared to Cu-Al (milled) alloys. This could be possible due to the interconnectivity of α-Cu solid solution phase in these alloys.

5.6 Abrasive wear behaviour of Cu-Al (mixed) alloys

5.6.1 Coefficient of friction (COF)

The COF of Cu-Al (mixed) alloys after sliding against SiC emery paper having a grit size of 220 mesh is shown in **Fig. 5.12**. The COF of Cu-Al (mixed) alloys was decreased with the addition of Al. The slight rise of COF values during the run-in period were observed in all the samples due to the initial roughness of the sample.

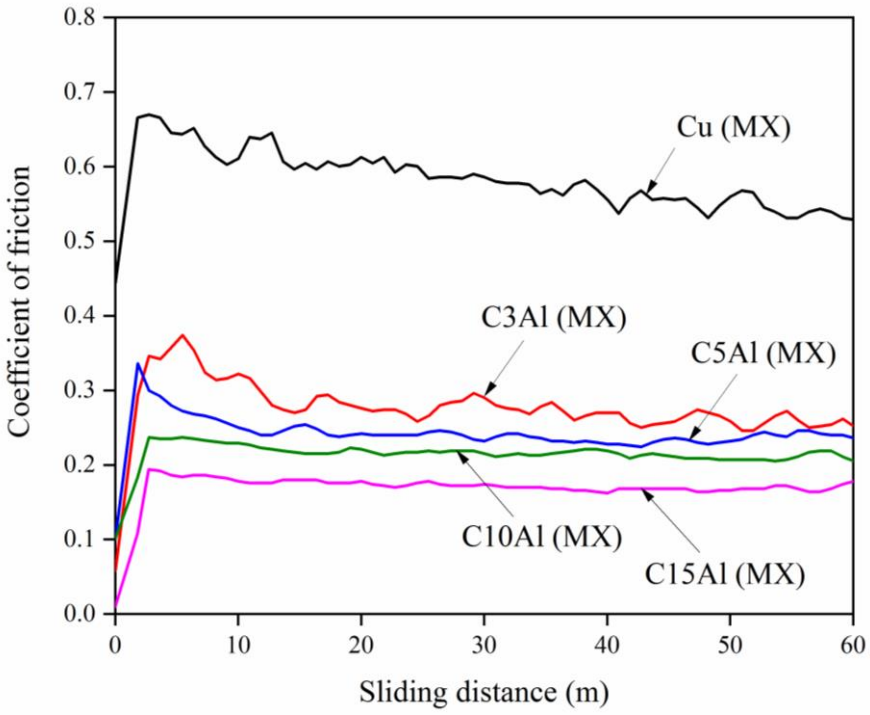

Fig. 5.12 Coefficient of friction of Cu-Al (mixed) alloys sliding against SiC emery paper of 220 grit size at a sliding velocity of 1 m/s.

The COF of pure copper reached a steady-state at the initial stage of the wear test. While the COF of Cu-Al (mixed) alloys attained the steady-state at a sliding distance around 15 m. The steady-state COF values were attained in the wear specimens after the contact pressure reduced. In Cu (MX), the minor fluctuations were observed in COF values; whereas the Cu-Al (mixed) samples exhibited very negligible fluctuations.

The COF and sp. wear rate of the Cu-Al (mixed) alloys after the wear test are given in **Table 5.3**. The COF of the Cu (MX) was found to be high (0.56 ± 0.05) compared to the Cu (ML) samples (0.49 ± 0.05). In case of Cu-Al (mixed) alloys having the Al content ranging from 3 to 10 wt.%, showed the COF values in the range between 0.27 ± 0.04 to 0.21 ± 0.02. In C15Al (MX) alloys, the COF was found to decrease upto 0.17 ± 0.03. The low COF of C15Al (MX) can be attributed to the presence of a high amount of intermetallic phases and its high hardness.

Table 5.3 The wear results of the Cu-Al (mixed) alloys after the abrasive wear test

Sample reference	**Coefficient of friction**	**Sp. wear rate ($\times 10^{-3}$ mm^3/Nm)**
Cu (MX)	0.56 ± 0.05	197.80 ± 06
C3Al (MX)	0.27 ± 0.04	14.30 ± 03
C5Al (MX)	0.24 ± 0.04	10.10 ± 05
C10Al (MX)	0.21 ± 0.02	6.87 ± 02
C15Al (MX)	0.17 ± 0.03	3.85 ± 03

5.6.2 Effect of Al on wear rate of Cu-Al (mixed) alloys

The specific wear rate of hot-pressed Cu-Al (mixed) alloys processed at 500 ^{o}C, 500 MPa for 30 min is presented in **Fig. 5.13**. The wear rate of the Cu-Al (mixed) alloys significantly reduced from the 197.8 $\times 10^{-3}$ to 3.8 $\times 10^{-3}$ mm^3/Nm. The high sp. wear rate of 197.8 $\times 10^{-3}$ mm^3/Nm was found in Cu (MX). Since the hardness of Cu (MX) is 50% lower than the Cu (ML), the COF of Cu (MX) and its wear were also high.

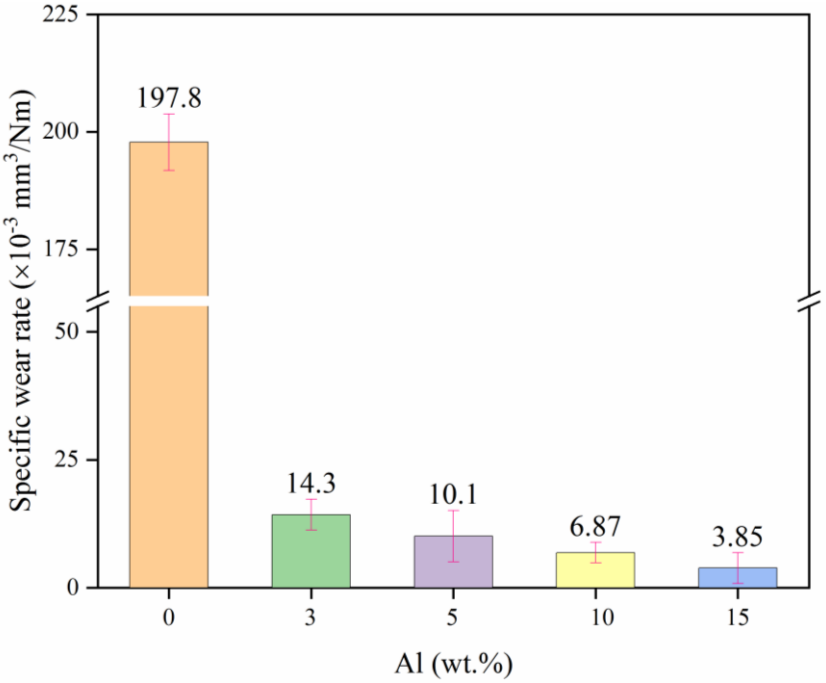

Fig. 5.13 Sp. wear rate of Cu-Al (mixed) alloys sliding against SiC emery paper of 220 grit size at a sliding velocity of 1 m/s.

The high sp. wear rate of 197.8 $\times 10^{-3}$ mm^3/Nm was noticed with Cu (MX). The extraordinarily low sp. wear rate of 3.8 $\times 10^{-3}$ mm^3/Nm was observed with C15Al (MX) alloys which is 52 times lower compared to pure copper.

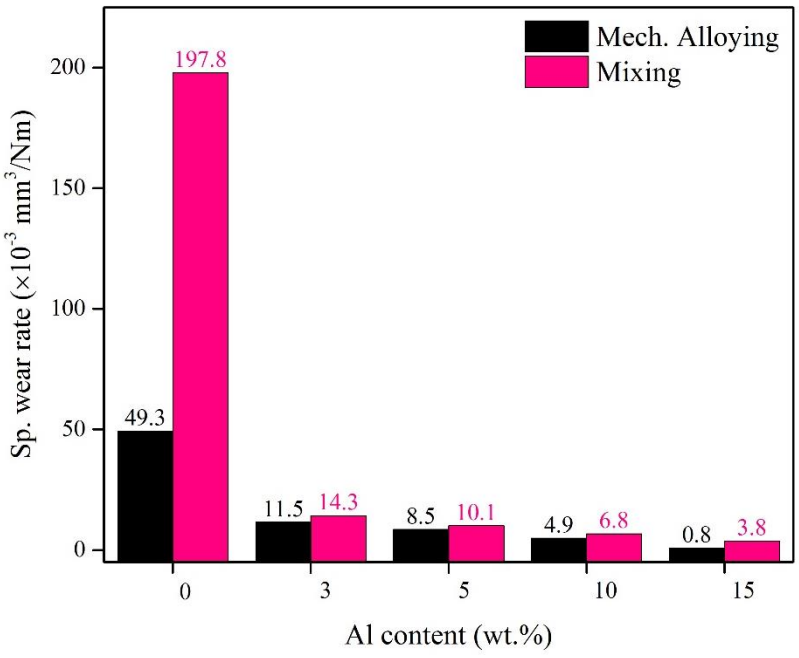

Fig. 5.14 Comparison of mechanical and wear properties of Cu-Al (milled and mixed) alloys.

The reduction of specific wear rate of C15Al (MX) alloys is mainly because of the formation of intermetallic compounds and core-shell microstructure which consist of the interconnectivity of intermetallic phases. However, the of C15Al (ML) alloys showed better wear resistance compared to C15Al (MX) alloys due to the presence of high intermetallic phase (~75 wt.%) and fine microstructure (see **Fig. 5.14**).

5.6.3 Worn surface analysis and wear mechanisms

Fig. 5.15 presents the worn surfaces of Cu-Al (mixed) alloys after sliding against SiC emery paper. The worn surface of the Cu (MX) sample is shown in **Fig. 5.15 (a,d)**. The pure copper showed the presence of narrow grooves and ridges along with large debris formation on the worn surface which is similar to the characteristic features of Cu (ML) worn surface. The wear loss of the Cu (MX) sample took place by the plowing mechanism. Hence, the high wear rate (197.8 mm^3/Nm) was observed in the Cu (MX) samples. In C10Al (MX) alloys, the worn surface consists of broad grooves and fine debris (**Fig. 5.15 b,e**). Also, it can be observed that no ridges were noticeable on the worn surfaces of C10Al (MX) and C15Al (MX) samples. This indicates that the material removal occurred by the cutting mechanism.

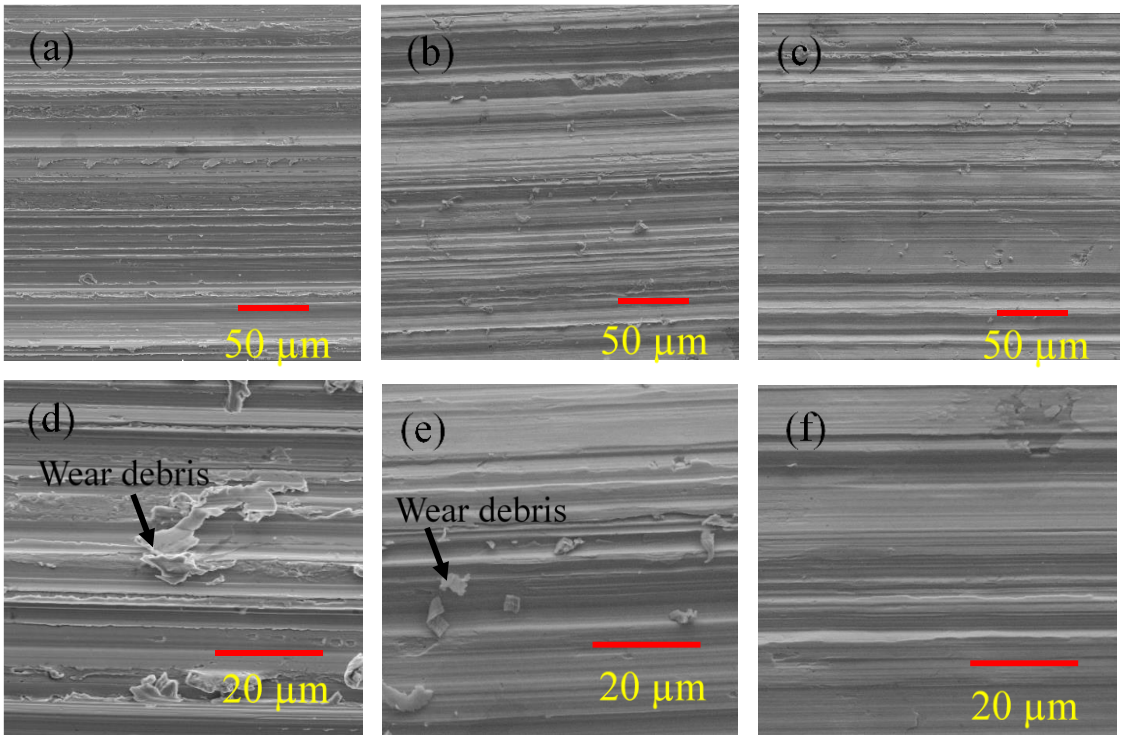

Fig. 5.15 SEM images of worn surfaces. Lower and higher magnifications of Cu-Al (mixed) alloys (a,d) Cu (MX), (c,e) C10Al (MX) and (e,f) C15Al (MX).

5.6.4 Wear debris and counter-body analysis

The wear debris of Cu-Al (mixed) alloys produced during abrasive wear test is shown in **Fig. 5.16**. The continuous chips were formed during wear test in Cu (MX) specimens due to the plowing action by the SiC abrasives. Also, the presence of SiC abrasives was found in the wear debris of Cu (MX); which indicates higher frictional forces (COF: 0.56 ± 0.05) development between two contacting surfaces and it leads to the detachment of SiC abrasives from the emery paper. The presence of various phases in shell and core structures resulted in the formation of fine debris in Cu-Al (mixed) alloys. The thickness of wear debris decreased with the addition of Al and it can be attributed to its microstructure, high hardness and strength properties of Cu-Al (mixed) alloys. In case of C15Al (MX) alloys, broken and shorter chips were observed due to the interconnectivity of intermetallic phases causing the fracture.

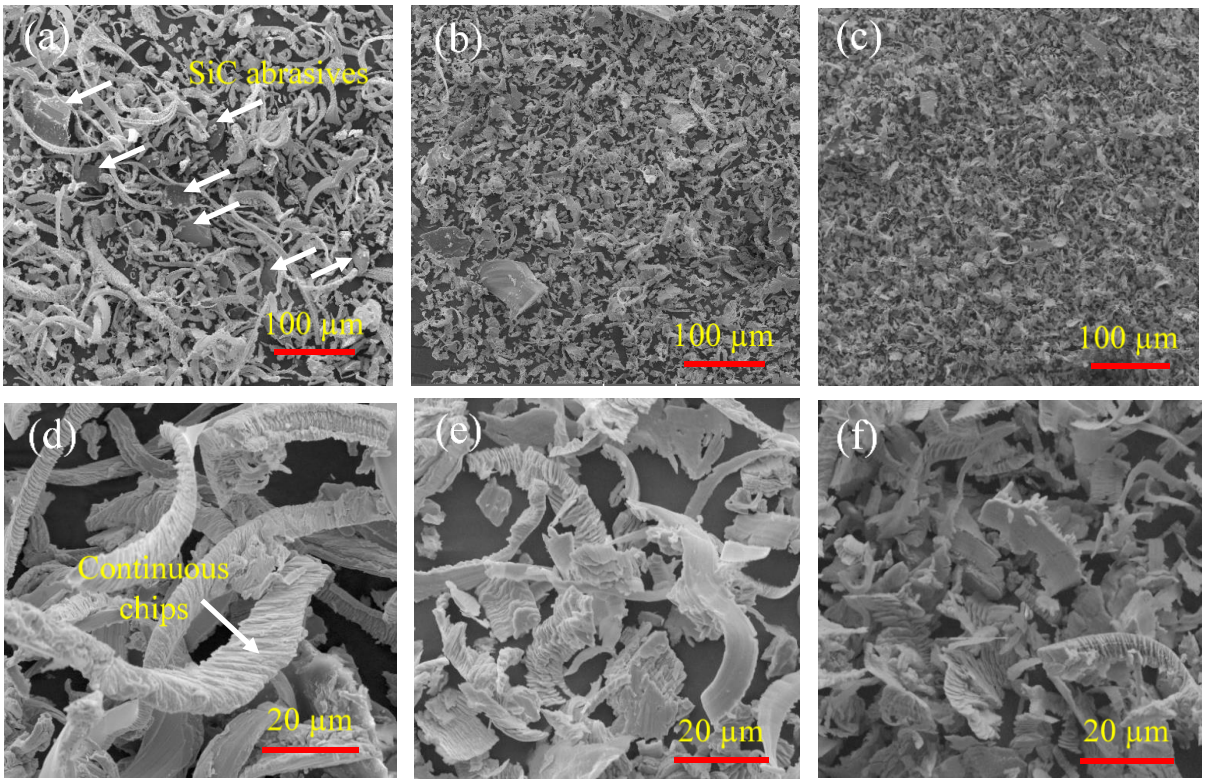

Fig. 5.16 SEM images of wear debris. Lower and higher magnifications of Cu-Al (mixed) alloys (a,d) Cu (MX), (c,e) C10Al (MX) and (e,f) C15Al (MX)

The SEM images of counter-body (SiC emery paper) before and after abrasive wear test is presented in **Fig. 5.17**. Deboning and fracture of SiC abrasives were observed in counter-body after sliding against pure Cu (MX) due to the high frictional forces. In case of C15Al

(MX), the cutting edges of SiC particles were worn out when the SiC abrasives slide against the hard intermetallic phases.

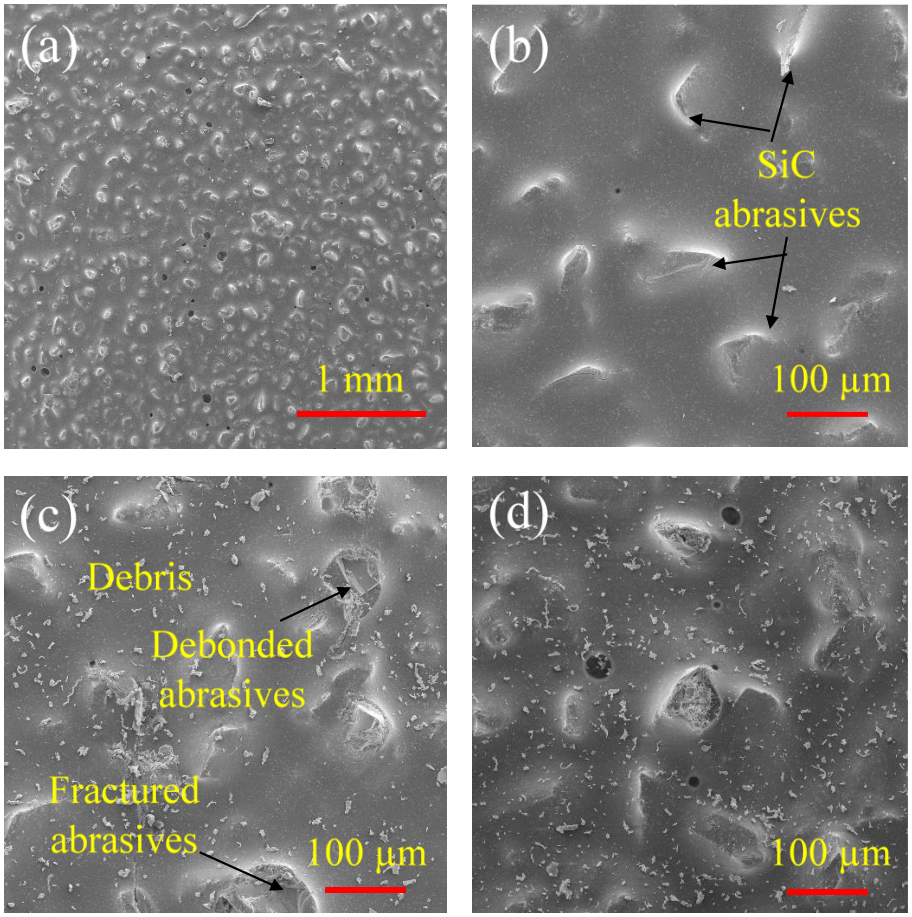

Fig. 5.17 Worn surface analysis of counter body (SiC emery paper: 220 grit size) (a) Morphology of abrasives before wear test, (b) higher magnification of unworn abrasives. The worn surface of counterbody after wear against (c) Cu (MX) sample and (d) C15Al (MX)

5.7 Electrical conductivity of Cu-Al (mixed) alloys

The effect of Al content on the electrical conductivity of Cu (MX) is plotted in **Fig. 5.18**. The electrical conductivity of Cu-Al (mixed) alloys was found to be in the range of 29.5 – 97.0% IACS. The Cu (MX) samples showed the maximum electrical conductivity of 97.0% IACS compared to Cu (ML) samples (75.7% IACS). This could be due to the absence of lattice strains in the Cu (MX) sample along with high density; while the Cu (ML) developed the lattice strains during milling of powders. The electrical conductivity of Cu-Al (mixed) alloys decreased with the addition of Al. A slight reduction in electrical conductivity was observed in C3Al (MX) samples (73.5% IACS) due to the presence of a low amount of core-shell

microstructures (solid solution and intermetallic phases) and interconnectivity of Cu and Cu rich α-Cu solid solution phase. Whereas a drastic decrement of electrical conductivity was found in the C3A (ML) milled samples (23.6% IACS) compared to Cu (ML) due to the presence of α solid solution phase. In case of C5Al (MX) and C10Al (MX) alloys, the interconnectivity of Cu and Cu rich α-Cu phases decreased as Al content increased. Thus, the decrease in electrical conductivity of 49.5% IACS and 35.0% IACS was noticed with C5Al (MX) and C10Al (MX) alloys, respectively.

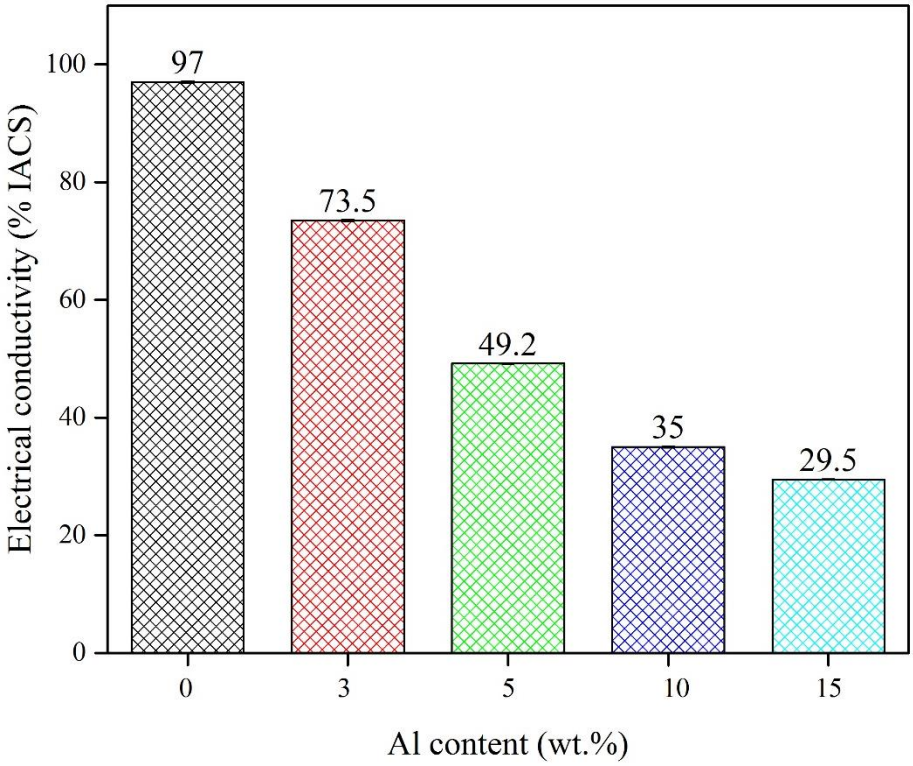

Fig. 5.18 Effect of Al content on the electrical conductivity of Cu-Al (mixed) alloys.

In C15Al (MX) alloys, the interconnectivity of Cu and Cu rich α-Cu phases diminished and high amount of α solid solution and intermetallic phases present. This lead to a further decrease in electrical conductivity of C15Al (MX) alloys (29.5% IACS). Overall, the electrical conductivity of Cu-Al (MX) alloys found to be high when compared to the Cu-Al (ML) alloys. Based on the above results, it can be noted that the mixing route for preparing Cu-Al alloys is advantageous when the electrical properties are considered.

Chapter 6

Effect of ZrB_2 reinforcement on the densification, mechanical, wear and electrical properties of Cu processed via milling route

Chapter 6

This chapter presents the effect of hard ZrB_2 reinforcement on densification and various properties of Cu. Also, the microstructure and phase identification of Cu-ZrB_2 (milled) powders as well as hot-pressed compacts have been characterized using SEM-EDS and XRD. Later, the densification mechanisms of Cu-ZrB_2 (milled) composites have been studied by varying the ZrB_2 content in Cu matrix. The mechanical properties such as hardness and compression strength of Cu-ZrB_2 composites were discussed in detail. The abrasive wear test of Cu-ZrB_2 (milled) composites was conducted against SiC emery paper. Further, the wear of Cu-ZrB_2 (milled) composites was compared with the literature. The morphology of worn surface and wear debris was analyzed using SEM to understand the underlying wear mechanisms. In the end, the effect of ZrB_2 addition on the electrical conductivity of Cu-ZrB_2 (milled) composites was studied.

6.1 Morphology of Cu-ZrB_2 (milled) powders

Nowadays, due to the demand for a good combination of mechanical and electrical properties, several copper-based composites reinforced with different ceramics have been developed. Many attempts have been made by the researchers to improve mechanical and tribological properties of Cu with the incorporation of various ceramic reinforcements/additives (Al_2O_3, ZrO_2, B_4C, SiC, TiC, Si_3N_4, TiB_2, ZrB_2) [14,27,121,122]. Among all the ceramic additives, borides and carbides (such as TiB_2, SiC, and TiC) were widely used as the reinforcements to prepare Cu matrix composites [14,121,122].

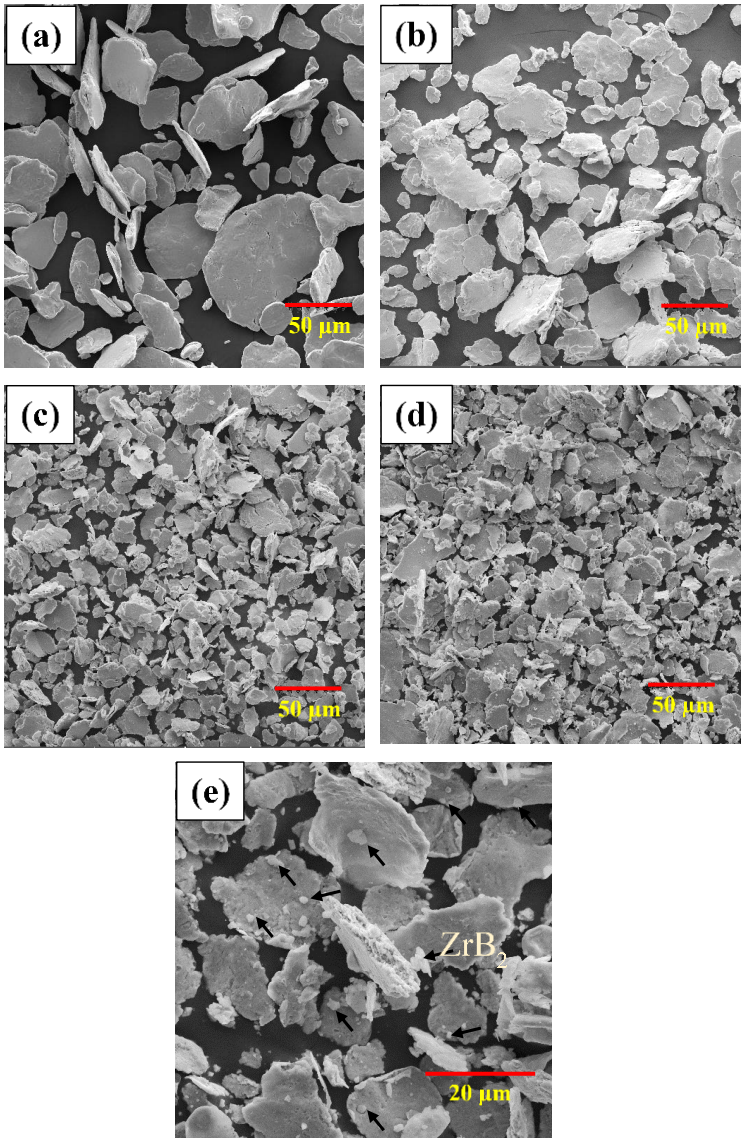

Fig. 6.1 SEM images of milled powders after 10 h ball milling at 260 rpm (a) Cu (ML), (b) C3Z (ML), (c) C5Z (ML) (d) C10Z (ML) and (e) high magnification image of C10Z (ML) (arrows indicating the ZrB_2 particles).

Especially, ZrB_2 is a potential candidate to improve the strength and hardness of Cu without much affecting the electrical and thermal properties [27]. From **Fig. 6.1**, it can be observed that the pure Cu becomes flaky after milling due to the repeated cold welding of particles. Further, the Cu powder particles become small agglomerated aggregates with the addition of ZrB_2. Also, the size of Cu-ZrB_2 powder particles further reduced due to the repeated cold welding and fracture of powder particles. The fine ZrB_2 powder particles were embedded into the Cu agglomerated particles at severe milling conditions (Milling speed: 260 rpm, time: 10 h, BPR: 10:1).

6.2 Phase analysis of hot-pressed Cu-ZrB_2 (milled) composites

Fig. 6.2a represents the XRD patterns of hot-pressed Cu (ML) composites. The patterns revealed the presence of Cu and ZrB_2 only. The low intensity of ZrB_2 peaks attributed to a low ZrB_2 content (1, 3 and 5 wt.%) in Cu. More importantly, the XRD patterns of samples showed the sharp intense and narrow peaks which confirms the fine grain size and crystallinity. The study of grain size and lattice strains is essential in understanding the properties of the Cu-ZrB_2 (milled) composites.

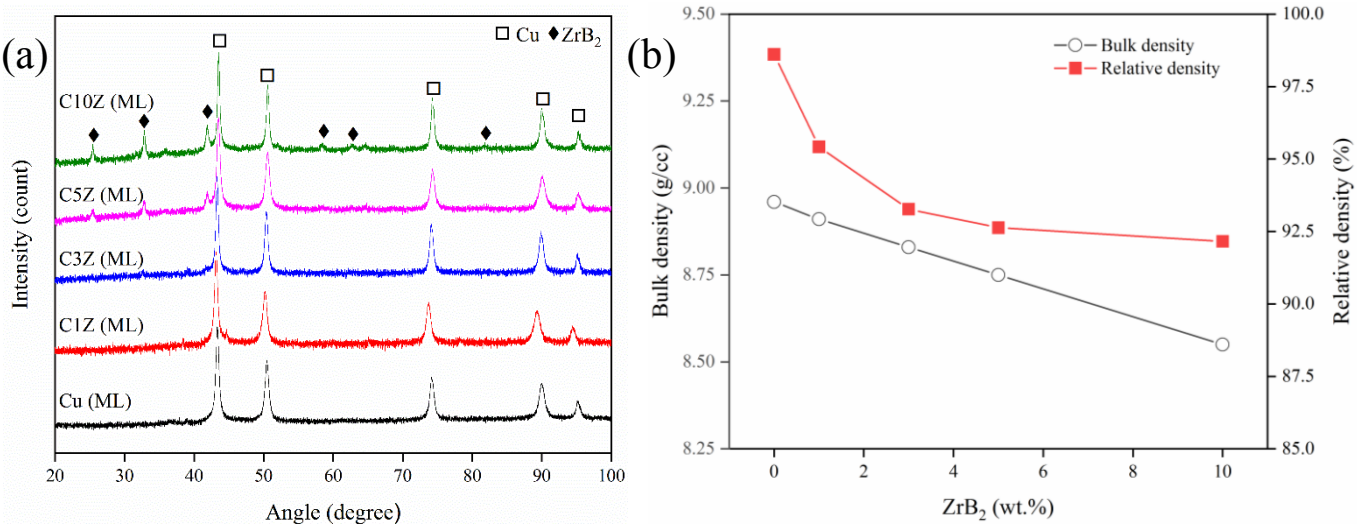

Fig. 6.2 (a) X-ray diffraction patterns of hot-pressed Cu-ZrB_2 (milled) composites and (b) the effect of ZrB_2 reinforcement on densification of hot-pressed Cu-ZrB_2 composites (Processing conditions: 500 ^oC, 500 MPa for 30 min.)

The grain size, lattice strain and dislocation density of milled powders and hot-pressed Cu-ZrB_2 samples are reported in **Table 6.1**. The grain size of the milled powders varied from 55.4 nm to 42.0 nm. Similarly, the grain size of the hot-pressed Cu (ML) samples varied from

123.7 nm to 67.6 nm. The grain size of the milled powders and sintered samples decreased with the addition of ZrB_2 to Cu. The lattice strain found to be increased in milled powders from 0.32% to 0.38%; in the case of hot-pressed powders, the lattice strain increased slightly from 0.22% to 0.28% with the ZrB_2. The grain size of the sample affects the lattice strains. The smaller grains cause more effect on lattice strain than the larger sized grains [278].

Table 6.1 Grain size, lattice strain and dislocation density of Cu-ZrB_2 milled powders and bulk samples

Sample reference	Milled powders			Hot-pressed samples		
	Grain size (nm)	Lattice strain (%)	Dislocation density ($\times 10^{14}$ m^{-2})	Grain size (nm)	Lattice strain (%)	Dislocation density ($\times 10^{14}$ m^{-2})
Cu (ML)	55.46	0.32	3.25	123.79	0.22	0.65
C1Z (ML)	53.33	0.34	3.52	101.94	0.23	0.96
C3Z (ML)	51.35	0.35	3.79	87.20	0.24	1.32
C5Z (ML)	44.72	0.37	5.00	73.75	0.26	1.84
C10Z (ML)	42.01	0.38	5.67	67.63	0.28	2.19

The increase of grain size and decrease of lattice strain and dislocation density was observed after hot-pressing at 500 ^oC. This can be attributed to the recovery of Cu (ML) samples from the lattice strains by absorbing the high activation energy at a sintering temperature (500 ^oC). The dislocation density of the milled powders and composites found to be increased with the ZrB_2 content. The dislocation density of the milled powders was calculated to be in the range of $3.52 \times 10^{14} – 5.67 \times 10^{14}$ m^{-2}; whereas, the hot-pressed samples varied from $0.65 \times 10^{14} – 2.19 \times 10^{14}$ m^{-2}.

6.3 Densification and microstructure of Cu-ZrB_2 (milled) composites

The bulk density of the Cu-ZrB_2 (ML) composites decreased from 8.84 g/cc to 8.16 g/cc. Also, the relative density of hot-pressed samples decreased from 98.6% to 92.1% with the addition of ZrB_2 (see **Fig. 6.2b**). The agglomerated powder particles formed during ball milling

and the use of the highly refractory compound (ZrB_2 reinforcement) might have caused micro-porosity and led to a decrease in the densification of Cu-ZrB_2 (milled) composites. As a representative, the SEM image and corresponding EDS patterns of C10Z (ML) composite are presented in **Fig. 6.3**. The microstructure of C10Z (ML) composites reveals the presence of uniformly distributed fine ZrB_2 particles in the Cu matrix. From the EDS analysis, the bright phase could be identified as ZrB_2 particles and grey phase as a Cu matrix.

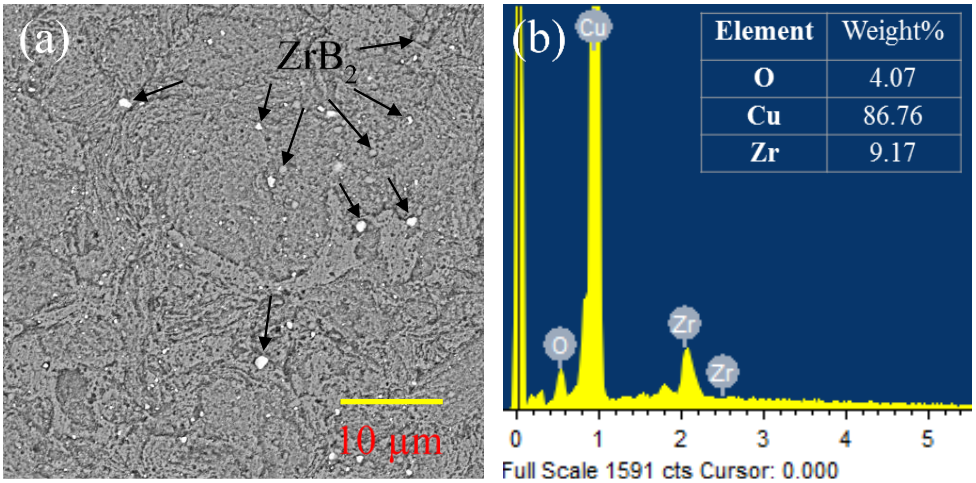

Fig. 6.3 (a) SEM image and (b) corresponding EDS of C10Z (ML) composite.

The densification details of Cu-ZrB_2 (milled) composites are listed in **Table 6.2.** Clinktan et al. [144] prepared the (Cu-Zn-Si)-B_4C composites through hot-pressing technique at a temperature of 900 °C and pressure of 25 MPa. The relative density of these Cu alloy composites reduced considerably from 97% to 91% with the B_4C addition.

In a different work, Fathy et al. [118] studied the effect of Al_2O_3 on the mechanical and wear properties of Cu. The composites were processed by the conventional pressureless sintering technique at a high sintering temperature of 950 ^oC for a prolonged duration of 2 h. The relative density of Cu-Al_2O_3 composites found to be reduced from 92.5 % to 87.8% because of the agglomeration of nano Al_2O_3 particles.

Table 6.2 The bulk density, theoretical density and porosity of the hot-pressed Cu-ZrB_2 (milled) composites

Property	**ZrB_2 content (wt.%)**				
	0	**1**	**3**	**5**	**10**
Sample reference	Cu (ML)	C1Z (ML)	C3Z (ML)	C5Z (ML)	C10Z (ML)
Bulk density (g/cc)	8.84	8.51	8.24	8.11	8.16

Theoretical density (g/cc)	8.96	8.91	8.83	8.75	8.55
Porosity (%)	1.39	4.58	6.73	7.37	7.84

It is interesting to note that the presently developed Cu-ZrB_2 (milled) composites (despite a considerably low hot pressing temperature of 500 ^oC) exhibited similar densification behaviour as that of (Cu-Zn-Si)-B_4C and Cu-Al_2O_3 composites. It corroborates the advantage of high-pressure hot pressing in developing Cu-ZrB_2 composites.

6.4 Mechanical properties of Cu-ZrB_2 (milled) composites

Fig. 6.4 shows the various mechanical properties of the hot-pressed Cu-ZrB_2 (milled) composites. From **Fig. 6.4b**, it can be observed that the hardness of Cu composites increased with the increase of ZrB_2 content in the Cu matrix. Interestingly, even the small amount of ZrB_2 (1 wt.%) addition to Cu, significantly enhanced the hardness of pure copper (55.3%).

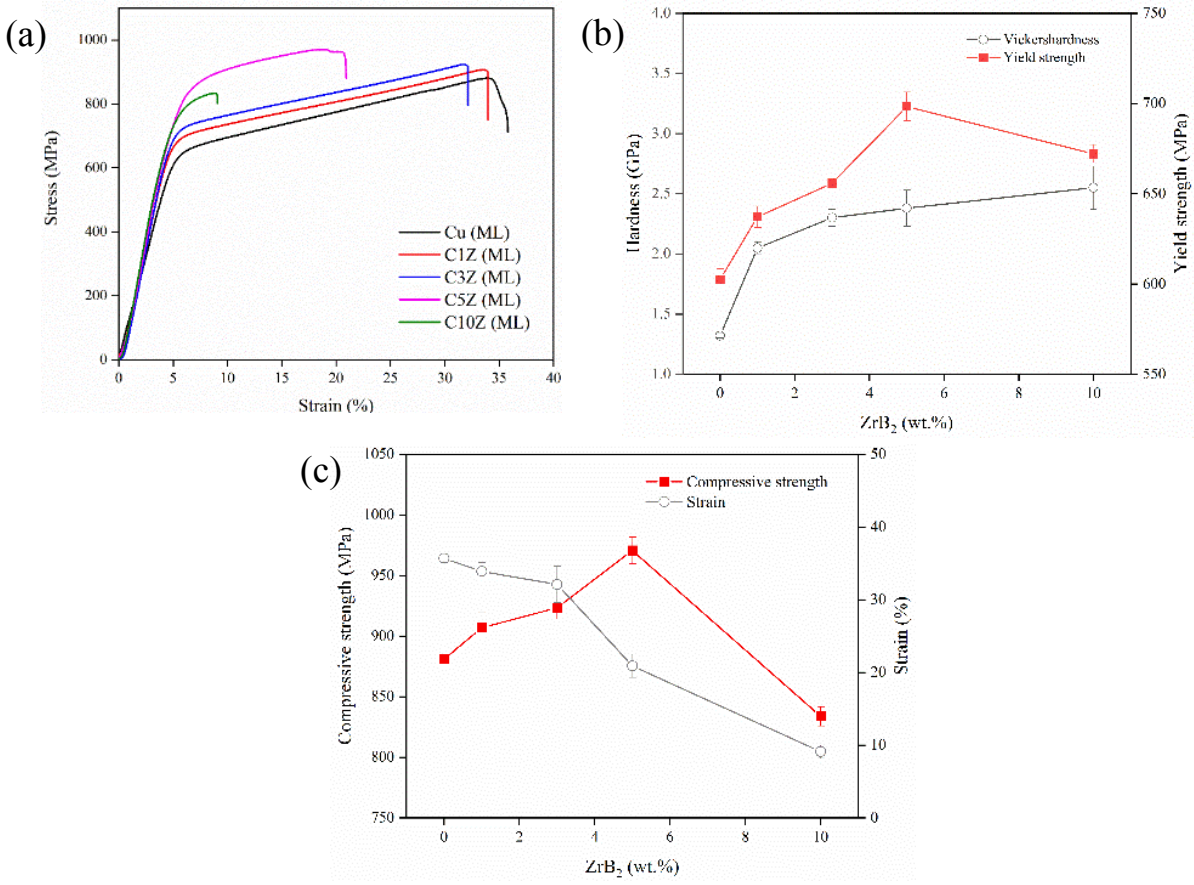

Fig. 6.4 Effect of ZrB_2 on mechanical properties of Cu. (a) Compressive stress-strain curves of hot-pressed Cu-ZrB_2 (milled) composites, (b) hardness and yield strength and (c) compressive strength and strain

The maximum average hardness of 2.5 GPa was noted for C10Z (ML) sample. It was found that the hardness of Cu (ML) was increased by 93.1% with the addition of 10 wt.% ZrB_2. The increase in hardness of Cu- ZrB_2 composites can be attributed to the combined effect of lattice strains produced during the milling of powders; also by the presence of the ultra-fine ZrB_2 particles which restricts the dislocation movement in Cu matrix [12]. Recently, Fan et al. [9] stated the use of 4.2 wt.% Zr-1wt.% B improved the hardness of Cu upto 1.39 GPa because of restricting the dislocation movement by the fine ZrB_2 reinforcement.

In another study, it was revealed that the addition of 10 wt. % ZrB_2 improved the hardness of Cu upto 0.95 GPa [279]. Whereas the inclusion of 9 wt.% ZrO_2 enhanced the hardness of Cu upto 0.5 GPa [44]. Also, the hardness of the Cu-Al_2O_3 composites was reportedly increased to 0.79 GPa with the Al_2O_3 (12.5 wt.%) [118]. On the other hand, significantly high hardness of 4.75 GPa was reported for Cu alloy (Cu-14Zn-4Si)-12B_4C composites [144]. As it was discussed in Chapter 4, extremely high hardness of 6.16 GPa for C15Al (ML) alloy [83]. From this, it can be realized that the selection of additive and processing conditions influences the hardness of Cu. It also reflects that the alloying element is advantageous in improving the hardness of Cu than the ceramic additives. Alternatively, it can be implied that solid solution strengthening and precipitation hardening is more effectively contributing to the hardness of Cu than the dispersion hardening.

Table 6.3 Mechanical properties of Cu-ZrB_2 (milled) hot-pressed composites.

Sample reference	Hardness (GPa)	Compressive strength (MPa)	Strain (%)
Cu (ML)	1.32 ± 0.02	880.90 ± 6	35.70 ± 0.6
C1Z (ML)	2.05 ± 0.05	906.90 ± 13	33.90 ± 1.2
C3Z (ML)	2.30 ± 0.07	923.30 ± 9	32.10 ± 2.5
C5Z (ML)	2.38 ± 0.05	970.60 ± 11	20.90 ± 1.6
C10Z (ML)	2.55 ± 0.08	833.70 ± 8	9.10 ± 0.9

The hardness, mechanical strength and strain of Cu-ZrB_2 (milled) composites are given in **Table 6.3**. The yield strength and compressive strength of the Cu-ZrB_2 (milled) composites are enhanced with the addition of ZrB_2 (**Fig. 6.4 a-b**). In particular, the yield strength and compressive strength of Cu composites increased upto 5 wt.% ZrB_2, and further addition of ZrB_2 lowered its strength. The yield strength of Cu (ML) samples varied from 602.5 ± 6 MPa to 672.1 ± 5 MPa and the compressive strength of composites was found to be 833.7 ± 8 to 970.6 ± 11 MPa. Interestingly, low strength and strain were observed for Cu-10 wt.% ZrB_2 (**Fig. 6.4c).**

The compression strength of C10Z (ML) is dramatically reduced when compared to C5Z (ML) and other materials. In particular, it is surprising to note that the strength of C10Z (ML) significantly low when compared to C5Z (ML), even though the densification of C5Z (ML) and C10Z (ML) is almost identical. Similarly, Wang et al. [27] also reported that the mechanical properties of the hot-pressed Cu-ZrB_2 composites reduced with the addition of fine ZrB_2 (above 7 wt.%). Such a reduction in strength properties was attributed to the presence of agglomeration of ZrB_2 particles in the Cu composites. In another work, Prajapati et al. [11] mentioned that the compressive strength of the Cu-B_4C composites reduced with the high amount of B_4C addition (>10 wt.%) due to the brittleness nature of the material. The present results also showed the similar behaviour of reduction in compressive strength of Cu-ZrB_2 composites with increased ZrB_2 content (10 wt.%). It is believed that weak interfacial bonding between Cu/ZrB_2 and ZrB_2/ZrB_2 phases and the brittle nature might have led to such reduction in the strength of C10Z (ML). Also from Table 6.3, it can be observed that the compression strain of C10Z (ML) significantly lowered from 35.7 to 9.1%.

From **Table 2.2**, the different Cu-based composites reinforced with oxides, borides and carbides showed the maximum compressive strength ranging between ~175 to 1077 MPa with the strain varying from 15% to 30% [118,144,146,147]. These results reveal that the compressive strength of Cu alloy composites was significantly high and can be attributed to the involvement of different strengthening mechanisms such as solid solution and dispersion strengthening along with grain refinement. In the present work, the Cu-ZrB_2 (milled) composites exhibited comparable hardness and strength properties of other Cu composites. Achieving such properties at low sintering temperature and time with the Cu-ZrB_2 (milled) composites is a promising outcome. To achieve very high strengths for structural applications, it is motivating further studies to focus on studying the effect of ZrB_2 on Cu alloys.

6.5 Abrasive wear properties

6.5.1 Frictional coefficient and specific wear rate

Fig. 6.5 represents the effect of ZrB_2 on the wear properties of Cu-ZrB_2 (milled) composites. The coefficient of friction (COF) of the hot-pressed samples becomes steady-state after a sliding distance of 25 m (see **Fig. 6.5a**). A small fluctuation was observed in Cu (ML) due to the high frictional forces developed and sudden pull out of SiC abrasives from the

counter-body. Also, it is observed that the fluctuations were reduced with the addition of ZrB_2 and no fluctuations were witnessed in C5Z (ML) and C10Z (ML).

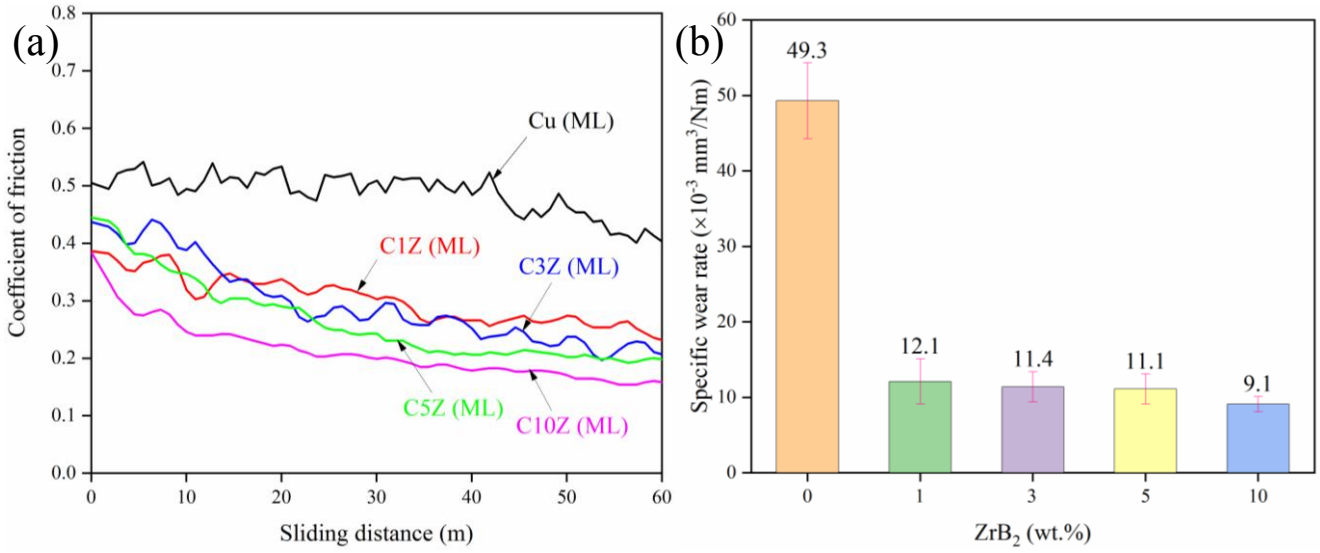

Fig. 6.5 (a) Coefficient of friction (COF) plots and (b) specific wear rate of Cu-ZrB_2 (milled) composites after sliding at a velocity of 1 m/s and a load of 5 N.

The COF of Cu-ZrB_2 (milled) samples decreased with the addition of ZrB_2 and it varied in the range of 0.49 ± 0.05 to 0.18 ± 0.02. **Fig. 6.5b** demonstrates the variation in the specific wear rate of Cu-ZrB_2 (milled) composites. The wear rate of the Cu composites decreased extremely with the ZrB_2 amount. A drastic reduction of wear rate was observed even with the very low amount of ZrB_2 addition (1 wt.%) because the hard ZrB_2 particles obstruct the wear loss of the soft Cu matrix. The wear rate decreased from 49.3×10^{-3} mm^3/Nm to 9.1×10^{-3} mm^3/Nm. Lowest wear rate was observed with C10Z (ML) samples, which is 5.41 times less compared to Cu (ML).

6.5.2 Wear mechanisms of Cu-ZrB_2 (milled) composites

The worn surface of Cu (ML) (sliding against SiC emery paper) after sliding at a velocity of 1 m/s and the load of 5 N is presented in **Fig. 6.6**.

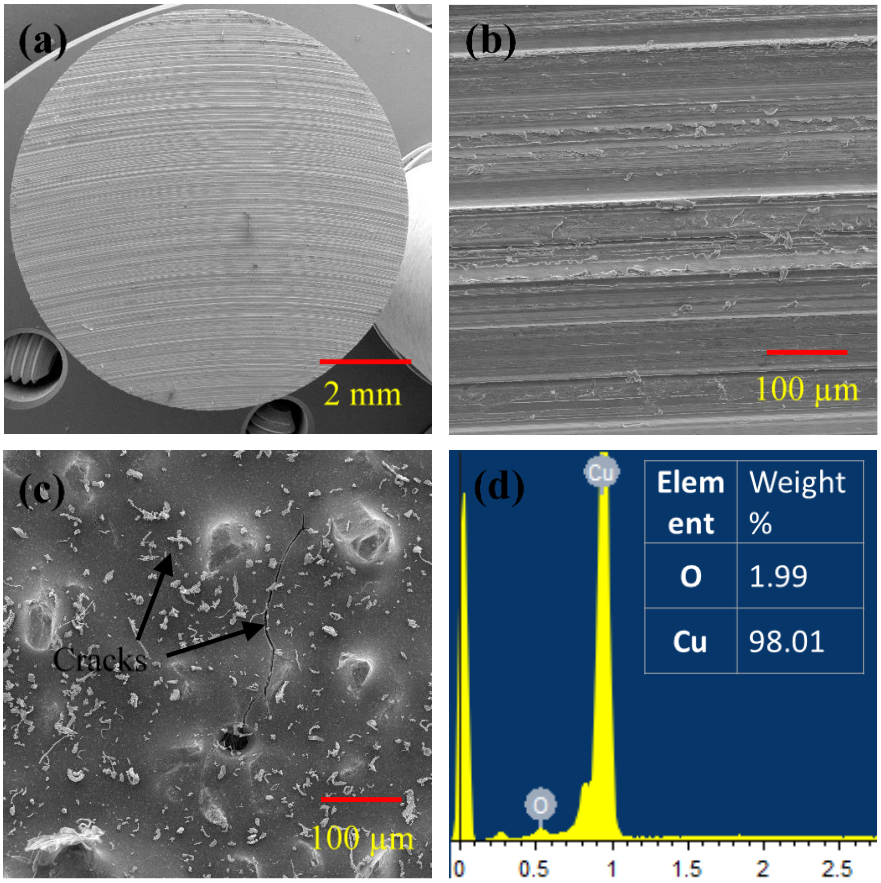

Fig. 6.6 SEM images of worn surface of Cu (ML) after sliding against SiC emery paper (220 grit size abrasives) at a load of 5 N and sliding velocity of 1 m/s. (a) Overview of the worn surface at low magnification, (b) higher magnification of Cu worn surface, (c) counter body (Emery paper: 220 grit size) and (d) EDS spectrum of the Cu (ML) worn surface.

The overview of the worn surface indicates that the entire surface gets worn out uniformly (**Fig. 6.6a**). From **Fig. 6.6b**, it can be observed that the narrow grooves were formed after the wear. The presence of ridges along with wear debris indicates the plowing mechanism, while the hard SiC abrasives may form deep grooves on soft Cu by plowing mechanism and result in high wear loss of the material. The presence of microcracks on the counter-body can be seen in **Fig. 6.6c**. It represents the high frictional forces developed during sliding of pure Cu against SiC emery paper; which leads to the oxidation (1.99 wt.%) of worn surface.

In the case of C10Z (ML), the worn surface consists of broad and smooth grooves with no ridge formation (**Fig. 6.7b**). It specifies that the material is removed by the abrasive cutting mechanism, which correlated well with the hardness of composites (2.55 GPa). During the abrasive wear, the major amount of material loss occurs due to the plowing mechanism; while, the addition of hard ZrB_2 enhances the wear resistance by resisting the plastic deformation of the material.

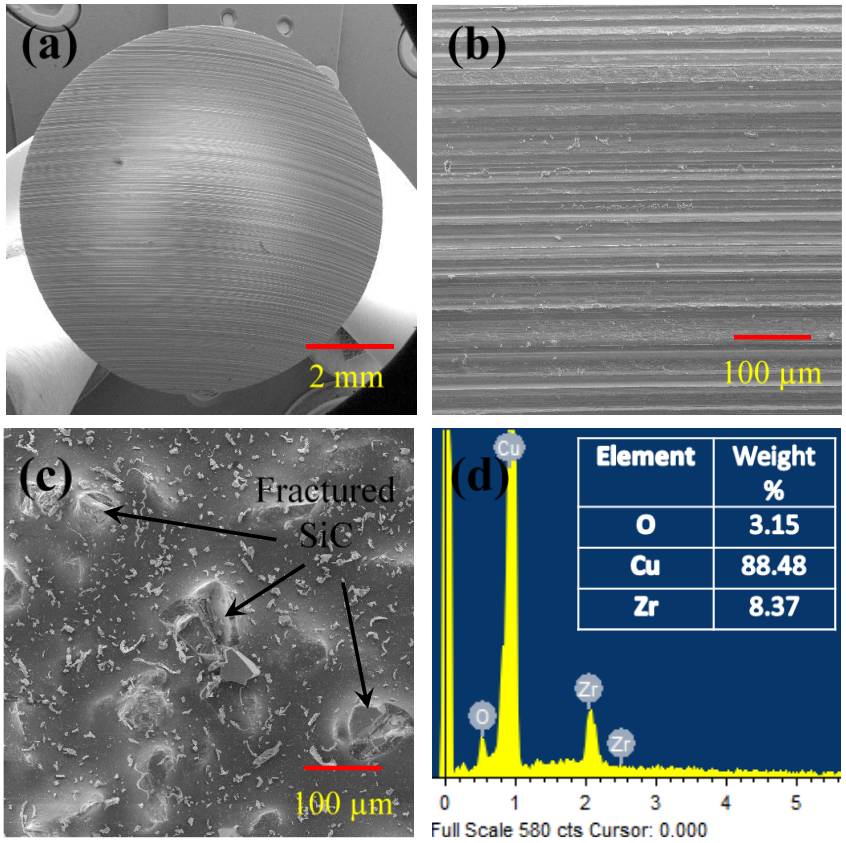

Fig. 6.7 SEM images of worn surface of C10Z (ML) after sliding against SiC emery paper (220 grit size abrasives) at a load of 5 N and sliding velocity of 1 m/s. (a) Overview of the worn surface at low magnification, (b) higher magnification of C10Z (ML) worn surface, (c) counter body (Emery paper: 220 grit size) and (d) EDS spectrum of the C10Z (ML) worn surface.

When the hard ZrB_2 particles hit the SiC abrasives, some of the SiC abrasives were fractured and dislodged from their sites, which is evident from **Fig. 6.7c**. The increase of ZrB_2 content in the Cu matrix causes more damage to the counter-body. Thus, the wear resistance of the Cu enhanced with the ZrB_2. The oxygen presence on the worn surface was identified by EDS. The worn surfaces get oxidised wherever the agglomerated ZrB_2 particles are exposed to the environment. This phenomenon was more prevailing with the increasing addition of ZrB_2 in the matrix. The high oxygen content of 3.15 wt.% was observed in the C10Z (ML) sample.

6.5.3 Morphology of worn surfaces and wear debris

Fig. 6.8 shows the SEM images of worn surfaces of all the Cu-ZrB_2 (milled) composites for comparison purpose. The number of ridges and debris formation on the worn surface was reduced with the addition of ZrB_2. This indicates the transformation of wear mechanisms from the plowing mechanism of Cu (ML) to the cutting mechanism of C10Z (ML).

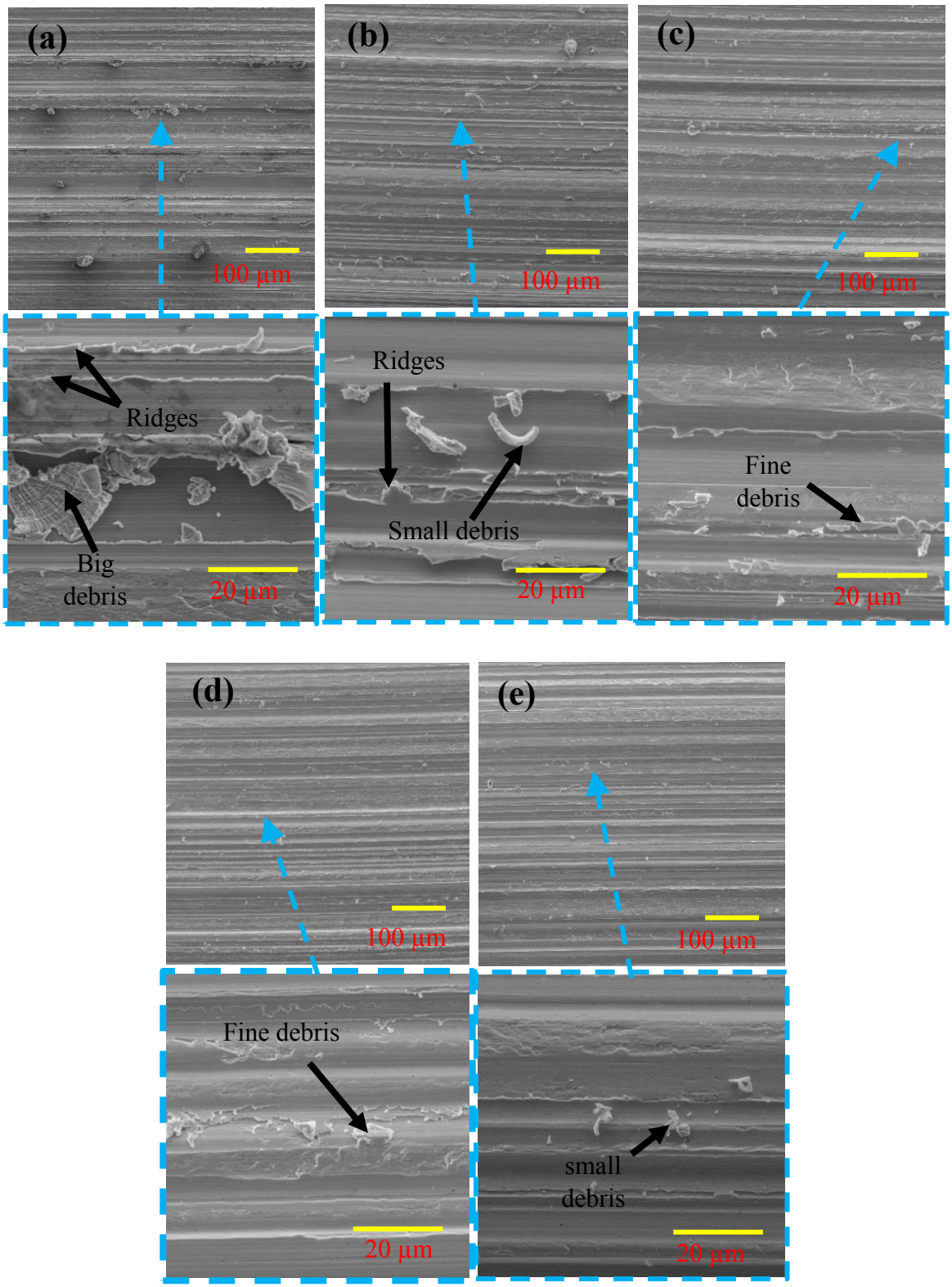

Fig. 6.8 SEM images of worn surfaces of Cu-ZrB_2 (milled) composites (a) Cu (ML), (b) C1Z (ML), (c) C3Z (ML), (d) C5Z (ML) and (e) C10Z (ML).

Fig. 6.9 demonstrates the SEM images of wear debris formed during abrasive wear of samples. In pure copper, the continuous chips (wear debris) were formed during sliding wear

by the plowing mechanism, which indicates more loss of the material. In case of Cu-ZrB_2 (milled) composites, the presence of ZrB_2 particle in the matrix causes discontinuity of chips (C1Z (ML) and C3Z (ML)), and the further increase of the reinforcement content leads to the formation of short chips (C5Z (ML) and C10Z (ML)).

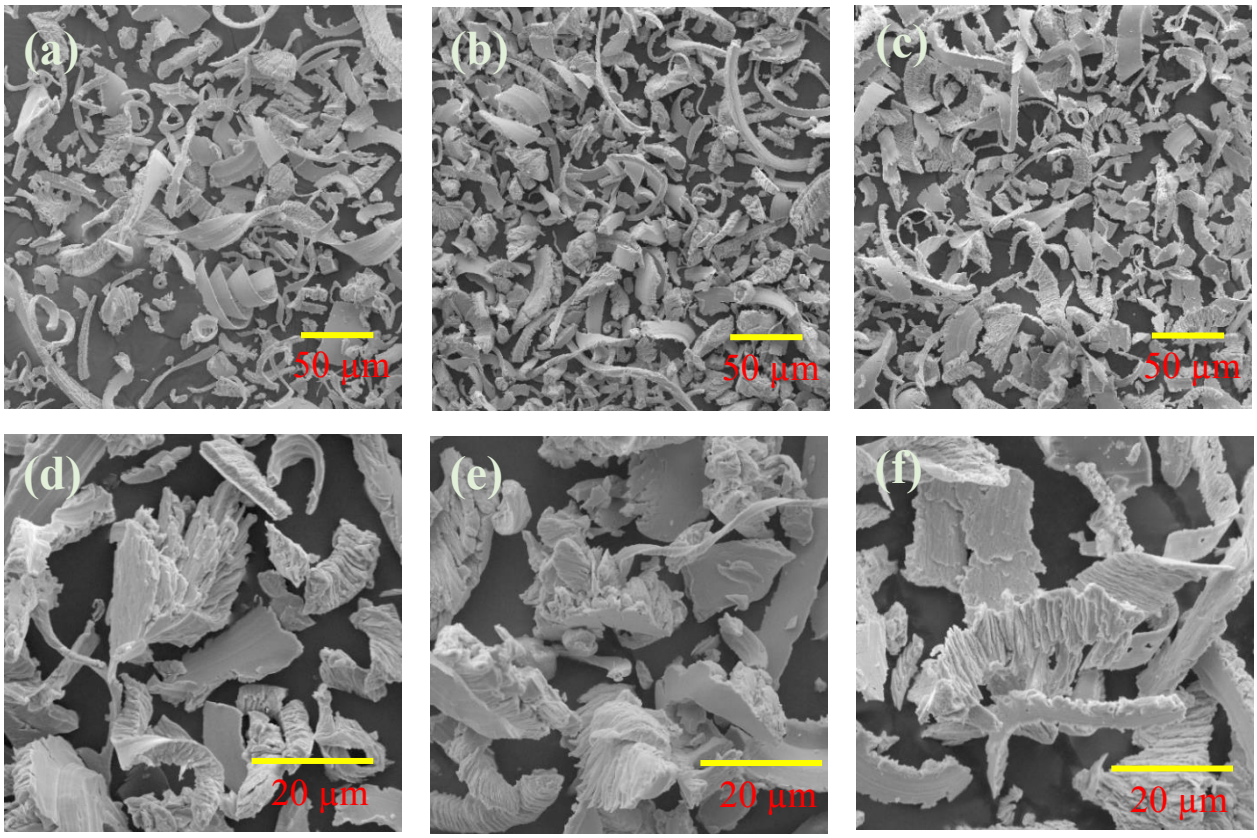

Fig. 6.9 SEM of wear debris of Cu-ZrB_2 (milled) composites after sliding against SiC emery paper (220 grit size abrasives). Wear debris of (a,d) Cu (ML) (b,e) C3Z (ML) (c,f) C10Z (ML). Corresponding lower magnification (a,b,c) and high magnification (d,e,f) SEM of wear debris.

Fig. 6.10 demonstrates the wear of SiC counter-body after abrasive wear. The counter-body after sliding against Cu (ML) showed less damage to SiC emery paper and minor cracks were observed due to the high frictional forces developed during the wear process (**Fig. 6.10a**). Whereas, the counter-body which was slide against Cu-ZrB_2 (milled) composites showed more damaged sites (**Fig. 6.10b-c**). The presence of hard ZrB_2 in composites hits the sharp SiC abrasives and causes more fractures of the abrasives. It resulted in more damage to the counter-body rather than the sample surface. Thus the wear resistance of Cu-ZrB_2 (milled) composites enhanced with the addition of ZrB_2.

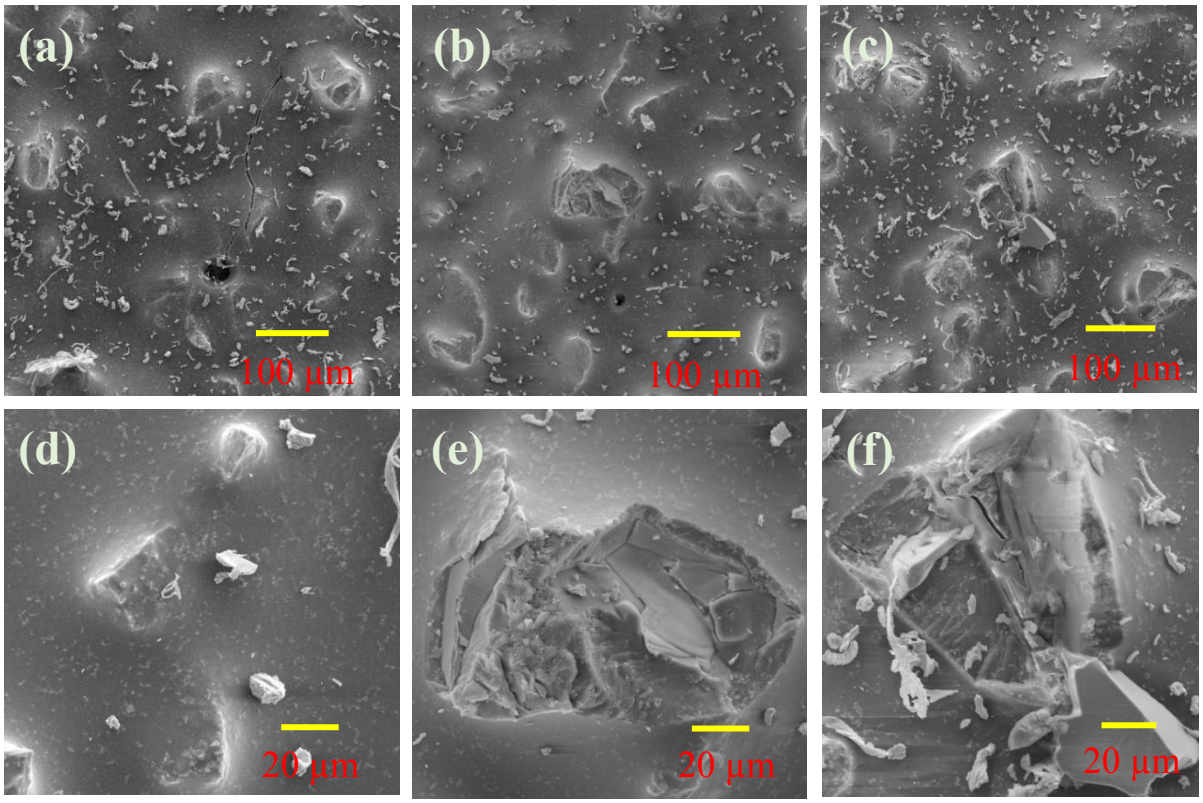

Fig. 6.10 SEM of worn surface analysis of counter body (SiC emery paper: 220 µm grit size). SEM of (a,d) C1Z (ML) (b,e) C3Z (ML) and (c,f) C10Z (ML). Corresponding lower magnification (a,b,c) and high magnification (d,e,f) worn surfaces of counterbody.

6.6 Electrical properties of Cu-ZrB_2 (milled) composites

Fig. 6.11 shows the effect of ZrB_2 on the electrical conductivity of Cu. The electrical conductivity of samples varied from 75.7% IACS to 44.1% IACS. The electrical conductivity of C10Z (ML) composites decreased by 1.7 times compared to Cu (ML). This can be attributed to the porosity, lattice strain and presence of ultra-fine ceramic (ZrB_2) particles [147]. In case of C1Z (ML) (71.5% IACS) and C3Z (ML) (66.8% IACS) composites, no significant change in electrical conductivity was observed. Further addition of ZrB_2 (above 3 wt.%) lowered the electrical conductivity of Cu upto 44.1% IACS; however, the electrical conductivity of C10Z (ML) composites was around 50% higher than the C15Al (MX) alloys. The decrease in electrical conductivity of Cu composites can be attributed to: (i) low densification, thereby the sintered samples have a certain amount of porosity, these pores (insulating sites) make the charge transfer break off and increase the scattering of electrons [190]; (ii) the lattice strain developed in the materials, which leads to more scattering for electrons movement; (iii) the nano-sized ZrB_2 (~ 290 nm) develops large fraction of grain boundary in the Cu matrix; this

results in the scattering of the movement of the electrons, and (iv) low electrical conductivity of the ZrB_2 reinforcement compared to pure Cu. As per the above results, it is observed that the Cu (milled) composites showed better electrical properties compared to Cu-Al (milled and mixed) alloys.

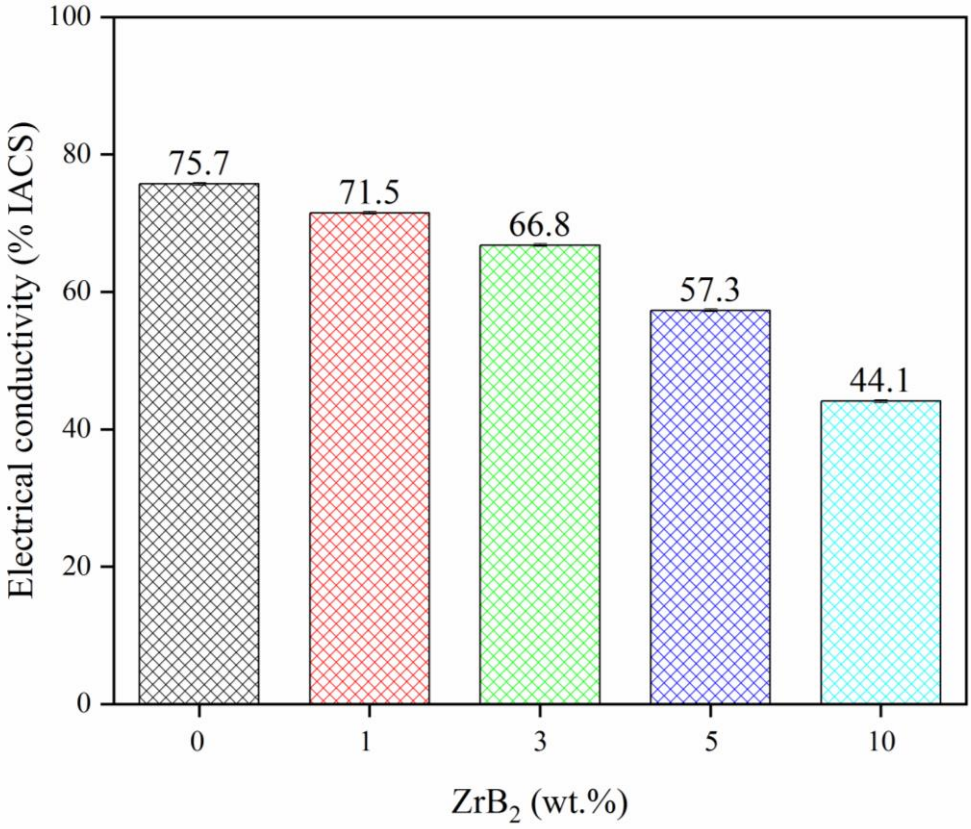

Fig. 6.11 Effect of ZrB_2 content on the electrical conductivity of Cu.

Thus, the electrical conductivity will be reduced by incorporating the reinforcement into the Cu matrix which is directly proportional to it. Other factors include the impurity atoms in the copper lattice causing scattering of electrons. The electrical conductivity of different copper composites processed via different processing techniques is listed in **Table 6.4**. From the literature [9,118,148,175], the electrical conductivity of various Cu-based composites was found to be in the range between ~18% IACS to 90% IACS. Also, it is observed that the high-temperature process or secondary processes such as heat treatment were carried out to enhance the electrical conductivity of composites, which can potentially decrease either the mechanical or other properties and increase the production cost.

Table 6.4 Electrical conductivity of different copper composites fabricated through powder metallurgy route.

Alloy	**Processing technique**	**Electrical conductivity (% IACS)**	**Ref.**
Cu (ML)	HP: 500 ^{o}C, 500 MPa, 30 min.	75.70	Present study
C1Z (ML)	,,	71.50	,,
C3Z (ML)	,,	66.80	,,
C5Z (ML)	,,	57.30	,,
C10Z (ML)	,,	44.10	,,
Cu-5Cr-3Al_2O_3	HP: 950 ^{o}C, 35 MPa, 4 h	66.40	[175]
Cu-2.5Al_2O_3	PS: 950 ^{o}C, 2 h	61.80	[118]
Cu-7.5Al_2O_3	,,	31.80	[118]
Cu-12.5Al_2O_3	,,	18.50	[118]
Cu-0.2La_2O_3	PS: 850 ^{o}C for 3 h, HT: 650^{o}C for 3 h, Ex: 750^{o}C	90.50	[148]
Cu-0.6La_2O_3	,,	86.40	[148]
Cu-1La_2O_3	,,	81.90	[148]
Cu-1.3La_2O_3	,,	78.10	[148]
Cu-1.05Zr-0.25B	Casting: 1150-1250 ^{o}C	76.80	[9]
Cu-2.11Zr-0.5B	,,	65.40	[9]
Cu-3.15Zr-0.75B	,,	56.30	[9]
Cu-4.25Zr-1.0B	,,	52.90	[9]

Note: HP: Hot-pressing, PS: Pressureless sintering, HT: Heat treatment, and Ex: Extrusion

The present study demonstrates that the incorporation of ZrB_2 has significantly enhanced the strength and wear properties of Cu without much compromising on the electrical conductivity. Based on these results, the hot-pressed Cu-ZrB_2 (milled) composites can become a very promising material for EDM electrodes.

Chapter 7

Densification, mechanical, wear and electrical properties of Cu-ZrB_2 composites processed via mixing route

Chapter 7

The present chapter reports the processing of Cu-ZrB_2 composites via hot-pressing (mixing route). The effect of mixing of powder compositions on the densification of Cu-ZrB_2 (mixed) composites has been studied. The microstructural phases in composites after hot-pressing was confirmed by SEM-EDS and XRD. Also, the hardness and compressive strength of Cu-ZrB_2 (mixed) composites were measured. The abrasive wear behaviour of Cu-ZrB_2 (mixed) composites was studied against SiC emery paper. Further, SEM analysis of worn surfaces, wear debris and counter body was carried out to determine the underlying wear mechanisms. Finally, the electrical conductivity of Cu-ZrB_2 (mixed) composites was determined to predict the suitable applications for the same materials.

7.1 Morphology of Cu-ZrB_2 (mixed) powders

The SEM images of the Cu-ZrB_2 (mixed) powders using a planetary ball mill at 100 rpm for 1 h with BPR of 2:1 is presented in **Fig. 7.1**. The pure copper and milled ultra-fine ZrB_2

powder particles were shown in **Fig. 7.1 (a-b)**. In mixing route, the ultra-fine ZrB_2 particles adhered on the surface of Cu powder particles unlike ZrB_2 particles embedded into Cu at severe milling conditions (see **Fig. 6.1** in **Chapter 6**). The ultra-fine ZrB_2 powders were loosely bonded with the Cu particles after mixing operation. From **Fig. 7.1 (a-b)**, it can be observed that the Cu and ZrB_2 powders were uniformly mixed using the milling operation.

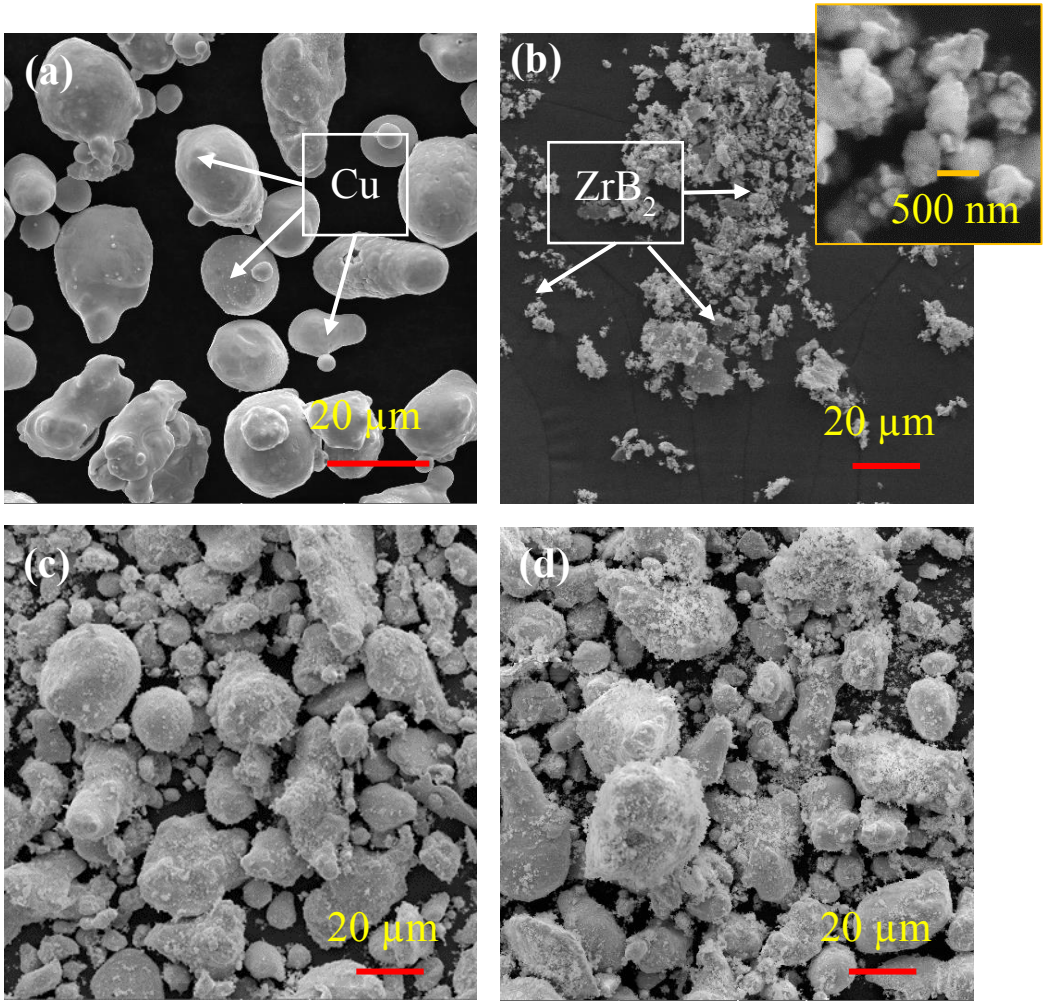

Fig. 7.1 SEM images mixed powders after 1 h ball milling at 2:1 BPR ratio (a) Cu, (b) ZrB_2, (c) C5Z (MX) and (d) C10Z (MX).

7.2 XRD phases and microstructural studies of hot-pressed Cu-ZrB_2 (mixed) composites

Pure Cu is one of the suitable materials for industrial applications that require good electrical and thermal conductivities, but it possesses low strength and wear resistance. In alloying, the strength of the Cu can be increased by solid solution strengthening but other

properties like electrical and thermal conductivities may be adversely affected [48,280]. In this regard, dispersion strengthening will become a good choice to improve the strength of Cu (by reinforcing with ceramic or any suitable reinforcement) without losing much of its conductivity and tribological properties.

Fig. 7.2 represents the X-ray diffraction patterns of hot-pressed Cu-ZrB_2 (mixed) samples. The XRD patterns showed the presence of Cu and ZrB_2 peaks. The X-ray diffraction phase analysis indicated the absence of any new phases during the hot press sintering process. The ZrB_2 peaks have lower intensity than it is expected since there could be a possibility of the low concentrated nano/submicron-sized ZrB_2 particles which embedded in the Cu matrix. The microstructure of sintered C3Z (MX) and C10Z (MX) samples is shown in **Fig. 7.3**. From **Fig. 7.3 (a-b),** it is noticeable that the ZrB_2 reinforcement was uniformly distributed in the C3Z (MX) composites. The grey contrast phase represents Cu, whereas the dark contrasting phase denotes ZrB_2.

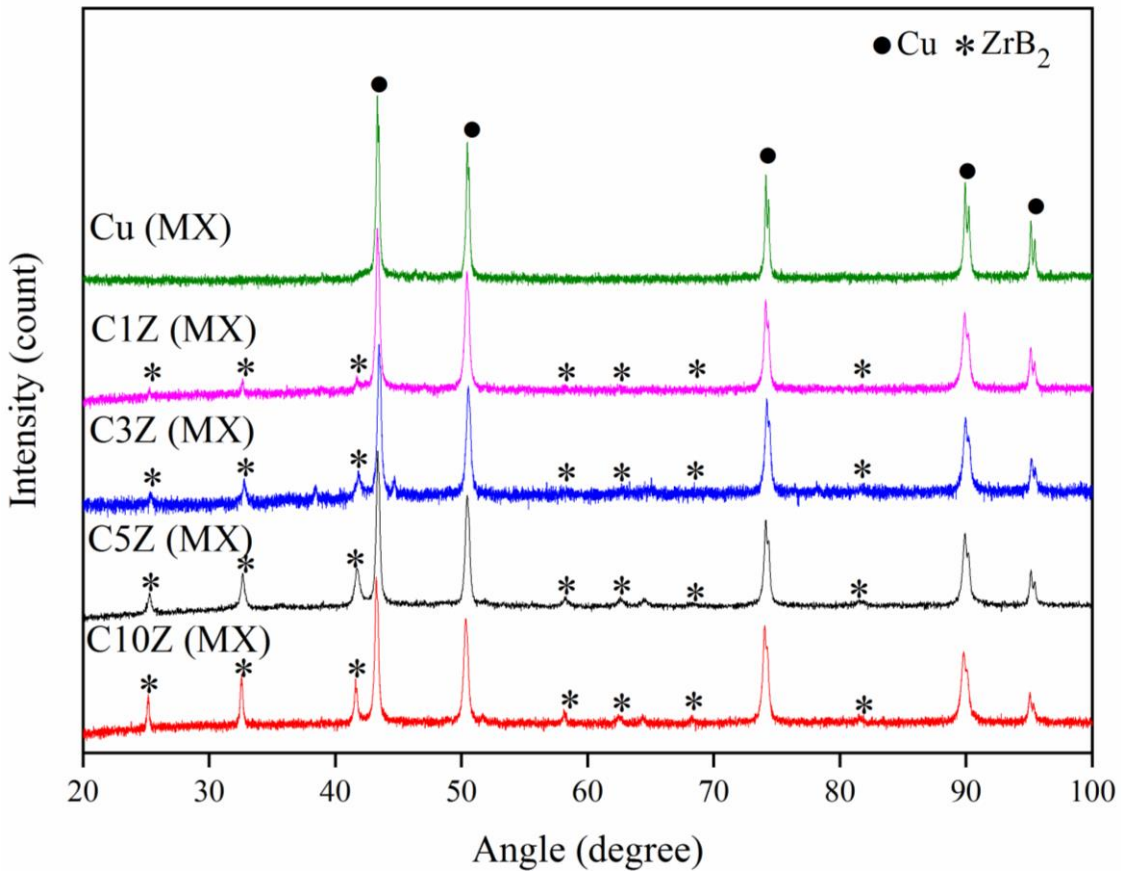

Fig. 7.2 X-ray diffraction patterns of hot-pressed Cu-XZrB_2 (X: 0, 1, 3, 5 and 10 wt.%) composites after hot pressing at a sintering temperature of 500 ˚C, 500 MPa pressure for 30 min.

In case of C10Z (MX), the SEM image reveals that the ultra-fine ZrB_2 particles were unevenly distributed at the grain boundaries of Cu grains (see **Fig. 7.3c and 7.3d**). The corresponding elemental mapping of C10Z (MX) composites confirms the presence of ZrB_2 at the grain boundaries of Cu.

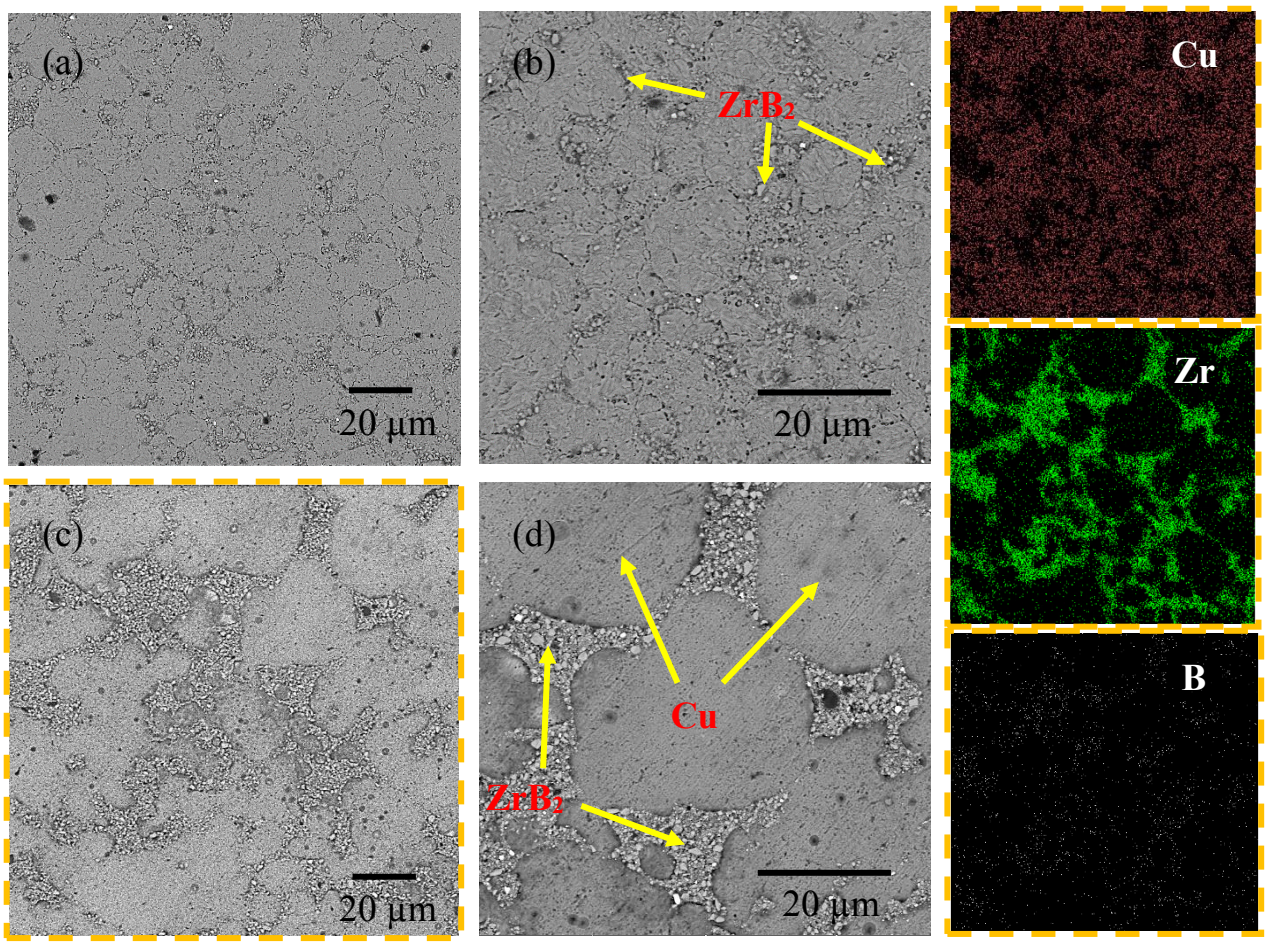

Fig. 7.3 SEM images showing the distribution of ZrB_2 reinforcement in Cu composites (a) C3Z (MX) (low magnification), (b) higher magnification of the C3Z (MX), (c) C10Z (MX) (low magnification) and (d) higher magnification of C10Z (MX). Corresponding elemental mapping of C10Z (MX) is presented.

7.3 Densification of the Cu-ZrB_2 (mixed) composites

The density of hot-pressed Cu-ZrB_2 (mixed) composites was tabulated in **Table 7.1**. The measured bulk density of Cu-ZrB_2 (mixed) composites decreased from 8.93 to 8.21 g/cc with an increase of ZrB_2 content. The reduction in Cu composites density with the addition of ZrB_2 was mainly due to the low density of ZrB_2 (6.10 g/cc). The densification of Cu composites also observed to lower (99.76 - 96.02%) with ZrB_2 addition. A decrease in the densification of

Cu composites with the ZrB_2 addition can be attributed to refractoriness, agglomeration and its non-uniform distribution at the Cu-Cu grain boundaries which restricted the densification (see **Fig. 7.3**).

Table 7.1 The bulk density, theoretical density and relative density of the Cu-ZrB_2 (mixed) composites

Sample reference	Bulk density (g/cc)	Theoretical density (g/cc)	Relative density (%)
Cu (MX)	8.93	8.96	99.76
C1Z (MX)	8.81	8.91	98.85
C3Z (MX)	8.71	8.83	98.66
C5Z (MX)	8.52	8.75	97.39
C10Z (MX)	8.21	8.55	96.02

Nevertheless, the densification results indicate that the relative densities of all Cu-ZrB_2 (mixed) composites could be densified more than 96% (despite the use of low processing temperature of 500 ^oC). Wang et al. [27] processed the Cu-ZrB_2 composites via hot-pressing route (high sintering temperature: 840 ^oC and pressure: 25 MPa and time: 2 h). They reported that considerable reduction of Cu-ZrB_2 composites densification (from 96.1 to 91.3%) with ZrB_2 content (1-9 wt.%). Such reduction was attributed to Cu particles agglomeration and ZrB_2. From the above discussion, it should be realised that the selected hot-press parameters are advantageous in achieving good densification of Cu-ZrB_2 composites even at low processing temperatures.

7.4 Mechanical properties of Cu-ZrB_2 (mixed) composites

7.4.1 Hardness and compressive strength

Fig. 7.4 demonstrates the variation in the hardness of Cu & Cu-ZrB_2 (mixed) composites. As the ZrB_2 content increased the Cu hardness increased. The average hardness value of 0.88 GPa was measured for Cu (MX) and it increased to a maximum of 1.25 GPa with the further addition of 10 wt.% ZrB_2 to Cu. The hardness (by 42.0%) enhanced considerably for C10Z (MX) compared with Cu (MX). Pouyani et al. [279] fabricated the Cu-ZrB_2

nanocomposites by microwave-assisted sintering. They achieved a maximum hardness of 0.95 GPa with the 10 wt.% ZrB_2 content.

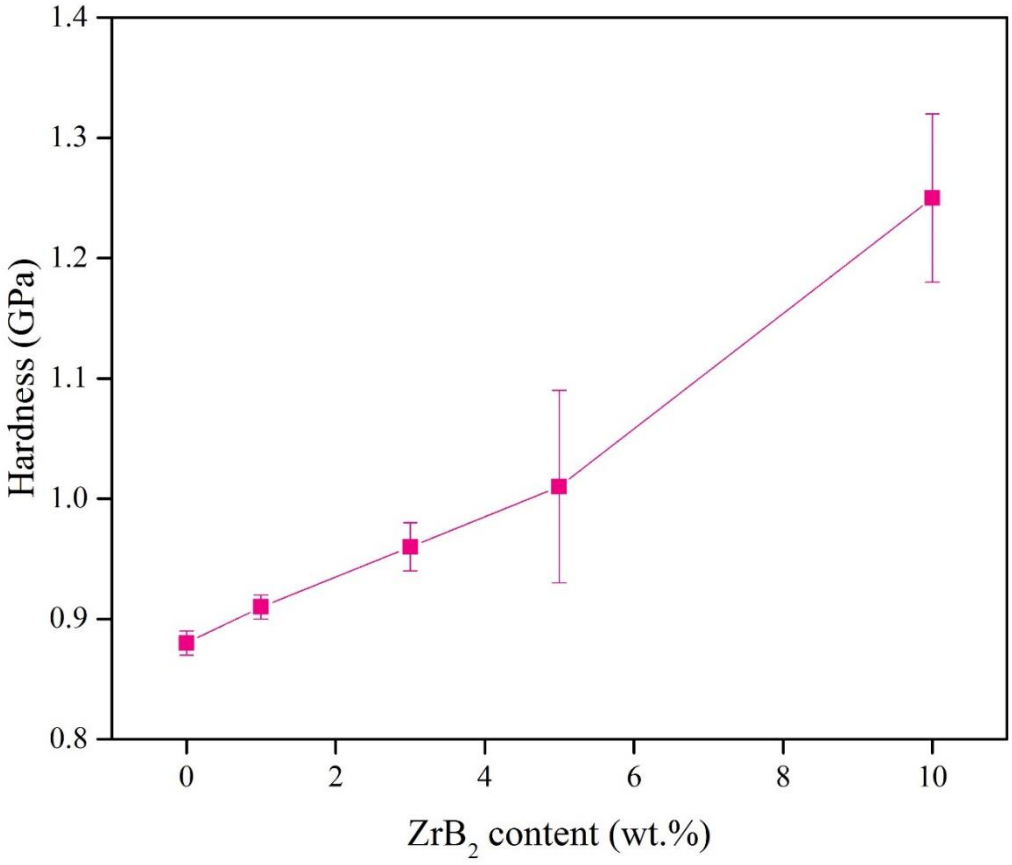

Fig. 7.4 Effect of ZrB_2 content on the hardness of hot-pressed Cu-ZrB_2 composites.

Fathy et al. [44] processed Cu-ZrO_2 composites via in-situ reactions and observed an increase in hardness with the ZrO_2 content. They could observe maximum hardness of 0.5 GPa for Cu and it increased to 0.75 GPa for Cu- 9 wt.% ZrO_2. The occurrence of ultra-fine reinforcement particles at grain boundaries of copper restricted the plastic flow of the material; thus improving the hardness of the composites [44,186]. Also, the good interfacial bonding between Cu and secondary reinforcement particles responsible for a rise in the hardness of composites. Since the more difference in the coefficient of thermal expansions of Cu and ZrB_2 is expected, it results in the development of residual stress in the composites. Thus, the hardness of Cu-ZrB_2 materials increased with the increase of ZrB_2 content. In recent work, it was reported that the use of fine ZrB_2 particles (~10 µm) enhanced the hardness of Cu-(0-9 wt.%) ZrB_2 composites (up to ~1.0 GPa) with the ZrB_2 reinforcing content (up to 7 wt.%) and then more addition of ZrB_2 lowered hardness due to the poor interfacial bonding and severe agglomeration of particles [118].

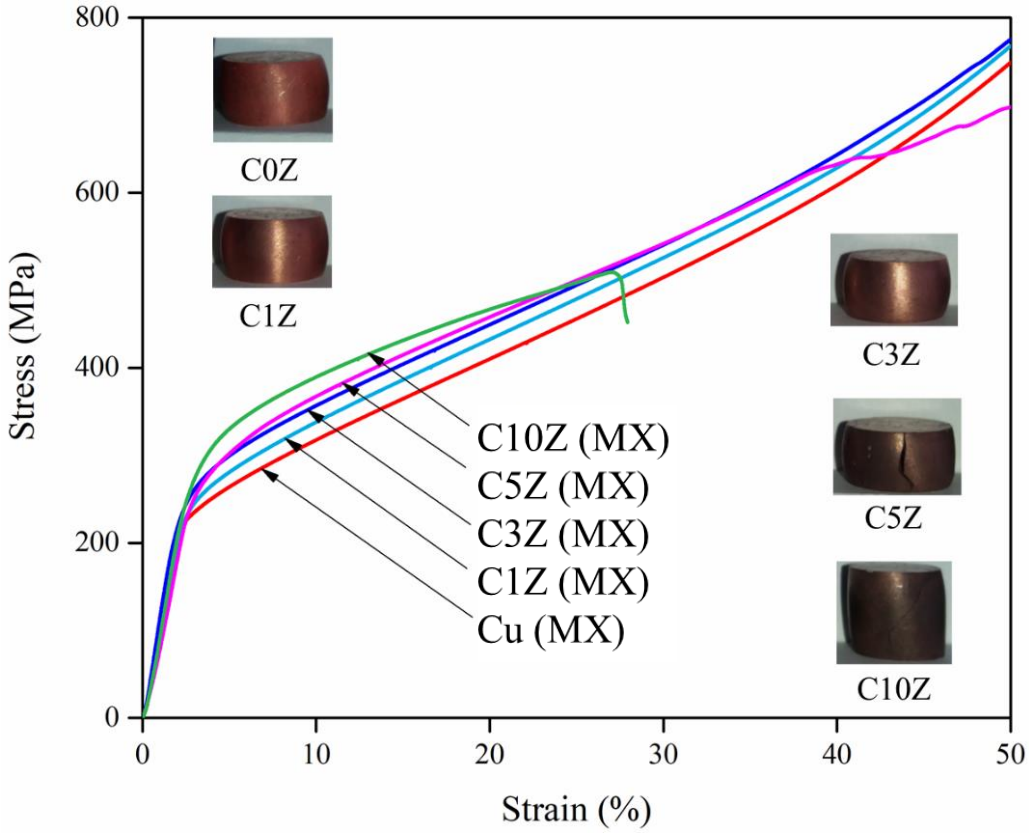

Fig. 7.5 Compression stress-strain curves of Cu-ZrB_2 (mixed) composites and photographs of fractured samples after compression test.

The compression (stress-strain) plots of Cu-ZrB_2 (mixed) composites presented in **Fig. 7.5**. From the plot, it can be observed that no fracture has occurred in the Cu (MX), C1Z (MX) and C3Z (MX) samples during a compression test because of its high ductile nature of Cu. These samples bulged without fracture and the test was continued upto 50 % strain. In C5Z (MX) and C10Z (MX) samples, the occurrence of fracture was observed during the compression test at a strain of 37.5% and 28.6%, respectively. The common observation from **Fig. 7.5** is that the compressive strength of Cu increased and the percentage of strain was lowered with ZrB_2. The compression strength and strain properties of Cu-ZrB_2 (mixed) composites are tabulated in **Table 7.2**. The pure copper yield strength was found to be 214.0 ± 2 MPa. The yield strength of Cu improved with the ZrB_2 (10 wt.%), it reached a maximum of 261.5 ± 1 MPa, which is ~ 22% higher than the yield strength of Cu (MX). A very nominal increase in the strength was witnessed in Cu composites with the ZrB_2 reinforcement.

Table 7.2 The hardness and compression test results of Cu-ZrB_2 (mixed) composites.

Sample reference	Hardness (GPa)	Compressive strength (MPa)	Strain (%)
Cu (MX)	0.88 ± 0.01	551.3 ± 8	50.00*
C1Z (MX)	0.91 ± 0.01	575.4 ± 6	50.00*
C3Z (MX)	0.96 ± 0.02	589.6 ± 4	50.00*
C5Z (MX)	1.01 ± 0.08	588.1 ± 5	38.50 ± 1.3
C10Z (MX)	1.25 ± 0.07	508.5 ± 3	28.60 ± 0.6

* Fracture was not observed in the specimens even up to 50% elongation.

In summary, the addition of ultra-fine reinforcement enhances the compressive strength of Cu by restricting the movements of dislocations during compressive loading [11]. In case of Cu-(0-15 wt.%) Al alloys, the hardness of Cu (ML) increased to 6.16 GPa and strength above 1000 MPa [50,281]. Surprisingly in the Cu-ZrB_2 (mixed) composites, the maximum hardness of 1.25 GPa could be realized despite the addition of hard ZrB_2 reinforcement. It appears that solid solution and or insitu-intermetallic formation in Cu alloys is more effective in improving the mechanical properties of ductile metals like Cu than dispersion strengthening.

7.5 Abrasive wear behaviour of Cu-ZrB_2 (mixed) composites

7.5.1 Coefficient of friction (COF)

The COF vs sliding distance of ZrB_2 reinforced Cu composites is shown in **Fig. 7.6**. The COF of Cu composites was found to decrease with the ZrB_2 reinforcement. The COF curve of any material is classified into run-in and steady-state segments [261]. From **Fig. 7.6**, it can be observed that the run-in curve of Cu (MX) appears to be a normal shape; where the higher frictional forces developed in the initial stage of the run-in period due to the initial roughness of sample [261]. This roughness performs the interlocking phenomenon between the new surface and counter-body asperities. In Cu-ZrB_2 (mixed) composites, the high contact pressure drops the COF more steeply during the initial run-in period [282].

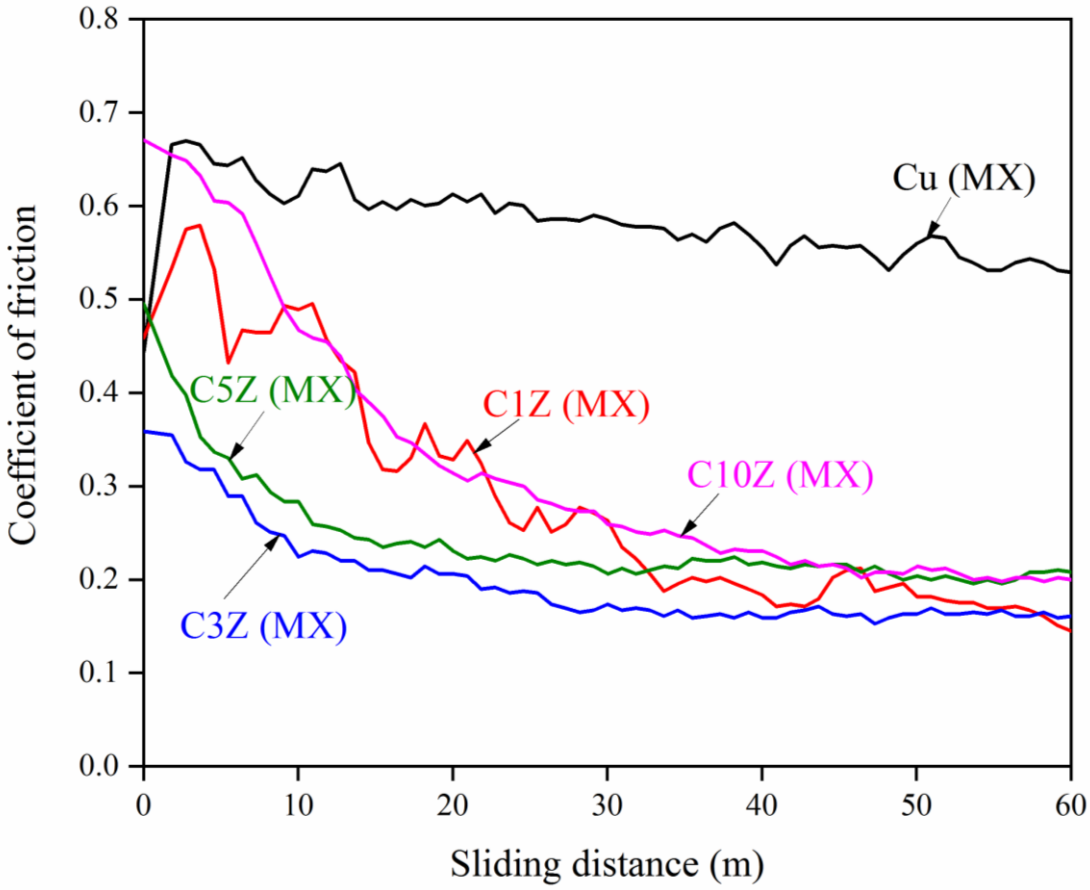

Fig. 7.6 Coefficient of friction of Cu-ZrB_2 (mixed) composites sliding against SiC emery (220 grit size) at a sliding velocity of 1 m/s.

In the present work, the SiC asperities were worn out slowly which prolong the run-in period of COF curves in Cu-ZrB_2 (mixed) composites. The steeper curves can be observed in the composites during the run-in stage (see **Fig. 7.6**). It was observable that the steady-state COF attained at about a sliding distance of 20 m for Cu (MX) which was happened due to the rapid penetration of hard SiC abrasives into the softer Cu and the COF stabilized as the contact pressure reduces. In the case of Cu-ZrB_2 (mixed) composites, the COF stabilized at around 40-45 m. This was happened because of the presence of ZrB_2 particles restrict the penetration of SiC abrasives into Cu matrix which further maintains high contact pressure (or low contact area) until the sharp asperities of SiC get worn out. Then the COF curve of composites becomes steady-state after the contact pressure reduces.

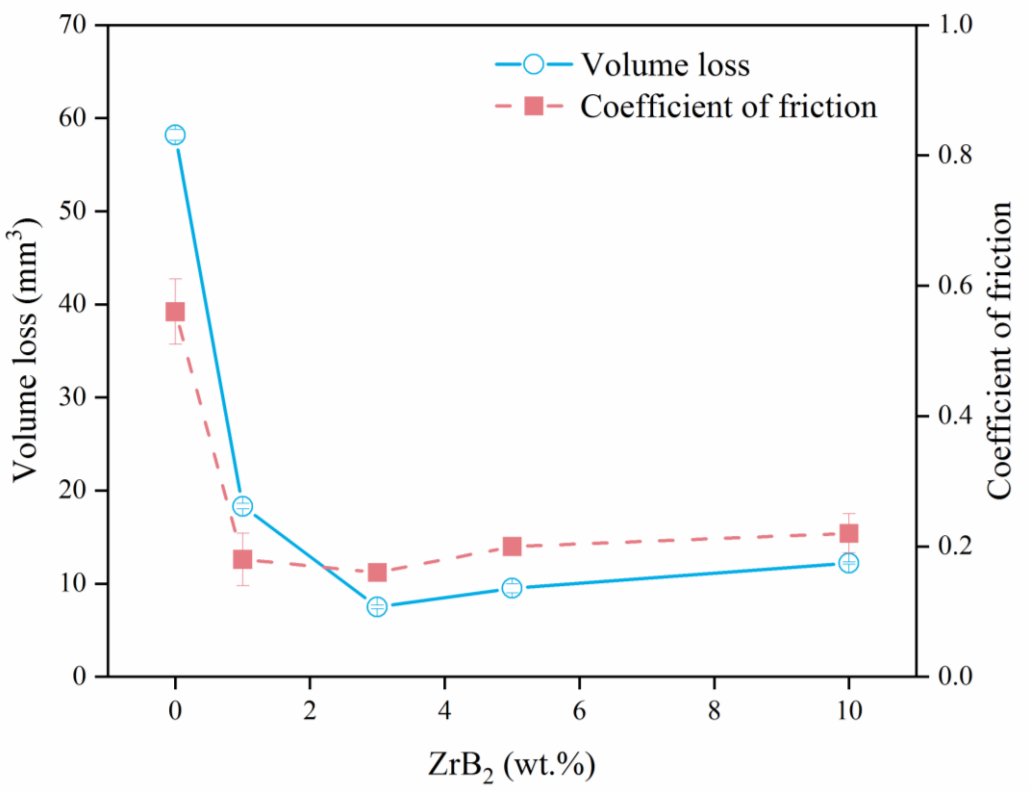

Fig. 7.7 Comparison of the coefficient of friction and volume loss of Cu-ZrB_2 (mixed) composites sliding against SiC emery of 220 grit size at a sliding velocity of 1 m/s.

The high COF (0.56 ± 0.05) of Cu (MX) was obtained due to high frictional forces developed between soft Cu matrix and hard SiC abrasives. As the penetration depth increases, the contact area between the two bodies will be increased which further increases the frictional forces as well as the COF of the material. The COF of ZrB_2 added Cu composites varied between 0.56 ± 0.05 and 0.16 ± 0.01. The composites including C3Z (MX), C5Z (MX) and C10Z (MX) showed slight fluctuations and almost smooth curves. Interestingly, C3Z (MX) composite showed a low COF of 0.16 ± 0.01 and it was reduced by 3.5 times compared to Cu (MX). The lower COF obtained in C3Z (MX) was mainly caused due to the presence of uniformly distributed ZrB_2 in the matrix which developed the low frictional forces as they slide against hard SiC (hard particles interaction). Also, the entrap of wear debris and third body (ZrB_2 particles) in the spacing between the SiC abrasives provides more contact area and rolling effect between the sample surface and counterbody.

Table 7.3 The wear results of the Cu-ZrB_2 (mixed) composites after the abrasive wear test

Sample reference	Coefficient of friction	Vol loss (mm^3)	Sp. wear rate ($\times 10^{-3}$ mm^3/Nm)	Wear coefficient ($\times 10^{-2}$)
Cu (MX)	0.56 ± 0.05	58.20 ± 0.6	198.00 ± 06	17.33
C1Z (MX)	0.18 ± 0.04	18.30 ± 0.3	62.30 ± 02	5.64
C3Z (MX)	0.16 ± 0.01	7.50 ± 0.2	25.60 ± 02	2.40
C5Z (MX)	0.20 ± 0.01	9.50 ± 0.5	32.50 ± 03	3.23
C10Z (MX)	0.22 ± 0.03	12.20 ± 0.1	52.00 ± 04	5.12

Nevertheless, further addition of ZrB_2 (up to 10 wt.%), there could also be chances of getting more amount of ZrB_2 particle interaction from the specimen surface with SiC emery paper during wear. Also, the low relative density, agglomeration of ZrB_2 at grain boundaries of Cu, weak bonding between ZrB_2 particles and presence of the third body (ZrB_2) influence the slight increase of COF up to 0.22 ± 0.03 (see **Fig. 7.7**). The summary of wear test results after the wear test is given in **Table 7.3**.

7.5.2 Effect of ZrB_2 on wear coefficient

The difference in wear volume of Cu with the ZrB_2 amount is shown in **Fig. 7.7**. The wear volume reduced significantly from 58.2 ± 0.6 mm^3 to 7.5 ± 0.2 mm^3. The wear volume plot of composites was similar to the COF trend, i.e., low wear loss was observed in the case of C3Z (MX) composites and it increased with the further addition of ZrB_2. The low wear loss of 7.5 ± 0.2 mm^3 was recorded for C3Z (MX) composite. The influence of ZrB_2 on the wear coefficient of Cu composites is demonstrated in **Fig. 7.8**. Substantial diminution in the Sp. wear rate and wear coefficient of Cu composites was observed with ZrB_2. The Sp. wear rate of the Cu-ZrB_2 composites varied between 198 ± 0.5 to 52 ± 0.6 mm^3/Nm. The wear coefficient of ZrB_2 reinforced Cu (MX) samples varied in the range of 17.33×10^{-2} to 2.4×10^{-2}. The wear coefficient of C3Z (MX) was lowered by 7.22 times than Cu (MX). This increase in wear resistance of C3Z (MX) can be credited to even distribution of ZrB_2 in Cu, its high hardness and strength.

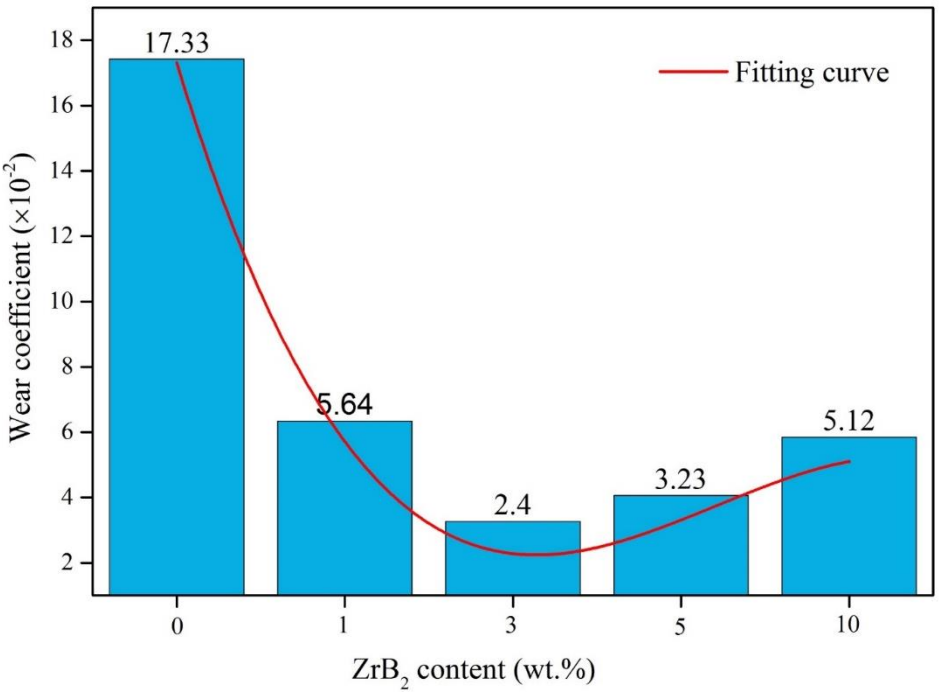

Fig. 7.8 Wear coefficient of Cu-ZrB_2 (mixed) composites sliding at a speed of 1 m/s and a load of 5 N.

The tribological properties of various Cu-based composites [45,118,120,188] tested under abrasive wear conditions are presented in **Table 7.4.** Based on the literature, the wear coefficient of various Cu-based composites under abrasive test conditions varied in the range from ~1.00×10^{-4} to ~4.88×10^{-2}. From the above discussion, it can be noted that the present Cu-ZrB_2 (mixed) composites showed moderate wear performance. Such difference in the wear of materials depends on the processing conditions, densification, mechanical properties of composites, the hardness of reinforcement and counterbody characteristics and wear test conditions [45].

Table 7.4 The abrasive wear of various Cu composites prepared by various processing methods.

Alloy	**Processing conditions**	**Wear test conditions**	**Hardness, Hv (GPa)**	**Wear coefficient**	**Ref.**
Cu-2.5Al_2O_3	Thermochemical treatment, *CP*: 950 °C, 600 MPa, for 2 h	*l*: 4, *v*: 1.07, *d*: 200, *t*: 3.1, *C.B:* SiC (400 grit)	0.78	~13.25 E-3	[118]
Cu-7.5Al_2O_3	,,	,,	0.86	~9.84 E-3	[118]
Cu-12.5Al_2O_3	,,	,,	0.97	~4.83 E-3	[118]

Cu-5vol.% SiC	*HIP*: 880 ^{o}C, 100 MPa for 1.5 h	*l*: 15, *v*: 1.0, *d*: 40, *t*: 0.6, *C.B:* SiC (240 grit)	0.99	0.77 E-2	[120]
Cu-10vol.% SiC	,,	,,	1.13	1.40 E-2	[120]
Cu-15vol.% SiC	,,	,,	1.00	1.67 E-2	[120]
Cu-20vol.% SiC	,,	,,	1.01	2.74 E-2	[120]
Cu-5vol.% TiB_2	*HIP*: 800 ^{o}C, 100 MPa for 1.5 h	*l*: 15, *v*: 1.0, *d*: 100, *t*: 1.6, *C.B:* SiC (240 grit)	0.85	6.69 E-4	[45]
Cu-10vol.% TiB_2	,,	,,	0.88	3.30 E-4	[45]
Cu-15vol.% TiB_2	,,	,,	0.93	2.89 E-4	[45]
Cu-20vol.% TiB_2	,,	,,	1.01	1.00 E-4	[45]
Cu-3ZrO_2	Thermochemical treatment, *CP*: 950 ^{o}C, 700 MPa, for 2 h	*l*: 6, *v*: 1.0, *d*: 200, *t*: 3.3, *C.B:* SiC (240 grit)	0.88	~4.23 E-2	[188]
Cu-6ZrO_2	,,	,,	1.20	~4.88 E-2	[188]
Cu-9ZrO_2	,,	,,	1.36	~4.25 E-2	[188]

* *HIP*: Hot isostatic pressing, *CP*: Cold pressing, *l*: Load (N), *v*: Sliding velocity (ms^{-1}), *d*: Sliding distance, *t*: Time (min) and *C.B*: Counter-body.

7.5.3 Characterization of worn surfaces of Cu composites and wear mechanisms

The depth of worn surfaces was characterized by the 3D optical surface profiler (Model: HRM 300A, Huvitz, Korea). **Fig. 7.9** presents the 3D profiles of worn surfaces of Cu-ZrB_2 (mixed) composites. The depth of worn surface profiles of Cu was reduced with the addition of ZrB_2. The depth of grooves for Cu-ZrB_2 (mixed) composites varied from 24.5 µm to 5.6 µm. From **Fig. 7.9**, it can be observed that the worn surface of Cu (MX) characterized with deep grooves with a depth (R_z) of 24.5 µm. The minimum depth was observed in C3Z (MX) composites (R_z: 5.6 µm) and a further increase of ZrB_2 content increased the depth slightly. These observations corroborate with the wear measurements of Cu (MX) samples. As mentioned earlier, the high wear coefficient was measured with Cu (MX) and it was low for C3Z (MX).

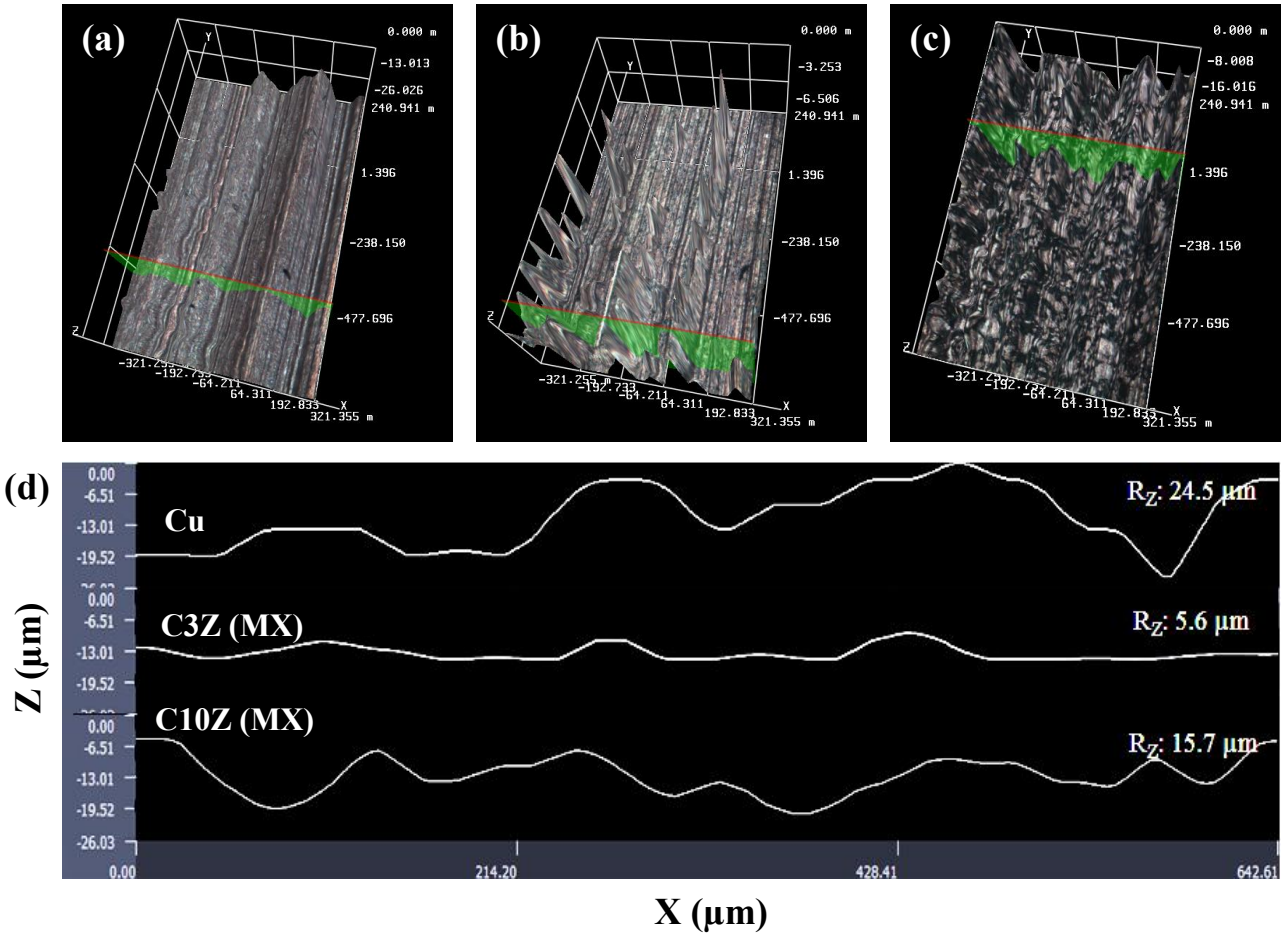

Fig. 7.9 The 3D surface profiles of Cu-ZrB_2 (mixed) composite worn surfaces after abrasive wear test. (a) Cu (MX), (b) C3Z (MX) and (c) C10Z (MX). (d) The roughness profiles of corresponding wear tracks for Cu, C3Z (MX) and C10Z (MX).

The detailed microstructural characterization of worn surfaces was carried out to understand the underlying wear mechanisms. **Fig. 7.10 (a,c)** indicates the worn surface of the Cu (MX) sample after sliding against 220 grit size SiC emery paper. **Fig. 7.10a** represents the worn surface with deep and narrow grooves which indicates the severe plastic deformation of Cu caused by hard SiC abrasive asperities. Such observations can also be related to the surface profiles of worn surfaces presented in **Fig. 7.9** which supports well of those characteristics. **Fig. 7.10c** indicates the sample surface produced the sharp ridges by plowing mechanism; further it leads to the development of big wear debris. From EDS analysis of the Cu (MX) surface after wear test, no evidence of oxygen presence was found which indicates that no tribo-oxidation took place as SiC removed the sample material during sliding (see **Fig. 7.10b**).

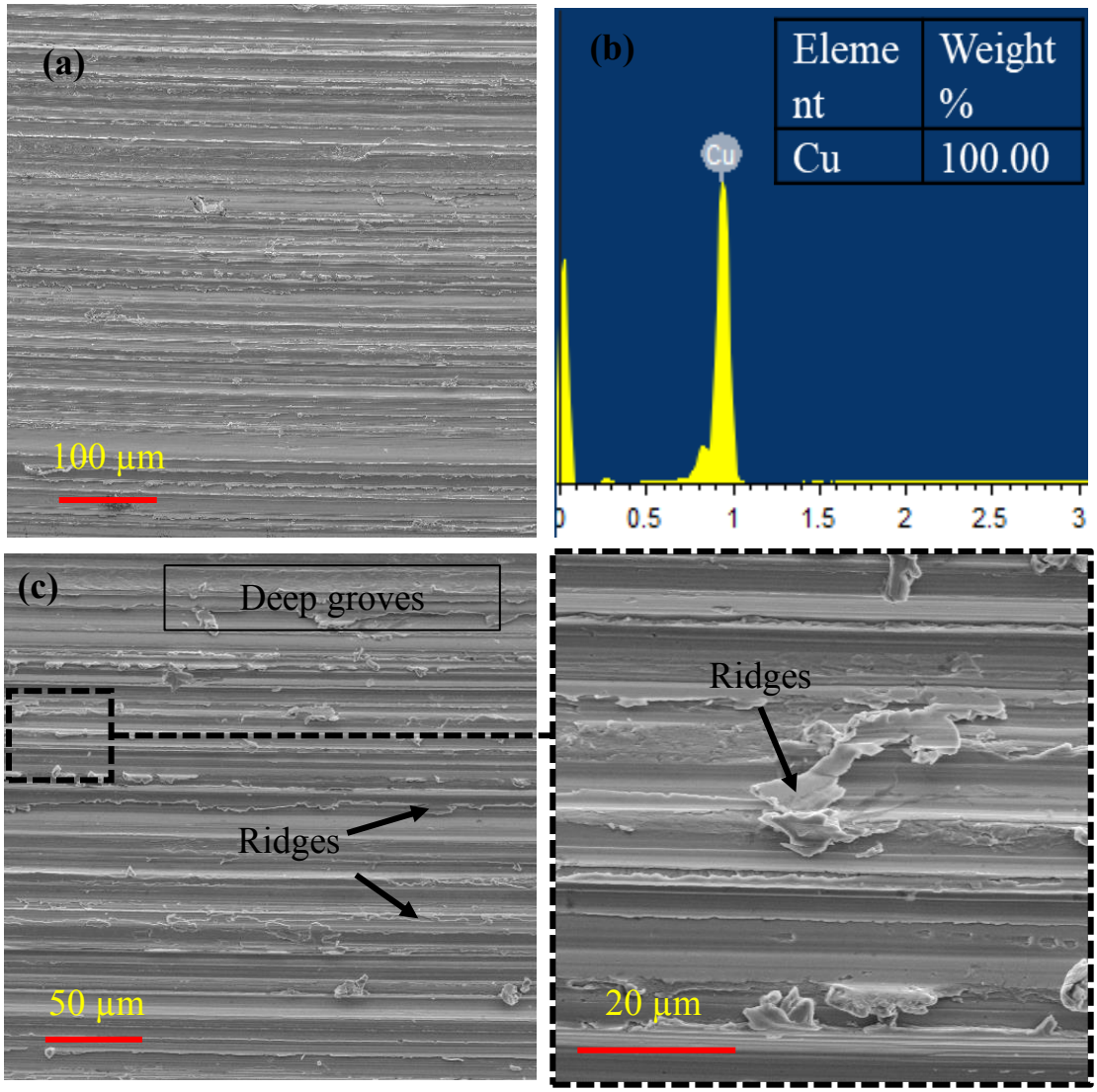

Fig. 7.10 SEM images of worn surface of Cu (MX) after sliding against 220 grit size SiC emery paper at 5 N and sliding velocity of 1 m/s. (a) Low magnification image of the worn surface, (b) EDS of wear worn surface and (c) high magnification image of worn surface.

This implies that a new surface was exposed whenever the hard SiC slid over the ductile Cu which leads to the high material removal rate of Cu. **Fig. 7.11 (a,c)** shows the SEM of worn surfaces of C1Z (MX). From **Fig. 7.11a**, it can be observed that the amount of ridges formed due to plastic deformation is reduced with the addition of ZrB_2. Also, it can be understood that the ultra-fine ZrB_2 restrict the plastic flow of Cu; thereby, improvement in the hardness, strength, and wear properties of composites can be achieved; which is evidenced by the transformation of wear tracks from deep groves to shallow groves during the wear of C1Z (MX) (compare **Figs. 7.10 and 7.11**).

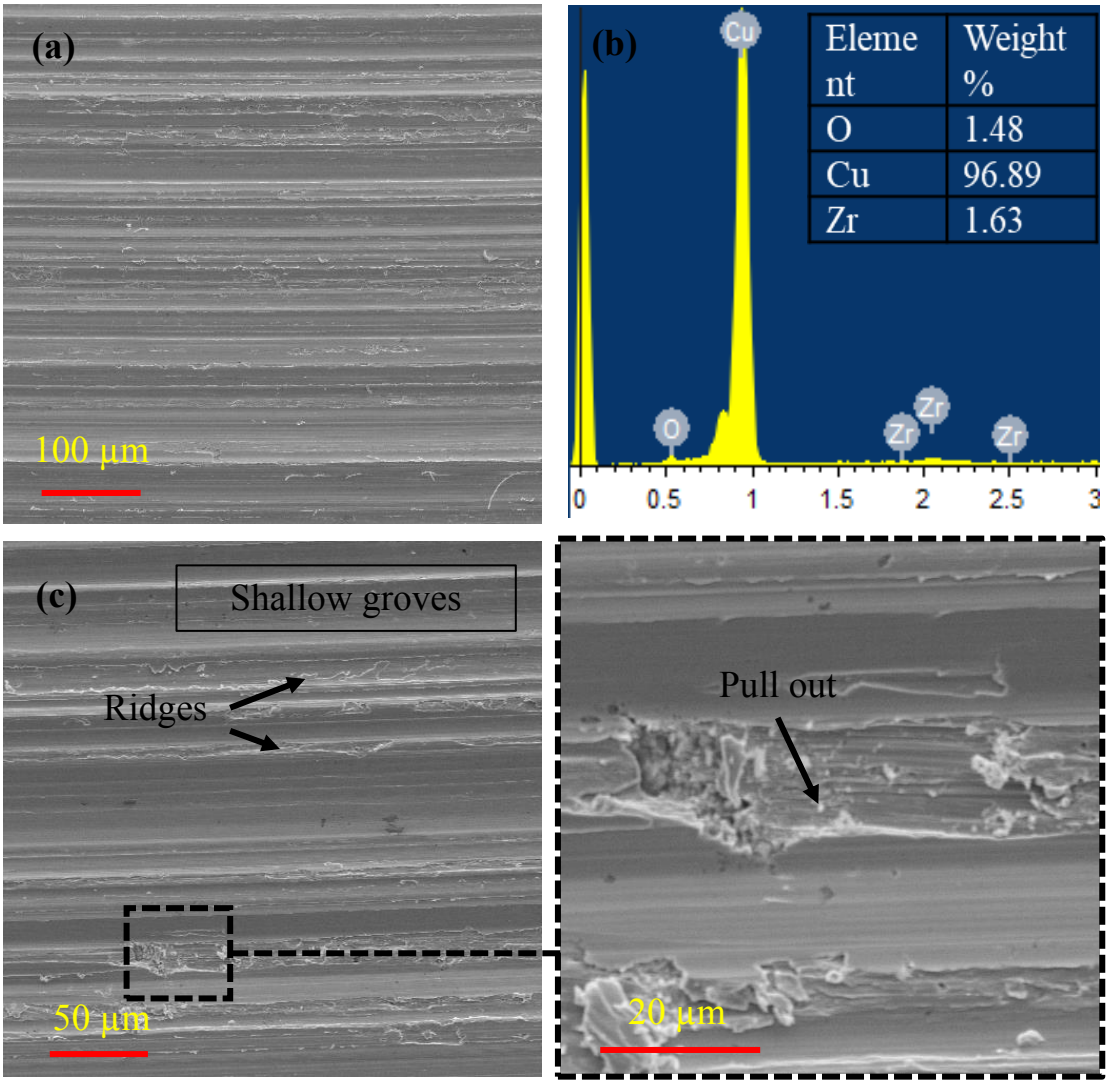

Fig. 7.11 SEM images of worn surface of C1Z (MX) after sliding against 220 grit size SiC emery paper at 5 N and sliding velocity of 1 m/s. (a) Low magnification image of the worn surface, (b) EDS of wear worn surface and (c) high magnification image of worn surface.

During the abrasive wear of C1Z (MX), the majority of the material was found to be removed by the plowing action and the minor amount of material was pulled out when the hard SiC abrasives hit the hard ZrB_2 particles during sliding wear. These damaged sites were shown with the dotted line (see **Fig. 7.11c**). Also, EDS (**Fig. 7.11b**) showed the presence of oxygen due to the presence of ZrB_2 agglomerates at the grain boundaries of Cu. The worn surface of C3Z (MX) composites after sliding against 220 grit size abrasives are shown in **Fig. 7.12**. The C3Z (MX) samples produced the shallow and wide groves after wear test similar to the C1Z (MX). Also, the wear takes place by plowing which is the predominant wear mechanism in C3Z (MX). **Fig. 7.12a** shows the minor damaged sites over the worn surface.

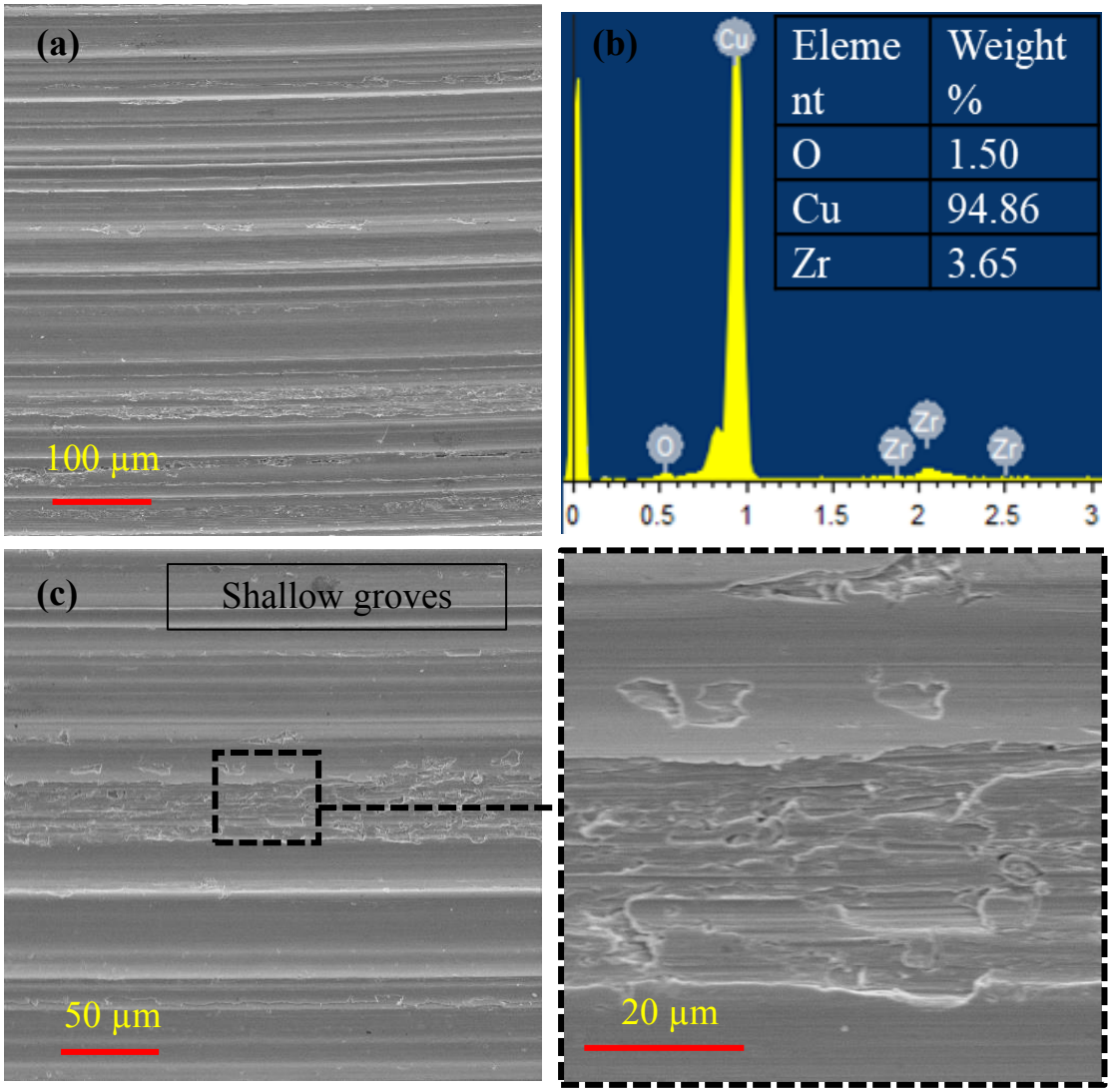

Fig. 7.12 SEM images of worn surface of C3Z (MX) after sliding against 220 grit size SiC emery paper at 5 N and sliding velocity of 1 m/s. (a) Low magnification image of the worn surface, (b) EDS of wear worn surface and (c) high magnification image of worn surface.

As the ZrB_2 content increased up to 3 wt.%, no ridge formation has appeared on the surface of the composite which represents the reduction of plastic deformation of material and enhancement in wear resistance. These observations are well correlated with shallow wear depth profiles and the low wear coefficient (2.4×10^{-2}) for C3Z (MX) composites (see **Figs. 7.8 and 7.9**). The presence of low oxygen content (1.5%) on worn surface resulted due to the development of heat during the wear process.

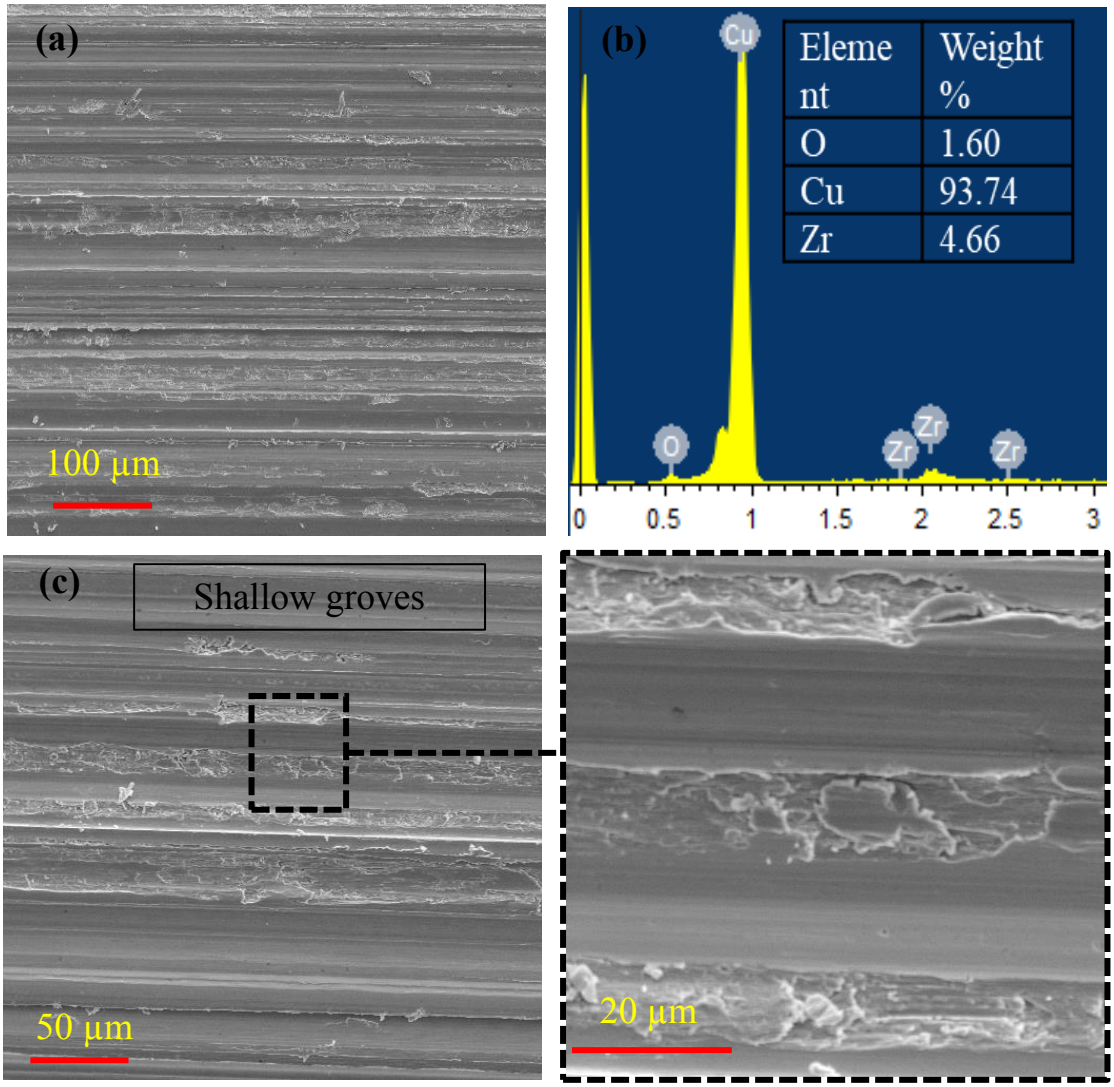

Fig. 7.13 SEM images of worn surface of C5Z (MX) after sliding against 220 grit size abrasive emery paper at 5 N and sliding velocity of 1 m/s. (a) Low magnification image of the worn surface, (b) EDS of wear worn surface and (c) high magnification image of worn surface.

Fig. 7.13 shows shallow and wide grooves presence on the C5Z (MX) wear sample surface. As the ZrB_2 reinforcement content increased to 5 wt.%, the damaged sites caused by SiC abrasives were increased. Also, there is a possibility of the more ZrB_2 particles get loosen from its grain boundary sites of composite (due to ZrB_2 agglomeration at the grain boundaries) during the wear process. Further, it exhibited more wear loss than C3Z (MX) composites. **Fig. 7.14** presents the worn tracks of C10Z (MX) composite after the abrasive wear test. From **Fig. 7.14a**, it can be seen that the C10Z (MX) sample showed severe damage over the entire worn surface as the ZrB_2 content increased.

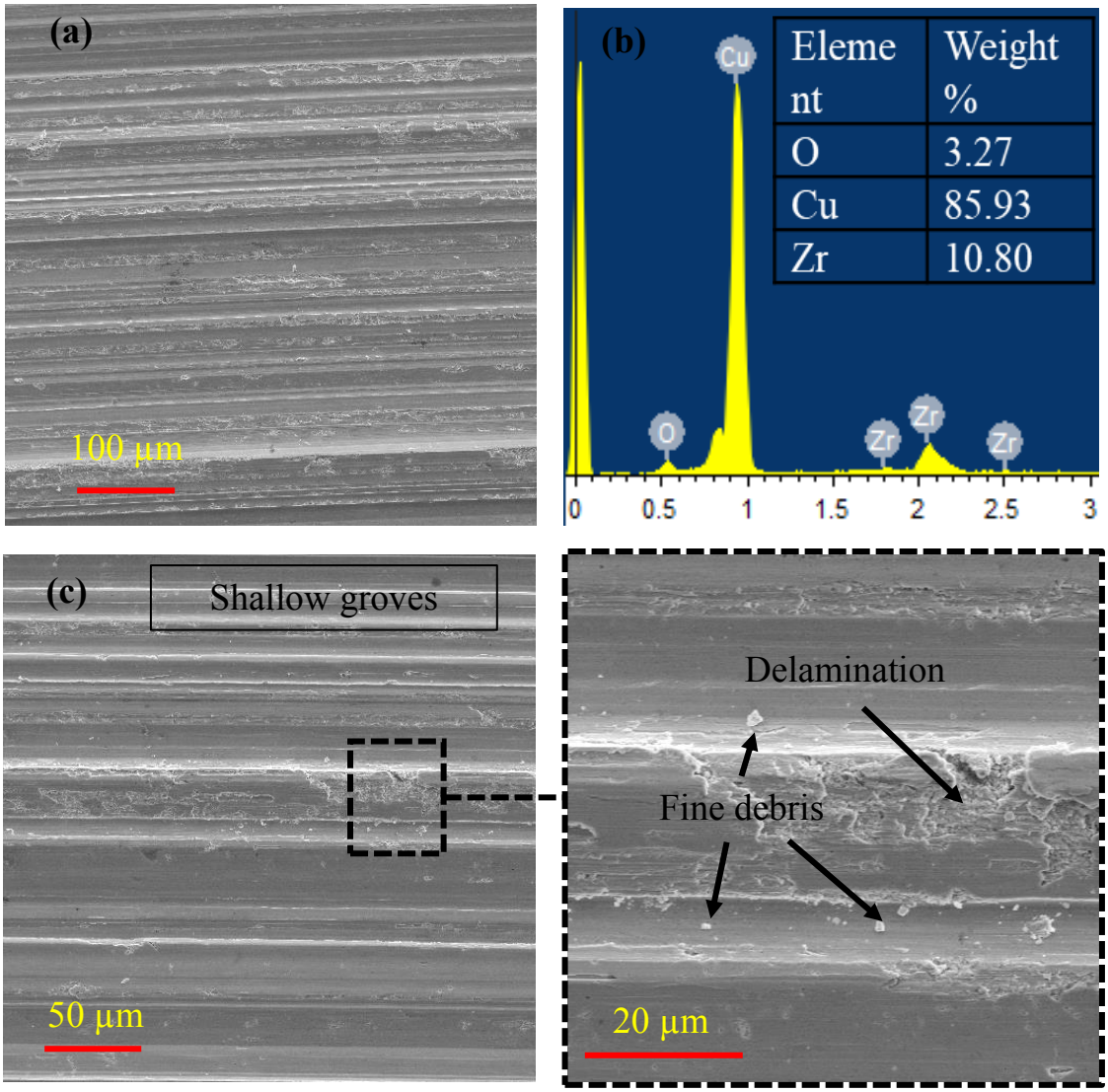

Fig. 7.14 SEM images of worn surface of C10Z (MX) after sliding against 220 grit size abrasive emery paper at 5 N and sliding velocity of 1 m/s. (a) Low magnification image of the worn surface, (b) EDS of wear worn surface and (c) high magnification image of worn surface.

The Cu grains are delaminated during sliding against the hard SiC abrasives and loosened hard ZrB_2 reinforcement. The low relative density of C10Z (MX) composites (96.02 %) also might cause a high material removal (5.12×10^{-2}) which is increased by 64 % compared to C3Z (MX). **Fig. 7.15** represents the schematic of possible abrasive wear mechanisms in Cu and Cu-ZrB_2 (mixed) composites. **Fig. 7.15a** indicates the plowing mechanism of pure Cu, in which repeatedly materials get removed by hard abrasive particles.

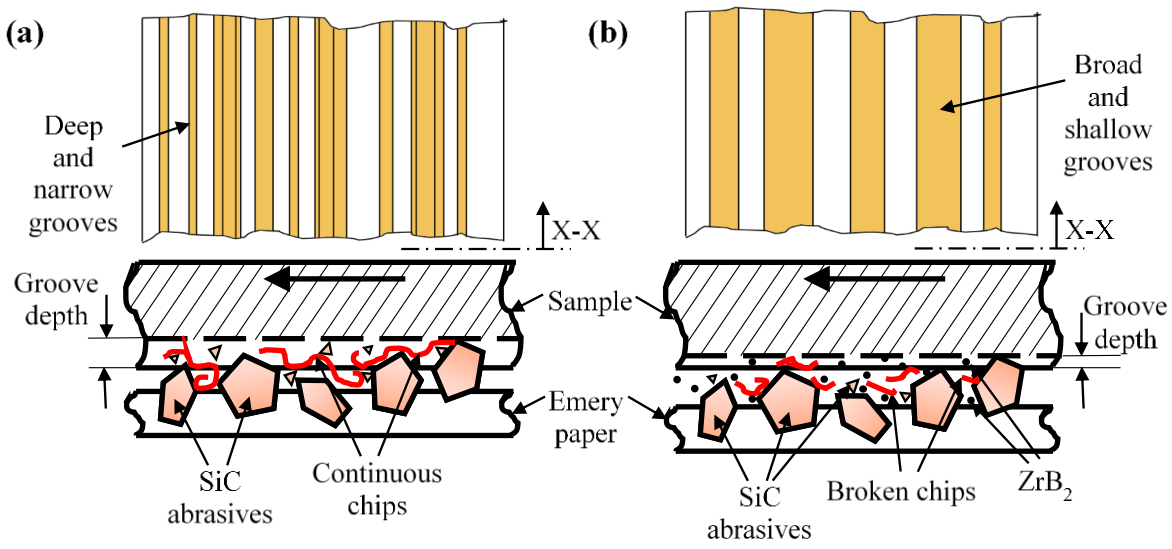

Fig. 7.15 Schematic of possible abrasive wear mechanisms. (a) Plowing abrasion in pure copper and (b) cutting mechanism due to abrasion in Cu-ZrB_2 (mixed) composites.

Further, it causes deep groves on the worn surface due to the severe plastic deformation. **Fig. 7.15b** indicates the conventional cutting mechanism; where, the presence of hard reinforcement interrupts the continuous chip formation and breaks the chips wherever the reinforcement is present. This kind of wear mechanism was observed in the C1Z (MX), C3Z (MX), C5Z (MX) and C10Z (MX) samples.

7.5.4 Wear of counter-body and surface analysis

The SEM images of counter-body (emery paper of 220 grit size) worn surface after abrasive wear test were carried out are represented in **Fig. 7.16**. The morphology of clean abrasives before wear test demonstrated in **Fig. 7.16 (a-b)**. The emery paper with bonded SiC abrasives has an average particle size of ~ 68 µm. **Fig. 7.16c** shows the morphology of emery paper after sliding against pure copper. Some of the SiC abrasives were subsequently undergone fracture, wear debris and debonding processes due to high frictional forces (COF: 0.56) developed between soft Cu and hard SiC abrasives during the wear test. In case of emery paper sliding against the C3Z (MX), sample exhibits fracture surface of SiC abrasives and wear debris due to low COF of 0.16 (**Fig. 7.16d**).

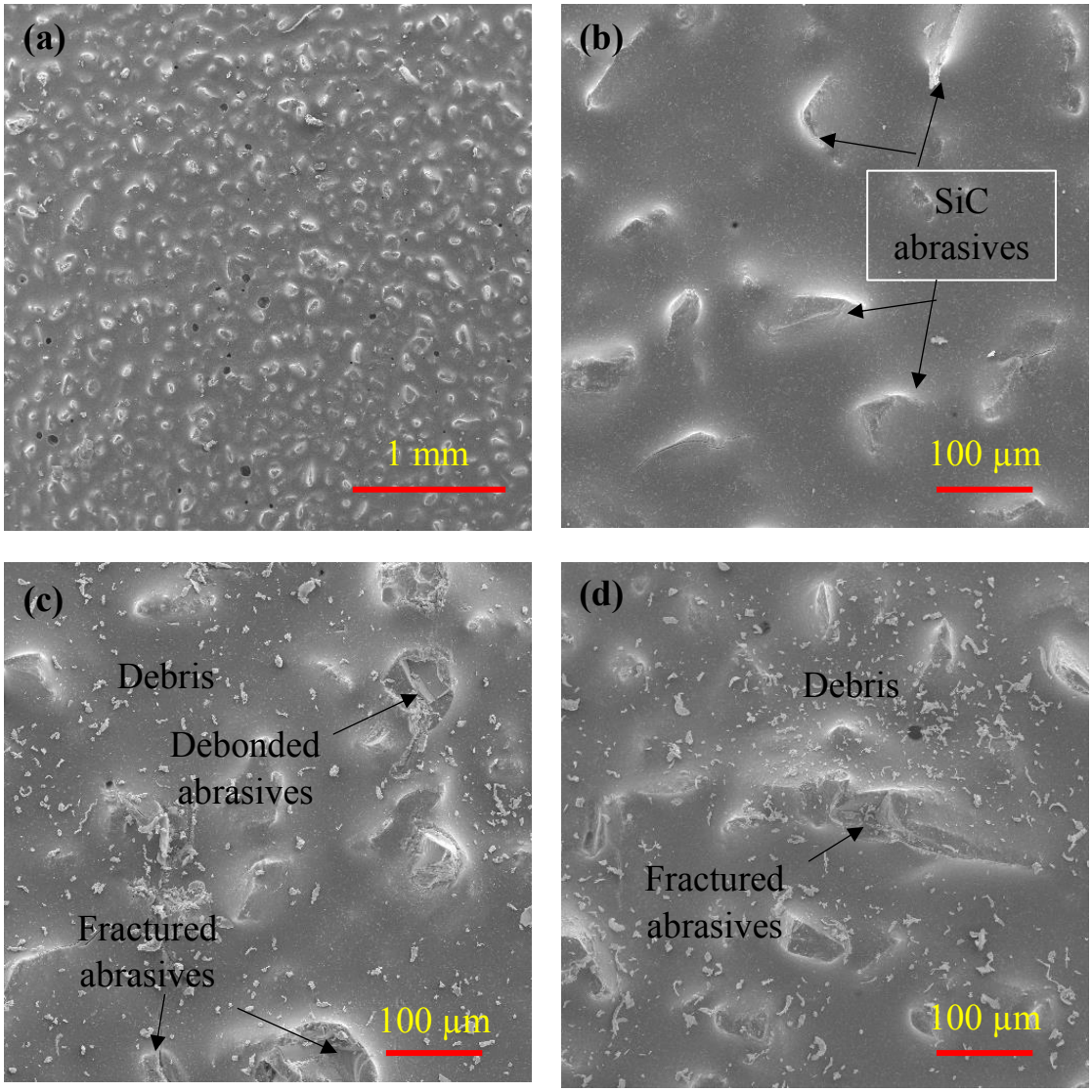

Fig. 7.16 Worn surface analysis of counter body (SiC emery paper: 220 grit size) used in wear test carried out at 5 N for a sliding distance of 60 m (a) Morphology of abrasives before wear test (b) Higher magnification of unworn abrasives (c) Cu (MX) sample, (d) C3Z (MX) composite.

In both cases, it is observed that the wear debris are fragmented over some portions of the emery paper surface and is mainly by detaching the debris from the wear sample or emery paper.

7.5.5 Analysis of wear debris

Fig. 7.17 presents the resulted wear debris morphology of Cu-ZrB_2 (mixed) samples after sliding against SiC emery paper (220 grit size). **Fig. 7.17 (a-b)** indicates the continuous long chips were formed during abrasive wear test of pure copper due to its soft ductile nature.

Due to the plowing and abrasive wear in Cu (MX) samples, deep groves made by hard SiC abrasives and produced the wear debris in the form of continuous chips.

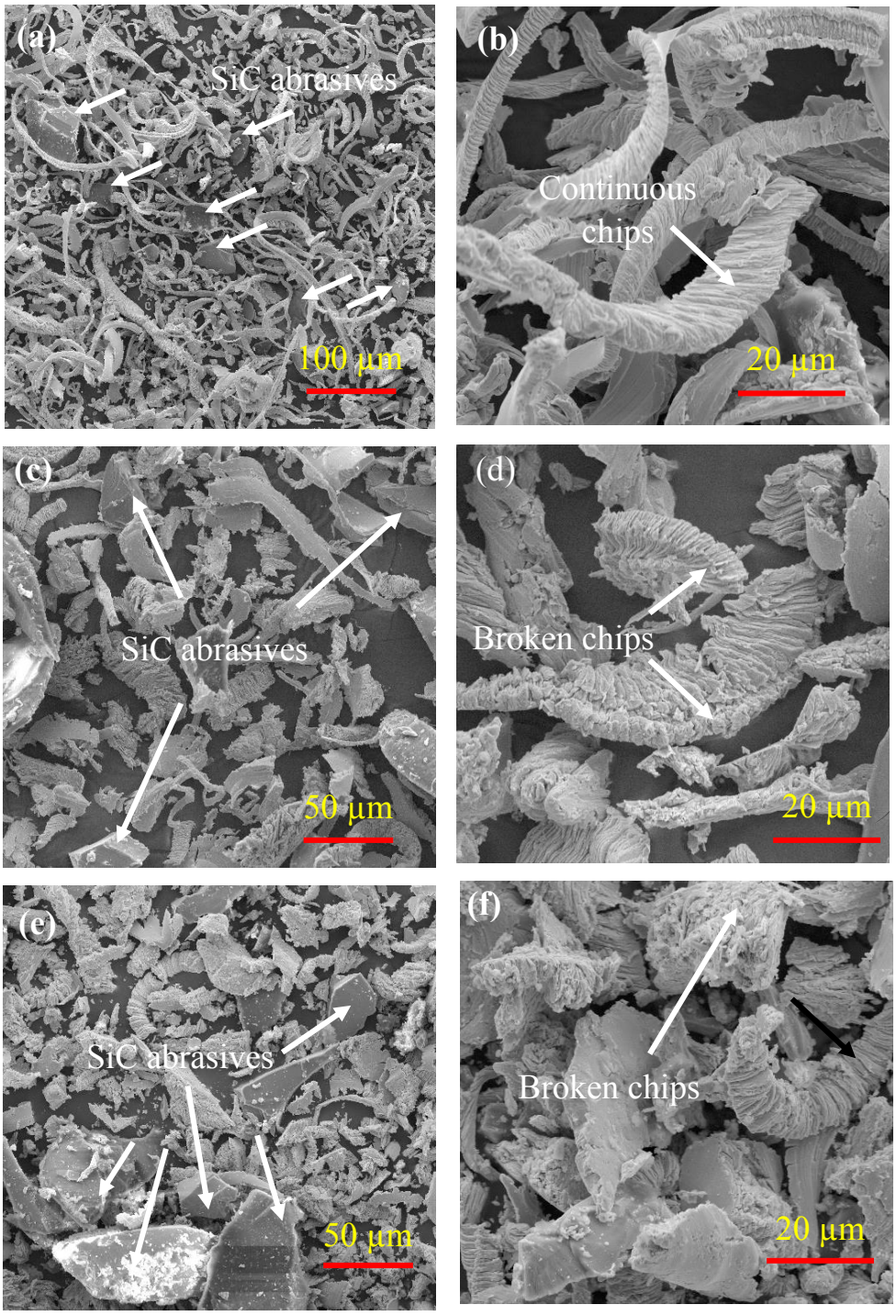

Fig. 7.17 SEM images of worn debris of Cu-ZrB_2 (mixed) composites (a) Cu (MX) (low magnification), (b) higher magnification of Cu (MX), (c) low magnification image of C3Z (MX), (d) Higher magnification of C3Z (MX), (e) low magnification image of C10Z (MX) and (f) higher magnification of C10Z (MX).

Due to high COF (0.56) of Cu (MX) against 220 grit emery paper, it has a high tendency to exhibit more shear forces with SiC abrasives and results in pulling out of more abrasive particles (see **Fig. 7.17a**). This phenomenon of producing continuous chips along with SiC particles promotes high material loss in the Cu (MX) sample (58.2 ± 0.6 mm^3). **Fig. 7.17 (c-d)** indicates the broken chips of C3Z (MX) after sliding for 60 m. In the case of C3Z (MX) composites, the broken chips of shorter length were identified after abrasive wear test.

Ultra-fine ZrB_2 particles segregated at the Cu-Cu grain boundaries, which resists the plastic deformation of matrix and further promotes the breakdown of chips into small pieces. **Fig. 7.17 (e-f)** shows the increase of SiC abrasives during wear test with an increase in ZrB_2 content upto 10 wt.%. This happened due to the increase of the high amount of ZrB_2 particle agglomeration at grain boundaries; further, these loosely bonded reinforcement particles come out from the grain boundary sites and cause more damage to the sample surface. The developed broken wear debris from C10Z (MX) composites was small in size compared to C3Z (MX) composites. In this work, the addition of ultra-fine ZrB_2 reinforcement to Cu matrix significantly enhanced the tribological properties of Cu-ZrB_2 (mixed) composites. Especially, C3Z (MX) composites showed better wear properties compared to Cu (MX) and other compositions.

7.6 Effect of ZrB_2 on the electrical conductivity of Cu-ZrB_2 (mixed) composites

The effect of ZrB_2 on the electrical conductivity of Cu is presented in **Fig. 7.18**. The electrical conductivity of Cu-ZrB_2 (mixed) composites was found to be in the range of 68.2 – 97.0% IACS. The high electrical conductivity of 97.0% IACS was found in Cu (MX) samples. Whereas, the electrical conductivity of Cu-ZrB_2 (mixed) composites found to decrease with the addition of ZrB_2. In Cu-ZrB_2 (mixed) composites with ZrB_2 content in the range between 1 to 5 wt.%, no significant change in the electrical conductivity was observed (reduction from 92.8 to 81.8% IACS) due to the use of a low amount of fine ZrB_2 particles in Cu matrix. In case of C10Z (MX) samples, the low electrical conductivity of 68.2% IACS was observed. Even at a high amount of ZrB_2 content, the C10Z (MX) showed better electrical conductivity which is 54.6% high compared to C10Z (ML) alloys and similar to C3Z (ML). Thus, the Cu-ZrB_2

(mixed) composites exhibited better electrical properties compared to the Cu-ZrB_2 (milled) composites and Cu-Al (milled and mixed) alloys.

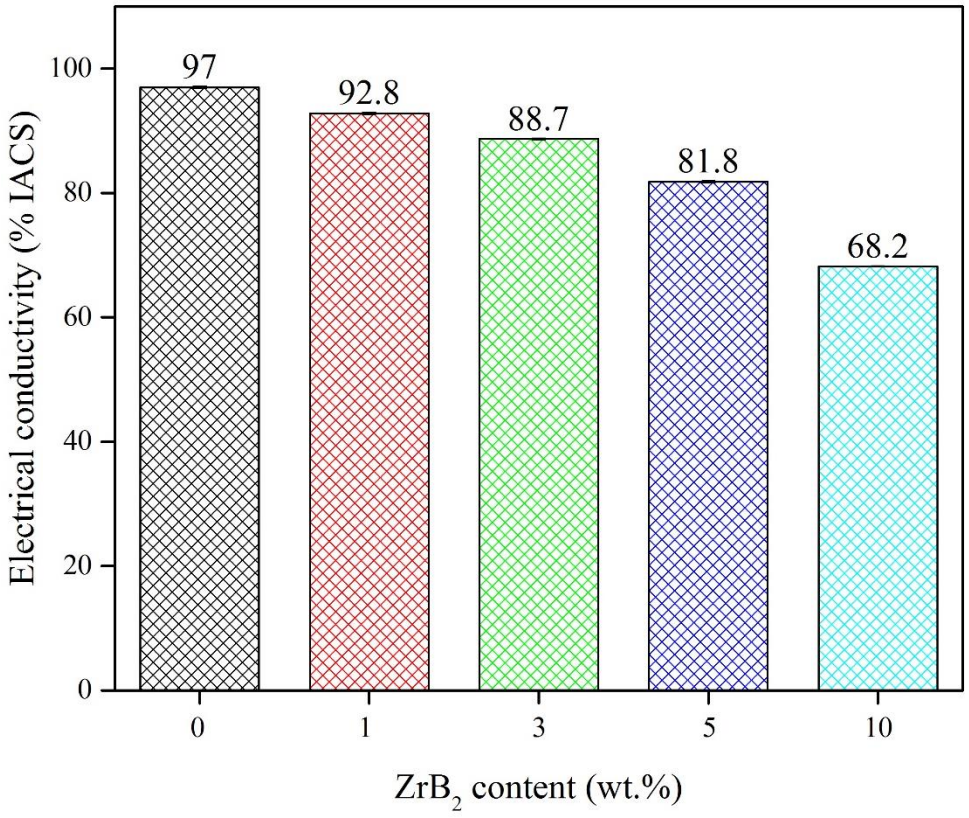

Fig. 7.18 Effect of ZrB_2 content on the electrical conductivity of Cu-ZrB_2 (mixed) composites.

Based on the above results, the electrical conductivity mechanisms of Cu materials will be discussed. The electrical conductivity of Cu-ZrB_2 (mixed) composites are higher when compared to Cu-ZrB_2 (milled) composites (Fig. 6.11 and Fig. 7.18). In case of pure Cu (mixed), a maximum electrical conductivity of 97.0% IACS was noticed and it reduced to 75.7% IACS for the pure Cu with the milled condition. Such a reduction in conductivity of pure Cu (milled) can be related to its low densification and lattice strains which will cause scattering of electrons.

In case of Cu-ZrB_2 composites (milled and mixed), the conductivity of Cu decreased (97.0%-44.1% IACS) with increasing addition of ZrB_2 (Fig. 6.11 and Fig. 7.18). The reduction of the conductivity in the Cu-ZrB_2 composites can be attributed to the lowering of densification, the low electrical conductivity of ZrB_2 reinforcement and the increased electrical resistance of interface boundaries (Cu/ZrB_2 and ZrB_2/ZrB_2). In particular, the electrical conductivity of Cu-

ZrB_2 (milled) composites considerably lower than the Cu-ZrB_2 (mixed) composites, and it is mainly due to the considerable decrease in the density and presence of lattice strains in Cu-ZrB_2 (milled) composites as well.

In case of Cu-Al alloys (milled and mixed), the conductivity of Cu decreased (97.0%-12.3% IACS) with increasing addition of Al (Fig. 4.34 and Fig. 5.18). It is interesting to note that despite the similar densification for Cu-Al (mixed) and Cu-Al (milled) samples, the Cu-Al (mixed) samples measured with better electrical conductivity than the Cu-Al (milled) samples. In fact, the Cu-Al alloys exhibited very low electrical conductivity than the Cu-ZrB_2 composites. Overall, the reduction of the conductivity in the Cu-Al alloys is mainly related to its microstructure, the presence of low conductivity microstructural phases, and the increased resistance at the grain boundaries and interphase boundaries. The Cu-Al (mixed) alloys exhibited core-rim structure and consisted of Cu, α-Cu, γ_1 (Cu_9Al_4), δ (Cu_3Al_2), ζ_1 (Cu_4Al_3), η_2 (CuAl) and θ ($CuAl_2$) phases. In case of the Cu-Al (milled) samples, no core-rim structure was observed. However, the Cu-Al (milled) samples consisted of α-Cu in Cu containing Al (up to 5 wt.%) and α-Cu and (Cu_9Al_4) phases in Cu containing up to 15 wt.% Al. The electrical conductivity of all the microstructural phases in the Cu-Al alloys is lower than pure Cu and ZrB_2 as well. Therefore, the Cu-Al alloys exhibited poor electrical conductivity than the pure Cu and Cu-ZrB_2 composites.

Chapter 8

Conclusions and future scope

Conclusions and future scope

Summary and conclusions

Cu-Al (milled) alloys

- The density of Cu-X wt.% Al (X = 0, 3, 5, 10, 15) alloys varied between 95-98% ρ_{th} after subjecting the mechanically alloyed powders at a hot pressing temperature of 500 ^{o}C, 500 MPa pressure for 30 minutes under a vacuum environment. The measured experimental/bulk density of samples varied between 6.61 to 8.84 g/cc.
- According to Williamson-Hall model, the lattice strain of Cu-Al (milled) powders after ball milling process was calculated to be in the range between 0.31×10^{-2} - 0.62×10^{-2}, whereas the lattice strain of hot-pressed samples was in the range of 0.22×10^{-2} - 0.36×10^{-2}. The crystallite size for Cu decreased for both the milled powders (from 53.33 to 26.16 nm) and hot-pressed materials (from 126.04 to 49.52 nm) with the addition of Al.
- The dislocation density of Cu-Al (milled) powders was calculated using the Williamson-Hall model varied from $3.52\text{x}10^{14}$ m^{-2} to $14.61\text{x}10^{14}$ m^{-2}. Also, the dislocation density of hot-pressed Cu-Al (milled) compacts varied in the range of $0.63\text{x}10^{14}$ m^{-2} - $4.08\text{x}10^{14}$ m^{-2}.

- The XRD and SEM-EDS analysis of hot-pressed samples revealed that Cu samples with Al up to 5 wt.% consisted of a copper-rich solid solution ($Cu_{0.92}Al_{0.08}$) phase and the presence of both $Cu_{0.78}Al_{0.22}$ and Cu_9Al_4 intermetallic phases for Cu containing a high amount of Al (≥10 wt.%). The hardness of Cu enhanced significantly from 1.32 to 6.16 GPa with the addition of Al.
- Also, the nanoindentation tests revealed an increase of hardness (2.4 to 7.9 GPa) and elastic modulus (121.1 to 177.4 GPa) and decrease in the plasticity of the index (0.85-0.66) for Cu-Al (milled) alloys with increasing Al content. Solid solution strengthening, intermetallic compound presence, good densification and fine microstructure of Cu-Al (milled) alloys can be attributed to such better properties.
- The compressive strength of Cu-Al (milled) increased (from 813.75 to 1120.18 MPa) significantly and the compressive strain decreased (from 29.81 to 5.81%) with the addition of Al.
- A comparison of mechanical properties of presently developed Cu-Al (milled) hot pressed alloys with the existing literature indicated that the presently developed alloys exhibited superior mechanical properties. It is very obvious that the use of low hot press sintering temperature with high pressure is effective in achieving good mechanical properties of Cu-Al alloys.
- From the abrasive wear characterization, it can be observed that the COF (0.49 to 0.16) and sp. wear rate (49.3 $\times 10^{-3}$ to 0.8 $\times 10^{-3}$ mm^3/Nm) of Cu decreased with Al addition. Such reduction in COF and wear of Cu-Al alloys can be attributed to its microstructure and hardness, which played a role in controlling its wear.
- The material removal during the abrasive wear of Cu was caused by the plowing mechanism; whereas, the micro-cutting was the predominant mechanism in Cu-Al (milled) alloys.
- In case of sliding wear of Cu-Al (milled) alloys against SS disc, both the COF (0.54 to 0.16) and wear rate (18.26×10^{-5} to 0.92 $\times 10^{-5}$ mm^3/N-m) of Cu decreased with the addition of Al.
- The sliding wear of pure copper is mainly dominated by adhesive wear after sliding against steel disc. A large number of fine Cu_2O wear debris were observed on the worn surface of Cu. Adhesive wear and oxidative wear were the major wear mechanisms for Cu alloyed with Al (upto 5 wt.%).
- Oxide layer formation influenced the wear of Cu-10Al, while abrasion is the predominant wear mechanism for Cu-15Al. A common observation was that the wear debris formation decreased considerably with increased Al addition to Cu.

- From the COF, wear measurements, microstructure and surface roughness measurements, it is obvious that Al addition is very beneficial in improving the wear resistance of Cu.
- From corrosion analysis, it can be observed that the localized corrosion takes place on Cu sample and it is mainly due to pitting and intergranular corrosion. In case of Cu-Al alloy, mild corrosion noticed at α phase region, pitting and intergranular type of corrosion at regions of the γ phase. It indicates that the stable oxide layer presence at α phase and poor stability of the layer at γ phase regions.
- Drastic reduction in corrosion of C15A (L) alloy (1.6 mpy) than the pure Cu (20.7 mpy) was noticed despite the low densification of Cu-Al alloy. This remarkable decrease in the corrosion rate of the Cu alloy is due to the formation of the Al_2O_3 layer on the surface. The higher impedance of the Nyquist plot confirms the formation of a protective oxide layer on the sample surface of the Cu-15Al alloy. This work clearly shows the efficacy of the use of a high amount of Al in improving the corrosion resistance of Cu.
- The electrical conductivity of Cu-Al (milled) alloys decreased from 75.7 to 12.3% IACS. In Cu (ML) samples, the electrical conductivity was affected by the lattice strain in the material along with residual porosity. Whereas it was effected by the lattice strain, porosity, crystallite size, solid solution and intermetallic phases for Cu-Al alloys.

Cu-Al (mixed) alloys

- The relative density of Cu-Al (mixed) alloys decreased with Al addition (99.7 to 96.0%). The mixing route exhibited better densification of copper when compared to the Cu-Al (milled).
- From the XRD and SEM-EDS analyses, it was confirmed that the Cu, α-Cu, γ_1 (Cu_9Al_4), δ (Cu_3Al_2), ζ_1 (Cu_4Al_3), η_2 (CuAl) and θ ($CuAl_2$) phases were formed in Cu-Al (mixed) alloys with the addition of Al.
- The shell and core microstructure consist of solid solution and intermetallic phases in the Cu-Al (mixed) samples. The interconnectivity of the shell-core structure was increased with the increase of Al content.
- The hardness of Cu-Al (mixed) increased with Al from 0.88 to 4.56 GPa due to the formation of solid solution and intermetallic phases.
- The maximum yield strength of 653 MPa with a reasonable amount of strain (6.5%) was obtained with Cu-15Al sample. In the case of C3A (MX) to C10A (MX) alloys, the strain

was observed to be more than 50% due to the inter-connectivity of the solid solution phase. However, the compressive strength of Cu-Al (mixed) alloys found to be ~41% lower and strain 6.25 times higher than Cu-Al (milled) alloys.

- The COF of Cu-Al (mixed) alloys decreased with Al addition (0.56 to 0.17). The sp. wear rate of Cu-Al (mixed) alloys was significantly reduced with Al addition. High sp. wear rate of (198×10^{-3} mm^3/Nm) was observed in Cu (X), while the C15A (X) measured with low sp. wear rate (3.85×10^{-3} mm^3/Nm).
- The wear of pure Cu occurred due to severe plastic deformation of Cu during wear by hard SiC abrasive particles. The worn surface of pure Cu characterized with sharp ridges by plowing mechanism; further, it leads to the development of big wear debris.
- The micro-cutting was the predominant wear mechanism in Cu-Al (mixed) alloys (3 to 15 wt.% Al). The decrease in plastic deformation of the material in Cu-Al (mixed) alloys causes the decrease of chip thickness thereby less loss of material.
- Though the Cu-Al (mixed) alloys showed better relative density, the Cu-Al (milled) alloys exhibited improved abrasive wear resistance (4.8 times) compared to Cu-Al (mixed) alloys.
- The electrical conductivity of Cu-Al (mixed) alloys decreased from 97 to 29.5% IACS. The decrease in electrical conductivity of alloys attributed to the presence of solid solution and intermetallic phases. Whereas significantly low electrical conductivity was obtained in Cu-Al (milled) alloys compared to Cu-Al (mixed) alloys and is due to the combined effect of lattice strains and the microstructure.

Cu-ZrB_2 (milled) composites

- The bulk density of hot-pressed Cu-ZrB_2 (milled) composites decreased from 8.84 g/cc to 8.16 g/cc and the relative density of samples decreased from 98.6% to 92.1% with the addition of ZrB_2.
- The incorporation of hard ZrB_2 (upto 10 wt.%) improved the hardness of Cu (1.32 to 2.55 GPa). However, the yield strength and compressive strength of Cu composites increased upto 5 wt.% ZrB_2, and further addition of ZrB_2 lowered its strength. The yield strength of Cu samples varied from 602 to 672 MPa and the compressive strength between ~834 and 971 MPa.

- On the other hand, the COF (0.49 - 0.18) and wear rate (from 49.3×10^{-3} mm^3/N-m to 9.1×10^{-3} mm^3/N-m) of Cu-ZrB_2 samples considerably decreased with the addition of ZrB_2. Lowest wear was observed with C10Z (L) samples, which is 5.41 times less than pure Cu.
- The electrical conductivity of Cu-ZrB_2 (milled) samples decreased from 75.7% IACS to 44.1% IACS. However, Cu with ZrB_2 upto 3 wt.% could retain the conductivity of 66.8% IACS. This study demonstrates that the addition of ZrB_2 (up to 5 wt.%) is advantageous to have a good combination of properties for Cu.
- Though the Cu-ZrB_2 composites exhibited good electrical conductivity and compressive strain, they possessed moderate compressive strength and wear resistance than the Cu-Al alloys (milled and mixed).

Cu-ZrB_2 (mixed) composites

- The relative density of Cu-(0-10 wt.%) ZrB_2 composites varied in the range between 96.0 to 99.7%. The densification of copper was observed to lower with increasing of ZrB_2 amount.
- The microstructure of the Cu-ZrB_2 (mixed) composites reveals that the ZrB_2 particles were located at the grain boundaries of the Cu.
- Both the hardness and compression strength of Cu enhanced with ZrB_2 addition. Among all the composites, C10Z (MX) showed maximum hardness (1.25 GPa) and yield strength (261 MPa).
- The COF of ZrB_2 added Cu composites was lowered (0.56 to 0.16). In contrast, the wear resistance was improved with the ZrB_2 reinforcement. Pure copper exhibited a high wear coefficient (17.33×10^{-2}) and the very low wear coefficient of 2.4×10^{-2} was evident for C3Z (MX) composites.
- The material removal in Cu (MX) samples takes place by the plowing mechanism. Whereas the C3Z (MX) worn sample consisted of shallow and wide groves after the wear test. Also, the wear takes place by plowing which is the predominant wear mechanism.
- As the ZrB_2 content increased up to 3 wt.%, no ridge formation has appeared on composites surface which represents the reduction of plastic deformation of material and enhancement in wear resistance.
- Further addition of ZrB_2 (above 3 wt.%) slightly lowered the wear of Cu. It is due to the agglomeration of ZrB_2 along the grain boundary for these samples. Due to this, the loose

ZrB_2 particles pull out from the materials during wear and the SiC abrasives (from counterbody) its wear gets aggravated.

- Cu-ZrB_2(mixed) composites showed better electrical properties (68.2-97.0% IACS) than other Cu-Al alloys and Cu-ZrB_2 (milled) composite systems.
- Overall, Cu-Al alloys are suitable (bearings in mining machines) for the applications that require high strength and wear-resistance.
- Cu-ZrB_2 composites are suitable for the applications (EDM electrodes and rail overhead power collectors) where moderate strength, wear resistance and high conductivity required.
- On the whole, the Cu-Al/Cu-ZrB_2 materials processed via mixing exhibited moderate or better combination of properties than the Cu materials (milled). Since it lowers the processing costs as it did not involve in using expensive milling operations, the Cu-Al/Cu-ZrB_2 (mixed) materials are advantageous.

Future scope of the present work

- More detailed microstructural characterization can be carried out using Transmission Electron Microscope (TEM) and Electron Backscatter Diffraction (EBSD) studies to comprehensively understand the microstructure of Cu-Al and Cu-ZrB_2 materials.
- The presently developed Cu based materials can be suitable for the electrical discharge machining (EDM) electrode applications due to their excellent strength, wear-resistance and electrical conductivity. Hence, in-depth EDM studies are required in future to understand the electrode wear behaviour and its practical applicability.
- In the present thesis, the effect of alloying element (Al) and reinforcing particles (ZrB_2) on the electrical conductivity of Cu was studied. Further improvement in electrical conductivity of Cu can be possible by the use of metallic coatings on ZrB_2 ceramic particles.
- It is interesting to explore tensile, fatigue, creep, oxidation and corrosion properties of Cu-Al and Cu-ZrB_2 materials for finding more appropriate applications of the materials.

Disseminations

Research publications from the thesis work:

1. **Mahammad Ali S**, Brahma Raju G. Mechanical, tribological and electrical properties of ZrB_2 reinforced Cu processed via milling and high-pressure hot press. Ceramics International 46 (2020) 20226-20235. (Impact factor, **I.F: 3.83**)
2. **Mahammad Ali S**, Brahma Raju G. Two-body abrasion wear properties of Cu-ZrB_2 composites against SiC emery paper. Wear. 450-451 (2020) 203260 (Impact factor, **I.F: 4.10**)
3. **Mahammad Ali S**, Brahma Raju G. Processing and characterization of mechanically alloyed and extremely hard Cu-Al alloys. Metallurgical and Materials Transactions A. 51A (2020) 708-724 (Impact factor, **I.F: 2.05**).
4. **Mahammad Ali S**, Brahma Raju G. Development of highly wear-resistant Cu - Al alloys processed via powder metallurgy. Tribology International 136 (2019) 127–139 (**I.F: 4.27**).
5. **Mahammad Ali S**, Khader Hussain S, Brahma Raju G. Electrochemical behaviour of mechanically alloyed hard Cu-Al alloys in marine environment. Corrosion Science 153 (2019) 249–257 (**I.F: 6.48**).
6. **Mahammad Ali S**, Brahma Raju G. Densification, microstructure and properties of mechanically alloyed and hot-pressed Cu–15 wt.% Al alloy. Journal of Materials Science 53 (2018) 14694–712 (**I.F: 3.55**).

Research publications outside the thesis work (research collaborations):

1. Akhil P. S, **Mahammad Ali S**, Brahma Raju G. Mechanical, wear, and dielectric behaviour of TiO_2 reinforced high-density polyethene composites. Journal of Applied Polymer Science 136 (2019) 47611-476113. (**I.F: 2.52**).
2. Vignesh Raja S, Brahma Raju G, **Mahammad Ali S**, Ankit Y, Sarath Chandra D. T and Shivkumar K. Modeling and Characterization of Porous Tantalum Scaffolds. Transactions of the Indian Institute of Metals 72 (2019) 935–949.
3. **Mahammad Ali S**, Unnikrishnan G and Joseph M. A. Essential Work of Fracture of Low-Filled Poly(methyl methacrylate)/Starch Composites**.** Journal of Applied Polymer Science 128 (2013) 1409-1416. (**I.F: 2.52**).

International conferences attended:

1. Mahammad Ali S, Brahma Raju G, "Abrasive wear behaviour of Cu-Al alloys processed via powder metallurgy", *Advanced Materials for Industrial and Societal Applications (NMD ATM 2019),* Indian Institute of Metals, Trivandrum during 13-16 Nov 2019
2. Mahammad Ali S, Brahma Raju G, "Processing and characterization of high strength Cu-Al alloys fabricated through the high-pressure hot press", *International Conference on Advances in Minerals, Metals, Materials, Manufacturing and Modelling (ICAM5),* National Institute of Technology, Warangal during 25-27 Sep 2019

Workshops attended:

1. *National Workshop & Continuous Medical Education* on Clinical Immunology: Past and present at National Institute of Technology, Warangal on 20 - 21 January 2016
2. *National Workshop* on Advances in Composite Materials at JNTUK, Kakinada on 14 – 15 March 2014
3. *National Workshop* on Advances in Manufacturing Processes at KL University, Vijayawada on 25 Jan 2014

Annexure

Table I: The comparison of densification and microstructural characteristics of Cu-Al (milled and mixed) alloys and Cu-ZrB_2 (milled and mixed) composites.

Sample Reference	**Bulk density (g/cc)**	**Theritical density (g/cc)**	**Relative density (%)**	**Microstru-ctural phases**	**lattice strain (%)**	**crystallite size (nm)**	**Dislocation density ($\times 10^{14}$ m^{-2})**
Cu (ML)	8.84	8.96	98.66	Cu	0.22	126.04	0.63
C3Al (ML)	8.07	8.38	96.30	$Cu_{0.92}Al_{0.08}$	0.24	106.65	0.88
C5Al (ML)	7.97	8.38	95.16	$Cu_{0.92}Al_{0.08}$	0.27	81.56	1.50
C10Al (ML)	7.01	7.37	95.10	$Cu_{0.78}Al_{0.22}$, Cu_9Al_4	0.31	57.77	3.00
C15Al (ML)	6.61	6.98	94.60	$Cu_{0.78}Al_{0.22}$, Cu_9Al_4	0.36	49.52	4.08
Cu (MX)	8.93	8.96	99.76	Cu	-	-	-
C3Al (MX)	8.26	8.67	95.26	Cu, α-Cu, (Cu_9Al_4), (Cu_3Al_2), (Cu_4Al_3), (CuAl) and ($CuAl_2$)	-	-	-
C5Al (MX)	8.04	8.45	95.13	,,	-	-	-
C10Al (MX)	7.34	7.73	95.02	,,	-	-	-
C15Al (MX)	6.75	7.10	95.01	,,	-	-	-
Cu (ML)	8.84	8.96	98.61	Cu	0.22	123.79	0.65
C1Z (ML)	8.51	8.91	95.42	Cu, ZrB_2	0.23	101.94	0.96
C3Z (ML)	8.24	8.83	93.27	,,	0.24	87.20	1.32
C5Z (ML)	8.11	8.75	92.63	,,	0.26	73.75	1.84
C10Z (ML)	8.16	8.55	92.16	,,	0.28	67.63	2.19
Cu (MX)	8.93	8.96	99.76	Cu	-	-	-
C1Z (MX)	8.81	8.91	98.85	Cu, ZrB_2	-	-	-
C3Z (MX)	8.71	8.83	98.66	,,	-	-	-
C5Z (MX)	8.52	8.75	97.39	,,	-	-	-
C10Z (MX)	8.21	8.55	96.02	,,	-	-	-

Table II: The comparison of hardness, compression strength, COF and sp. wear rate and electrical conductivity of Cu-Al (milled and mixed) alloys and Cu-ZrB_2 (milled and mixed) composites.

Sample reference	Hardness (GPa)	Compression strength (MPa)	Strain (%)	COF	Sp. wear rate ($\times 10^{-3}$ mm^3/Nm)	Electrical conductivity (% IACS)
Cu (ML)	1.32 ± 0.02	813.75 ± 11	29.81 ± 0.9	0.49 ± 0.05	49.30 ± 05	75.7 ± 0.1
C3Al (ML)	2.33 ± 0.15	954.71 ± 21	8.61 ± 0.6	0.27 ± 0.08	11.50 ± 02	23.6 ± 0.1
C5Al (ML)	2.73 ± 0.13	1120.18 ± 28	8.00 ± 0.7	0.24 ± 0.08	8.50 ± 03	18.3 ± 0.1
C10Al (ML)	3.41 ± 0.18	1077.05 ± 30	5.93 ± 0.4	0.19 ± 0.02	4.90 ± 01	16.4 ± 0.1
C15Al (ML)	6.16 ± 0.28	1013.82 ± 25	5.81 ± 0.3	0.16 ± 0.03	0.80 ± 0.4	12.3 ± 0.1
Cu (MX)	0.88 ± 0.05	540.30 ± 08	50.00 ± 0*	0.56 ± 0.05	197.80 ± 06	97.0 ± 0.2
C3Al (MX)	1.72 ± 0.11	547.50 ± 04	50.00 ± 0*	0.27 ± 0.04	14.30 ± 03	73.5 ± 0.2
C5Al (MX)	2.33 ± 0.13	658.80 ± 09	50.00 ± 0*	0.24 ± 0.04	10.10 ± 05	49.2 ± 0.1
C10Al (MX)	3.28 ± 0.15	682.80 ± 11	50.00 ± 0*	0.21 ± 0.02	6.87 ± 02	35.0 ± 0.2
C15Al (MX)	4.56 ± 0.21	747.90 ± 14	6.50 ± 0.4	0.17 ± 0.03	3.85 ± 03	29.5 ± 0.1
Cu (ML)	1.32 ± 0.02	880.90 ± 06	35.70 ± 0.6	0.49 ± 0.05	49.30 ± 05	75.7 ± 0.1
C1Z (ML)	2.05 ± 0.05	906.90 ± 13	33.90 ± 1.2	0.28 ± 0.03	12.10 ± 03	71.5 ± 0.1
C3Z (ML)	2.30 ± 0.07	923.30 ± 09	32.10 ± 2.5	0.24 ± 0.03	11.40 ± 02	66.8 ± 0.1
C5Z (ML)	2.38 ± 0.05	970.60 ± 11	20.90 ± 1.6	0.21 ± 0.02	11.10 ± 02	57.3 ± 0.1
C10Z (ML)	2.55 ± 0.08	833.70 ± 08	9.10 ± 0.9	0.18 ± 0.02	9.10 ± 01	44.1 ± 0.1
Cu (MX)	0.88 ± 0.01	551.3 ± 08	50.00 ± 0*	0.56 ± 0.05	198.00 ± 06	97.0 ± 0.2
C1Z (MX)	0.91 ± 0.01	575.4 ± 06	50.00 ± 0*	0.18 ± 0.04	62.30 ± 02	92.8 ± 0.2
C3Z (MX)	0.96 ± 0.02	589.6 ± 04	50.00 ± 0*	0.16 ± 0.01	25.60 ± 02	88.7 ± 0.1
C5Z (MX)	1.01 ± 0.08	588.1 ± 05	38.50 ± 1.3	0.20 ± 0.01	32.50 ± 03	81.8 ± 0.2
C10Z (MX)	1.25 ± 0.07	508.5 ± 03	28.60 ± 0.6	0.22 ± 0.03	52.00 ± 04	68.2 ± 0.1

* Fracture was not observed in the specimens even up to 50% strain.

References

[1] H. Jang, K. Ko, S.J. Kim, R.H. Basch, J.W. Fash, The effect of metal fibers on the friction performance of automotive brake friction materials, Wear. 256 (2004) 406–414. http://www.sciencedirect.com/science/article/pii/S0043164803004459.

[2] H.M. Zaw, J.Y.H. Fuh, A.Y.C. Nee, L. Lu, Formation of a new EDM electrode material using sintering techniques, J. Mater. Process. Technol. 89 (1999) 182–186. https://doi.org/10.1016/S0924-0136(99)00054-0.

[3] D. Prokoshkina, V.A. Esin, S. V Divinski, Experimental evidence for anomalous grain boundary diffusion of Fe in Cu and Cu-Fe alloys, Acta Mater. 133 (2017) 240–246. https://doi.org/10.1016/j.actamat.2017.05.024.

[4] A. Heidarzadeh, T. Saeid, Correlation between process parameters, grain size and hardness of friction-stir-welded Cu–Zn alloys, Rare Met. 37 (2016) 1–11. https://doi.org/10.1007/s12598-016-0704-9.

[5] A.E. Nassef, A.I. Alateyah, M.A. El Hadek, W.H. El Garaihy, Mechanical behavior and fracture surface characterization of liquid-phase sintered Cu-Sn powder alloys, Adv. Mater. Lett. 8 (2017) 717–722. https://doi.org/10.5185/amlett.2017.1485.

[6] G.S. Jawaharram, S.J. Dillon, R.S. Averback, Hardening mechanisms in irradiated Cu–W alloys, J. Mater. Res. 32 (2017) 3156–3164. https://doi.org/10.1557/jmr.2017.295.

[7] J. Guo, J. Rosalie, R. Pippan, Z. Zhang, On the phase evolution and dissolution process in Cu-Cr alloys deformed by high pressure torsion, Scr. Mater. 133 (2017) 41–44. https://doi.org/10.1016/j.scriptamat.2017.02.009.

[8] ASM International Handbook Committeee, ASM Speciality Handbook, Copper and Copper Alloys, ASM International, 2001.

[9] X. Fan, X. Huang, Q. Liu, H. Ding, H. Wang, C. Hao, The microstructures and properties of in-situ ZrB_2 reinforced Cu matrix composites, Results Phys. 14 (2019) 102494. https://doi.org/10.1016/j.rinp.2019.102494.

[10] Y. Shi, W. Chen, L. Dong, H. Li, Y. Fu, Enhancing copper infiltration into alumina using spark plasma sintering to achieve high performance Al_2O_3/Cu composites, Ceram. Int. 44 (2018) 57–64. https://doi.org/10.1016/j.ceramint.2017.09.062.

[11] P.K. Prajapati, D. Chaira, Fabrication and characterization of Cu–B_4C metal matrix composite by powder metallurgy: Effect of B_4C on microstructure, mechanical properties and electrical conductivity, Trans. Indian Inst. Met. 72 (2019) 673–684. https://doi.org/10.1007/s12666-018-1518-2.

[12] M.R. Akbarpour, H. Mousa Mirabad, S. Alipour, Microstructural and mechanical characteristics of hybrid SiC/Cu composites with nano- and micro-sized SiC particles, Ceram. Int. 45 (2019) 3276–3283. https://doi.org/10.1016/j.ceramint.2018.10.235.

[13] N. Radhika, J.A. Jefferson, Studies on mechanical and abrasive wear properties of Cu-Ni-Si/Si_3N_4 functionally graded composite, Silicon. 10 (2018) 1–15. https://doi.org/10.1007/s12633-018-9957-2.

[14] H. Ding, W. Chu, Q. Liu, H. Wang, C. Hao, H. Jia, J. Wang, T. Ci, Microstructure

evolution of Cu-TiC composites with the change of Ti/C ratio, Results Phys. 14 (2019) 102369. https://doi.org/10.1016/j.rinp.2019.102369.

[15] J.R. Davis, ASM Specialty Handbook: Copper and Copper Alloys,(2001), ASM Int. Met. Park. Ohio, USA, Pp. I-600. (2008).

[16] A. Korneva, B. Straumal, A. Kilmametov, R. Chulist, P. Straumal, P. Zięba, Phase transformations in a Cu Cr alloy induced by high pressure torsion, Mater. Charact. 114 (2016) 151–156. https://doi.org/10.1016/j.matchar.2016.02.017.

[17] A.T. Vijayashakthivel, T.N. Srikantha Dath, R. Krishnamurthy, Response of copper to Equal Channel Angular pressing with different processing temperature, Procedia Eng. 97 (2014) 56–63. https://doi.org/10.1016/j.proeng.2014.12.224.

[18] M.I. Latypov, E.Y. Yoon, D.J. Lee, R. Kulagin, Y. Beygelzimer, M. Seyed Salehi, H.S. Kim, Microstructure and mechanical properties of copper processed by twist extrusion with a reduced twist-line slope, Metall. Mater. Trans. A Phys. Metall. Mater. Sci. 45 (2014) 2232–2241. https://doi.org/10.1007/s11661-013-2165-1.

[19] S. Tamimi, M. Ketabchi, N. Parvin, M. Sanjari, A. Lopes, Accumulative Roll Bonding of Pure Copper and IF Steel, Int. J. Met. 2014 (2014) 1–9. https://doi.org/10.1155/2014/179723.

[20] W. Głuchowski, J. Stobrawa, Z. Rdzawski, W. Malec, Ultrafine grained copper alloys processed by continuous repetitive corrugation and straightening method, Mater. Sci. Forum. 674 (2011) 177–188. https://doi.org/10.4028/www.scientific.net/MSF.674.177.

[21] Y.L. Gong, S.Y. Ren, S.D. Zeng, X.K. Zhu, Unusual hardening behaviour in heavily cryo-rolled Cu-Al-Zn alloys during annealing treatment, Mater. Sci. Eng. A. 659 (2016) 165–171. https://doi.org/10.1016/j.msea.2016.02.060.

[22] H.S. Park, T. Kimura, T. Murakami, Y. Nagano, K. Nakata, M. Ushio, Microstructures and mechanical properties of friction stir welds of 60% Cu–40% Zn copper alloy, Mater. Sci. Eng. A. 371 (2004) 160–169.

[23] H. Wen, T.D. Topping, D. Isheim, D.N. Seidman, E.J. Lavernia, Strengthening mechanisms in a high-strength bulk nanostructured Cu–Zn–Al alloy processed via cryomilling and spark plasma sintering, Acta Mater. 61 (2013) 2769–2782. https://doi.org/10.1016/j.actamat.2012.09.036.

[24] H. Wen, E.J. Lavernia, Twins in cryomilled and spark plasma sintered Cu–Zn–Al, Scr. Mater. 67 (2012) 245–248. https://doi.org/10.1016/j.scriptamat.2012.04.024.

[25] J.P. Kruth, P. Peeters, T. Smolderen, J. Bonse, T. Laoui, L. Froyen, Comparison between CO_2 and Nd: YAG lasers for use with selective laser sintering of steel-copper powders, Rev. Int. CFAO Dinformatique Graph. 13 (1998) 95–110.

[26] J.P. Kruth, P. Mercelis, J. Van Vaerenbergh, L. Froyen, M. Rombouts, Binding mechanisms in selective laser sintering and selective laser melting, Rapid Prototyp. J. 11 (2005) 26–36.

[27] C. Wang, H. Lin, Z. Zhang, W. Li, Fabrication, interfacial characteristics and strengthening mechanisms of ZrB_2 microparticles reinforced Cu composites prepared by hot-pressed sintering, J. Alloys Compd. 748 (2018) 546–552. https://doi.org/10.1016/j.jallcom.2018.03.169.

[28] W. Shang, H. Wang, S. Zhao, X. Zhao, H. Xu, H. Lu, D. Chen, B. Fan, R. Zhang, Processing and properties of ZrB_2-Cu composites sintered by hot-pressing sintering, Key Eng. Mater. 602–603 (2014) 447–450. https://doi.org/10.4028/www.scientific.net/KEM.602-603.447.

[29] A.K. Shukla, S.V.S. Narayana Murty, R. Suresh Kumar, K. Mondal, Densification behavior and mechanical properties of Cu-Cr-Nb alloy powders, Mater. Sci. Eng. A. 551 (2012) 241–248. https://doi.org/10.1016/j.msea.2012.04.120.

[30] S. Krebs, F. Gartner, T. Klassen, Cold spraying of Cu-Al-Bronze for cavitation protection in marine environments, J. Therm. Spray Technol. 24 (2015) 126–135.

[31] L. Meyer, M. Thedens, M. Beyer, Incendivity of aluminium bronze in mechanical friction contacts, J. Loss Prev. Process Ind. 49 (2017) 947–952. https://doi.org/10.1016/j.jlp.2017.02.003.

[32] L. Arnberg, S. Westman, Crystal perfection in a noncentrosymmetric alloy. Refinement and test of twinning of the γ-Cu_9Al_4 structure, Acta Crystallogr. Sect. A Cryst. Physics, Diffraction, Theor. Gen. Crystallogr. 34 (1978) 399–404. https://doi.org/10.1107/S0567739478000807.

[33] G.K. Gyimah, P. Huang, D. Chen, Dry sliding wear studies of copper-based powder metallurgy brake materials, J. Tribol. 136 (2014) 41601.

[34] H.N. Soliman, N. Habib, Effect of ageing treatment on hardness of Cu-12.5 wt.% Al shape memory alloy, Indian J. Phys. 88 (2014) 803–812. https://doi.org/10.1007/s12648-014-0480-z.

[35] K.M. Youssef, M.A. Abaza, R.O. Scattergood, C.C. Koch, High strength, ductility, and electrical conductivity of in-situ consolidated nanocrystalline Cu-1%Nb, Mater. Sci. Eng. A. 711 (2018) 350–355. https://doi.org/10.1016/j.msea.2017.11.060.

[36] M. Rabiee, H. Mirzadeh, A. Ataie, Processing of Cu-Fe and Cu-Fe-SiC nanocomposites by mechanical alloying, Adv. Powder Technol. 28 (2017) 1882–1887. https://doi.org/10.1016/j.apt.2017.04.023.

[37] A. Kumar, S.K. Pradhan, K. Jayasankar, M. Debata, R.K. Sharma, A. Mandal, Structural investigations of nanocrystalline Cu-Cr-Mo Alloy Prepared by High-Energy Ball Milling, J. Electron. Mater. 46 (2017) 1339–1347. https://doi.org/10.1007/s11664-016-5125-x.

[38] S. Chakravarty, K. Sikdar, S.S. Singh, D. Roy, C.C. Koch, Grain size stabilization and strengthening of cryomilled nanostructured Cu 12 at.% Al alloy, J. Alloys Compd. 716 (2017) 197–203. https://doi.org/10.1016/j.jallcom.2017.05.093.

[39] V. Rajkovic, D. Bozic, M.T. Jovanovic, V. Rajkovic, D. Bozic, M. Jovanovic, Characteristics of copper and copper-Al_2O_3 composites prepared by high-energy milling, Metalurgija. 13 (2007) 309–316.

[40] Traleski, A. Victor, V. JR, Selauco, Cintho, O. Mitsuyuki, Processing of Cu-Al-Ni and Cu-Zn-Al alloys by mechanical alloying, Mater. Sci. Forum. 727–728 (2012) 200–205.

[41] M. Saiprasad, R. Atchayakumar, K. Thiruppathi, S. Raghuraman, Consolidation of copper and aluminium powders by spark plasma sintering, IOP Conf. Ser. Mater. Sci. Eng. 149 (2016). https://doi.org/10.1088/1757-899X/149/1/012057.

[42] G. Abbas Gohar, T. Manzoor, A.N. Shah, Investigation of thermal and mechanical properties of Cu-Al alloys with silver addition prepared by powder metallurgy, J. Alloys Compd. 735 (2018) 802–812. https://doi.org/10.1016/j.jallcom.2017.11.176.

[43] B.Z. Zhang, Y. Sheng, X. Xu, W. Li, Microstructural features and mechanical properties of in situ formed ZrB_2/Cu composites, Adv. Eng. Mater. 17 (2015) 1338–1343. https://doi.org/10.1002/adem.201400532.

[44] A. Fathy, O. Elkady, A. Abu-oqail, Production and properties of Cu-ZrO_2 nanocomposites, J. Compos. Mater. 52 (2018) 1519–1529. https://doi.org/10.1177/0021998317726148.

[45] S.C. Tjong, K.C. Lau, Abrasive wear behavior of TiB_2 particle-reinforced copper matrix composites, Mater. Sci. Eng. A. 282 (2000) 183–186. https://doi.org/10.1016/S0921-5093(99)00752-2.

[46] An overview of copper alloys, Eur. Copp. Inst. (2018). https://copperalliance.eu/about-copper/copper-and-its-alloys/alloys.

[47] K.J.A. Kundig, Copper and Copper Alloys, in: Handb. Mater. Sel., John Wiley & Sons, Inc., New York, 2001: pp. 135–200. https://doi.org/10.1002/9780470172551.ch5.

[48] K. Maki, Y. Ito, H. Matsunaga, H. Mori, Solid-solution copper alloys with high strength and high electrical conductivity, Scr. Mater. 68 (2013) 777–780. https://doi.org/10.1016/j.scriptamat.2012.12.027.

[49] A.I. Heim, Corrosion resistance of copper and copper alloys, Ind. Eng. Chem. 49 (1957) 63A-66A. https://doi.org/10.1021/i650572a754.

[50] M.A. Shaik, B.R. Golla, Development of highly wear resistant Cu - Al alloys processed via powder metallurgy, Tribol. Int. 136 (2019) 127–139. https://doi.org/10.1016/j.triboint.2019.03.055.

[51] S. Liu, J. Jie, Z. Guo, S. Yue, T. Li, A comprehensive investigation on microstructure and magnetic properties of immiscible Cu-Fe alloys with variation of Fe content, Mater. Chem. Phys. 238 (2019) 121909. https://doi.org/10.1016/j.matchemphys.2019.121909.

[52] X. Cao, A. Nolting, Autogenous fiber laser welding of 70/30 Cu-Ni alloy plates, Mater. Des. 181 (2019) 108075. https://doi.org/10.1016/j.matdes.2019.108075.

[53] B. Luo, D. Li, C. Zhao, Z. Wang, Z. Luo, W. Zhang, A low Sn content Cu-Ni-Sn alloy with high strength and good ductility, Mater. Sci. Eng. A. 746 (2019) 154–161. https://doi.org/10.1016/j.msea.2018.12.120.

[54] L. Meng, Z. Zhang, Y. Zhang, J. Zhang, X. Yang, H. Gao, B. Shu, X. Zhu, The in fl uence of stacking fault energy on mechanical properties of Cu-Al-Zn alloys processed by surface mechanical attrition treatment, Mater. Sci. Eng. A. 744 (2019) 235–240. https://doi.org/10.1016/j.msea.2018.12.021.

[55] P. Chand, N. Kumar, S. Sahu, S. Shekhar, Influence of short heat-treatment on microstructural and mechanical inhomogeneity of constrained groove pressed Cu-Zn alloy, Mater. Chem. Phys. 238 (2019) 121912. https://doi.org/10.1016/j.matchemphys.2019.121912.

[56] J. Zhou, D. Zhu, L. Tang, X. Jiang, S. Chen, X. Peng, C. Hu, Microstructure and

properties of powder metallurgy Cu-1 % Cr-0 . 65 % Zr alloy prepared by hot pressing, Vacuum. 131 (2016) 156–163.

[57] A.S. Sharma, K. Biswas, B. Basu, D. Chakravarty, Spark plasma sintering of nanocrystalline Cu and Cu-10 wt Pct Pb alloy, Metall. Mater. Trans. A. 42 (2011) 2072–2084. https://doi.org/10.1007/s11661-010-0589-4.

[58] A. Nassef, M. El-Hadek, Microstructure and mechanical behavior of hot pressed Cu-Sn powder alloys, Adv. Mater. Sci. Eng. 53 (2016) 38–42. https://doi.org/10.1155/2016/9796169.

[59] A.G. Shivasiddaramiah, U.S. Mallik, R. Mahato, C. Shashishekar, Evaluation of corrosion behaviour of Cu-Al-Be-Mn Quaternary shape memory alloys, Mater. Today Proc. 4 (2017) 10971–10977. https://doi.org/10.1016/j.matpr.2017.08.054.

[60] H. Wei, L. Hou, Y. Cui, Y. Wei, Effect of Ti content on corrosion behavior of Cu − Ti alloys in 3 . 5 % NaCl solution, Trans. Nonferrous Met. Soc. China. 28 (2018) 669–675.

[61] L. Jia, X. Lin, H. Xie, Z. Lu, X. Wang, Abnormal improvement on electrical conductivity of Cu–Ni–Si alloys resulting from semi-solid isothermal treatment, Mater. Lett. 77 (2012) 107–109.

[62] H. Fernee, J. Nairn, A. Atrens, Precipitation hardening of Cu-Fe-Cr alloys: Part I mechanical and electrical properties, J. Mater. Sci. 36 (2001) 2711–2719. https://doi.org/10.1023/A:1017916930459.

[63] S. Chabri, S. Bera, B.N. Mondal, A. Basumallick, P.P. Chattopadhyay, Microstructure and magnetic behavior of Cu – Co – Si ternary alloy synthesized by mechanical alloying and isothermal annealing, J. Magn. Magn. Mater. 426 (2017) 454–458.

[64] M. Rabiee, H. Mirzadeh, A. Ataie, Unraveling the effects of process control agents on mechanical alloying of nanostructured Cu-Fe alloy, J. Ultrafine Grained Nanostructured Mater. 49 (2016) 17–21. https://doi.org/10.7508/jufgnsm.2016.01.03.

[65] C. Martinez, F. Briones, P. Rojas, S. Ordonez, C. Aguilar, D. Guzman, Microstructure and mechanical properties of copper, nickel and ternary alloys Cu-Ni-Zr Obtained by Mechanical Alloying and Hot Pressing, MRS Adv. 2 (2017) 2831–2836. https://doi.org/10.1557/adv.2017.

[66] J. Li, J. Wongsa-Ngam, J. Xu, D. Shan, B. Guo, T.G. Langdon, Wear resistance of an ultrafine-grained Cu-Zr alloy processed by equal-channel angular pressing, Wear. 326–327 (2015) 10–19. https://doi.org/10.1016/j.wear.2014.12.022.

[67] A.J. Ardell, Precipitation hardening, Metall. Trans. A. 16 (1985) 2131–2165. https://doi.org/10.1007/BF02670416.

[68] A.K. Bhargava, M.K. Banerjee, 2.14 Heat-treating copper and nickel alloys, in: M.S.J. Hashmi (Ed.), Compr. Mater. Finish., Elsevier, Oxford, 2017: pp. 398–420. https://doi.org/10.1016/B978-0-12-803581-8.09196-7.

[69] J. Ruzic, J. Stasic, V. Rajkovic, D. Bozic, Strengthening effects in precipitation and dispersion hardened powder metallurgy copper alloys, Mater. Des. 49 (2013) 746–754. https://doi.org/10.1016/j.matdes.2013.02.030.

[70] D. Bozic, M. Mitkov, Strengthening of Cu–Ti alloys by rapid solidification processing,

Powder Metall. 34 (1991) 199–204. https://doi.org/10.1179/pom.1991.34.3.199.

[71] P. Jain, Influence of heat treatment on microstructure and hardness of nickel aluminium bronze (Cu-10Al-5Ni-5Fe), IOSR J. Mech. Civ. Eng. 4 (2013) 16–21. https://doi.org/10.9790/1684-0461621.

[72] A.G. Guy, Elements of physical metallurgy, Addison-Wesley Pub. Co., 1959.

[73] F. Hasan, J. Iqbal, F. Ahmed, Development of microstructure in silicon-aluminum-bronze, J. Engg. Appl. Sci. 3 (2008) 47–53.

[74] U. Donatus, J.A. Omotoyinbo, I.M. Momoh, Mechanical properties and microstructures of locally produced aluminium-bronze alloy, J. Miner. Mater. Charact. Eng. 11 (2012) 1020–1026. https://doi.org/10.4236/jmmce.2012.1110105.

[75] F. Hasan, J. Iqbal, N. Ridley, Microstructure of as-cast aluminium bronze containing iron, Mater. Sci. Technol. (United Kingdom). 1 (1985) 312–315. https://doi.org/10.1179/mst.1985.1.4.312.

[76] G. Ghosh, J. Miyake, M.E. Fine, The systems-based design of high-strength , high-conductivity alloys, J. Miner. Met. Mater. Soc. 49 (1997) 56–60.

[77] Q. Chang, J. Xie, A. Mao, W. Wang, Study on interface structure of Cu/Al clad plates by roll casting, Metals (Basel). 8 (2018) 770. https://doi.org/10.3390/met8100770.

[78] Y. Gong, J. Gu, S. Ni, H. Wu, M. Song, A good combination of strength and ductility of ultra-coarse-grained Cu-Al alloy with coarse-grained surface layer via pre-torsional treatment, Micron. 129 (2020). https://doi.org/10.1016/j.micron.2019.102783.

[79] J. Gu, S. Ni, M. Song, Effects of torsional deformation on the mechanical properties and microstructures of a commercial pure copper, J. Mater. Eng. Perform. 28 (2019) 543–548. https://doi.org/10.1007/s11665-018-3825-5.

[80] Y. Liu, Y. Cao, H. Zhou, X. Chen, Y. Liu, L. Xiao, X. Huan, Y. Zhao, Y. Zhu, Mechanical properties and microstructures of commercial-purity aluminum processed by rotational accelerated shot peening plus cold rolling, Adv. Eng. Mater. 22 (2020) 1–8. https://doi.org/10.1002/adem.201900478.

[81] K. Lu, J. Lu, Nanostructured surface layer on metallic materials induced by surface mechanical attrition treatment, Mater. Sci. Eng. A. 375–377 (2004) 38–45. https://doi.org/10.1016/j.msea.2003.10.261.

[82] X. Chen, Z. Han, K. Lu, Wear mechanism transition dominated by subsurface recrystallization structure in Cu – Al alloys, 320 (2014) 41–50.

[83] M.A. Shaik, B.R. Golla, S.B. Pitchuka, Processing and Characterization of Extremely Hard and Strong Cu-(0-15 wt pct)Al Alloys, Metall. Mater. Trans. A. 51 (2020) 708–724. https://doi.org/10.1007/s11661-019-05545-x.

[84] I. Cenoz, Metallography of aluminium bronze alloy as cast in permanent iron die, Metalurgija. 16 (2010) 115–122. https://doi.org/10.1007/978-81-322-2517-1_45.

[85] K.S. Lee, K. Yong-Nam, Solid-state bonding between Al and Cu by vacuum hot pressing, Trans. Nonferrous Met. Soc. China. 23 (2013) 341–346. https://doi.org/10.1016/S1003-6326(13)62467-X.

[86] D.Y. Ying, D.L. Zhang, Solid-state reactions between Cu and Al during mechanical alloying and heat treatment, J. Alloys Compd. 311 (2000) 275–282.

[87] F. Ji, S.B. Xue, J.Y. Lou, Y. Bin Lou, S.Q. Wang, Microstructure and properties of Cu/Al joints brazed with Zn-Al filler metals, Trans. Nonferrous Met. Soc. China (English Ed. 22 (2012) 281–287. https://doi.org/10.1016/S1003-6326(11)61172-2.

[88] M. Abbasi, A.K. Taheri, M.T. Salehi, Growth rate of intermetallic compounds in Al/Cu bimetal produced by cold roll welding process, J. Alloys Compd. 319 (2001) 233–241.

[89] T.A. Mai, A.C. Spowage, Characterisation of dissimilar joints in laser welding of steel–kovar, copper–steel and copper–aluminium, Mater. Sci. Eng. A. 374 (2004) 224–233. https://doi.org/10.1016/j.msea.2004.02.025.

[90] W.B. Lee, K.S. Bang, S.B. Jung, Effects of intermetallic compound on the electrical and mechanical properties of friction welded Cu/Al bimetallic joints during annealing, J. Alloys Compd. 390 (2005) 212–219. https://doi.org/10.1016/j.jallcom.2004.07.057.

[91] M. Pintore, J. Wölck, T. Mittler, T. Greß, B. Tonn, W. Volk, Composite Casting and Characterization of Cu–Al Bilayer Compounds, Int. J. Met. 14 (2020) 155–166. https://doi.org/10.1007/s40962-019-00344-x.

[92] S. Alex, K. Chattopadhyay, B. Basu, Tailored specular reflectance properties of bulk Cu based novel intermetallic alloys, Sol. Energy Mater. Sol. Cells. 149 (2016) 66–74. https://doi.org/10.1016/j.solmat.2016.01.002.

[93] S. Alex, R. Kumar P, K. Chattopadhyay, H.C. Barshilia, B. Basu, Thermally evaporated Cu–Al thin film coated flexible glass mirror for concentrated solar power applications, Mater. Chem. Phys. 232 (2019) 221–228. https://doi.org/10.1016/j.matchemphys.2019.04.078.

[94] M.A. Shaik, B. raju Golla, Densification, microstructure and properties of mechanically alloyed and hot-pressed Cu–15 wt % Al alloy, J. Mater. Sci. 53 (2018) 14694–14712. https://doi.org/10.1007/s10853-018-2638-0.

[95] F.A. Calvo, A. Ureng, J.M. Gomez De Salazar, F. Molleda, Special features of the formation of the diffusion bonded joints between copper and aluminium, J. Mater. Sci. 23 (1988) 2273–2280. https://doi.org/10.1007/BF01115800.

[96] Y. Guo, G. Liu, H. Jin, Z. Shi, G. Qiao, Intermetallic phase formation in diffusion-bonded Cu/Al laminates, J. Mater. Sci. 46 (2011) 2467–2473. https://doi.org/10.1007/s10853-010-5093-0.

[97] C.-Y. Chen, W.-S. Hwang, Effect of Annealing on the Interfacial Structure of Aluminum-Copper Joints, Mater. Trans. 48 (2007) 1938–1947. https://doi.org/10.2320/matertrans.MER2006371.

[98] L. Wu, L. Liu, J. Liu, R. Zhang, Effects of high pressure heat treatment on microstructure and micro-mechanical properties of Cu77. 96Al22. 04 alloy, Mater. Trans. 53 (2012) 504–507. https://doi.org/10.1111/j.1748-5827.2012.01242.x.

[99] H.Y. Wang, Y. Chen, Y.W. Liu, F. Li, J.H. Liu, G.-R. Peng, W.K. Wang, Pressure effects on solid state phase transformation of aluminium bronze in cooling process, Chinese Phys. Lett. 26 (2009) 106201. https://doi.org/10.1088/0256-307X/26/10/106201.

[100] J.B.C. It, H.A. Davies, C.M. Sellars, Strenghtening in rapidly solidified age hardened Cu-Cr and Cu-Cr-Zr alloys, Acta Mater. 45 (1997) 177–190. https://doi.org/doi.org/10.1016/S1359-6454(96)00142-5.

[101] R.F. Schmidt, D.G. Schmidt, M. Sahoo, Copper and Copper Alloys, ASM Handbo, ASM International, 1998.

[102] S. Patra, Gouthama, K. Mondal, Densification behavior of mechanically milled Cu-8at.% Cr alloy and its mechanical and electrical properties, Prog. Nat. Sci. Mater. Int. 24 (2014) 608–622. https://doi.org/10.1016/j.pnsc.2014.10.006.

[103] S. Zhang, H. Zhu, L. Zhang, W. Zhang, H. Yang, X. Zeng, Microstructure and properties of high strength and high conductivity Cu-Cr alloy components fabricated by high power selective laser melting, Mater. Lett. 237 (2019) 306–309. https://doi.org/10.1016/j.matlet.2018.11.118.

[104] K. Biswas, A.S. Sharma, B. Basu, On the densification mechanisms and properties of Cu-Pb and Cu-Pb-TiB_2 nanocomposites densified using spark plasma sintering, Scr. Mater. 69 (2013) 122–126. https://doi.org/10.1016/j.scriptamat.2013.02.046.

[105] R. Yang, J. Wen, Y. Zhou, K. Song, Z. Song, Effect of Al Element on the Microstructure and Properties of Cu-Ni-Fe-Mn Alloys, Materials (Basel). 11 (2018) 1–11. https://doi.org/10.3390/ma11091777.

[106] P. Han, F. Xiao, W. Zou, B. Liao, Influence of hot pressing temperature on the microstructure and mechanical properties of 75% Cu–25% Sn alloy, Mater. Des. 53 (2014) 38–42.

[107] M. Yaşar, Y. Altunpak, The effect of aging heat treatment on the sliding wear behaviour of Cu-Al-Fe alloys, Mater. Des. 30 (2009) 878–884. https://doi.org/10.1016/j.matdes.2008.05.041.

[108] W.A. Soffa, D.E. Laughlin, High-strength age hardening copper-titanium alloys: Redivivus, Prog. Mater. Sci. 49 (2004) 347–366. https://doi.org/10.1016/S0079-6425(03)00029-X.

[109] V. Rajkovic, D. Bozic, A. Devecerski, M.T. Jovanovic, Characteristic of copper matrix simultaneously reinforced with nano- and micro-sized Al_2O_3 particles, Mater. Charact. 67 (2012) 129–137. https://doi.org/10.1016/j.matchar.2012.02.022.

[110] V. Rajkovic, D. Bozic, M.T. Jovanovic, Effects of copper and Al_2O_3 particles on characteristics of Cu- Al_2O_3 composites, Mater. Des. 31 (2010) 1962–1970. https://doi.org/10.1016/j.matdes.2009.10.037.

[111] F. Shehata, A. Fathy, M. Abdelhameed, S.F. Moustafa, Preparation and properties of Al_2O_3 nanoparticle reinforced copper matrix composites by in situ processing, Mater. Des. 30 (2009) 2756–2762. https://doi.org/10.1016/j.matdes.2008.10.005.

[112] X. Zhang, Y. Zhang, B. Tian, Y. Jia, Y. Liu, K. Song, A.A. Volinsky, Thermal deformation behavior of the Al_2O_3 -Cu/(W, Cr) electrical contacts, Vacuum. 164 (2019) 361–366. https://doi.org/10.1016/j.vacuum.2019.03.054.

[113] R.K. Gautam, S. Ray, S.C. Jain, S.C. Sharma, Tribological behavior of Cu–Cr–SiCp in situ composite, Wear. 265 (2008) 902–912. https://doi.org/10.1016/j.wear.2008.01.023.

[114] S. Tjong, Microstructural and mechanical characteristics of in situ metal matrix composites, Mater. Sci. Eng. R Reports. 29 (2000) 49–113. https://doi.org/10.1016/S0927-796X(00)00024-3.

[115] G.A. Bagheri, The effect of reinforcement percentages on properties of copper matrix composites reinforced with TiC particles, J. Alloys Compd. 676 (2016) 120–126. https://doi.org/10.1016/j.jallcom.2016.03.085.

[116] C. Zou, H. Kang, W. Wang, Z. Chen, R. Li, X. Gao, T. Li, T. Wang, Effect of La addition on the particle characteristics, mechanical and electrical properties of in situ Cu-TiB2composites, J. Alloys Compd. 687 (2016) 312–319. https://doi.org/10.1016/j.jallcom.2016.06.129.

[117] M.A. Shaik, B.R. Golla, Two body abrasion wear behaviour of Cu–ZrB_2 composites against SiC emery paper, Wear. 450–451 (2020) 203260. https://doi.org/10.1016/j.wear.2020.203260.

[118] A. Fathy, F. Shehata, M. Abdelhameed, M. Elmahdy, Compressive and wear resistance of nanometric alumina reinforced copper matrix composites, Mater. Des. 36 (2012) 100–107. https://doi.org/10.1016/j.matdes.2011.10.021.

[119] R. Harichandran, N. Selvakumar, ScienceDirect Effect of nano/micro B_4C particles on the mechanical properties of aluminium metal matrix composites fabricated by ultrasonic cavitation-assisted solidification process, Arch. Civ. Mech. Eng. 16 (2015) 147–158. https://doi.org/10.1016/j.acme.2015.07.001.

[120] S.C. Tjong, K.C. Lau, Tribological behaviour of SiC particle-reinforced copper matrix composites, Mater. Lett. 43 (2000) 274–280. https://doi.org/10.1016/S0167-577X(99)00273-6.

[121] A.S. Prosviryakov, SiC content effect on the properties of Cu–SiC composites produced by mechanical alloying, J. Alloys Compd. 632 (2015) 707–710. https://doi.org/10.1016/j.jallcom.2015.01.298.

[122] I. Dinaharan, S. Saravanakumar, K. Kalaiselvan, S. Gopalakrishnan, Microstructure and sliding wear characterization of Cu/TiB_2 copper matrix composites fabricated via friction stir processing, J. Asian Ceram. Soc. 5 (2017) 295–303. https://doi.org/10.1016/j.jascer.2017.06.002.

[123] S. Buytoz, F. Dagdelen, S. Islak, M. Kok, D. Kir, E. Ercan, Effect of the TiC content on microstructure and thermal properties of Cu-TiC composites prepared by powder metallurgy, J. Therm. Anal. Calorim. 117 (2014) 1277–1283. https://doi.org/10.1007/s10973-014-3900-6.

[124] F. Wang, Y. Li, X. Wang, Y. Koizumi, Y. Kenta, A. Chiba, In-situ fabrication and characterization of ultrafine structured Cu–TiC composites with high strength and high conductivity by mechanical milling, J. Alloys Compd. 657 (2016) 122–132.

[125] B. Basu, G.B. Raju, A.K. Suri, Processing and properties of monolithic TiB_2 based materials, Int. Mater. Rev. 51 (2006) 352–374. https://doi.org/10.1179/174328006X102529.

[126] S.N. Basu, K.M. Hubbard, J.-P. Hirvonen, T.E. Mitchell, M. Nastasi, Microstructure and Stabiulty of TiB 2 and Cu Multilayers , MRS Proc. 187 (1990).

https://doi.org/10.1557/proc-187-157.

[127] A.S. Sharma, N. Mishra, K. Biswas, B. Basu, Densification kinetics, phase assemblage and hardness of spark plasma sintered Cu-10 wt.% TiB_2 and Cu-10 wt.% TiB_2-10 wt.% Pb composites, J. Mater. Res. 28 (2013) 1517–1528. https://doi.org/10.1557/jmr.2013.119.

[128] X.H. Zhang, C. Van, Z.Z. Yu, In-situ combustion synthesis of ultrafine TiB2 particles reinforced Cu matrix composite, J. Mater. Sci. 39 (2004) 4683–4685. https://doi.org/10.1023/B:JMSC.0000034171.47412.7f.

[129] T. Venkateswaran, B. Basu, G.B. Raju, D.Y. Kim, Densification and properties of transition metal borides-based cermets via spark plasma sintering, J. Eur. Ceram. Soc. 26 (2006) 2431–2440. https://doi.org/10.1016/j.jeurceramsoc.2005.05.011.

[130] G. Lojen, I. Anžel, A. Kneissl, A. Križman, E. Unterweger, B. Kosec, M. Bizjak, Microstructure of rapidly solidified Cu-Al-Ni shape memory alloy ribbons, J. Mater. Process. Technol. 162–163 (2005) 220–229. https://doi.org/10.1016/j.jmatprotec.2005.02.196.

[131] X. Wu, C. Wen, Y. Gong, S. Ren, J. Tao, L. Chen, Y. Long, X. Zhu, Effect of stacking fault energy and strain rate on the mechanical properties of Cu and Cu alloys, J. Alloys Compd. 573 (2013) 1–5. https://doi.org/10.1016/j.jallcom.2013.03.292.

[132] M. Mihovsky, V. Hadzhiyski, L. Todorov, D. Dimitrova, Plasma-induction technology for reduction processing of copper concentrate pellets, J. Univ. Chem. Technol. Metall. 41 (2006) 55–60.

[133] F. Shehata, M. Abdelhameed, A. Fathy, M. Elmahdy, Preparation and Characteristics of Cu- Al_2O_3 Nanocomposite, Open J. Met. 01 (2011) 25–33. https://doi.org/10.4236/ojmetal.2011.12004.

[134] W. Wang, W. Zeng, C. Li, J. Liang, D. Zhang, Microstructure and mechanical properties of ultrafine grained Cu-0.8 wt.%C alloy with a bimodal microstructure produced by powder metallurgy techniques, Mater. Sci. Eng. A. 712 (2018) 214–222. https://doi.org/10.1016/j.msea.2017.11.116.

[135] G. Sethi, A. Upadhyaya, D. Agarwal, microwave and conventional sintering of premixed and prealloyed Cu-12Sn bronze, Sci. Sinter. 35 (2003) 49–65.

[136] M. Gojic, L. Vrsalovic, S. Kozuh, A. Kneissl, I. Anzel, S. Gudic, B. Kosec, M. Klisskic, Electrochemical and microstructural study of Cu-Al-Ni shape memory alloy, J. Alloys Compd. 509 (2011) 9782–9790. https://doi.org/10.1016/j.jallcom.2011.07.107.

[137] S.R. Kawk, T.A. Ring, B.S. Choi, A simple two-step fabrication route for Cu composite reinforced by three-dimensional graphene network, J. Ind. Eng. Chem. 70 (2019) 484–488. https://doi.org/10.1016/j.jiec.2018.11.011.

[138] C.Y. Yap, C.K. Chua, Z.L. Dong, Z.H. Liu, D.Q. Zhang, L.E. Loh, S.L. Sing, Review of selective laser melting: Materials and applications, Appl. Phys. Rev. 2 (2015). https://doi.org/10.1063/1.4935926.

[139] L. Collini, Copper Alloys: Early Applications and Current Performance - Enhancing Processes, IntechOpen, 2012.

[140] M. Rohan, D. Ahirrao, B.G. Marlapalle, "A review paper on analysis and optimization of aluminium casting parameters," Int. Res. J. Eng. Technol. 6 (2019) 1129–1132.

[141] D.M. Wankhede, B.E. Narkhede, S.K. Mahajan, C.M. Choudhari, Influence of pouring temperature and external chills on mechanical properties of aluminum silicon alloy castings, Mater. Today Proc. 5 (2018) 17627–17635. https://doi.org/10.1016/j.matpr.2018.06.081.

[142] A. Juriani, Casting defects analysis in foundry and their remedial measures with industrial case studies, J. Mech. Civ. Eng. 12 (2015) 43–53. https://doi.org/10.9790/1684-12614354.

[143] S.D. El Wakil, Processes and Design for Manufacturing, Three, CRC Press, 2019. https://doi.org/10.1201/9780429506635.

[144] R. Clinktan, V. Senthil, K.R. Ramkumar, S. Sivasankaran, F.A. Al-Mufadi, Influence of B_4C nanoparticles on mechanical behaviour of Silicon brass nanocomposite through mechanical alloying and hot pressing, Ceram. Int. 45 (2019) 18691–18700. https://doi.org/10.1016/j.ceramint.2019.06.094.

[145] S. Nagarjuna, M. Srinivas, K. Balasubramanian, D.S. Sarma, The alloy content and grain size dependence of flow stress in Cu-Ti alloys, Acta Mater. 44 (1996) 2285–2293. https://doi.org/10.1016/1359-6454(95)00358-4.

[146] M.R. Akbarpour, E. Salahi, F. Alikhani Hesari, A. Simchi, H.S. Kim, Fabrication, characterization and mechanical properties of hybrid composites of copper using the nanoparticulates of SiC and carbon nanotubes, Mater. Sci. Eng. A. 572 (2013) 83–90. https://doi.org/10.1016/j.msea.2013.02.039.

[147] A.K. Shukla, N. Nayan, S.V.S.N. Murty, S.C. Sharma, P. Chandran, S.R. Bakshi, K.M. George, Processing of copper-carbon nanotube composites by vacuum hot pressing technique, Mater. Sci. Eng. A. 560 (2013) 365–371. https://doi.org/10.1016/j.msea.2012.09.080.

[148] R. Zheng, N. Li, Z. Zhan, Friction and wear behavior of Cu-La2O3 composite sliding against 52100 bearing steel in vacuum, Vacuum. 161 (2019) 55–62. https://doi.org/10.1016/j.vacuum.2018.12.019.

[149] W. Zhu, C. Zhao, C.T. Kwok, J. Zhou, F. Ren, Effects of nanocrystalline microstructure on the dry sliding wear behavior of a Cu-10 at.% Ag-10 at.% W ternary alloy against stainless steel, Wear. 402–403 (2018) 1–10. https://doi.org/10.1016/j.wear.2018.01.013.

[150] G. Purcek, H. Yanar, D. V. Shangina, M. Demirtas, N.R. Bochvar, S. V. Dobatkin, Influence of high pressure torsion-induced grain refinement and subsequent aging on tribological properties of Cu-Cr-Zr alloy, J. Alloys Compd. 742 (2018) 325–333. https://doi.org/10.1016/j.jallcom.2018.01.303.

[151] P. Zhang, L. Zhang, K. Fu, J. Cao, C. Shijia, X. Qu, Effects of different forms of Fe powder additives on the simulated braking performance of Cu-based friction materials for high-speed railway trains, Wear. 414–415 (2018) 317–326. https://doi.org/10.1016/j.wear.2018.09.006.

[152] B. Chen, Q. Bi, J. Yang, Y. Xia, J. Hao, Tribological properties of solid lubricants (graphite, h-BN) for Cu-based P/M friction composites, Tribol. Int. 41 (2008) 1145–

1152. https://doi.org/10.1016/j.triboint.2008.02.014.

[153] M. Pellizzari, G. Cipolloni, Tribological behaviour of Cu based materials produced by mechanical milling/alloying and spark plasma sintering, Wear. 376–377 (2017) 958–967. https://doi.org/10.1016/j.wear.2016.11.050.

[154] C. Zou, Z. Chen, H. Kang, W. Wang, R. Li, T. Li, T. Wang, Study of enhanced dry sliding wear behavior and mechanical properties of Cu-TiB_2 composites fabricated by in situ casting process, Wear. 392–393 (2017) 118–125. https://doi.org/10.1016/j.wear.2017.09.016.

[155] A. Rohatgi, K.S. Vecchio, I.G.T. Gray, A metallographic and quantitative analysis of the influence of stacking fault energy on shock-hardening in Cu and Cu–Al alloys, Acta Mater. 49 (2001) 427–438. https://doi.org/10.1016/j.proeng.2012.03.045.

[156] Y.H. Zhao, Y.T. Zhu, X.Z. Liao, Z. Horita, T.G. Langdon, Tailoring stacking fault energy for high ductility and high strength in ultrafine grained Cu and its alloy, Appl. Phys. Lett. 89 (2006) 121906.

[157] Y.H. Zhao, J.F. Bingert, Y.T. Zhu, X.Z. Liao, R.Z. Valiev, Z. Horita, T.G. Langdon, Y.Z. Zhou, E.J. Lavernia, Tougher ultrafine grain Cu via high-angle grain boundaries and low dislocation density, Appl. Phys. Lett. 92 (2008) 81903. https://doi.org/10.1063/1.2870014.

[158] J.R. Davis, A.S.M.I.H. Committee, Copper and Copper Alloys, ASM International, 2001.

[159] A. Azushima, R. Kopp, A. Korhonen, D.Y. Yang, F. Micari, G.D. Lahoti, P. Groche, J. Yanagimoto, N. Tsuji, A. Rosochowski, A. Yanagida, Severe plastic deformation (SPD) processes for metals, CIRP Ann. - Manuf. Technol. 57 (2008) 716–735. https://doi.org/10.1016/j.cirp.2008.09.005.

[160] G. Sakai, K. Nakamura, Z. Horita, T.G. Langdon, Developing high-pressure torsion for use with bulk samples, Mater. Sci. Eng. A. 406 (2005) 268–273. https://doi.org/10.1016/j.msea.2005.06.049.

[161] N. Tsuji, Y. Saito, H. Utsunomiya, S. Tanigawa, Ultra-fine grained bulk steel produced by accumulative roll-bonding (ARB) process, Scr. Mater. 40 (1999) 795–800. https://doi.org/10.1016/S1359-6462(99)00015-9.

[162] V.. Segal, Severe plastic deformation: simple shear versus pure shear, Mater. Sci. Eng. A. 338 (2002) 331–344.

[163] S. Qu, X.H. An, H.J. Yang, C.X. Huang, G. Yang, Q.S. Zang, Z.G. Wang, S.D. Wu, Z.F. Zhang, Microstructural evolution and mechanical properties of Cu-Al alloys subjected to equal channel angular pressing, Acta Mater. 57 (2009) 1586–1601. https://doi.org/10.1016/j.actamat.2008.12.002.

[164] H. Jiang, Y.T. Zhu, D.P. Butt, I. V. Alexandrov, T.C. Lowe, Microstructural evolution, microhardness and thermal stability of HPT-processed Cu, Mater. Sci. Eng. A. 290 (2000) 128–138. https://doi.org/10.1016/S0921-5093(00)00919-9.

[165] N. Takata, S.H. Lee, C.Y. Lim, S.S. Kim, N. Tsuji, Nanostructured bulk copper fabricated by accumulative roll bonding, in: J. Nanosci. Nanotechnol., 2007: pp. 3985–3989. https://doi.org/10.1166/jnn.2007.073.

[166] S.H. Lee, C.H. Lee, S.J. Yoon, S.Z. Han, C.Y. Lim, Annealing characteristics of nanostructured Cu-Fe-P alloy processed by accumulative roll-bonding, in: J. Nanosci. Nanotechnol., 2007: pp. 3872–3875. https://doi.org/10.1166/jnn.2007.050.

[167] G. Liu, J. Gu, S. Ni, Y. Liu, M. Song, Microstructural evolution of Cu–Al alloys subjected to multi-axial compression, Mater. Charact. 103 (2015) 107–119. https://doi.org/10.1016/j.matchar.2015.03.021.

[168] F. Glas, Ziehen von edelstahlblechen mit werkzeugen aus aluminium-mehrstoffbronzen, Tribol. Und Schmierungstechnik. 52 (2005) 55–63.

[169] B.K. Prasad, Dry sliding wear response of some bearing alloys as influenced by the nature of microconstituents and sliding conditions, Metall. Mater. Trans. A. 28 (1997) 809–815. https://doi.org/10.1007/s11661-997-1008-3.

[170] D. V. Kudashov, R. Zauter, H.R. Müller, Spray-formed high-aluminium bronzes, Mater. Sci. Eng. A. 477 (2008) 43–49. https://doi.org/10.1016/j.msea.2007.06.085.

[171] C.N. Nwambu, I.M. Anyaeche, G.C. Onwubiko, E.E. Nnuka, Modification of the structure and mechanical properties of aluminum bronze (Cu-10%Al) alloy with Zirconium and Titanium, Int. J. Sci. Eng. Res. 8 (2017) 1048–1057.

[172] G. Purcek, H. Yanar, O. Saray, I. Karaman, H.J. Maier, Effect of precipitation on mechanical and wear properties of ultrafine-grained Cu-Cr-Zr alloy, Wear. 311 (2014) 149–158. https://doi.org/10.1016/j.wear.2014.01.007.

[173] A. Rohatgi, K.S. Vecchio, G.T. Gray, The influence of stacking fault energy on the mechanical behavior of Cu and Cu-Al alloys: Deformation twinning, work hardening, and dynamic recovery, Metall. Mater. Trans. A. 32 (2001) 135–145. https://doi.org/10.1007/s11661-001-0109-7.

[174] A. Paknia, A. Pramanik, A.R. Dixit, S. Chattopadhyaya, Effect of Size, Content and Shape of Reinforcements on the Behavior of Metal Matrix Composites (MMCs) Under Tension, J. Mater. Eng. Perform. 25 (2016) 4444–4459. https://doi.org/10.1007/s11665-016-2307-x.

[175] J. Ruzic, J. Stasic, S. Markovic, K. Raic, D. Bozic, Synthesis and characterization of Cu-ZrB_2 alloy produced by PM techniques, Sci. Sinter. 46 (2014) 217–224. https://doi.org/10.2298/SOS1402217R.

[176] W. Ma, J. Lu, B. Wang, Sliding friction and wear of Cu-graphite against 2024, AZ91D and Ti6Al4V at different speeds, Wear. 266 (2009) 1072–1081. https://doi.org/10.1016/j.wear.2009.01.051.

[177] S.G. Sapate, A. Uttarwar, R.C. Rathod, R.K. Paretkar, Analyzing dry sliding wear behaviour of copper matrix composites reinforced with pre-coated SiCp particles, Mater. Des. 30 (2009) 376–386. https://doi.org/10.1016/j.matdes.2008.04.055.

[178] C. Martinez, F. Briones, P. Rojas, C. Aguilar, D. Guzman, S. Ordonez, Microstructural and mechanical characterization of copper , nickel , and Cu-based alloys obtained by mechanical alloying and hot pressing, Mater. Lett. 209 (2017) 509–512.

[179] J.P. Tu, W.X. Qi, Y.Z. Yang, F. Liu, J.T. Zhang, G.Y. Gan, N.Y. Wang, X.B. Zhang, M.S. Liu, Effect of aging treatment on the electrical sliding wear behavior of Cu-Cr-Zr alloy, Wear. 249 (2002) 1021–1027. https://doi.org/10.1016/S0043-1648(01)00843-2.

[180] J.P. Tu, W. Rong, S.Y. Guo, Y.Z. Yang, Dry sliding wear behavior of in situ Cu-TiB_2 nanocomposites against medium carbon steel, Wear. 255 (2003) 832–835. https://doi.org/10.1016/S0043-1648(03)00115-7.

[181] F. Ren, S.N. Arshad, P. Bellon, R.S. Averback, M. Pouryazdan, H. Hahn, Sliding wear-induced chemical nanolayering in Cu – Ag , and its implications for high wear resistance, Acta Mater. 72 (2014) 148–158.

[182] J.A. Hawk, R.D. Wilson, Tribology of earthmoving, mining, and minerals processing, in: Mod. Tribol. Handb., 2nd ed., CRC Press, Boca Raton, London, New York, Washington DC, 2001: pp. 1331–1370.

[183] G.Y. Lee, C.K.H. Dharan, R.O. Ritchie, A physically-based abrasive wear model for composite materials, Wear. 252 (2002) 322–331. https://doi.org/10.1016/S0043-1648(01)00896-1.

[184] A.M. Soleimanpour, P. Abachi, K. Purazrang, Wear behaviour of in situ Cu – Al_2O_3 composites produced by internal oxidation of as cast alloys Wear behaviour of in situ Cu – Al_2O_3 composites produced by internal oxidation of as cast alloys, Tribology. 3 (2009) 125–131. https://doi.org/10.1179/175158309X12560424605150.

[185] E. Xu, J. Huang, Y. Li, Z. Zhu, M. Cheng, D. Li, H. Zhong, J. Liu, Y. Jiang, GXu, E., Huang, J., Li, Y., Zhu, Z., Cheng, M., Li, D., Zhong, H., Liu, J., Jiang, Y., 2019. Graphite cluster / copper-based powder metallurgy composite for pantograph slider with well-behaved mechanical and wear performance. Powder Technol. 344, 551–560., Powder Technol. 344 (2019) 551–560. https://doi.org/10.1016/j.powtec.2018.12.059.

[186] L. Poovazhagan, H.J. Thomas, M. Selvaraj, Microstructure and abrasive wear behavior of copper – boron carbide nanocomposites, in: A.K. (Department of M.E.C. of E.C. Lakshminarayanan, S. Idapalapati, M. Vasudevan (Eds.), Adv. Mater. Metall., Lecture No, Springer, Singapore, 2019: pp. 47–55.

[187] Y. Reddy, R.K. Khatitrkar, S.G. Sapate, S.A. Road, Abrasive wear behaviour of copper-SIC and copper-SIO_2 composites, Int. J. Mod. Phys. Conf. Ser. 22 (2013) 416–423. https://doi.org/10.1142/S2010194513010465.

[188] A. Fathy, O. Elkady, A. Abu-Oqail, Synthesis and characterization of Cu–ZrO_2 nanocomposite produced by thermochemical process, J. Alloys Compd. 719 (2017) 411–419. https://doi.org/10.1016/j.jallcom.2017.05.209.

[189] K.S. Al-rubaie, H.N. Yoshimura, D.B. De Mello, Two-body abrasive wear of Al–SiC composites, Wear. 233–235 (1999) 444–454.

[190] S. Fu, X. Chen, P. Liu, Preparation of CNTs/Cu composites with good electrical conductivity and excellent mechanical properties, Mater. Sci. Eng. A. 771 (2020) 138656. https://doi.org/10.1016/j.msea.2019.138656.

[191] L. Gomidželović, E. Pozega, A. Kostov, N. Vukovic, V. Krstic, D. Zivkovic, L. Balanovic, Thermodynamics and characterization of shape memory Cu-Al-Zn alloys, Trans. Nonferrous Met. Soc. China (English Ed. 25 (2015) 2630–2636. https://doi.org/10.1016/S1003-6326(15)63885-7.

[192] D. Bozic, J. Ruzic, J. Stasic, V. Rajkovic, Synthesis and characteristics of precipitation hardened Cu–Cr alloy and multiply hardened Cu–Cr–Al_2O_3 nanocomposite obtained

using powder metallurgy techniques, Int. J. Mater. Res. 105 (2014) 194–199. https://doi.org/10.3139/146.111000.

[193] W.A. Monteiro, J.A.G. Carrjo, C.R. Da Silveira, E. Vitor, S.J. Buso, Structural and electrical properties of copper-nickel-aluminum alloys obtained by conventional powder metallurgy method, Mater. Sci. Forum. 660–661 (2010) 41–45. https://doi.org/10.4028/www.scientific.net/MSF.660-661.41.

[194] A.K. Shukla, S.V.S.N. Murty, R.S. Kumar, K. Mondal, Effect of powder milling on mechanical properties of hot-pressed and hot-rolled Cu-Cr-Nb alloy, J. Alloys Compd. 580 (2013) 427–434. https://doi.org/10.1016/j.jallcom.2013.06.118.

[195] Z. Mountassir, A. Srhiri, Electrochemical behaviour of Cu – 40Zn in 3 % NaCl solution polluted by sulphides : Effect of aminotriazole, Corros. Sci. 49 (2007) 1350–1361.

[196] A. Drach, I. Tsukrov, J. Decew, J. Aufrecht, A. Grohbauer, U. Hofmann, Field studies of corrosion behaviour of copper alloys in natural seawater, Corros. Sci. 76 (2013) 453–464. http://dx.doi.org/10.1016/j.corsci.2013.07.019.

[197] A.M. Alfantazi, T.M. Ahmed, D. Tromans, Corrosion behavior of copper alloys in chloride media, Mater. Des. 30 (2009) 2425–2430. https://doi.org/10.1016/j.matdes.2008.10.015.

[198] E. Sidot, L. Bousselmi, Corrosion behaviour of Cu – 10Sn bronze in aerated NaCl aqueous media – Electrochemical investigation, Corros. Sci. 49 (2007) 3333–3347.

[199] U. Min, J.C.M. Li, The microstructure and dealloying kinetics of a Cu-Mn alloy, J. Mater. Res. 9 (1994) 2878–2883.

[200] A.M. Zaky, S.S.A. El-rehim, B.M. Mohamed, Effect of addition of sulphide ions on the electrochemical behaviour and corrosion of cu-ag alloys in alkaline solutions, Int. J. Electrochem. Sci. 1 (2006) 17–31.

[201] C.L. Zeng, P.Y. Guo, W.T. Wu, Electrochemical impedance spectra for the corrosion of two-phase Cu-15Al alloy in eutectic (Li, K)$2CO_3$ at 650 °C in air, Electrochim. Acta. 49 (2004) 1445–1450. https://doi.org/10.1016/j.electacta.2003.10.031.

[202] M.A. Migahed, M.M. El-rabiei, H. Nady, M. Fathy, Synthesis, Characterization of some ethoxylated tolyltriazole derivatives and evaluation of their performance as corrosion inhibitors for Cu-10Al alloy in seawater, J. Environ. Chem. Eng. 4 (2016) 3741–3752.

[203] B.G. Ateya, E.A. Ashour, S.M. Sayed, Stress Corrosion Behavior of α-Aluminum Bronze in Saline Water, Corrosion. 50 (1994) 20–25.

[204] S.N. Saud, E. Hamzah, T. Abubakar, S. Farahany, A. Abdolahi, M.M. Taheri, Influence of Silver nanoparticles addition on the phase transformation , mechanical properties and corrosion behaviour of Cu – Al – Ni shape memory alloys, J. Alloys Compd. 612 (2014) 471–478.

[205] L.I.N. Gaoyong, Z. Yuxiong, Z. Juhua, Z.O.U. Yanming, L.I.U. Jian, S.U.N. Liping, Influence of rare earth elements on corrosion behavior of Al-brass in marine water, J. Rare Earths. 29 (2011) 638–644.

[206] S.N. Saud, E. Hamzah, T. Abubakar, H.R. Bakhsheshi-Rad, Correlation of microstructural and corrosion characteristics of quaternary shape memory alloys Cu–Al–

Ni–X (X=Mn or Ti), Trans. Nonferrous Met. Soc. China. 25 (2015) 1158–1170. https://doi.org/10.1016/S1003-6326(15)63711-6.

[207] M.S. Parvizi, A. Aladjem, J.E. Castle, Behaviour of 90–10 cupronickel in sea water, Int. Mater. Rev. 33 (1988) 169–200. https://doi.org/10.1179/imr.1988.33.1.169.

[208] G.T. Burstein, G. Gao, The 1st Stages of Dezincification of Freshly Generated Brass Surfaces in Sulfuric-Acid-Solution, J. Electrochem. Soc. 141 (1994) 912–921. https://doi.org/10.1149/1.2054857.

[209] F. Mansfeld, G. Liu, H. Xiao, C.H. Tsai, B.J. Little, The corrosion behavior of copper alloys, stainless steels and titanium in seawater, Corros. Sci. 36 (1994) 2063–2095. https://doi.org/10.1016/0010-938X(94)90008-6.

[210] S.H.& S.M. M. Yamashita , T. Mimaki, Intergranular corrosion of copper and α-Cu-Al alloy bicrystals, Philos. Mag. A. 63 (1991) 695–705.

[211] M. Yamashita, T. Mimaki, S. Hashimoto, S. Miura, Stress corrosion cracking of [110] and [100] tilt boundaries of α-Cu-Al alloy, Philos. Mag. A Phys. Condens. Matter, Struct. Defects Mech. Prop. 63 (1991) 707–726.

[212] K.F. Khaled, Studies of the corrosion inhibition of copper in sodium chloride solutions using chemical and electrochemical measurements, Mater. Chem. Phys. 125 (2011) 427–433. https://doi.org/10.1016/j.matchemphys.2010.10.037.

[213] Z.Z. Tasic, M.B. Petrovic Mihajlovic, M.B. Radovanovic, A.T. Simonovic, M.M. Antonijevic, Cephradine as corrosion inhibitor for copper in 0.9% NaCl solution, J. Mol. Struct. 1159 (2018) 46–54. https://doi.org/10.1016/j.molstruc.2018.01.031.

[214] A.K. Satpati, A.V.R. Reddy, Electrochemical Study on Corrosion Inhibition of Copper in Hydrochloric Acid Medium and the Rotating Ring-Disc Voltammetry for Studying the Dissolution, Int. J. Electrochem. 2011 (2011) 1–8. https://doi.org/10.4061/2011/173462.

[215] A. Carreon-Alvarez, R.C. Valderrama, J.A. Martínez, A. Estrada-Vargas, S. Gómez-Salazar, M. Barcena-Soto, N. Casillas, Corrosion of aluminum, copper, brass and stainless steel 304 in tequila, Int. J. Electrochem. Sci. 7 (2012) 7877–7887.

[216] Y. Chen, D.M. Qi, H.P. Wang, Z. Xu, C.X. Yi, Z. Zhang, Corrosion behavior of aluminum bronze under thin electrolyte layers containing artificial seawater, Int. J. Electrochem. Sci. 10 (2015) 9056–9072. https://doi.org/10.1007/s00595-006-3290-x.

[217] Z. Qin, Z. Wu, X. Zen, Q. Luo, L. Liu, W. Lu, W. Hu, Improving corrosion resistance of a nickel-aluminum bronze alloy via nickel ion implantation, Corrosion. 72 (2016) 1269–1280. https://doi.org/10.5006/2097.

[218] H. Nady, N.H. Helal, M.M. El-Rabiee, W.A. Badawy, The role of Ni content on the stability of Cu-Al-Ni ternary alloy in neutral chloride solutions, Mater. Chem. Phys. 134 (2012) 945–950. https://doi.org/10.1016/j.matchemphys.2012.03.096.

[219] W.A. Badawy, M.M. El-Rabiei, H. Nady, Synergistic effects of alloying elements in Cu-ternary alloys in chloride solutions, Electrochim. Acta. 120 (2014) 39–45. http://linkinghub.elsevier.com/retrieve/pii/S0013468613024833.

[220] G. Joseph, K.J.A. Kundig, I.C. Association, Copper: Its Trade, Manufacture, Use, and

Environmental Status, ASM International, 1998.

[221] C.D.A. Pub, Resistance to Wear of Aluminium Bronzes Resistance to Wear of Aluminium Bronzes, Copp. Dev. Assoc. (2000).

[222] J.H. Cooper, Bearing materials for earthmoving equipment, in: SAE Tech. Pap., 1983. https://doi.org/10.4271/830818.

[223] T.A. Blanchet, S.J. Shaffer, A.-C. Christiaen, J.M. Kolly, Grease-lubricated wear of aluminum bronze for jackscrew application, Wear. 255 (2003) 1238–1250.

[224] M.Z. Hussain, U. Khan, R. Jangid, S. Khan, Hardness and wear analysis of Cu/ Al_2O_3 composite for application in EDM electrode, in: IOP Conf. Ser. Mater. Sci. Eng., 2018. https://doi.org/10.1088/1757-899X/310/1/012044.

[225] A.K. Khanra, B.R. Sarkar, B. Bhattacharya, L.C. Pathak, M.M. Godkhindi, Performance of ZrB_2-Cu composite as an EDM electrode, J. Mater. Process. Technol. 183 (2007) 122–126. https://doi.org/10.1016/j.jmatprotec.2006.09.034.

[226] Z.J. Jin, M. Zhang, D.M. Guo, R.K. Kang, Electroforming of copper/ZrB_2 composite coating and its performance as electro-discharge machining electrodes, Key Eng. Mater. 291–292 (2005) 537–542. https://doi.org/10.4028/www.scientific.net/kem.291-292.537.

[227] Y. Xiao, Z. Zhang, P. Yao, K. Fan, H. Zhou, T. Gong, L. Zhao, M. Deng, Mechanical and tribological behaviors of copper metal matrix composites for brake pads used in high-speed trains, Tribol. Int. 119 (2018) 585–592. https://doi.org/10.1016/j.triboint.2017.11.038.

[228] T. Ram Prabhu, V.K. Varma, S. Vedantam, Tribological and mechanical behavior of multilayer Cu/SiC + Gr hybrid composites for brake friction material applications, Wear. 317 (2014) 201–212. https://doi.org/10.1016/j.wear.2014.06.006.

[229] M. Sam, N. Radhika, Development of functionally graded Cu–Sn–Ni/ Al_2O_3 composite for bearing applications and investigation of its mechanical and wear behavior, Part. Sci. Technol. 37 (2019) 220–231. https://doi.org/10.1080/02726351.2017.1364312.

[230] S. Norasetthekul, P.T. Eubank, W.L. Bradley, B. Bozkurt, B. Stucker, Use of zirconium diboride-copper as an electrode in plasma applications, J. Mater. Sci. 34 (1999) 1261–1270. https://doi.org/10.1023/A:1004529527162.

[231] D.S. Zhou, D.L. Zhang, C. Kong, P. Munroe, Factors controlling the tensile properties of ultrafine structured Cu-5vol% Al_2O_3 nanocomposite prepared by high energy mechanical milling and powder compact extrusion, Mater. Sci. Eng. A. 584 (2013) 67–72. https://doi.org/10.1016/j.msea.2013.07.005.

[232] M.F. Giordana, N. Munoz-vasquez, M. Garro-gonzalez, M.R. Esquivel, Study of the formation of Cu-24at .% Al by reactive milling, Procedia Mater. Sci. 9 (2015) 262–270. https://doi.org/10.1016/j.mspro.2015.04.033.

[233] R.H. Palma, A.H. Sepúlveda, R.A. Espinoza, R.C. Montiglio, Performance of Cu-TiC alloy electrodes developed by reaction milling for electrical-resistance welding, J. Mater. Process. Technol. 169 (2005) 62–66. https://doi.org/10.1016/j.jmatprotec.2005.02.260.

[234] F. Wang, Y. Li, K. Yamanaka, K. Wakon, K. Harata, A. Chiba, Influence of two-step ball-milling condition on electrical and mechanical properties of TiC-dispersion-

strengthened Cu alloys, Mater. Des. 64 (2014) 441–449. https://doi.org/10.1016/j.matdes.2014.08.027.

[235] Copper Development Association, Equilibrium Diagrams the major types of phase transformation, 1992.

[236] H. Baker, A.S.M. Handbook, Vol. 3: Alloy Phase Diagrams, 1992.

[237] Massalski T, Binary Alloy Phase Diagrams, AIP, Materials Park, Ohio, 1990. https://doi.org/10.1063/1.1306229.

[238] V. Raghavan, Physical Metallurgy: Principles and practice, Third edition:, Prentice Hall India Pvt., Limited, 2015.

[239] H.M. Otte, X-Ray diffraction line shifts in the Debye-Scherrer pattern from wire specimens with preferred orientation, J. Appl. Phys. 33 (1962) 2892–2893. https://doi.org/10.1063/1.1702573.

[240] J.S. Llewelyn Leach, On the structure of a phase formed in copper-aluminum alloys at low temperatures, J. Inst. Met. 92 (1964) 93–94.

[241] W. He, E. Wang, L. Hu, Y. Yu, H. Sun, Effect of extrusion on microstructure and properties of a submicron crystalline Cu–5wt.%Cr alloy, J. Mater. Process. Technol. 208 (2008) 205–210. https://doi.org/10.1016/j.jmatprotec.2007.12.107.

[242] A. Khorsand Zak, W.H. Abd. Majid, M.E. Abrishami, R. Yousefi, X-ray analysis of ZnO nanoparticles by Williamson–Hall and size–strain plot methods, Solid State Sci. 13 (2011) 251–256. https://doi.org/10.1016/j.solidstatesciences.2010.11.024.

[243] S.F. Varol, G. Babur, G. Cankaya, U. Kolemen, Synthesis of sol–gel derived nano-crystalline ZnO thin films as TCO window layer: effect of sol aging and boron, RSC Adv. 4 (2014) 56645–56653. https://doi.org/10.1039/c4ra11324a.

[244] Y. Han, J. Fan, T. Liu, H. Cheng, J. Tian, The effects of ball-milling treatment on the densification behavior of ultra-fine tungsten powder, Int. J. Refract. Met. Hard Mater. 29 (2011) 743–750. https://doi.org/10.1016/j.ijrmhm.2011.06.010.

[245] B. Kieback, W. Hermel, Mechanical stresses and dislocation density in the contact zone between sintering particles, in: Tagungsband Pm-Gr. Meet., 1984: pp. 1–11.

[246] W.C. Oliver, G.M. Pharr, An improved technique for determining hardness and elastic modulus using load and displacement sensing indentation experiments, J. Mater. Res. 7 (1992) 1564–1583. https://doi.org/10.1557/JMR.1992.1564.

[247] R. Saha, W.D. Nix, Effects of the substrate on the determination of thin film mechanical properties by nanoindentation, Acta Mater. 50 (2002) 23–38. https://doi.org/10.1016/S1359-6454(01)00328-7.

[248] D.M. Ebenstein, L.A. Pruitt, Nanoindentation of biological materials, Nano Today. 1 (2006) 26–33. https://doi.org/10.1016/S1748-0132(06)70077-9.

[249] L.L. Wu, L. Liu, M.S. Qi, J.H. Liu, R.J. Zhang, Effects of cryogenic treatment on micro-mechanical properties of a Cu-Al alloy, in: Adv. Mater. Res., Trans Tech Publ, 2012: pp. 196–199. https://doi.org/10.4028/www.scientific.net/AMR.562-564.196.

[250] P. Kucita, S.C. Wang, W.S. Li, R.B. Cook, M.J. Starink, Microstructure characterization

of hypereutectoid aluminium bronze composite coating, in: J. Phys. Conf. Ser., IOP Publishing, 2015: p. 12010. https://doi.org/10.1088/1742-6596/644/1/012010.

[251] J. Chen, Y.N. Shi, K. Lu, Strain rate sensitivity of a nanocrystalline Cu–Ni–P alloy, J. Mater. Res. 20 (2005) 2955–2959. https://doi.org/10.1557/JMR.2005.0387.

[252] R.R. Chromik, R.P. Vinci, S.L. Allen, M.R. Notis, Nanoindentation measurements on Cu–Sn and Ag–Sn intermetallics formed in Pb-free solder joints, J. Mater. Res. 18 (2003) 2251–2261. https://doi.org/10.1557/JMR.2003.0314.

[253] J.Y. Zhang, J.T. Zhao, X.G. Li, Y.Q. Wang, K. Wu, G. Liu, J. Sun, Alloying effects on the microstructure and mechanical properties of nanocrystalline Cu-based alloyed thin films: Miscible Cu-Ti vs immiscible Cu-Mo, Acta Mater. 143 (2018) 55–66. https://doi.org/10.1016/j.actamat.2017.09.039.

[254] F. Misjak, P.B. Barna, A.L. Toth, T. Ujvari, I. Bertoti, G. Radnoczi, Structure and mechanical properties of Cu–Ag nanocomposite films, Thin Solid Films. 516 (2008) 3931–3934. https://doi.org/10.1016/j.tsf.2007.07.202.

[255] B.J. Briscoe, L. Fiori, E. Pelillo, Nano-indentation of polymeric surfaces, J. Phys. D. Appl. Phys. 31 (1998) 2395. https://doi.org/10.1088/0022-3727/31/19/006.

[256] M.M. Shokrieh, M.R. Hosseinkhani, M.R. Naimi-Jamal, H. Tourani, Nanoindentation and nanoscratch investigations on graphene-based nanocomposites, Polym. Test. 32 (2013) 45–51. https://doi.org/10.1016/j.polymertesting.2012.09.001.

[257] D. Beegan, S. Chowdhury, M.T. Laugier, Work of indentation methods for determining copper film hardness, Surf. Coatings Technol. 192 (2005) 57–63. https://doi.org/10.1016/j.surfcoat.2004.02.003.

[258] S.-R. Jian, C.-H. Tasi, S.-Y. Huang, C.-W. Luo, Nanoindentation pop-in effects of Bi_2Te_3 thermoelectric thin films, J. Alloys Compd. 622 (2015) 601–605. https://doi.org/10.1016/j.jallcom.2014.10.133.

[259] B. Lauterbach, D. Gross, Crack growth in brittle solids under compression, Mech. Mater. 29 (1998) 81–92. https://doi.org/10.1016/S0167-6636(97)00069-0.

[260] E. van der Heide, E.D. Stam, H. Giraud, G. Lovato, N. Akdut, F. Clarysse, P. Caenen, I. Heikillä, Wear of aluminium bronze in sliding contact with lubricated stainless steel sheet material, Wear. 261 (2006) 68–73. http://www.sciencedirect.com/science/article/pii/S0043164805004771.

[261] P.J. Blau, Friction science and technology: From concepts to applications, second edition, 2008.

[262] A. Moshkovich, V. Perfilyev, I. Lapsker, L. Rapoport, Friction, wear and plastic deformation of Cu and α/β brass under lubrication conditions, Wear. 320 (2014) 34–40. https://doi.org/10.1016/j.wear.2014.08.016.

[263] R.A. Poggie, J.J. Wert, The role of oxidation in the friction and wear behavior of solid solution Cu-Al alloys in reciprocating sliding contact with sapphire and D2 tool steel, Wear. 156 (1992) 315–326. https://doi.org/10.1016/0043-1648(92)90225-W.

[264] F. Ren, W. Zhu, K. Chu, C. Zhao, Tribological and corrosion behaviors of bulk Cu-W nanocomposites fabricated by mechanical alloying and warm pressing, J. Alloys Compd.

676 (2016) 164–172. https://doi.org/10.1016/j.jallcom.2016.03.141.

[265] H. Sarmadi, A.H. Kokabi, S.M. Seyed Reihani, Friction and wear performance of copper–graphite surface composites fabricated by friction stir processing (FSP), Wear. 304 (2013) 1–12. https://doi.org/10.1016/j.wear.2013.04.023.

[266] A. Sinha, Z. Farhat, Effect of Surface Porosity on Tribological Properties of Sintered Pure Al and Al 6061, Mater. Sci. Appl. 06 (2015) 549–566. https://doi.org/10.4236/msa.2015.66059.

[267] M.D. Sanderson, J.C. Scully, Protective oxide formation on Cu-7.5Al-2Si alloy, Metall. Mater. Trans. 1 (1970) 1273–1279. https://doi.org/10.1007/BF02900243.

[268] R.A. Poggie, J.J. Wert, L.A. Harris, The effects of surface oxidation and segregation on the adhesional wear behavior of aluminum-bronze alloys, J. Adhes. Sci. Technol. 8 (1994) 11–28. https://doi.org/10.1163/156856194X00023.

[269] G. Kear, B.D. Barker, F.C. Walsh, Electrochemical corrosion of unalloyed copper in chloride media -- a critical review, Corros. Sci. 46 (2004) 109–135. https://doi.org/10.1016/S0010-938X(02)00257-3.

[270] S. Chen, D. Zhang, Study of corrosion behavior of copper in 3.5 wt.% NaCl solution containing extracellular polymeric substances of an aerotolerant sulphate-reducing bacteria, Corros. Sci. 136 (2018) 275–284. https://doi.org/10.1016/j.corsci.2018.03.017.

[271] R. Vedalakshmi, V. Saraswathy, H.W. Song, N. Palaniswamy, Determination of diffusion coefficient of chloride in concrete using Warburg diffusion coefficient, Corros. Sci. 51 (2009) 1299–1307. https://doi.org/10.1016/j.corsci.2009.03.017.

[272] K. Miyake, Y. Hirata, T. Shimonosono, S. Sameshima, The effect of particle shape on sintering behavior and compressive strength of porous alumina, Materials (Basel). 11 (2018). https://doi.org/10.3390/ma11071137.

[273] A. Ekpy, S. Saritap, Effects of powder hardness and particle size on the densification of cold isostatically pressed powders, Turkish J. Eng. Environ. Sci. 26 (2002) 377–384. https://doi.org/10.3906/sag-1206-65.

[274] M. Divandari, A.R. Vahid Golpayegani, Study of Al/Cu rich phases formed in A356 alloy by inserting Cu wire in pattern in LFC process, Mater. Des. 30 (2009) 3279–3285. https://doi.org/10.1016/j.matdes.2009.01.008.

[275] P. Rojas, R. Vera, C. Martínez, M. Villarroel, Effect of the Powder Metallurgy Manufacture Process on the Electrochemical Behaviour of Copper, Nickel and Copper-Nickel Alloys in Hydrochloric Acid, Int. J. Electrochem. Sci. 11 (2016) 4701–4711.

[276] W.S. Li, Z.P. Wang, Y. Lu, Y.H. Jin, L.H. Yuan, F. Wang, Mechanical and tribological properties of a novel aluminum bronze material for drawing dies, Wear. 261 (2006) 155–163. http://www.sciencedirect.com/science/article/pii/S0043164805004667.

[277] P.K. Jayakumar, K. Balasubramanian, G.R. Tagore, Recrystallisation and bonding behaviour of ultra fine grained copper and Cu–Cr–Zr alloy using ECAP, Mater. Sci. Eng. A. 538 (2012) 7–13.

[278] V. Rajkovic, D. Bozic, M.T. Jovanovic, Characteristics of Cu- Al_2O_3 composites of various starting particle size obtained by high-energy milling, J. Serbian Chem. Soc. 74

(2009) 595–605.

[279] M. Rahimi Pouyani, M. Rajabi, Microwave-assisted synthesis of Cu–ZrB_2 MM Nano-composite using double pressing double sintering method, J. Mater. Sci. Mater. Electron. 30 (2019) 266–276. https://doi.org/10.1007/s10854-018-0289-1.

[280] R. Li, H. Kang, Z. Chen, G. Fan, C. Zou, W. Wang, S. Zhang, Y. Lu, J. Jie, Z. Cao, T. Li, T. Wang, A promising structure for fabricating high strength and high electrical conductivity copper alloys, Sci. Rep. 6 (2016) 1–9. https://doi.org/10.1038/srep20799.

[281] Nc. Kaushik, C. Sri Chaitanya, R.N. Rao, Abrasive grit size effect on wear depth of stir cast hybrid Al–Mg–Si composites at high stress condition, Proc. Inst. Mech. Eng. Part J J. Eng. Tribol. 232 (2018) 672–684. https://doi.org/10.1177/1350650117726182.

[282] P.J. Blau, On the nature of running-in, Tribol. Int. 38 (2005) 1007–1012. https://doi.org/10.1016/j.triboint.2005.07.020.